Surface Microlenses for Enhanced Photodegradation of Organic Contaminants in Water

by

Qiuyun Lu

A thesis submitted in partial fulfillment of the requirements for the degree of

Doctor of Philosophy

in

Chemical Engineering

Department of Chemical and Materials Engineering
University of Alberta

Abstract

The global need for clean water requires sustainable technology for purifying contaminated water. Highly efficient solar-driven photodegradation is a sustainable strategy for wastewater treatment. However, solar-driven water treatment suffers from reduced efficiency due to the energy loss in the light treatment, difficulties of facility maintenance, and decentralized and intermittent features of solar irradiation. One promising solution is coupling microlenses (MLs) with solar-driven reactors, optimizing the distribution of solar irradiation in contaminated water for higher photodegradation efficiency of organic contaminants. However, the fabrication of customized MLs for solar-water treatment remains to be developed. Furthermore, understandings of the mechanisms of MLs-enhanced photodegradation are required for the optimization of MLs-involved reactors. Last but not least, the adaptability and scalability of MLs need to be verified before the practical applications of the technology.

This Ph.D. thesis focuses on understanding the mechanisms of MLs-enhanced photodegradation in water treatment and maximizing the performance of MLs under the guidance of the discovered principles. On one hand, the fabrication methods of MLs are developed based on a solvent exchange process followed by in-situ photopolymerization to meet the requirements of reactors for solar-driven water decontamination. Both microscopy and optical simulations are applied to characterize the optical properties of different types of MLs. Furthermore, the photodegradation of multiple typical organic pollutants in different water matrices is monitored in the MLs-functionalized reactors under varied irradiation conditions to verify the effectiveness of MLs. The combination of optical simulations and the experimental results helps to further im-

prove the efficiency of solar-driven photodegradation by MLs and assist the design of MLs-functionalized reactors for broader applications.

This thesis will start with an Introduction, then a Literature review. The main findings are covered in Chapter 3 to 6.

In Chapter 3, we successfully improve the photodegradation efficiency of micropollutants in water by $\sim$ 2-24 times with leveraging polymeric MLs. Photodegradation efficiency (η) in water correlates approximately linearly with the sum of the intensity from all focal points of MLs, although no differences in the photodegradation pathway are detected from the chemical analysis of the byproducts. With the same overall power over a given surface area, η is doubled by using ordered microlens arrays (MLA), compared to heterogeneous MLs on an unpatterned substrate. Higher η from MLAs may be attributed to a coupled effect from the focal points on the same plane that creates high local concentrations of active species to further speed up the rates of photodegradation. Three representative micropollutants (norfloxacin, sulfadiazine, and sulfamethoxazole) in the bottles functionalized by MLs were photodegraded by 30% to 170% faster than in bare bottles. The findings demonstrate the possible mechanisms of MLs-enhanced photodegradation and suggest the potential of MLs in developing highly efficient and compact solar water purification devices.

In Chapter 4, we have demonstrated that surface MLs not only work in direct photodegradation but also contribute to more efficient photocatalytic water decontamination. Both random microlenses (MLR) and microlenses array (MLA) could enhance the η in photocatalytic degradation of four representative pollutants, including methyl orange (MO), norfloxacin (NFX), sulfadiazine (SFD), sulfamethoxazole (SMX), spiked in ultra-pure water, synthetic natural water, or real river water. Under both visible LED light and simulated solar light and for two photocatalysts zinc oxide (ZnO) and titanium dioxide (TiO_2), higher η is observed in the presence of MLs. Our findings suggest that the enhancement factor by MLs becomes higher at lower catalyst concentrations, or at lower light intensity. By controlling the conditions of light treatment, η could be enhanced by up to 402%. Based on optical simulations and experimental results, we demonstrate that the enhancement of photocatalytic degradation by surface MLs surface MLs comes from the promoted formation of active species since the light distribution in the water phase has been optimized. Therefore, the use of MLs may serve as a novel strategy to improve the photocatalytic degradation of micropollutants, especially in places where the available light source is weak, such as indoors or in cloudy regions.

In Chapter 5, the fabrication of surface MLs has been expanded from 2D to 3D space, enabling more flexible utilization of MLs in solar-water reactors. With this flexible and scalable method, precursor microdroplets form in a dilution process and are converted to MLs by photopolymerization. The surface coverage and size distribution of MLs on curved surfaces can be adjusted by varying the solution concentration and the dilution rate when generating microdroplets. In addition, larger scale fabrication of MLs in a larger scale is achieved over an area up to 250 cm^2. We find that surface MLs on all-shaped reactors significantly enhance the η of organic contaminants under simulated solar light or natural indoor light, with a maximum improvement of 83 folds. Optical simulations and experiments are combined to establish the correlation between the optical properties of MLs and the performance of ML-functionalized reactors in photodegradation. MLs on 3D curved surfaces fabricated by the technique enables significantly enhanced, highly customized, and sustainable solar-driven water treatment.

In Chapter 6, taking advantage of the aforementioned work, we develop a highly-tunable and scalable method to fabricate convex and concave MLAs with variable curvatures. The convex MLAs are prepared through multiple rounds of solvent change and local photopolymerization. With soft lithography, concave MLAs with adjustable curvatures are obtained by repeatedly imprinting the structure of convex MLAs on PDMS films. Focusing effects of both convex MLAs and concave MLAs are demonstrated by the 3D intensity profiles by confocal microscopy, which is consistent with

the optical simulation results. The enhanced photodegradation efficiency of organic pollutants using either convex or concave MLAs is attributed to the much higher intensity at focal points, which is dependent on the strength of focusing effects of MLAs with different curvatures. The presence of convex or concave MLAs leads to up to 5.4-fold higher degradation efficiency of organic contaminants. Compared with convex MLAs, the unique features of concave MLAs embedded in PDMS films, such as flexibility, stability, and reproducibility, make the concave MLAs more suitable for practical applications. The obvious enhancement observed by concave MLAs under irradiation with lower intensity, in real river water, or in water with high turbidity, further verifies the potential of the concave MLAs in broader applications.

This thesis concludes with the mechanisms of MLs-involved photolysis and photocatalytic degradation, supported by both experimental findings and simulation results. The study also encompasses an investigation into how parameters during the solvent exchange or dilution process affect the shape, size, and arrangement of MLs, thereby enhancing our understanding in this area. Through a quantitative analysis of the strength of MLs focusing effects, the properties of MLs can be effectively adjusted to maximize their performance in enhancing the photodegradation efficiency of organic contaminants in water. Furthermore, the scale-up fabrication of MLs is realized and can be expanded to 3D space. This significant advancement broadens the possible applications of MLs in various types of solar-driven reactors for water treatment.

Preface

This thesis is an original work by Qiuyun Lu, which is composed of several papers that have been published, submitted, or are under preparation.

Published Journal Papers:

1. **Qiuyun Lu**, Qiwei Xu, Jia Meng, Zuo Tong How, Pamela Chelme-Ayala, Xihua Wang, Mohamed Gamal El-Din*, Xuehua Zhang*. Surface Microlenses for Much More Efficient Photodegradation in Water Treatment. *ACS ES&T Water*, 2022, 2(4), 644-657.

Qiuyun Lu performed the experiments and data analysis, and wrote the manuscript. Qiwei Xu helped with the optical simulations. Jia Meng assisted with the fabrication of prepatterned substrate with photolithography. Zuo Tong How assisted with the water sample analysis. Pamela Chelme-Ayala supported the revision of the manuscript. Mohamed Gamal El-Din and Xuehua Zhang was involved in the experimental design and supervised the work. All the authors contributed to the discussion and commented on the manuscript.

2. **Qiuyun Lu**, Lingling Yang, Pamela Chelme-Ayala, Yanan Li, Xuehua Zhang*, Mohamed Gamal El-Din*. Enhanced Photocatalytic Degradation of Organic Contaminants in Water by Highly Tunable Surface Microlenses. *Chemical Engineering Journal*, 2023, 463, 142345.

Qiuyun Lu performed the experiments, optical simulations, data analysis, and wrote the manuscript. Lingling Yang helped with the water sample analysis. Pamela

Chelme-Ayala supported the revision of the manuscript. Yanan Li assisted with the fabrication of prepatterned substrate with photolithography. Mohamed Gamal El-Din and Xuehua Zhang was involved in the experimental design and supervised the work. All the authors contributed to the discussion and commented on the manuscript.

Submitted Journal Paper:

1. **Qiuyun Lu**, Pranav Khanna, Pamela Chelme-Ayala, Ben Bin Xu, Mohamed Gamal El-Din*, Xuehua Zhang*. Scalable and Facile Formation of Microlenses on Curved Surfaces Enabling a Highly Customized Sustainable Solar-Water Nexus. Submitted to *Small Methods*.

Qiuyun Lu performed the experiments, optical simulations, data analysis, and wrote the manuscript. Pranav Khanna assisted with the sample preparation and data analysis. Pamela Chelme-Ayala supported the revision of the manuscript. Ben Bin Xu helped with the concept development and figure revision. Mohamed Gamal El-Din and Xuehua Zhang was involved in the experimental design and supervised the work. All the authors contributed to the discussion and commented on the manuscript.

Paper in preparation:

1. **Qiuyun Lu**, Yanan Li, Ben Bin Xu, Mohamed Gamal El-Din*, Xuehua Zhang*. Convex and concave microlens arrays with tunable curvatures for enhanced photodegradation of organic pollutants in water: a contact or non-contact approach. In preparation.

Qiuyun Lu performed the experiments, optical simulations, data analysis, and wrote the manuscript. Yanan Li assisted with the fabrication of prepatterned substrate with photolithography. Yanan Li assisted with the fabrication of prepatterned substrate with photolithography. Mohamed Gamal El-Din and Xuehua Zhang was involved in the experimental design and supervised the work. All the authors contributed to the discussion and commented on the manuscript.

Co-authored Papers:

1. Wei, Zixiang*, Tulsi Satyavir Dabodiya, Jian Chen, **Qiuyun Lu**, Jiasheng Qian, Jia Meng, Hongbo Zeng, Hui Qian, and Xuehua Zhang. "In-situ fabrication of metal oxide nanocaps based on biphasic reactions with surface nanodroplets." *Journal of Colloid and Interface Science*, 2022, 608, 2235-2245.

2. Dabodiya, Tulsi Satyavir, Somasekhara Goud Sontti, Zixiang Wei, **Qiuyun Lu**, Romain Billet, Arumugam Vadivel Murugan, and Xuehua Zhang*. Ultrasensitive Surface-Enhanced Raman Spectroscopy Detection by Porous Silver Supraparticles from Self–Lubricating Drop Evaporation. *Advanced Materials Interfaces*, 2022, 2201998.

3. Wang, Hui, Razieh Firouzi-Haji, Maryam Aghajamali, Mariana Arpini Vieira, Jae-Young Cho, **Qiuyun Lu**, Xuehua Zhang, Adam Johan Bergren, Jonathan G. C. Veinot, Hassan Hassanzadeh, and Alkiviathes Meldrum*. Graphene Quantum Dot Bearing Liquid Droplets for Ultrasensitive Fluorescence-Based Detection of Nitroaromatics. *ACS Applied Nano Materials*, 2022, 5. 10, 14639-14645.

Acknowledgments

When I recall my four-year Ph.D. career, I am filled with gratitude for the unwavering support and assistance I have received from numerous individuals.

First and foremost, I would like to express my sincere appreciation to my esteemed supervisors, Professor Xuehua Zhang and Professor Mohamed Gamal El-Din. Your invaluable guidance, strong support, infinite patience, and constant encouragement have been instrumental throughout my Ph.D. study. The wealth of knowledge you have imparted to me, encompassing the true essence of research, a thirst for the unknown, critical thinking abilities, academic writing and problem-solving skills, project management expertise, and adherence to academic ethics, will forever be kept in my heart and memory, empowering me in my future endeavors.

I extend my deep gratitude to Dr. Qiwei Xu, Dr. Jia Meng, Yanan Li, Dr. Lingling Yang, Dr. Zuo Tong How, and Dr. Pamela Chelme-Ayala for their precious suggestions, assistance, and encouragement in my research projects. I am also grateful to Professor Xu Bin Ben from Northumbria University, UK, and Professor Xihua Wang from University of Alberta, Canada, whose indispensable advice greatly contributed to my work. Additionally, I would like to acknowledge the inspiring contributions of Pranav Khanna during his DRA projects, which played a significant role in advancing my research. Furthermore, I would like to express my sincere appreciation to numerous fellow researchers in the relevant fields, including but not limited to Dr. Lei Bao, Dr. Brendan Dyett, Dr. Lei Lei, Dr. Haitao Yu, Dr. Ziyang Lu, and many others.

My heartfelt thanks go to my helpful and intelligent colleagues, including but not limited to Dr. Zixiang Wei, Dr. Zhengxin Li, Yawen Gao, Hongyan Wu, Dr. Binglin

Zeng, Dr. Tulsi Dabodiya, Kehinde Kassim, Dr. Jia Li, Dr. Isaac Sánchez Montes, and all other members of the Soft Matter & Interfaces Group and Gamal Group. Their support, encouragement, and companionship over the years provided me with the strength and resilience to face and overcome challenges.

I am grateful for the support I received from the Canada First Research Excellence Fund as part of the University of Alberta's Future Energy System (FES) research initiative. Their financial support, covering research funding, tuition, and living expenses, significantly facilitated the smooth progression of my Ph.D. study. I would also like to express my gratitude to the administrative and technical staff at nanoFAB, the Institute for Oil Sands Innovation (IOSI), and the Department of Chemical Engineering at the University of Alberta for their assistance and support during my Ph.D. journey.

Finally, but most importantly, I want to express my deepest gratitude to my family and friends. To my parents and grandparents, I am incredibly thankful for their profound comprehension and unconditional affection throughout the years. To my partner, Mingze Gu, your constant solace and unshakable backing during moments of despondency and self-doubt have meant a lot to me. To my cherished friends, Dr. Xinyuan Zhang, Shuke Li, Peipei Mao, Jie Gao, and many others, I am truly appreciative of your unwavering faith in me and your genuine willingness to lend an ear when I feel upset.

Table of Contents

List of Tables

List of Figures

List of Symbols

Constants

ϵ_λ	Extinction coefficient at the wavelength of λ
ε	Molar attenuation coefficient
D	Diffusion coefficient

Latin

$\bar{U}$	Flow rate during the solvent exchange process
A	Absorbance value
a or b	Fitting parameters in Equation (3.5)
C	Concentration of analytes
$C_{MMA,0}$	Initial concentration of MMA in solution A for the solvent dilution process
f	Enhancement factor, i.e. the ratio of photodegradation efficiency with MLs to that without MLs
$f(r)$	Probability density function of lateral size of microlenses
H	Channel height of the fluidic chamber for solvent exchange
h	Height of a single microlens
I	Light intensity
I_{Total}	The sum of the light intensity at focal points of MLs within a certain area
K	Conversion constant in Equation (3.8)

L	Length of the light path
l	Bin size of lateral radius in probability density function analysis
N	Counts of microlenses
$n_{catalyst}$	Number of active species generated due to the excitation of a photocatalyst
n_{MLs}	Number of active species attributed to the focusing effect of MLs
N_{total}	Total counts of microlenses on a substrate
n_{total}	Total number of active species during photocatalytic degradation
P	Probability in probability density function analysis
Pe	Peclet number
Q	Flow rate during the solvent dilution process
r	Lateral size of a single microlens
S	Height of a single microlens
S_{Bare}	Substrate area not occupied by MLs
S_{MLs}	Substrate area occupied by MLs
S_{Total}	Total area of a MLs-functionalized substrate
t	Dilution time of the solvent dilution process
t_f	Duration of light treatment
t_R	Dilution time when V_T is the same as V_R
V_R	Volume of the reactor used in the solvent dilution process
V_{SolA}	Initial volume of solution A for the solvent dilution process
V_{SolB}	Volume of solution B used for the solvent dilution process
V_T	Total volume of all the solution consumed in the solvent dilution process

Greek

η	Area occupied by a single micorlens
λ	Wavelength of light
ϕ_λ	Quantum yield at the wavelength of λ
θ	Reverse contact angle of the ML defined in Figure 6.6

Abbreviations & Acronyms

1D	One dimensional.
2D	Two dimensional.
3D	Three dimensional.
AFM	Atomic forces microscope.
CB	Conduction band.
CBZ	Carbendazim.
COD	Chemical oxygen demand.
DMPO	5,5-Dimethyl-1-pyrroline N-oxide.
DO	Dissolved oxygen.
ESR	Electron spin resonance.
h	Hour.
HDODA	1,6-Hexanediol diacrylate.
LED	Light-emitting diode.
LMA	Lauryl methacrylate.
min	Minute.

ML(s) Microlens(es).

MLA Microlens array.

MLR Microlenses with random spatial distribution.

MMA Methyl methacrylate.

MO Methyl orange.

NFX Norfloxacin.

OTS Octadecyltrichlorosilane.

PDF Probability density function.

PDMS Polydimethylsiloxane.

PFOTS Perfluorodecyltrichlorosilane.

PHDODA Poly (1,6-Hexanediol diacrylate).

PLMA Poly (lauryl methacrylate).

PMMA Poly (methyl methacrylate).

PNIPAM Poly(N-isopropylacrylamide).

PVA Poly(vinyl alcohol).

PW Ultrapure water, produced by Milli-Q Direct 16.

RW River water.

SEM Scanning electron microscope.

SFD Sulfadiazine.

SMZ/SMX Sulfamethoxazole.

SODIS Solar water disinfection.

TIRF Total internal reflection fluorescence.

TOC Total organic carbon.

UPLC-MS Ultra-performance liquid chromatography-mass spectrum.

UV Ultraviolet light.

UV-vis UV-visible spectroscopy.

VB Valence band.

Chapter 1

Introduction

1.1 Background and motivations

Global water shortage continues to grow, resulting in limited access to fresh water among a large number of populations.[1] The huge energy consumption and the maintenance of infrastructure for water treatment make it more difficult to satisfy the water demand of human beings in remote and offshore areas[2, 3]. Integrating solar energy with water treatment techniques to improve water quality is an alternative and sustainable strategy to relieve the scarcity of water.[4, 5] Solar-driven photodegradation of organic contaminants in wastewater is one of the essential directions to explore the potential of solar energy in water treatment.[4, 6]

The key issue of photodegradation driven by solar is how to make use of sunlight more sufficiently. From the aspect of degradation mechanisms, photocatalysis has been widely discussed in recent decades.[7, 8] Photocatalysts are activated by the photons that have an energy higher than the band gap of catalysts, generating active species to initiate the subsequent degradation steps, enabling higher photodegradation efficiency of target contaminants.[9] Alternatively, optimizing the design of the solar-driven reactors for water treatment contributes to improving the utilization efficiency of solar energy. The parabolic trough, inclines plate, fiber optics, and fixed or fluidized bed have been developed to make the most of the light source and optimize the treatment process. [10–12]

However, the challenges of the practical application of solar-driven photodegradation still exist, including but not limited to the restricted conversion rates of solar energy to chemical energy[13], the difficulty in scaling up the reactor[14], and the decentralized and intermittent features of solar irradiation[15, 16]. Many novel strategies have been put forward to address those problems, among which introducing lenses into solar-driven water treatment devices is a potential one. The application of microlenses (MLs) with strong focusing effects enables the redistribution of the light within the reactor. Simultaneously, MLs can be easily integrated with diverse devices due to their small dimensions. [17, 18]

Surface microlenses (MLs) have presented outstanding focusing effects and have been widely applied in various fields.[19–26] However, the investigation of the function of MLs in the photodegradation of real pollutants in water is not conducted yet. In order to figure out the feasibility of implementing MLs for enhanced photodegradation processes, firstly, the fabrication procedure of MLs needs to be tunable and enable the integration of MLs into a reactor for light treatment. The technology that combines the solvent exchange process with a local photopolymerization step is utilized to prepare MLs with controlled properties, including varied sizes, spatial arrangements, and curvatures, and is easy to immobilize MLs on different substrates.[27–31] Secondly, the design of MLs-functionalized reactors for the photodegradation of contaminants is necessary to conduct the light treatment on the aqueous solution.

Furthermore, understanding the mechanisms of MLs-involved photodegradation processes helps to establish relationships between the properties of MLs and the photodegradation efficiency of pollutants. Based on the understanding, ML-functionalized reactors can be optimized to achieve better decontamination performance. However, the pathway of photodegradation differs with multiple factors, such as pH value, contaminant type, and the existence of certain photocatalysts. A systematic discussion on the influence of MLs on various photodegradation processes is essential.

Last but not least, the technology of fabricating surface MLs through solvent exchange still faces some challenges. For example, the MLs fabrication process is run in a confined fluidic channel, limiting the formation of microdroplets and microlenses on 1D fibers or 2D planar surfaces. Therefore, MLs prepared with this method may occupy a larger space and are hard to be coupled with reactors with complex shapes. The modification of the fabrication technology is required to broaden the application of MLs in water treatment. Notably, the scalability and durability under irradiation of MLs ought to be considered in the modified methods. A non-contact set-up by integrating concave microlens arrays (MLAs) with tunable curvatures into solar-driven reactors is also built up as a sustainable approach to enhance solar-driven photodegradation in complicated water matrices and suppressed irradiation conditions.

In this study, we investigate the impact of surface microlens arrays (MLAs) with different sizes and spatial arrangements on the photodegradation of organic contaminants in water. We study the MLs-involved direct photodegradation of organic dyes and photocatalytic degradation of antibiotics and pesticides, using both experimental and optical simulation methods. By understanding the relationship between MLs properties and their influence on photodegradation processes, we develop a highly scalable and adaptable approach to produce MLAs on 3D surfaces, resulting in functionalized reactors with improved photodegradation efficiency. Additionally, we integrate highly ordered concave MLAs with tunable curvatures into solar-driven reactors in a non-contact way for more efficient light treatment of contaminated solutions, providing a sustainable solution to enhance solar-driven photodegradation under reduced irradiation conditions.

1.2 Research objectives

With those unsolved problems and current knowledge, the main objective of this thesis is to understand the mechanisms of the photodegradation of typical organic contaminants in water influenced by surface microlenses (MLs) and how to achieve higher photodegradation efficiency based on the mechanisms. Surface MLs and MLs-functionalized reactors are customized to optimize the light distribution for higher photodegradation efficiency under different conditions.

Specifically, the main objective of this Ph.D. project can be further split into the following sub-objectives, which are listed below:

1. To understand the mechanisms of photodegradation of organic contaminants in bulk solution with surface MLs and investigate the effectiveness of MLs with varied size distribution and spatial arrangement. Different types of photodegradation, such as direct photolysis and photocatalytic degradation, will be studied.

2. To study the influence of light treatment conditions and water chemistry, including the light intensity, types and concentrations of organic contaminants, and properties of water matrices, on the effectiveness of surface MLs.

3. To develop the fabrication methods of surface MLs on 3D curved surfaces. To understand the light distribution within ML-functionalized reactors and prepare the customized reactors with more enhancement in photodegradation efficiency of organic pollutants.

4. To fully explore the potential of highly ordered microlens arrays (MLAs) in improving the photodegradation efficiency of organic contaminants by tailoring the curvatures of MLA. In addition, to design the anti-contamination reactors integrated with MLAs based on the understanding of the mechanisms of MLs-enhanced photodegradation.

1.3 Thesis outline

According to the motivations and aims of this Ph.D. project, this thesis is outlined chapter by chapter.

Chapter 1 provides a brief introduction of the background and motivations, the objectives, and the structure of the thesis.

Chapter 2 is a review of the general information relevant to this Ph.D. research. This chapter mainly reviews the background and mechanisms of photoreactions, especially photodegradation in water treatment, and photocatalytic degradation. The properties of MLs are included, while the recent advances in the fabrication and applications of MLs are introduced in this chapter.

Chapter 3 is a concept-proof section, in which the function of surface MLs to enhance the photodegradation efficiency of organic pollutants has been validated under various solution conditions. Surface MLs with varied size distribution and spatial arrangement are prepared with a solvent exchange process followed by local photopolymerization. The pathway of the typical pollutants in the presence of MLs is tracked to compare with the control group. The optical properties of MLs are analyzed by simulations. By calculating the total intensity at the focal points of MLs, the focusing effects of MLs are quantitatively expressed and correlated with the photodegradation efficiency obtained in self-assembled reactors on a lab scale.

This chapter is based on the published paper: Lu, Q., Xu, Q., Meng, J., How, Z.T., Chelme-Ayala, P., Wang, X., Gamal El-Din, M., Zhang, X. Surface Microlenses for Much More Efficient Photodegradation in Water Treatment. ACS ES&T Water, 2022, 2(4), 644-657.[32]

Chapter 4 expands the investigation of MLs-enhanced photodegradation to the photocatalytic degradation of multiple organic pollutants. Specifically, the discussion involves two commonly-used photocatalysts, ZnO and TiO_2, and examines how surface MLs influence the degradation efficiency under visible or simulated solar light. To assess the effectiveness of surface MLs when the function of photocatalysts is significantly hindered, different scenarios are simulated by adjusting the irradiation intensity, water matrices, and reactor geometry to mimic situations with limited light exposure. Additionally, the optical properties of the MLs are characterized through a combination of experimental results from confocal microscopy and optical simulations, facilitating a quantitative analysis of their ability to enhance photodegradation through their focusing effects.

This chapter is based on the published paper: Lu, Q., Yang,L., Chelme-Ayala, P., Li, Y., Zhang, X., Gamal El-Din, M. Enhanced Photocatalytic Degradation of Organic Contaminants in Water by Highly Tunable Surface Microlenses. Chemical Engineering Journal, 2023, 463, 142345 [33]

Chapter 5 develops a novel approach to producing MLs on 3D topological surfaces through a dilution process and a local polymerization step, which is modified based on the aforementioned solvent exchange process. By investigating the influence of solution components, solution amount, and flow conditions during the dilution process on MLs formation, MLs with desired size distribution and surface coverage rate can be obtained. A systematic analysis of the light paths through the curved surfaces functionalized with MLs is conducted through optical simulations. The light treatment in the MLs-functionalized reactors with diverse shapes and large scales up to 500 mL is conducted to evaluate the performance of the MLs fabricated with the new method.

This chapter is based on a manuscript under review: Lu, Q., Khanna, P., Chelme-Ayala, P., Xu, B.B., Gamal El-Din, M., Zhang, X. Scalable and Facile Formation of Microlenses on Curved Surfaces Enabling a Highly Customized Sustainable Solar-Water Nexus. (Submitted to Small Methods)

Chapter 6 explores the potential of convex and concave microlens arrays (MLAs) to enhance the photodegradation efficiency of typical organic pollutants. The curvature of convex MLAs is well controlled by adjusting the volume of each ML in femtoliter scale through multi-rounds of solvent exchange and photopolymerization on pre-patterned substrates. Concave MLAs can be repeatably prepared by imprinting convex MLAs with different curvatures on elastic PDMS films by soft lithography. Optical simulations and confocal microscopy are employed to analyze the light intensity profiles of both convex and concave MLAs under irradiation, demonstrating their focusing effects. To minimize the risk of secondary contamination, a novel non-contact solar-driven reactor equipped with concave MLAs is designed and evaluated for direct photolysis and photocatalytic degradation under normal and suppressed irradiation conditions. Based on the optical properties of MLAs and the light treatment results, the influence of curvatures on the effectiveness of convex and concave MLs is investigated.

This chapter is based on a manuscript in preparation: Lu, Q., Li, Y., Xu, B.B., Gamal El-Din, M., Zhang, X. Convex and Concave Microlens Arrays with Tunable Curvatures for Enhanced Photodegradation of Organic Pollutants in Water: A Contact or Non-contact Approach.

Chapter 7 summarizes the main conclusions of the research and prospects for the future research direction.

Chapter 2

Literature review

2.1 Fundamentals of photoreactions

Photoreaction is the main object in photochemistry. It is a kind of reaction that happens after reactants absorb photons from light irradiation becoming excited states.[34] Photoreaction is related to the nature of radiation from light sources, the properties of chemicals, and the interactions between light and chemicals.[35] The energy transported by light is determined by the properties of light, including the wavelength (or frequency), the composition of light, and the coherence of light. [35] Photon energy is inversely proportional to the wavelength. The wavelength covered in photoreactions is from 200 to 2000 nm. Among the range, the 400-800 nm region is the visible region, and the 200 to 400 nm is the ultra-violet region, including UV-A (315-400 nm), UV-B (280-315 nm) and UV-C region (200-280 nm). The UV-B light has approximately the same range as the sunlight just reaching the surface of the earth. The light with a wavelength larger than 800 nm and less than 2000 nm is the near-infrared region. Except for the wavelength of light, the composition of a light source will influence energy absorption. For example, solar light is a typical and economical polychromatic light source, while in specific cases monochromatic beam (such as a laser) is more appropriate since that the reaction is most efficient under irradiation with a specific wavelength. [36] Physically, the intensity of light is defined as the power transferred through every unit area (unit: Watt/m^2), which determines

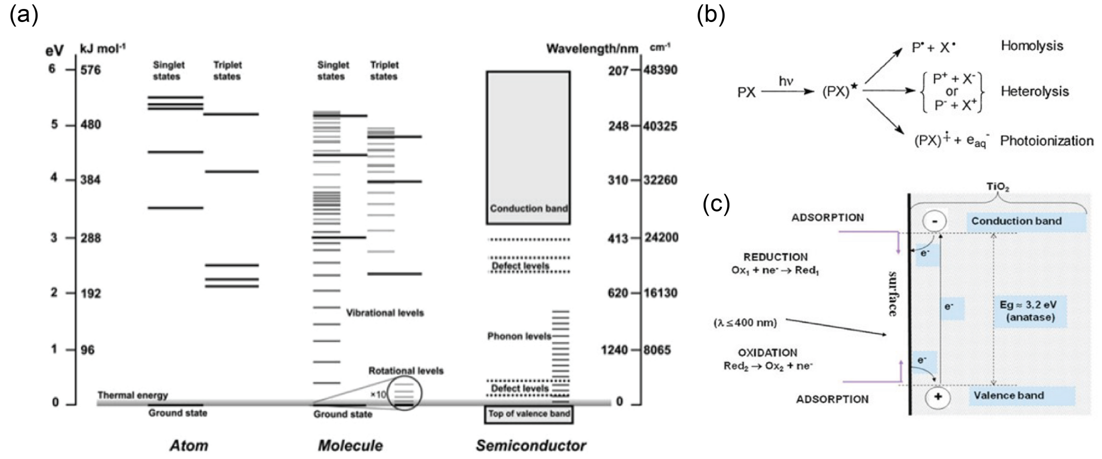

Figure 2.1: (a) The plot about the energy levels of atoms, molecules, and semiconductors. (b) Different types of direct photolysis processes (c) The schematic of the activation process of semiconductor, using titanium dioxide as an example.

the energy accepted by reaction systems.[35]

The properties of chemicals determine how they change in the decomposition process. Substances with different chemical bondings undergo different paths. Chemical bonding, or so-called intramolecular forces, includes ionic bonds, covalent bonds, and metallic bonds.[35] Generally, the covalent bonds and metallic bonds are relevant to the photodegradation of organic contaminants and photocatalytic reactions in water treatment. In the molecules formed with covalent bonds, the easiest electronic transition in molecules happens between the orbitals having the closest energy level, which is from the highest energy occupied orbital (HOMO) to the lowest energy unoccupied orbital (LUMO).[34] In species composed of metallic bonds, the molecule orbitals exist in the form of band structures. Semiconductor, a widely used type of material in photoreactions, also has energy levels with band structures. In the band structures, the band filled with electrons with lower energy is the valence band (VB) while the empty band with higher energy is the conduction band (CB), with bandgap sitting in between. The approximate data of substances with different types of chemical bonds are illustrated in Figure 2.1 (a).[35]

In photoreactions, the interactions between light and substances can be realized by the activities of photons, neutrons, electrons, and protons.[35] Through the activities of those particles, the photoreaction can be divided into several steps. Initially, chemicals absorb light and the energy in the species increases. Then the movement of electrons is excited. Finally, distinct transitions happen through different deactivation routes. Radiative and non-irradiative processes are the two types of deactivation processes. Furthermore, the non-radiative process can be classified as uni-molecular reactions (including ionization, dissociation, and isomerization) and bi-molecular reactions (i.e. quenching processes). [35]

From a macroscopic perspective, the photochemical processes can be classified into direct and indirect processes. In the direct photochemical process, the photons are absorbed by reactants, and then photoreactions proceed. In the indirect photochemical process, the target chemicals react with the active species generated by light irradiation.[37] The mechanisms of direct photoreaction can be summarized with the simplified scheme in Figure 2.1 (b), covering homolysis, heterolysis, and photoionization.[38] In indirect photoreactions, the chemicals at the ground state need to react with other excited species. If the excited species is the existing molecules, the reaction process is defined as photosensitization or quenching. If the species is the produced reactive particles from other steps, the process is photoinduced reactions. The photoreaction processes in reality tend to be a mixture of direct and indirect photoreactions. For instance, a photocatalytic reaction in water treatment is a multi-step process, which can be recognized as a cyclic photo-process. A typical mechanism of photocatalytic reactions is demonstrated in a system using titanium dioxide (TiO_2) as the catalyst in the sketch in Figure 2.1 (c). The electrons in VB of TiO_2 are excited from VB to CB after absorbing energy from light, generating electron-hole pairs. The migration of electrons and holes enables the redox reactions near the solid surface where reactants adsorb. However, the efficiency of catalysis will be weakened due to the recombination of electron-hole pairs.

Due to the abundant resource of light energy and relatively low cost to generate light, photoreactions are applied in different fields[34], such as data storage[39, 40], digital display[41], light generation[42, 43], water treatment [44], electricity generation [45], photosynthesis [36], polymerization[46, 47], medical diagnosis[48], and light-driven decontamination in wastewater [49, 50], etc. Among diverse types of light sources, sunlight especially attracts the attention of researchers as the earth receives abundant energy from solar irradiation.[51] However, improving the utilization efficiency of solar light is a challenging task in the design of light-driven water treatment devices. Understanding the mechanism of specific photochemical processes is essential for the optimization of technologies.

2.2 Progress of water treatment by photoreactions

The activities of human beings release many contaminants into the water system, which causes considerable demand and a serious shortage of clean water, attracting worldwide attention. Therefore, the recycling of wastewater is necessary to alleviate severe problems.[1–3] Lots of technologies are put forward to reuse polluted water.[9] In Alberta, a large amount of oil sands process water (OSPW) is produced when extracting bitumen from oil sands, which makes the treatment of OSPW essential for water recycling.[52] Especially, the removal of some chemicals hard to be naturally degraded, like Naphthenic acids (NAs), is a challenging problem.[53]

The overall water treatment is composed of different unit processes, including air stripping and aeration, chemical oxidation, coagulation, sedimentation and flotation, adsorption, disinfection, and light treatment.[54] Those unit processes have their advantages and preferred scenarios. Light treatment for water matrices is rapidly emerging due to its lower cost in construction and maintenance, less toxic residual, and less carbon emission. Many clean-energy technologies for water treatment benefit from photoreactions. [54] For instance, solar-based water disinfection (SODIS) utilizes solar energy to inactivate or eliminate pathogenic contaminants in water with portable containers, which is a low-cost and convenient method to provide safe household water.[55, 56] Based on the wavelength range of the light sources, the light treatment of contaminated water can be classified into the ultraviolet (UV) light treatment (Figure 2.2 (a))[57], visible light treatment[58, 59], and solar-driven treatment[60].

UV light was first found capable of inactivating microorganisms more than a century ago, then it was widely applied for biological processes of water treatment [54]. UV treatment is also effective in directive UV [61], advanced oxidation processes (AOPs) [62], and heterogeneous photocatalysis [63]. Apart from UV light, the capability of visible light has been widely investigated for decades, which means the range of light is broadened and the sunlight can be utilized more thoroughly. In some cases [8, 64], specific materials which are highly sensitive to visible light become the medium to transfer the energy from light to enable the reactions in the aqueous systems. However, those specific materials are usually well-designed in labs, which are expensive and difficult to apply in daily life and industry. Sunlight is also an important sustainable energy resource in the remediation of contaminated water, combing both visible light and partial UV light,[4, 65, 66] so a synergistic effect between UV irradiation and temperature is found in the solar-driven water decontamination.[67, 68]

Compared to conventional wastewater treatment, solar-driven photodegradation enhanced by catalysts [69–71] or sensitizers [72, 73] can be highly efficient in removing pollutants that are hardly decomposed, such as antibiotics and personal care products, while producing fewer carbon emissions and secondary pollution.[74] However, low efficiency of light energy utilization and complexity associated with scaling up the size of solar energy collectors still hinder the applications of solar energy in fast conversion processes[12, 75]. Innovative designs are needed to maximize the water decontamination efficiency of the incident solar energy per unit surface area for water purification.

Most of the reported devices for the light treatment of wastewater are bulky and complicated. However, human beings are not always in access to new materials and

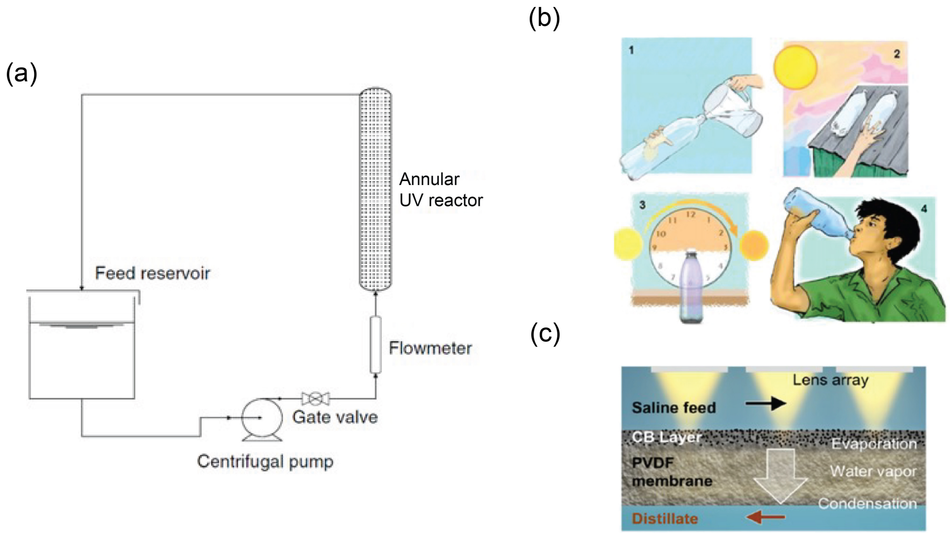

Figure 2.2: (a) The schematic of a flow-through device for UV exposure. (b) Schematic of a solar thermal membrane distillation device with lens array (c) A graphical description of the SODIS household water treatment technique.

advanced equipment, especially in rural areas.[76, 77] In order to realize the portable treatment of contaminated water, SODIS is developed for household use in regions where the drinking water is inadequate (Figure 2.2 (b)). The application of contact optical elements also contributes to the miniature of solar distillation devices. In the work of Dongare et al[78], the lens arrays were used in solar thermal membrane distillation devices (Figure 2.2 (c)), then the solar light is redistributed, realizing more efficient distribution of heat. Inspired by the design of portable reactors for solar-driven water treatment and the utilization of lenses, surface microlenses (MLs) with focusing effects are expected to be coupled with reactors to strengthen the efficiency of photodegradation. However, the scalability of fabrication, the mechanisms of MLs-enhanced photodegradation, the durability of MLs, and the toxicity of MLs materials need to be figured out in advance.

2.3 Recent advances in photocatalysis for water treatment

In many types of photoreactions[7], photocatalysis, which is the photoreactions accelerated by photocatalysts, is one of the dominant technologies to remove the organic micropollutants in natural water [79, 80]. Photocatalysis has received much attention because it is an effective approach to removing some pollutants that cannot be or are difficult to degrade in the traditional water treatment process. Photocatalysis for water treatment generally refers to the reactions with the assistance of semiconductor photocatalysts which absorb energy from photons.[81] The basic principle for photocatalytic reactions is that the catalyst can be activated by the photons whose energy is higher than the band gap.[9] Afterwards, the electron-hole pairs are generated by light illumination. Subsequently, the charge carriers separate from each other and participate in the redox reactions at the surface of catalysts. In this process, organic substances move to the surface of excited photocatalysts, inducing a series of reactions. (as shown in Figure 2.3 (a))[82, 83]. Usually, the degradation of pollutants is due to the generation of species with strong oxidizing abilities, such as hydroxyl radicals.

The semiconductor photocatalysts reported in the literature are versatile but there are some standards for choosing suitable photocatalysts in water treatment processes.[81] First, the band gap energy of catalysts should be less than the energy of absorbed photons. Second, the position of the valence band and conduction band need to enable the formation of active species to initiate the degradation of target species. The position of bands and the band gap for frequently-used semiconductors are shown in Figure 2.3 (b).[84] The third requirement is to guarantee the formation and separation of charge carriers, which is greatly influenced by the diffusion process.[85] The fourth standard is the existence of grain boundaries and the states on the surface of catalysts, which contribute to the elongation of charge carriers' lifetime.

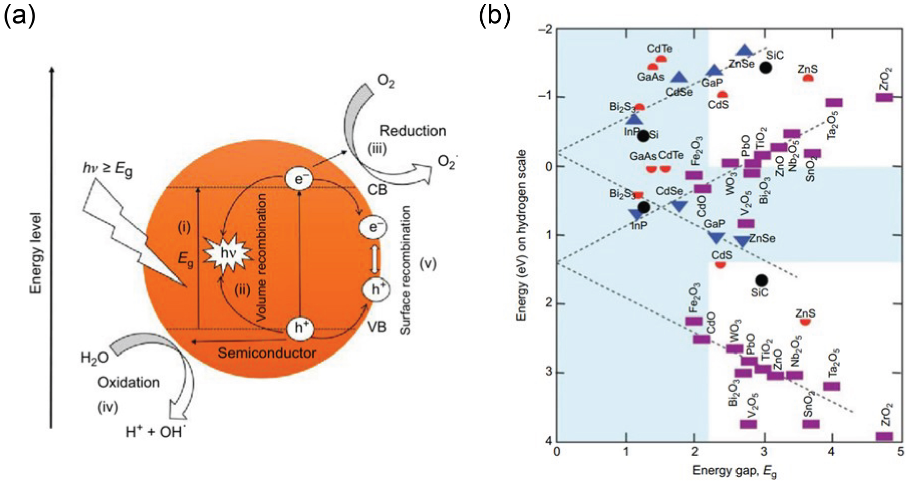

Figure 2.3: (a) The scheme of photocatalysis mechanisms (b) The plot of band gap and band positions for reported semiconductors.

The last but not least one is to ensure the strong adsorption of organic molecules onto the catalyst surface. The high specific surface of photocatalysts is favorable to the adsorption performance.

Among the reported photocatalyst, TiO_2[44] and ZnO[86] are traditional ones used in UV photocatalytic processes since they are efficient, low-cost, and non-toxic. However, the disadvantages of them are also obvious. The relatively large band gap and low absorbance of light of TiO_2 and ZnO limit the photolysis efficiency and their utilization under visible light or solar light.[9, 87] A lot of researchers have developed strategies to modify TiO_2 and ZnO for better performance. One of the modification methods is doping[88], introducing impurities into semiconductors to narrow the band gap, such as nitrogen doping[89] and carbon doping. Another method is to couple the photocatalytic degradation with dye sensitization.[90] The specific dyes with lower redox potential than semiconductors are excited by the visible light, then the electrons from excited dyes induce the generation of cationic radicals and electrons from photocatalysts. The third one is to make catalyst composites, and the catalyst with a narrower band gap leads to the secondary activation process for higher catalytic efficiency.[91] Introducing π-conjugated structures, which are contained in graphene[92],

C_3N_4[93], polyaniline[94] or polypyrrole[95], to modify photocatalysts is another alternative method to improve the performance of catalysts.[9]. Nanocomposites with tunable band gaps also attracted lots of attention, because the generation and separation of charge carriers on multiphase structures are more efficient compared with that in single-phase semiconductors[96]. Except for modifying traditional photocatalysts for enhanced catalytic efficiency, new materials that are directly responsive to visible light have been investigated as well, such as bismuth-based semiconductors[97, 98], molybdenum disulfide based materials[99, 100], and metal organic frameworks[101, 102].

One of the main reasons that restrict the development of solar-driven photocatalytic degradation of organic pollutants in the aqueous environment is the instability of solar light under different scenarios.[103, 104]. For example, sunlight is attenuated when the wastewater has high turbidity [105] or the rainy and cloudy weather appears [106]. As a result, the number of photons that can be absorbed into the system decreases, so the activity of photocatalysts is considerably inhibited. In order to maximize the potential of photocatalysts under insufficient light, strategies to increase the number of species undergoing a photo process with a given amount of photons are needed. Several strategies have been widely investigated for this purpose, including incorporating light engineering design in photoreactors to improve their performance[107, 108], establishing a flow reactor to enhance the mass transfer or shorten the light path[12], and preparing engineering photocatalytic materials for more efficient photocatalysis[109]. Introducing lenses into photoreaction systems is a potential alternative because of their ability of redistributing light.[110] The focusing effect of a lens creates high local light intensity at the focal point, accelerating the local photoreaction rates.

2.4 Fabrication and applications of microlenses

2.4.1 Focusing effect of microlenses

Lenses are optical elements made of transmissive materials with the function of focusing or dispersing light in light refraction, which is able to redistribute the light for different purposes. The nature of the focusing effect is the light redistribution of electromagnetic radiation and the effect is changeable with the features of light (light intensity, incident angle, etc.) and lens morphology. Lenses with lateral diameter from a few to hundreds μm are defined as MLs. In traditional geometric optics, the focal distance is much larger than the wavelength of light where far-field optics work well. As for MLs, near-field optics work instead of far-field optics because the influence of size on the interactions between light waves and objects is inevitable.[111] Dyett et al. have established a method to demonstrate the strong focusing effect of MLs immobilized on a planar substrate through the total internal reflection mode of confocal microscopy. [112] As illustrated in the light intensity profiles obtained by the laser scanning confocal microscopy (shown in Figure 2.4 (a) and (b)), the light intensity increases sharply within a short distance away from a single ML then exponentially decay as the distance increases. A similar conclusion has been drawn by Bao et al. as well (Figure 2.4 (c)), and they successfully fabricated the dual MLs with double focusing points enabling the control of light intensity at different depths.[30]

Previous studies have demonstrated that surface MLs can lead to spatial variations in photoreaction efficiency due to the focusing effects. One of the photo-process studied with surface MLs is the excitation of plasmonic particles.[112] In this process, the surface MLs are decorated by gold nanoparticles, and plasmonic bubbles form because the water around MLs is vaporized by the heat due to the plasmonic effect of gold particles (Figure 2.4 (d)). In comparison, there are no bubbles appear on the planar substrate under the same illumination conditions, indicating that the focusing effects of surface MLs enhance the plasmonic effect of gold particles. Another evidence of the existence of focusing effects of surface MLs is the selective deposition of silver during a photoreduction process (shown in Fig 5. (e) and (f)).[112] Silver particles tend to form in the regions with lower intensity, avoiding the deposition of particles at the spots with focusing effects.

Even though the focusing effect has been proved by the experiment results in some light-driven processes, some problems about the surface MLs in photoreactions have not been figured out, which is important for the photoreactions involved in water treatment. First of all, the study of chemical reactions enhanced by MLs is currently limited to the local surface near MLs. It remains to be understood how focusing effects from heterogeneous and homogeneous MLs impact the photodegradation efficiency of organic compounds dissolved in an aqueous solution. Besides, multiple types of photoreactions are involved in the light-driven water decontamination process, such as direct photolysis and photocatalytic degradation. The influence of surface MLs on different types of photoreactions in water treatment has not been systematically investigated yet. Furthermore, how to couple surface MLs with practical reactors for light treatment to achieve higher degradation efficiency is waiting to be addressed.

2.4.2 Recent advances in the fabrication of microlenses

Many bottom-up or top-down approaches have been developed for the fabrication of MLs, such as hot embossing [25, 113–115], inkjet printing [116], laser writing [117–120], soft lithography [121, 122], and drop-templating [123, 124]. In the mentioned methods above, hot pressing, inkjet printing, and laser writing cost more energy and require sophisticated devices in the fabrication process, and hence are costly for large-scale production of MLs for water treatment. [113] Soft lithography is a low-cost and effective method, in which an elastomeric stamp or mold is used.[121, 125] However, the use of molds restricts the modification of ML shapes and positions, which makes it tedious to optimize MLs for desired optical properties.[24] Recently an interesting droplet-templating method has been reported where concave MLs are fabricated by

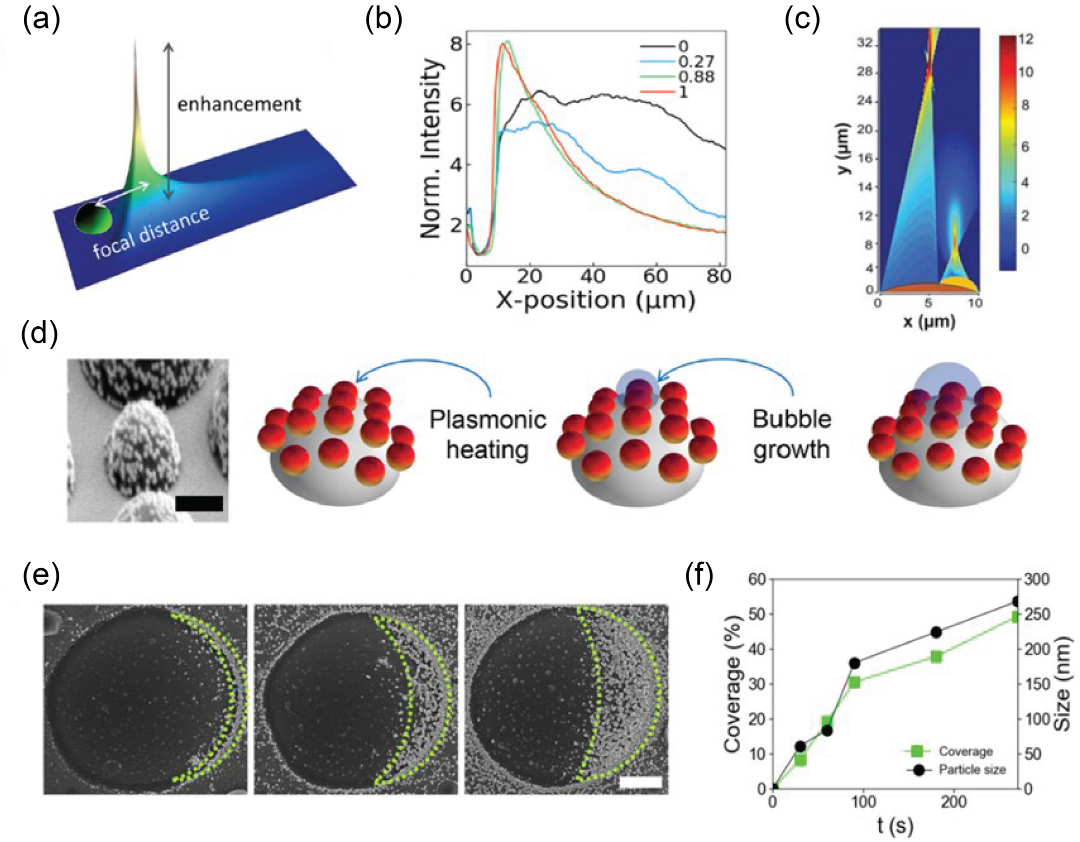

Figure 2.4: (a) 3D schematic of TIRF (total internal reflection fluorescence) image of a single PHDODA microlens. (b) The normalized intensity profile of a single PHDODA microlens at varied normalized angles of (0, 0.27, 0.88, 1). (c) Simulated results of dual microlens (the orange one is the base while the yellow one is on top). (d) Tilted SEM image of a single gold-decorated microlens (scale bar 1 μm) and the schematic of the generation process of plasmonic bubbles on the microlens. (e) The SEM images of silver particles deposited on microlens in the crescent zone with increasing reaction time from left to right (scale bar 2 μm). (f) The coverage change of silver particles on the microlens surface with time

covering curable polymers on templates of water microdroplets.[124] The curvatures of MLs are adjustable by varying the interfacial tension of water droplets at different cooling temperatures. While water droplet templating is a simple, flexible, and cost-effective method, the fluctuation in water droplet size occurs due to convection and heat transfer during water condensation, which is a common problem in the "breath figure" method[126].

Currently, most of the fabrication technologies of MLs are largely limited to flat substrates, small surface areas, and a low total number of MLs.[127] Even though MLs can be functionalized on some curved surfaces, multiple steps are required. For instance, an MLA can be prepared on a flexible poly(methyl methacrylate) (PMMA) substrate through screen printing followed by UV curing.[128] By combining a flexible mask and the reactive ion etching process, MLs were fabricated on photo-curable resin with a curved surface.[129, 130] In a multiple-templating method, arrays of MLs on a planar substrate are first copied to a flat film of siloxane elastomer that was bent into a curved template for a second round of templating.[131, 132] The technologies mentioned above are dependent on complicated devices[26, 133] and precise control of the dosage of the materials of MLs[134]. An alternative, scalable, and convenient technology is needed to functionalize curved surfaces by MLs.

Photopolymerization is one of the convenient and highly tunable methods to fabricate MLs with good uniformity. Conversion of surface microdroplets to MLs is one of the convenient and highly-tunable approaches based on the nucleation and diffusive growth of microdroplets in a solvent exchange process (Figure 2.5 (a)).[135, 136] Multiple types of monomers can be used for the preparation of MLs with the method, enabling adjustable refractive index of the polymeric MLs.[137] As most of the solvents are ethanol and water, the solvent exchange may be regarded as a green and environmentally-friendly approach with low energy cost for producing microdroplets and MLs. In this method, geometric properties and spatial arrangement of MLs are tunable by the controlling of monomer microdroplets forming in the solvent exchange process.

The solvent exchange process is based on the ouzo effect in a ternary liquid system. Solution A is prepared by dissolving monomers and photoinitiators in a good solvent or a mixture of good and poor solvents. Solution A is pumped into a specific chamber in advance. When adding a monomer-saturated poor solvent, defined as solution B, into solution A with controlled flow rates, the oversaturation of monomers will lead to the nucleation of microdroplets. The composition of solutions and the flow conditions closely influence the size of droplets. In the work by Peng et al. (shown in Figure 2.5 (d)), the larger microlenses and broader size distribution were observed with higher monomer concentration in solution A. [138] When the composition of solution A keeps the same, flow conditions within a confined fluidic chamber (Figure 2.5 (c)), including flow rate and chamber height, affect the volume of microdroplets. As shown in experiments and the interpretation of mechanisms, there is a scaling law between the average volume per area of microdroplets and Peclet number (Pe) [27] (Pe=$\bar{U}$H/D, $\bar{U}$ is the mean flow rate, H is the channel height and D is the diffusion coefficient). MLs converted from surface nanodroplets can be adjusted with the volume of an ML as small as subfemtoliters and be uniform over an entire 12-inch wafer[136].

Except for the composition of solution and flow conditions during the solvent exchange processes, the spatial arrangement and size distribution of surface microdroplets and microlenses are also dependent on the wettability of substrate surfaces. By combing photolithography technology, plasma treatment, and silane functionalization, hydrophobic domains with diverse shapes and patterns can be flexibly created on planar substrates, with which highly ordered surface microlens arrays (MLAs) can be prepared (Figure 2.5 (a) and (c)).[30, 139, 140]

Some simple decoration on the surface of polymeric MLs is feasible, which means the surface MLs are easy to be modified by adding functional groups or particles for more functions in photoreactions. As reported by Dyett et al., the poly (lauryl methacrylate) (PLMA) MLs, prepared with the solvent exchange process, could be decorated with gold nanoparticles.[112] The process can be roughly divided into two parts: lenses were functionalized with amine groups by poly (ethylene glycol)-diamine solution, and then emerged into solutions with gold nanoparticles under certain conditions after cleaning. However, the modification of surface MLs with solvent exchange processes is still limited in only several cases. To explore the function of surface lenses in photoreactions, especially photocatalytic ones, the modification of surface MLs requires further investigation. Compared with other fabrication technologies, the advantages of surface MLs prepared by a solvent exchange process followed by the local photopolymerization exchange include various available substrate materials, solution-based fabrication processes, and flexibility for adjusting the size, curvature, and surface properties of MLs[33]. However, surface MLs made by solvent exchange process also have a common problem with other methods, which is being restricted on 1D fiber or 2D planar surfaces, which limits the development of surface ML-functionalized reactors for a broader range of applications in solar water decontamination inside large reactors with curved surfaces.

2.4.3 Recent advances in the applications of microlenses

MLs play an important role in various fields for optoelectronic systems due to their strong directional control of the light field.[19–21, 24] For instance, light extraction efficiencies of light emitting devices (e.g., organic light-emitting diodes) are enhanced by MLs due to minimized total internal reflections. [23, 25, 141]

Among technologies to improve the efficiency of solar energy usage, MLs offer clear advantages in terms of flexibility[23], adaptability[78, 142], and scalability[128, 143]. Recently MLs are increasingly integrated with solar-driven optical devices [22, 144, 145]. MLs are able to redistribute and focus light and inhibit the loss of energy due to light reflection and scattering.[146, 147] Thanks to the strong near-field focus effect of MLs, the focal points of MLs were hot spots with higher local irradiance intensity and temperature.[29, 111, 112] In the work conducted by Dongare et al[78], the feasi-

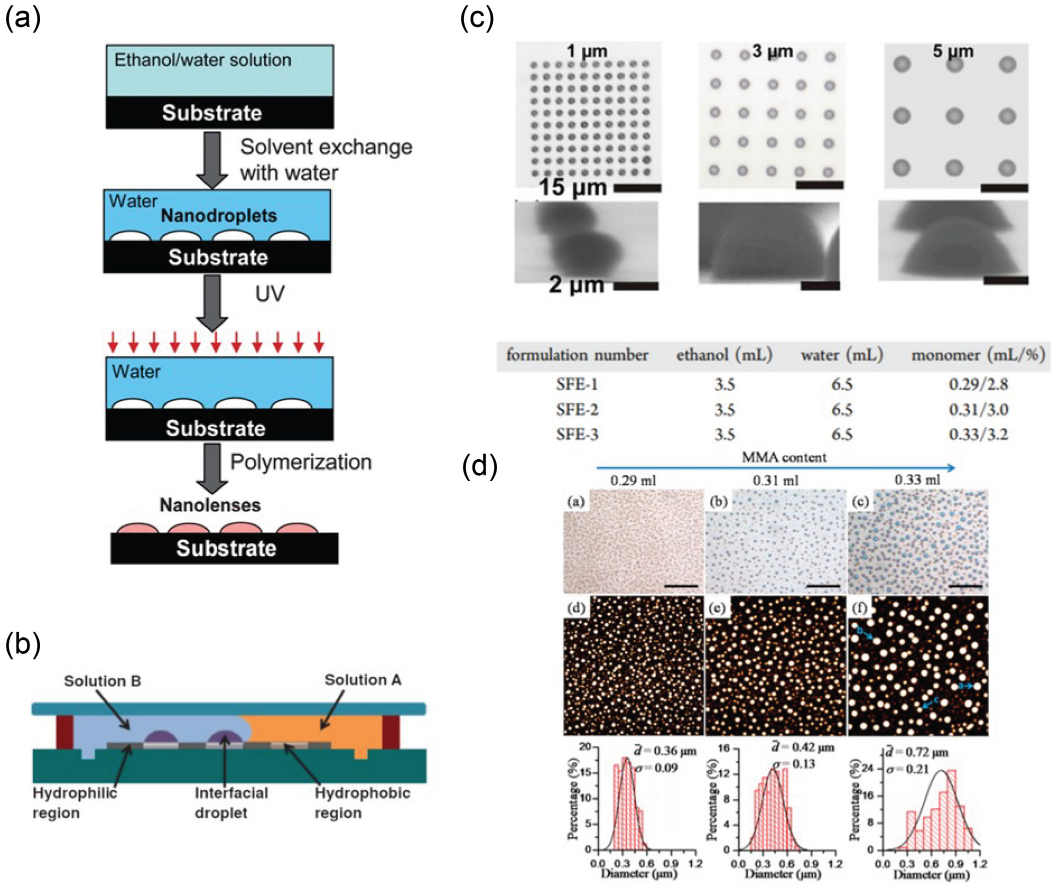

formulation number	ethanol (mL)	water (mL)	monomer (mL/%)
SFE-1	3.5	6.5	0.29/2.8
SFE-2	3.5	6.5	0.31/3.0
SFE-3	3.5	6.5	0.33/3.2

Figure 2.5: (a) The schematic of forming surface microlenses. (b) The front view of the solvent exchange in a specific chamber is composed of a patterned substrate, a spacer, and a cover glass. (c) The optical images of the microlenses on circular pre-patterned silicon substrates with different sizes. (d) Optical microscopy (scale bar = 10 μm) and AFM results ($20 \times 20\ \mu\text{m}^2$) of PMMA microlenses with different MMA concentrations.

bility of integrating lenses with light-driven membrane devices for water purification was demonstrated, where a higher energy conversion rate of the device was achieved because of the focus effect of lenses.

On a smaller scale, the acceleration of the photoreactions by surface MLs has been validated through the in-situ photoreduction of silver nitrate[112]. Therefore, surface MLs are also expected to be effective in enhancing the solar-driven photocatalytic degradation of contaminants in water. Implementing surface MLs based on the solvent exchange process as a candidate strategy for enhancing photodegradation efficiency under insufficient irradiation is worthy of investigation. However, the potential of MLs for wastewater treatment is restricted by not only the availability of a simple and low-cost approach for fabrication of MLs over a large surface area [24], but also the understanding of the effects of locally focused light on the photodegradation of organic contaminants in the aqueous matrix.

2.5 Summary of identified knowledge gaps from literature review

From the literature review above in Chapter 2, multiple knowledge gaps have been identified as below:

1. The understanding of the effects of locally focused light through MLs on the photodegradation of organic contaminants in the aqueous matrix is missing. In addition, it remains to be understood how the size distribution and spatial arrangement of MLs impact their performance in the photodegradation of organic compounds in an aqueous solution. The knowledge gap will be addressed in Chapter 3

2. The mechanisms of MLs-involved photocatalytic degradation of organic contaminants in water are undiscovered, and how the MLs affect the photocatalytic degradation efficiency needs to be investigated under different conditions, especially when the effectiveness of photocatalysts is suppressed. The knowledge gap will be discussed in Chapter 4.

3. Surface MLs made by solvent exchange process are still restricted on 1D fiber or 2D planar surfaces, which can be hardly applied in practical reactors for solar-driven water treatment. A flexible and scalable method to functionalize such reactors, which generally have curved surfaces, by surface MLs is required. The optical properties of microlenses on surfaces with different curvatures and the corresponding effect on photodegradation need to be investigated. The study regarding this knowledge gap will be included in Chapter 5.

4. Even though MLA presented a strong focus effect, the fabrication of MLA is still largely restricted within a chip scale. Furthermore, no systematic work has been conducted to optimize the method to prepare the MLAs suitable for solar-driven reactors for contaminated water. Therefore, a scalable technology to fabricate sustainable MLAs with tunable curvature, effectiveness in enhancing solar-driven photodegradation, and flexible substrate is worthwhile to develop. Our method and discussion in Chapter 6 will provide potential strategies for this knowledge gap.

Chapter 3

Surface microlenses for much more efficient photodegradation in water treatment

3.1 Introduction

Earth receives abundant energy from the sunlight [51]. Solar-driven photodegradation is a sustainable and effective strategy for wastewater treatment.[44, 148, 149] In some rural areas, especially remote regions, solar energy is one of the most popular resources to decontaminate water.[76, 77] Compared to conventional wastewater treatment, photodegradation enhanced by catalysts [69–71] or sensitizers [72, 73] can be highly efficient in removing pollutants that are hardly decomposed, such as antibiotics and personal care products.[74] However, currently low efficiency of light energy utilization and complexity associated with scaling up the size of solar energy collectors have hindered the applications of solar energy in fast conversion processes[12, 75]. Innovative designs are needed to maximize the water decontamination efficiency of the incident solar energy per unit surface area for water purification.

Microlens (ML) is an optical element used in various fields for optoelectronic systems due to its strong directional control of the light field.[19, 21, 24] However, the potential of MLs for wastewater treatment is restricted by not only the availability of a simple and low-cost approach for fabrication of MLs over a large surface area [24], but also the understanding of effects of locally focused light on the photodegradation of organic contaminants in the aqueous matrix. Many bottom-up or top-down approaches have been developed for MLs fabrication[114, 115, 117, 120]. The techniques that offer precision in the morphology of MLs often require high energy consumption, or sophisticated setups, and hence are costly for large scale production of MLs for water treatment. [113] Some technique has realize the lower expenses, such as soft lithography[121, 125] and droplet-templating method.[124] However, it is still challenging to make sure the precision of MLs while keep the flexibility of tuning the properties of MLs.

As reported in literature, MLs can be conveniently fabricated through locally photopolymerizing the micron-sized droplets of monomer and photoinitiators, which also have exhibited a strong focusing effect in a total internal reflection mode microscopy. The local light intensity can be boosted up to ~ 20 times, leading to a strong plasmonic effect of gold particles decorated on the MLs surface.[30, 112] Up to now, the study of chemical reactions enhanced by the MLs is limited to the local surface near MLs. It remains to be understood how focusing effects from heterogeneous and homogeneous MLs impact the photodegradation efficiency of organic compounds dissolved in an aqueous solution.

In this work, we demonstrate that surface MLs fabricated from polymerized surface nanodroplets could significantly enhance the photodegradation efficiency of three real micropollutants and a model compound in aqueous solutions by up to 24 times. The optical properties of MLs were tuned by varying the size distribution, surface coverage, and patterning of precursor droplets to maximize the photodegradation efficiency. As demonstrated, MLs were fabricated on the inner wall of a glass bottle to boost the photodegradation efficiency of a model dye and three micropollutants in water. Up to 24 times higher efficiency was measured for the model dye, and up to 170% for the micropollutants in water. Our work shows that surface MLs are promising to accelerate solar-based photodegradation for fast wastewater treatment.

3.2 Methodology

3.2.1 Fabrication of the PMMA surface microlenses (MLs) on a planar substrate

MLs of poly (methyl methacrylate) (PMMA) on planar substrates were prepared by following the procedure in the literature [31]. Briefly, the methyl methacrylate (MMA) droplets formed through a solvent exchange process, then the droplets were polymerized by UV light. In the solvent exchange process, the hydrophobic substrate, a glass slide ($25mm \times 75mm \times 1.0mm$, Fisher Scientific) coated with octadecyltrichlorosilane (OTS) (98.9%, Acros Organics, Fisher Scientific) was set on top of a customized chamber (height: 0.57 mm, width: 12.2 mm, length: 56.0 mm), as shown in Figure 3.1 (a).

The silicon wafer (thickness: 0.50 mm, University wafer) at the bottom was used to adjust the chamber height. The OTS-glass was firstly immersed into solution A, which was prepared using 3.5 mL MMA (98.5%, Fisher Scientific) and 350 μL initiator 2-hydroxy-2-methylpropiophenone (96%, Fisher) dispersed in water/ethanol solution (40 vol% ethanol, 60 vol% ultrapure water produced by with Milli Q system). Then, the MMA saturated ultrapure water solution (solution B) was pumped into the chamber with a fixed flow rate. The flow rate was controlled with a syringe pump (NE-1000, New Era Pump System). After solution A was replaced by solution B, the MMA droplets formed on the OTS glass substrate. The OTS glass with PMMA microlenses on the surface was rinsed with ultrapure water and ethanol for characterization and light treatment after removal from the chamber.

Two types of MLs were prepared on the planar substrates with different wettability. The MLs fabricated on the homogeneous hydrophobic substrate were considered as random MLs due to the uncontrollable positions. The size of random MLs was adjusted by the flow rate of solvent exchange, and the flow rate was varied from 30 to 50, 70, and 90 mL/h. Another type of MLs was fabricated on a prepatterned

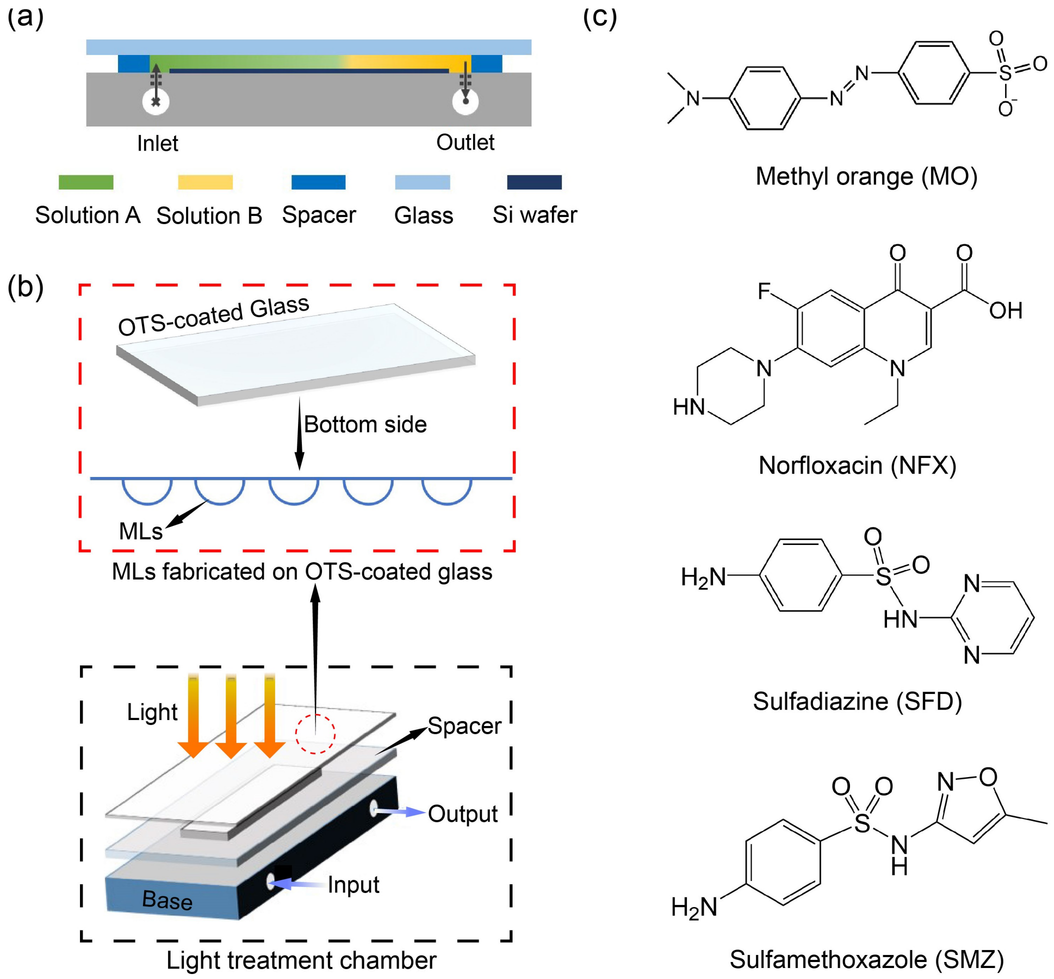

Figure 3.1: (a) The cross-sectional view of the flow chamber for solvent exchange (each component is labelled with different colors). (b) The schematic of the light treatment chamber for MO photodegradation with surface MLs.(c) Chemical structures of pollutants used in photodegradation experiments.

substrate. The prepatterned substrate was fabricated with a reported protocol [140, 150]. Photoresist (AZ 1512) was spun coated on the OTS-coated glass substrate, and a photomask was subsequently attached to the substrate. The circular domains were protected by photoresist while the other area was etched with plasma during a typical lithography process. After removal of photoresist, the prepatterned substrate with hydrophilic background and hydrophobic circular domains with 5 μm diameter and 10 μm center-to-center distance was obtained. The ML array was obtained with a similar solvent exchange process and the following UV curing. In the solvent exchange process, the solution B (MMA saturated water) was added into solution A (4.5 vol% MMA in 50 vol% ethanol aqueous solution) with a flow rate of 8 mL/h. After the fabrication of PMMA ML array with one round of solvent exchange (termed as ML array_1), the second round of solvent exchange with same solutions A and B was conducted to increase the height of MLs according to a method reported in the literature [30], and the flow rate was 5 mL/h when adding solution B. The ML array after two rounds of solvent exchange was represented as ML array_2.

3.2.2 Fabrication of the PMMA surface microlenses (MLs) on the inner wall of a bottle

The MLs of PMMA were fabricated on the inner wall of a cylindrical glass vial with a volume of 30 mL (Fisherbrand Class A clear glass vial). The inner surface of the glass vial was first hydrophobized by an OTS layer. In the formation of MLs, solution A was prepared by adding 3, 4, or 5 mL MMA and initiator with the volume one-tenth of MMA in 60 mL 50 vol% ethanol aqueous solution. Solution B was MMA saturated water containing 0.5 vol% initiator.

12 mL of solution A was put in an OTS-coated vial. 80 mL of solution B was added into the vial at the flow rate of 6 mL/min, while 62 mL of the mixture was taken out from the vial. After the solvent exchange process, the vial with droplets on the wall was put under the UV light for 30 min. The vial was rotated every 10

min to create uniform irradiation on the curved surface. After photopolymerization of the droplets, the vials with MLs were rinsed with water and ethanol subsequently, and labeled with MLs vial_1, MLs vial_2, and MLs vial_3 correspond to the volume of precursors in solution A of 3 mL, 4 mL, and 5 mL.

3.2.3 Characterization of surface MLs

The morphology of MLs was examined using an optical microscope (Nikon H600l) equipped with a camera (Nikon DSFi3) and an atomic force microscope (AFM, Bruker, tap mode). The bottom area (S) and surface coverage of MLs were measured by analyzing more than 5 optical images from one sample (each image covering more than 1 mm^2) with ImageJ. With the bottom area of each microlens, the corresponding lateral radius, r (r=$\sqrt{\frac{S}{\pi}}$), can be calculated. The size distribution of random MLs is described by the probability density function (PDF) of the radius of ML. The radius of MLs (x) are evenly divided into bins with the size of l. The PDF ($f_x(r)$) of a ML with the radius of r can be expressed with equation (3.1).

$$f_x(r) = \lim_{l \to 0} \frac{P(r < x \leq (r + l))}{l} \tag{3.1}$$

In equation (3.1), $P(r < x \leq (r + l)$ represents the probability that the radius of MLs is within the radius interval (r, r+l], which can be calculated with equation (3.2). $N_{R<x\leq(r+l)}$ is the counts of MLs with radius within the range of r to (r+l), and N_{total} is the total counts of MLs.

$$P(r < x \leq (r + l)) = \frac{N_{r<x\leq(r+l)}}{N_{total}} \tag{3.2}$$

The cross-sectional profiles of MLs were extracted from AFM images. The contact angle of MLs, which referred to the angle at the contact line of MLs and substrate surface, was calculated according to the cross-sectional profiles. An integrated photovoltaic testing system (Sciencetech, PTS-2) was applied to measure the transmission (300-700 nm) of the OTS glass decorated with PMMA MLs. The transmission (unit:

percent) was calculated as the ratio of transmitted light intensity through the samples to source intensity. The OTS glass without PMMA surface lenses was tested as the control group.

3.2.4 Photodegradation of the model compound and micropollutants in water

The performance of MLs and ML array on planar surface was evaluated with the photodegradation of model compound, methyl orange (MO, 85%, Sigma-Aldrich), in a home-made light treatment chamber illustrated in Figure 3.1 (b). The bare OTS glass or MLs decorated OTS glass was put on top of the chamber, and the side with MLs was set towards the chamber. The light treatment chamber is 13.1 mm in width, 56.2 mm in length, and 3.05mm in height. The performance of MLs in light treatment was evaluated with different environmental factors, including pH value, initial concentration of pollutants, and dissolved oxygen level in solution. In this part, the MLs were prepared on homogeneous OTS substrates for convenience and MO was used as the model compound. The MO stock solution with different concentrations (3.5 mg/L, 5 mg/L, 7.5 mg/L, 20 mg/L, and 50 mg/L) was prepared with ultrapure water in advance and stored in a dark environment. The pH value of the MO stock solution was adjusted with sulfuric acid (98%, Fisher) and measured with a pH meter (Accumet AE150, Fisher Scientific). To lower the dissolved oxygen level in the MO solution, the stock solution was degassed by an ultrasonic machine (degas mode) right before the light treatment. The dissolved oxygen level of the MO solution with and without the degassing step was detected with a dissolved oxygen probe (Model 50B, YSI Incorporated).

The MO solution was pumped into the light treatment chamber of which the inlet and outlet were then blocked. A simulated daylight LED with adjustable brightness (SOLIS-3C, Thorlabs) was set above the chamber with a fixed distance (23.5 cm) as the light source. The light intensity of irradiation at the upper surface of the chamber was measured with a miniature spectrometer (StellarNet Inc). After the light treatment, the MO solution was collected for subsequent characterization. The efficiency of photodegradation with and without MLs was measured after the light treatment of MO solution (initial concentration: 5 mg/L) for different time intervals, which can be calculated with the absorbance of the solution before and after light treatment. UV-vis spectrometer (Varian Cary 50) was utilized to obtain the absorbance value. The time of light treatment on MO solution was set as 15 min, 30 min, 45 min, 60 min, 240 min, and 480 min. The absorbance curves can provide information on the amount of MO because of Beer-Lambert law. According to Beer-Lambert law (equation (3.3)), the absorbance at a certain wavelength is proportional to the concentration of solute:

$$A = \log_{10}(\frac{I_0}{I}) = \varepsilon C L \tag{3.3}$$

A is the absorbance of the sample, I_0 and I are respectively the light intensity before and after the light passing through the solution, ε is the molar attenuation coefficient, C is the concentration of the analyte in the solution, and L is the length of the light path. Therefore, the ratio of the concentration of decomposed MO $(C_i - C_f)$ to the initial concentration C_i, which is defined as the photodegradation efficiency (η) of MO, is calculated with the absorbance values by equation (3.4).

$$\eta = \frac{C_i - C_f}{C_i} \times 100\% = \frac{A_i - A_f}{A_i} \times 100\% \tag{3.4}$$

A_i is the absorbance at the representative peak [151] of MO before light treatment and A_f is the absorbance at the peak after the treatment.

Besides, an ultra-performance liquid chromatography-quadrupole time-of-flight mass spectrometry (Xevo G_2-S, Waters), operated in negative mode was used to analyze the by-products formed from the photodegradation at 30, 60, and 240 min. Chromatographic separation was achieved using ACQUITY UPLC BEH C18, 50×2.1 mm column, at 40 °C with an injection volume of 10 µL. The mobile phase consisted of water with 0.1% formic acid (solvent A) and acetonitrile with 0.1% formic acid (solvent B). The chemical structures of MO is shown in Figure 3.1 (c) and the detected byproducts were listed in Appendix A, Figure S1, which were consistent with the reported pathway of MO photodegradation. [152, 153] Electron spin resonance (ESR) spectra of the irradiated MO solution in Appendix A, Figure S1 (b) were obtained with a spectrometer (Elexsys E-500, Bruker), using 50 mM DMPO (5,5-Dimethyl-1-pyrroline N-oxide) as the spin trap.

The photodegradation of MO solution was conducted under the indoor solar light with the wavelength starting from 380 nm. The vials were fully filled with MO solution (5mg/L, pH=3.0) and were exposed to sunlight through a glass window for 15 days. The location of light treatment was Room 12-380 in Donadeo Innovation Centre for Engineering, Edmonton, Canada, and the experiments started from Nov 11 in 2021. The temperature was constant at 21 °C.

Three types of micropollutants that have been found in wastewater secondary effluent were photodegraded, including norfloxacin (NFX, Alta aesar), sulfadiazine (SFD, 99.0-101.0%, Sigma Aldrich), and sulfamethoxazole (SMZ, analytical standard, Sigma Aldrich). The photodegradation mechanism of those pollutants has been well-studied in previous work. For the photodegradation of NFX, the hydroxylation and defluorination are the main processes.[154, 155] For both SFD and SMZ, both excited molecules and reactive oxygen species were involved in the photodegradation process.[156–158] The initial concentration of each pollutant in the solution was 5 mg/L. The vial was filled with the micropollutant solution and placed under the simulated solar light (1 sun, SS200AAA Solar Simulation Systems, Photo Emission Tech) for 4 hours. All samples after the light treatment were analyzed with UV-Vis spectrum to quantify the concentration of the degraded compound for the calculation of η. The enhancement of photodegradation efficiency was $(\eta_{MLs}\text{-}\eta_{bare})/\eta_{bare}$. Here, η_{MLs} is defined as the photodegradation efficiency with the MLs-decorated vial while η_{bare} is the efficiency in the control.

3.2.5 Optical simulations of surface MLs

All optical simulations were performed in three-dimensional spaces using Zemax OpticStudio. MLs were placed in the same X-Y plane and illuminated by a plane wave source along the Z direction. The source intensity was set to be the same as in the experiment (21.64 W/cm2). In the MO solution, four light-flux monitors were placed in the X-Y plane at different Z positions to record light flux profiles at different depths. To demonstrate the focusing effect of MLs, X-Z plane monitors were placed along ML central axis to view cross-section intensity profiles.

3.3 Results and discussion

3.3.1 Random MLs: morphology, size distribution, surface coverage, transparency and performance in MO photodegradation

MLs on the substrate are 3 μm to 200 μm in the lateral diameter and 1.5 μm in the maximal height (Figure 3.2 (a-b)). The cross-sectional profiles of MLs in Figure 3.2 (b) extracted from atomic force microscopic images show that the aspect ratio of MLs is equivalent to a droplet with a contact angle around 7.5 ($\pm$0.2)$^\circ$, similar to the morphology of microlenses fabricated by the same protocol in the literature [28]. The constant contact angle is a key morphological feature of MLs on the homogeneous surface, which is predetermined by the growth mode of the precursor droplets [29].

The properties of surface MLs can be tuned by altering the flow rate during solvent exchange.[27, 159] The size distributions of surface MLs fabricated with flow rates of 30 (MLs_30), 50 (MLs_50), 70 (MLs_70), and 90 (MLs_90) mL/h are shown in Figure 3.2 (c). In each size distribution curve, the peaks of frequency are located in the range smaller than 25 µm and the range larger than 30 µm. With a higher flow rate, the peaks move to larger radius while the amount of MLs decreased. The phenomenon is consistent with the optical images in Figure 3.2 (a). In Figure 3.2 (d), the surface coverage continuously increases from 39.6% to 47.2% when the flow rate

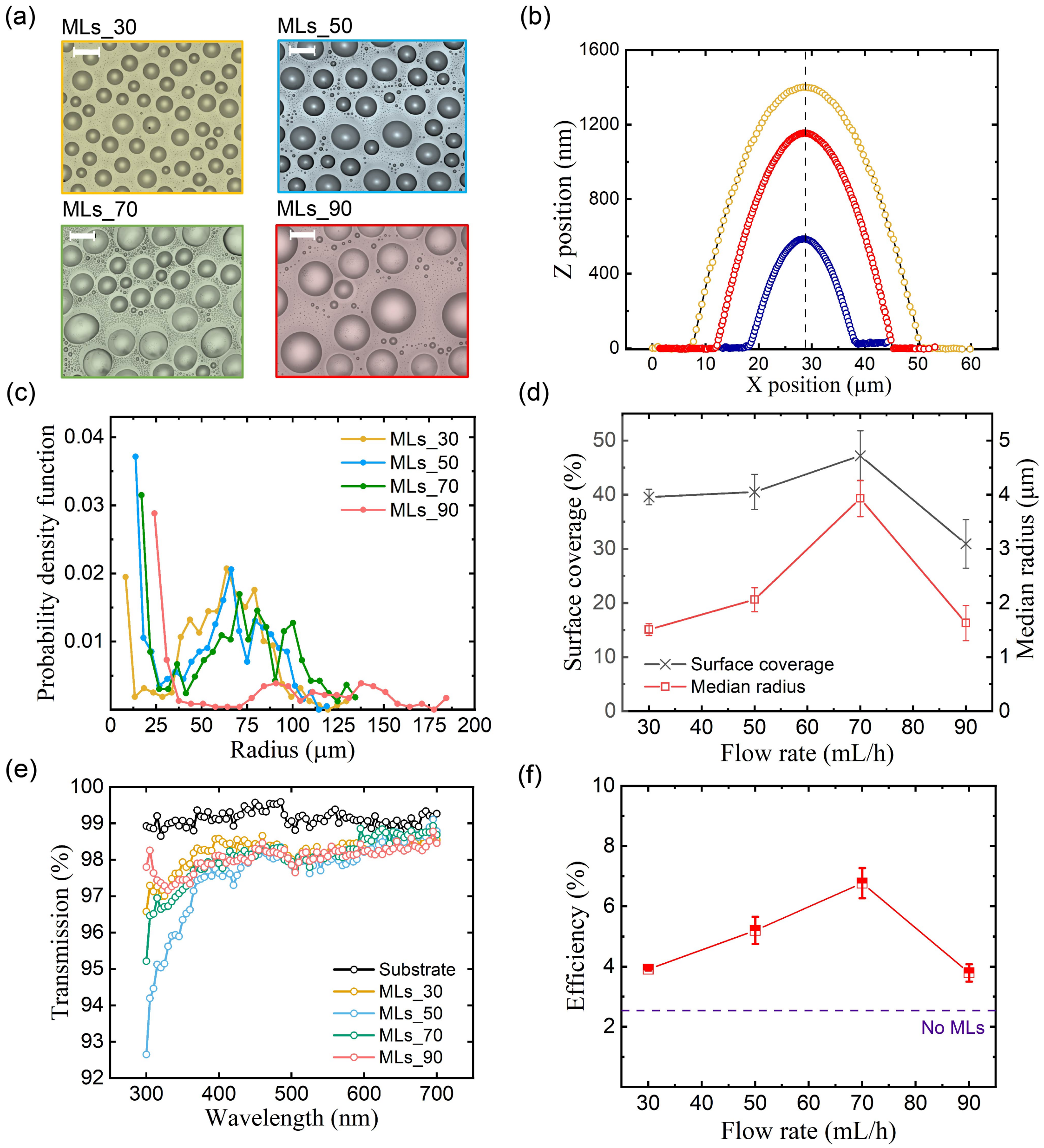

Figure 3.2: (a) Optical images of MLs fabricated with flow rates of 30 (MLs_30), 50 (MLs_50), 70 (MLs_70) and 90 (MLs_90) mL/h in solvent exchange process (scale bar 200 μm) (b) Cross-sectional profiles of MLs in homogeneous hydrophobic substrate by AFM. (c) Probability distribution function with MLs lateral radius. (d) The median lateral size and surface coverage of surface MLs fabricated with different flow rates. (e) The transmission of substrate (OTS glass) and the glass decorated by the surface MLs fabricated with different flow rates. (f) The photodegradation efficiency with MLs fabricated with different flow rates, and the dashed line represents the photodegradation efficiency without MLs. The MO solution used in the photodegradation has the concentration of 5 mg/L at pH 3, and the irradiation time is 30 min.

changes from 30 mL/h to 70 mL/h, and then decreases to 30.9% at a flow rate of 90 mL/h. The trend of median lateral size of MLs with different flow rates is similar, reaching a maximum value of 3.93 µm at a flow rate of 70 mL/h.

The surface ML-decorated glass has high transparency in the visible light range as displayed in Figure 3.2 (e). According to the full spectrum of the LED lamp (Appendix A, Figure S2), the wavelength of the light source is between 400 nm and 800 nm. Within the wavelength range of the light source, the transmission of bare OTS-coated glass reaches 99%, and the transmission of the MLs-decorated glass made with different flow rates is all over 97%. Therefore, those surface MLs are adequate for the following light treatment, and the difference of transmission among the MLs prepared with different flow rates can be neglected.

The photodegradation efficiency of MO after 30 min irradiation with random MLs prepared with different flow rates is plotted in Figure 3.2 (f). The photodegradation efficiency is obtained by inserting the absorbance peak value of MO solution before and after irradiation to equation (3.4). The photodegradation efficiency with all random MLs is higher than the result obtained without using MLs. The efficiency increases with flow rate until the flow rate reaches 70 mL/h, and then drops at 90 mL/h. The maximum photodegradation efficiency is 6.8% with the MLs made with a flow rate of 70 mL/h. The trend of photodegradation efficiency with flow rate is similar to that of surface coverage and median radius, indicating that the surface coverage and median size are possible factors that determine the performance of random MLs in the photodegradation enhancement.

3.3.2 ML arrays: 3D morphology and arrangement

The MLs are arranged in a highly ordered array with uniform size on the prepatterned substrate, as shown in Figure 3.3 (a). The MLs in the array prepared with one round (ML array_1, Figure 3.3 (a) left) and two rounds (ML array_2, Figure 3.3 (a) right) of solvent exchange have a similar lateral diameter around 9 µm, and the

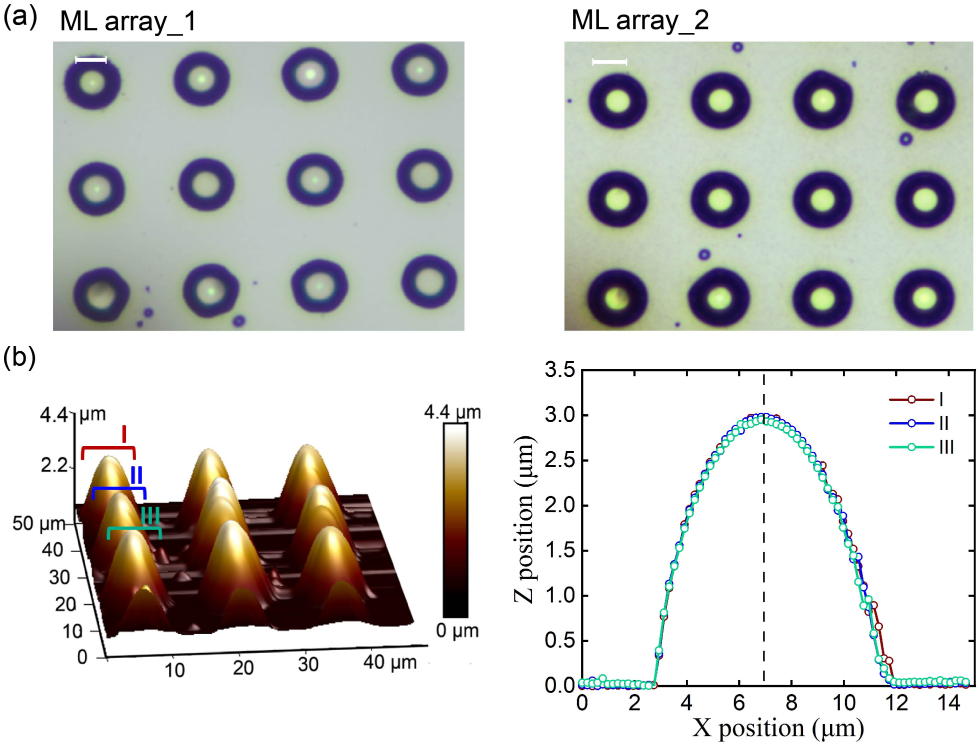

Figure 3.3: (a) Optical images of ML array fabricated with one round (left) and two rounds (right) of solvent exchange , and the contact angle of MLs in the array is 28 degree and 73 degree respectively (scale bar 5 µm). (b) 3D image of MLs after two rounds of solvent exchange by AFM and corresponding cross-sectional profiles.

center-to-center distance is about 16 µm. The light spots in ML array_2 are smaller but brighter than those in ML array_1, and the difference in optical images indicates that the curvature of MLs further increased after the second round of solvent exchange [160]. The 3D image and the cross-sectional profiles of ML array_2 in Figure 3 (c) show that the height of MLs in ML array_2 reaches 3.0 (±0.1) µm and the contact angle is 73 (±0.5)° with two rounds of solvent exchange. The high curvature of MLs in the array is attributed to the confinement of circular hydrophobic domains.[160] The characterization results prove the feasibility of curvature adjustment of ML array with constant radius via multiple rounds of solvent exchange.

3.3.3 Comparison of random MLs and ML arrays for photodegradation

The performance of ML arrays in the photodegradation of MO is compared with the random MLs that enhance photodegradation efficiency most (MLs_70). As illustrated in Figure 3.4 (a), the absorbance peak of MO solution (5 mg/L, pH=3.0) at 504 nm decreases after the light exposure for one hour, and the reduced peak value varies with the configurations of surface MLs. By inserting the absorbance value at 504 nm to equation (3.4), we can obtain the photodegradation efficiency with corresponding surface MLs (Figure 3.4 (b)). During the light treatment for 1 hour, MLs_70 enhances the degradation efficiency of MO by 186% in comparison with the treatment without MLs. In comparison, the degradation efficiency of MO increases by 471% and 607% when applying ML array fabricated with one round (ML array_1) and two rounds (ML array_2) of solvent exchange, respectively.

The performance of surface MLs was investigated under different light intensities. The full spectrum of the light source with four intensities that are applied in experiments is displayed in Appendix A, Figure S2. In Figure 3.4 (c), the degradation efficiency during irradiation for 30 min is plotted against the light intensity. Under the irradiation with the same light intensity of 21.64 W/m^2, the photodegradation

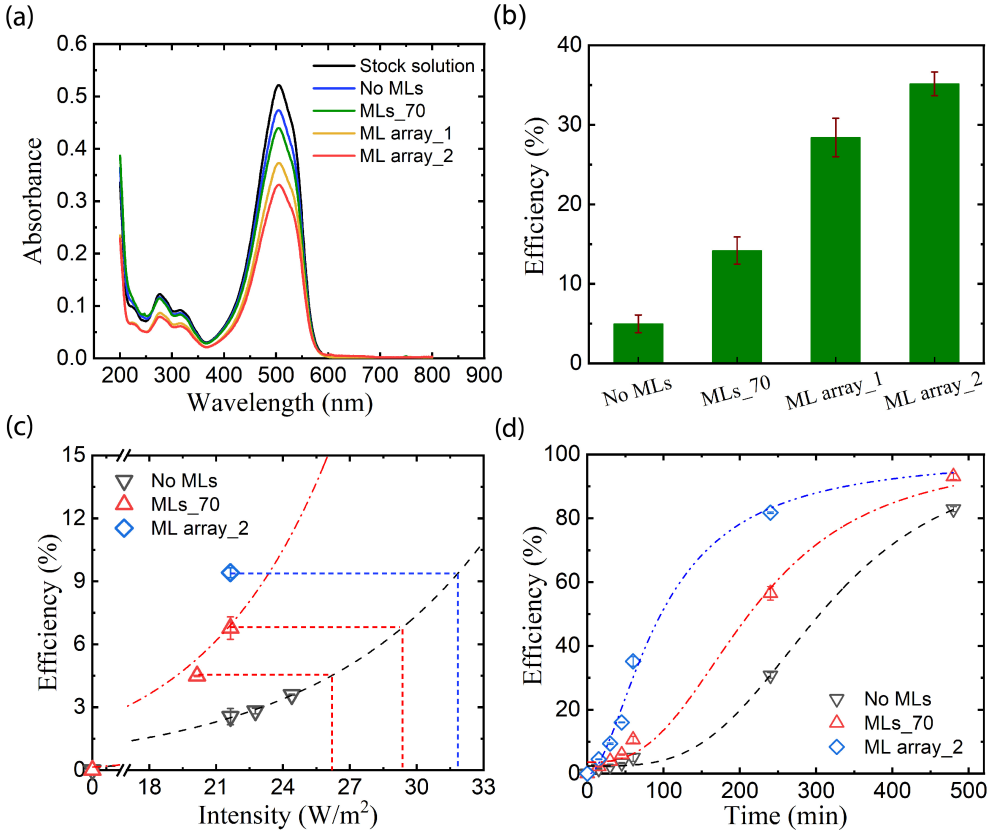

Figure 3.4: (a) Absorbance curves of methyl orange solution before and after 1 hour irradiation under different conditions. (b) Degradation efficiency of different types of surface MLs after light irradiation for 1 hour. (c) The photodegradation efficiency under the irradiation with different light intensity for 30 min. The red and blue dashed line is used to label the light intensity required without utilizing MLs to achieve the same photodegradation efficiency as MLs_70 and ML array_2 respectively. (d) The photodegradation efficiency with varied irradiation time, fitted with the logistic model. The concentration of MO solution is 5 mg/L, with pH=3.0 and degassed for 15 min, and the light intensity is 21.64 W/m^2 if not mentioned.

efficiency is 269% higher with MLs_70 and 165% higher with ML array_2 than that without using MLs. By fitting the curve of efficiency with the light source intensity, we can predict the photodegradation efficiency under higher light intensity. As shown in the red dashed line, the photodegradation efficiencies in the presence of MLs_70 under the intensity of 20.14 and 21.64 W/m^2 are similar to those observed under 26.20 and 29.38 W/m^2 in absence of MLs. To achieve the same level of MO degradation with ML array_2 at the intensity of 21.64 W/m^2, the light source should reach 31.82 W/m^2 without MLs based on the fitting results. By using ML array_2, 47.0% light energy is saved compared with the situation without MLs. The light energy required for the degradation of MO is reduced because the utilization of irradiation was more efficient through surface MLs, especially the ML array. The application of MLs significantly enhances the degradation efficiency under weaker irradiation, providing a potential solution for the light treatment of contaminated water under natural light sources.

To further analyze the photodegradation process with surface MLs, the degradation efficiency calculated with equation (3.4) and absorbance values (obtained from Appendix A, Figure S3) is plotted against the treatment time in Figure 3.4 (d). Throughout the irradiation time from 0 to 480 min, the degradation efficiency of MO with MLs_70 is higher than that without MLs but lower than that with ML array_2. By fitting the data in Figure 3.4 (d) with the logistic model, it is found that the degradation efficiency showed a non-linear growth with treatment time under each condition. The photodegradation efficiency grows exponentially at the early stage of the reaction, and the growth slows down when the photodegradation efficiency is around 50%. During the photodegradation in the first 100 min, it is obvious that the reaction rate with ML array_2 is the fastest, followed by that with MLs_70. The phenomenon confirms that the photodegradation can be accelerated by surface MLs, while the ML array is more efficient, especially in the first 100 min. To achieve the photodegradation efficiency of 80%, it takes 457 min without MLs and 354 min with

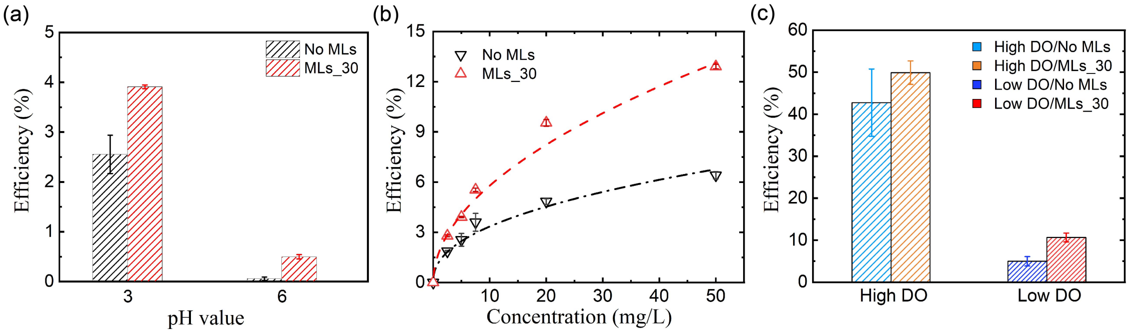

Figure 3.5: The photodegradation efficiency with (a) pH value and (b) concentration of MO solution without and with MLs (Fitting equation for the black curve: $y = 1.22 \cdot x^{0.44}$, the red curve: $y = 1.79 \cdot x^{0.51}$). (c) Photodegradation efficiency under different dissolved oxygen (DO) levels. The high DO level is 7.37(±0.08) mg/L, and the low DO level is 6.99(±0.13) mg/L.

MLs_70, and 214 min with ML array_2. The usage of surface MLs and ML array effectively shortens the treatment time in MO photodegradation.

3.3.4 Influence of chemical composition in MO solution on photodegradation

The pH value of the stock solution is one of the important factors affecting the photodegradation process. Figure 3.5 (a) shows the efficiency of MO photodegradation both with MLs and without MLs under two pH values, 3 and 6. Without surface MLs, 2.6% of MO is removed during the irradiation for 30 min at pH 3, while MO barely degrades at pH 6 under the same conditions. The degradation efficiency is enhanced to 3.9% at pH 3 and to 0.5% at pH 6.0 when using the surface MLs. The possible reason for the higher degradation efficiency at lower pH is that the MO molecules dominantly exist in the protonated forms that are easier to photodegrade at pH 3.[161] The surface MLs could accelerate the photodegradation of MO at both pH 3 and 6, and the effect is stronger at low pH value. Although the photodegradation efficiency is also improved by MLs at pH 6, the enhancement is limited because MO existed mainly as its inactive species at the pH value.

The effect of the initial concentration of MO solution on the performance of MLs was also investigated. Figure 3.5 (b) displays the photodegradation efficiency of the MO solution with the initial concentration ranging from 2.5 to 50 mg/L after light treatment for 30 min. Fitting curves are plotted only for describing the trend of photodegradation efficiency with the initial concentration of MO ($C_{MO,0}$). The fitting function is shown in equation (3.5), where η_{MO_30min} is the photodegradation efficiency of MO after the irradiation of 30 min, a and b are the fitting parameters.

$$\eta_{MO\_30min} = a{C_{MO,0}}^{b} \tag{3.5}$$

For the degradation process without MLs, the values of a and b are 1.48 and 0.39 respectively. For the fitting curve obtained with MLs, the value of a is 1.76 and that of b is 0.52. In other words, the degradation efficiency constantly increases with the MO initial concentration in the range between 2.5 and 50 mg/L. Furthermore, the photodegradation efficiency with MLs is consistently higher than that without MLs as the initial MO concentration varies. No matter the absence or presence of surface MLs, the enhancement of degradation efficiency slows down as the initial concentration increases, which is attributed to the limited amount of photons provided by the light source and the inhibition of light due to the high concentration of MO.[162] However, the photons participate in the MO degradation more efficiently due to the light redistribution by using surface MLs. As a result, the photodegradation efficiency would further increase with the existence of MLs even though the initial concentration of MO reaches 50 mg/L.

The dissolved oxygen (DO) level in the MO solution is another factor that influenced the degradation efficiency. The high DO level is 7.37 (±0.08) mg/L and is obtained from the MO solution without degassing step. The low DO level is 6.99(±0.13) mg/L and is from MO solution after degassing. With the absorbance curves before and after photodegradation (Appendix A, Figure S4) and equation (3.4), the photodegradation efficiency without and with surface MLs under two DO levels is plotted in Figure 3.5 (c). The photodegradation efficiency at the higher DO level is 38% higher than that with the lower DO level. By applying MLs in the light treatment, the efficiency is enhanced on average by 7.1% without degassing and by 5.7% with degassing. The results confirm that DO could promote the photodegradation of MO.[163, 164] However, the reproducibility of the experiments without the degassing step is worse compared with the tests under the lower DO level. We assume that the DO is not uniformly distributed in the sealed chamber because the DO is not in equilibrium without any mixing steps. This effect might be reduced by degassing the MO solution before filling the light treatment chamber with the solution. To guarantee the repeatability of results, the degassing step is done before the light treatment in all light treatment processes.

3.3.5 Optical simulations of surface MLs and ML arrays

To understand the effect of surface MLs in the whole light treatment chamber, the simulations of light paths through MLs on homogeneous hydrophobic substrates (random MLs, Figure 3.2 (a)) and ML array on a prepatterned substrate (ML array_-2, Figure 3.2 (f) right) are conducted. The top-view intensity profiles at the depths close to focal distances of MLs are demonstrated in Figure 3.6 (a-b). In the intensity profiles, the spots with higher light intensity are displayed with red color, indicating the focusing effect of MLs. As shown in Figure 3.6 (a), only part of the focal points of random MLs are observed in the simulated region between the depth of 75 μm and 522 μm. The uneven size of random MLs causes that the focal points of MLs distributed at varying depths. It is also found that the light intensity at the displayed focal points of the random MLs almost remained similar from the depth of 75 μm to 522 μm.

Figure 3.6 (b) illustrates the top-view intensity profiles of ML array at the depth from 15 to 45 μm. The focal points of MLs in the array are located in the same plane. Different from the random MLs, rapid decay of light intensity is observed when the depth increased in the situation of the ML array. Even though the decay is much more distinguished below the focal points of the ML array, the highest light

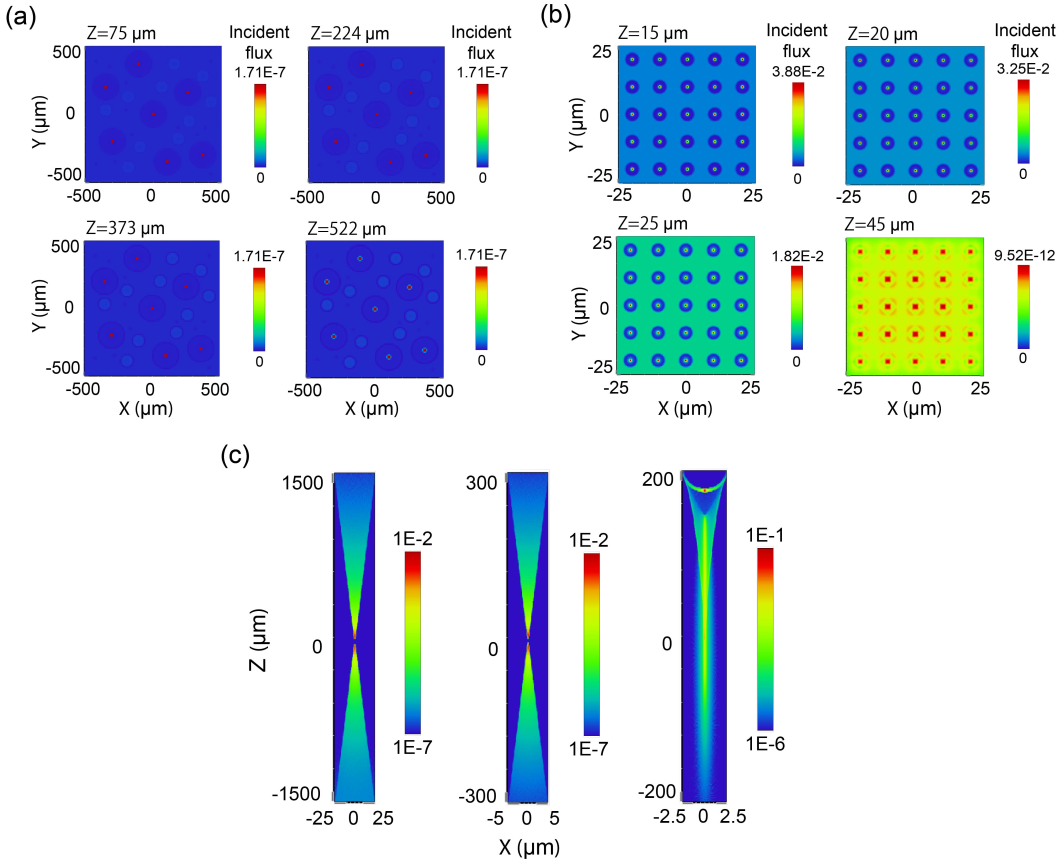

Figure 3.6: Top-view intensity profile of (a) random MLs at the depth of Z, and (b) ML array at the depth of Z. (c) Cross-sectional intensity profile of a single ML on homogeneous substrate with diameter of 50 µm and contact angle of 7.5° (left), on homogeneous substrate with diameter of 10 µm and contact angle of 7.5° (middle), and on a prepatterned substrate with diameter of 5 µm and contact angle of 73° (right).

intensity achieved by the ML array is 5 orders of magnitude larger than that by random MLs. Therefore, 'hotter' spots are created at the focal points of MLs are fabricated on a prepatterned substrate. In addition, the focal points of MLs on homogeneous substrates are located at varying depths, but the focal points of ML array are densely located on a specific plane. The uniform focal distance of the ML array leads to a region with a high concentration of active species and accelerates the local photodegradation more efficiently than random MLs, which can be considered as a 'regional effect'.

At the same depth in the light treatment chamber, as displayed in Appendix A, Figure S5, the top-view intensity profiles change with surface MLs arrangement. At the depth of 224 μm, the highest light intensity in the situation with random MLs is much higher than that with ML array. The reason is that this depth is close to the focal distances of some large MLs on homogeneous substrates and is much larger than those of MLs on prepatterned substrates. Therefore, the region with strengthened light intensity is significantly influenced by the configuration of surface MLs.

Based on the top-view intensity profiles obtained by optical simulations, we assume that the radius and curvature of MLs are the two main factors that influence the performance of MLs in photodegradation. As proof of the hypothesis, the cross-sectional intensity profiles of MLs with different radius and curvatures are simulated in Figure 3.6 (c). The MLs on homogeneous substrates have the same contact angle of 7.5°, and the focal distance increased from 0.3 mm to 1.5 mm as the diameter changed from 5 μm to 25 μm. Each ML on a prepatterned substrate has a larger contact angle of 73° and a diameter of 5 microns. The focal distance is only 17.5 μm but the light intensity is 10 times larger than that of MLs with similar lateral size on homogeneous substrates, which is attributed to the higher curvature of the MLs with array configuration.

3.3.6 Correlation between the intensity at focal points of MLs and photodegradation enhancement

Enhanced photodegradation by using surface MLs may be rationalized by effects from focused light on the kinetics of photodegradation. After the light treatment for the time from 0 to t_f, the efficiency η is determined by the initial concentration C_{ini} and the final concentration C_f.

$$\eta = \frac{C_{ini} - C_f}{C_{ini}} \times 100\% \tag{3.6}$$

$$C_{ini} - C_f = \int_0^{t_f} r(\lambda) dt \tag{3.7}$$

The treatment duration t_f is the same when the efficiency η is compared with and without MLs. According to the second law of photochemistry [165, 166], the production rate of active species at a given time t in an aqueous solution, $r(\lambda)$, is given by the equation as below.

$$r(\lambda) = K \times \int_{\lambda_{min}}^{\lambda_{max}} I_\lambda C'_\lambda d\lambda \tag{3.8}$$

$$C'_\lambda = C_m \epsilon_{\lambda,m} \phi_{\lambda,m} \tag{3.9}$$

Here K is a conversion constant, C_m is the concentration of reactant m that forms the rate-limiting species. λ is the wavelength of the light source, ranging from the minimum λ_{min} to the maximum λ_{max}. For the wavelength of λ, I_λ is the intensity that drives the photodegradation, $\epsilon_{\lambda,m}$ is the extinction coefficient, and $\phi_{\lambda,m}$, the quantum yield of m. For the model compound is the same in all our experiments, all the parameters in C'_λ except I_λ can be considered to be the same.

As sketched in Figure 3.7 (a), in the case without using surface MLs, the light intensity I_λ in equation (3.9) is constant in a horizontal plane, and, for certain wavelength, decays with depth into the solution due to absorption by water. MLs alter

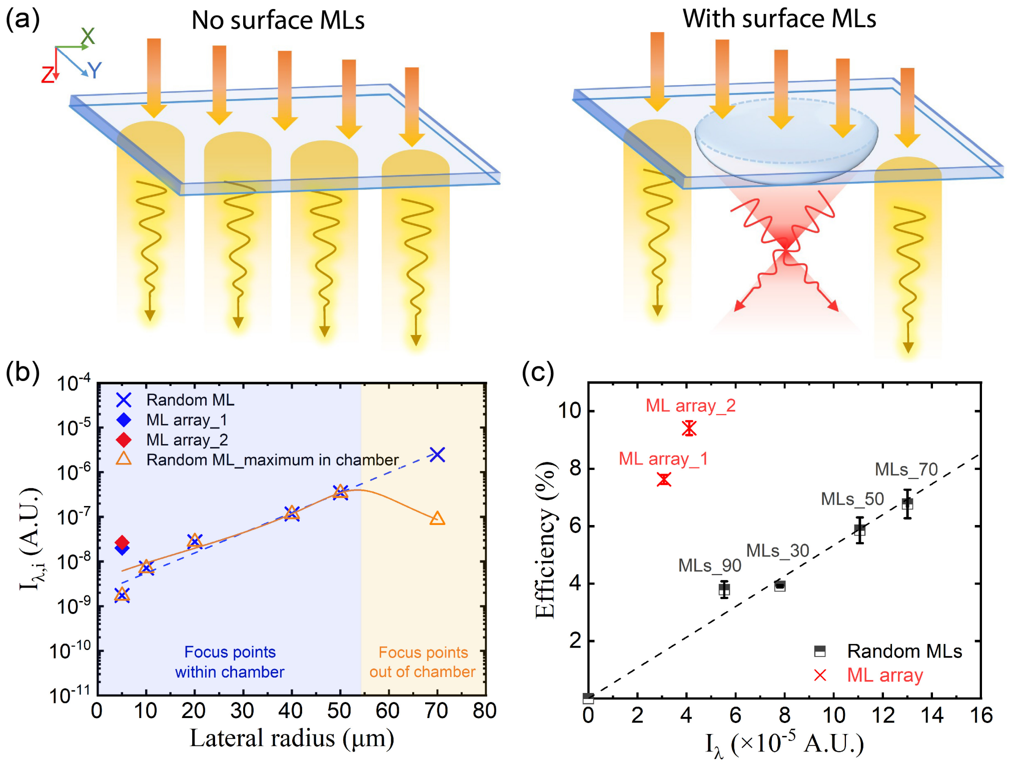

Figure 3.7: (a) Schematic of the light path without surface ML (left) and with surface ML (right) (b) Intensity ($I_{\lambda,i}$) at focal point of a single ML with different lateral radius. The intensity at the focal points of MLs is labelled with blue color, and the actual maximal intensity under random MLs is labelled with orange color. (c) The correlation between photodegradation efficiency and additive of intensity (I_λ) at focal points of MLs. For (b) and (c), the wavelength λ is 504 nm in optical simulations.

the spatial distribution of I_λ propagating in the solution. Beneath the surface areas without MLs, I_λ is uniform and decays with the depth, the same as the situation without MLs. Beneath the surface area with surface MLs, the light is concentrated on the focal points, resulting in a much higher I_λ at the focal points. The above analysis shows that the spatially modified profile of I_λ by MLs contributes to improved efficiency η in the photodegradation. In water treatment by solar light, the size of the surface area that can receive the light is limited by the size of containers or the water reserve. Using MLs to redistribute the light in water may lead to more effective use of the surface area available.

Below we will show that the enhancement from MLs is not simple additive, but exhibited coupled effects from multiple MLs. I_i is the light intensity at the focal point of ML labelled as i. The total number of MLs over a certain area S_{Total} is N.

$$I/S_{Total} = (1/S_{MLs}) \times \sum_{i=1}^{N} I_{\lambda,i} + I_\lambda/S_{Bare} \tag{3.10}$$

Here S_{MLs} is the substrate area occupied by MLs, and S_{Bare} is the bare area. I/S_{Total} is the averaged intensity beneath the entire surface area S_{Total} (=S_{MLs} + S_{Bare}). To simplify the comparison, we first neglect the second term (I_λ/S_{Bare}) on the right.

$$I_\lambda \approx \sum_{i=1}^{N} I_{\lambda,i} \tag{3.11}$$

The energy intensity per unit area $I_{\lambda,i}$ created by individual ML(i) is obtained from optical simulation. The plots in Figure 3.7 (b) show that $I_{\lambda,i}$ increases with the base radius of the MLs on homogeneous surfaces. For a given base radius, $I_{\lambda,i}$ is much higher from MLs in the array, thanks to their higher curvature. We note that $I_{\lambda,i}$ decreases for MLs with a radius larger than 54 μm, because the focal point of such large MLs is further than 3 mm, the depth of our reactor. The actual $I_{\lambda,i}$ contributing to photodegradation deviates from the simulated value for large MLs. A fitting line (the orange curve in Figure 3.7 (b)) is used to predict the irradiation power at the focal point or hot spot of a ML on homogeneous hydrophobic substrates.

Considering both $I_{\lambda,i}$ from the simulation results and the morphology and number of MLs extracted from optical images, we calculate I_{λ} of homogeneous substrates functionalized with MLs. Figure 3.7 (c) shows that the efficiency η increases with I_{λ}, and reaches the highest by MLs on homogeneous substrate fabricated with the flow rate of 70 mL/h. The reduced performance from MLs prepared at 90 mL/h is attributed to the energy loss due to the focal distance larger than the depth of the reactor. The overall efficiency η is approximately linear with the increase of the sum of I_i from all MLs obtained from homogeneous substrates.

Interestingly, the efficiency η from the ML array is 100 % higher than random MLs with the same I, and is 39% higher than the best results from random MLs on homogeneous substrates. Such high efficiency is much beyond the cumulative effect of I_i, as observed for homogeneous substrates. We propose that the photodegradation with MLs in an array could be attributed to the ordered arrangement of focal points on the same plane. Such ordered focal points may lead to a narrow distribution of spatial distribution of active species in water. The focal points on the same plane are also synchronized in certain zones of the aqueous solution. Such a focusing effect increases the local concentration of active intermediate products and speeds up the photodegradation rate. In future work, even higher η may be achieved as I_i of the ML array is optimized. For instance, making closely arranged patterns increases the surface coverage, and the size of ML in the array can be tuned by the size of each domain.

3.3.7 Proof-of-concept: MLs-enhanced photodegradation for water treatment

The potential application of MLs in the photodegradation of harmful compounds in water is demonstrated by using functionalized bottles as shown in Figure 3.8 (a).

The photos show these bottles with the inner wall coated with MLs.

Three micropollutant solutions in the bottles were treated by the simulated solar light with the set-up in Figure 3.8 (b). Each type of micropollutant solution is separately put in a bare vial and the MLs vial_3. The difference in the micropollutant concentrations at a given time was detectable in UV-Vis spectra as shown in Figure 3.8 (c-e)). The enhancement of photodegradation efficiency is plotted as a function of irradiation time in 3.8 (f). After 1 hour, η_{MLs} was already clearly higher than η_{bare} by approximately 20%. After the irradiation for 4 hours, η of NFX was improved by 1.2 times by MLs, the lowest among the three micropollutants. η of SFD and SMZ increased by 2.6 and 1.9 times, respectively. The results verify that surface MLs could increase the photodegradation efficiency of micropollutants in water. The divergent photodegradation enhancement over different micropollutants is attributed to the difference in the photodegradation mechanism of each pollutant. The degradation kinetic of each type of micropollutant is determined by its intrinsic photodegradation mechanism. The dependence of the photodegradation rate of each pollutant is not the same, implying that the enhancement from the local light intensity altered by the presence of MLs also varies.

The enhancement of photodegradation by MLs is also demonstrated with the light source of indoor sunlight. The dye aqueous solutions in the bottles were exposed to sunlight through a glass window (Figure 3.9 (a)). The short wavelength in natural solar light was cut off by the thick glass panels. As illustrated in Figure 3.9 (b) and (c), the color of the MO solution in the bottles functionalized with MLs decayed much faster than that in the bottle without MLs.

Figure 3.9 (d) displays that the enhancement is 9-23 times after 9-12 days. With the extension of light treatment, the dye was also degraded in the bare vial, so from then on the enhancement dropped a little to 7-20 times. Larger MLs on MLs vial_2 and 3 were more effective, compared to smaller MLs on MLs vial_1. The results clearly demonstrate that MLs on the inner wall of the bottles could speed up the

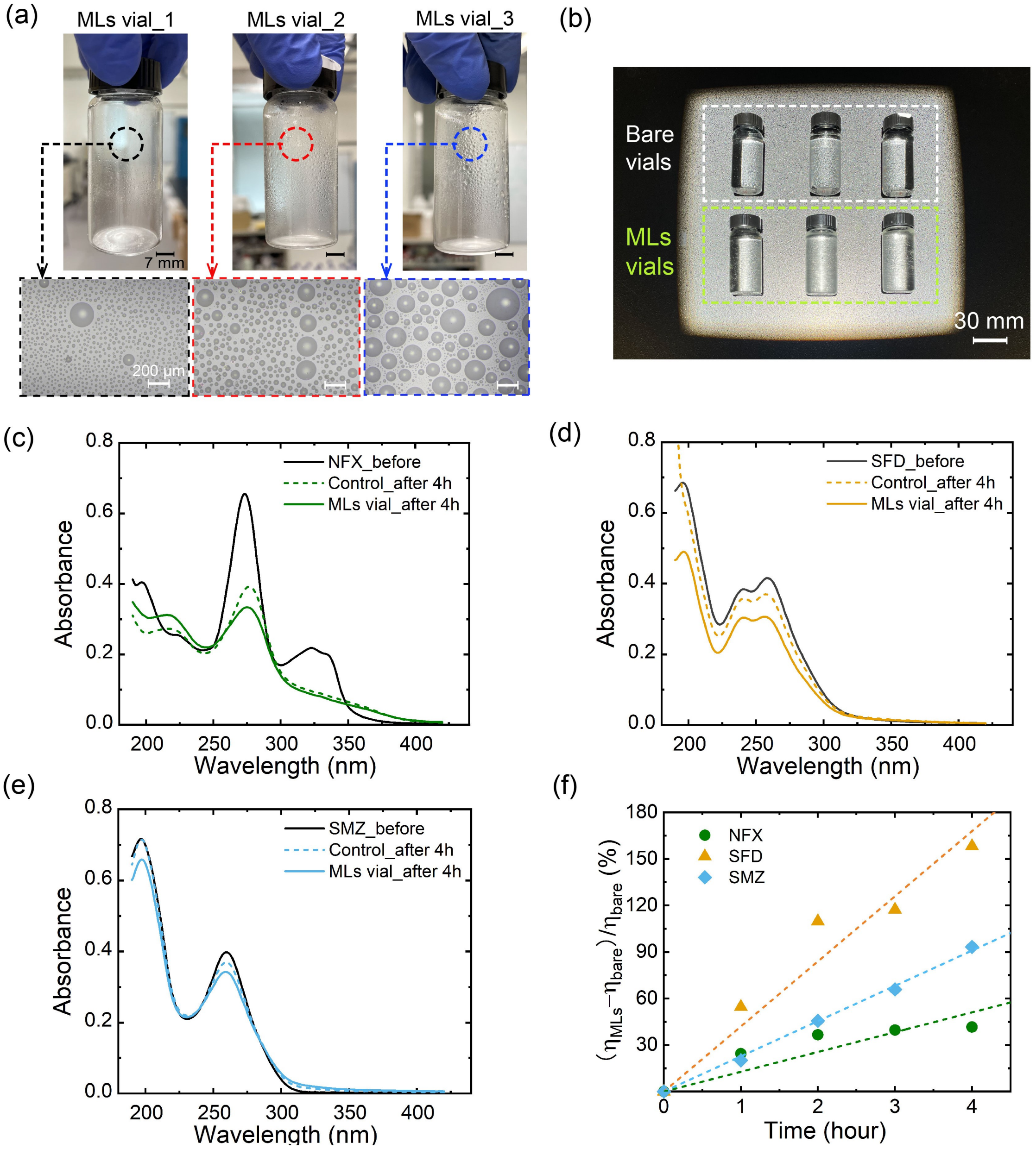

Figure 3.8: (a) Photos of the glass bottles functionalized by MLs. The bottles are labelled as MLs vial_1, 2, and 3. The optical microscope images of the zoom-in areas show the MLs on the inner wall of the bottles. (b) Experimental set-up of simulated solar light treatment of micropollutant aqueous solutions. In the bare vials, from left to right: NFX, SFD, and SMZ. In ML-coated vial MLs vial_3s, from left to right: NFX, SFD, and SMZ. Absorbance spectrum of (c) NFX, (d) SFD (e) SMZ solution (5 mg/L) before and after the exposure to simulated solar light for 4 hours. Dashed lines: solutions in bare vials; Solid lines: solutions in functionalized vials. (f) Enhancement of photodegradation efficiency of micropollutants as function of treatment time. η_{MLs} is defined as the photodegradation efficiency with the MLs-decorated vial, while η_{bare} is the efficiency in the control.

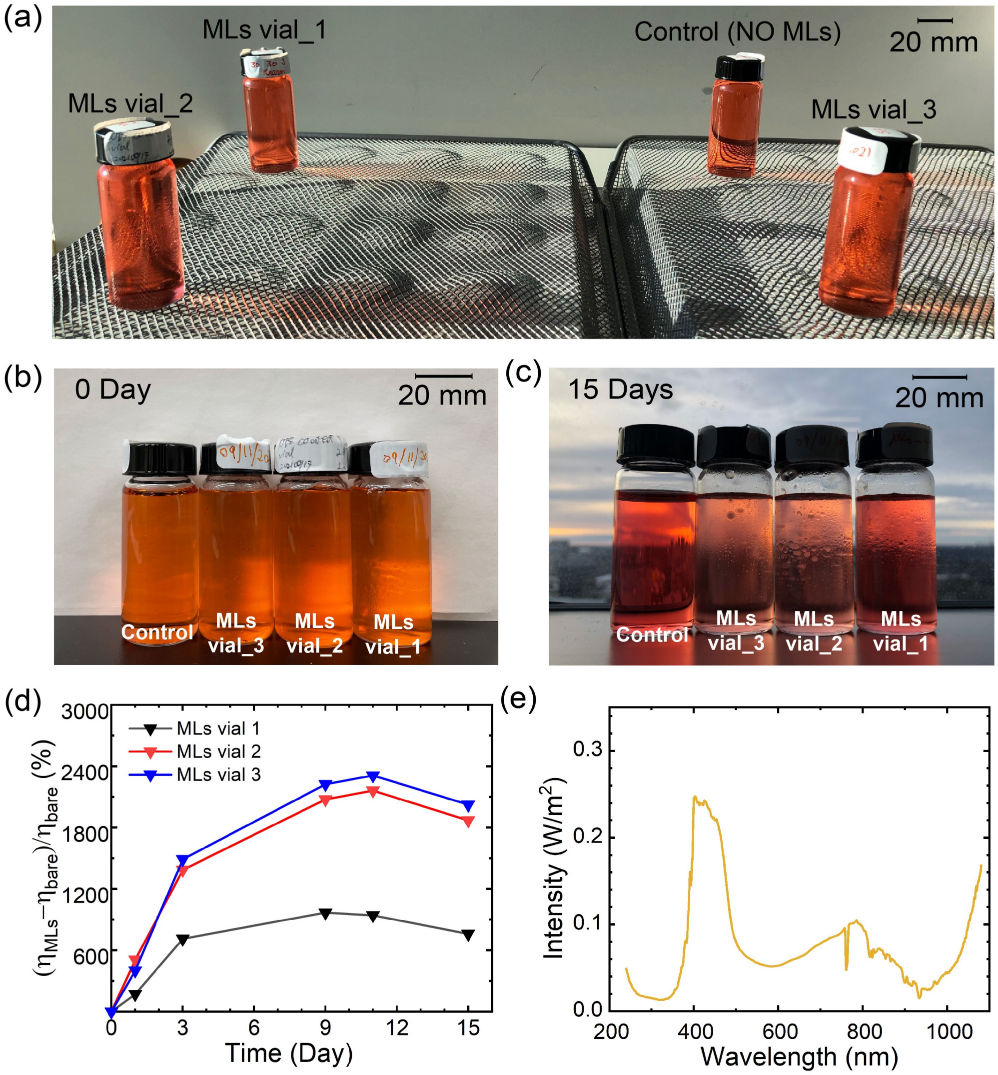

Figure 3.9: (a) Layout of four bottles receiving indoor sunlight. Photos of the bottles filled with the dye solution (b) Before and (c) after receiving sunlight for 15 days. From left to right: bare vial, MLs vial_3, MLs vial_2, MLs vial_1). (d) Enhancement of photodegradation efficiency of MO with the treatment time.(e) Spectrum of indoor solar light at the location of light treatment.

photodegradation of the dye in water. As the indoor light intensity lacks the UV region (Figure 3.9 (e)), the significant enhancement in photodegradation suggests that bottles functionalized by MLs may be potentially used for light treatment in situations where the sun elevation is low, the weather is cloudy, or the light source is a reflection from snow or local pollution. During the simulated solar light treatment and indoor solar treatment, MLs vial_1, 2, and 3 were repeatedly used. The photos of MLs vials after light treatment are displayed in Appendix A, Figure S8, indicating that the MLs-decorated MLs remained stable after indoor solar light of more than 30 days and simulated solar light of more than 30 hours.

We note that it is hard to simply compare the degradation efficiency of MLs with other photo-degradation enhancement techniques, as the efficiency depends on the light intensity, illumination duration, and physio-chemical properties of the compounds to be degraded. For instance, at very low light intensity, some catalysts may not work at well while the degradation efficiency of the MLs may reach a high value after a long duration. Our purpose of developing surface MLs is not to compete with other photodegradation enhancement techniques, such as photocatalysis and photosensitization, but to provide a complementary method that can be used alone or combined with other techniques to boost photo-degradation enhancement. With the development of MLs, other photodegradation enhancement techniques can be more efficient after the combination with surface MLs.

3.4 Conclusions

In summary, our work shows that the enhancement of photodegradation efficiency with surface MLs occurs under various solution conditions via the same photodegradation pathway. The morphology, number density, and spatial arrangement of MLs have a significant impact on photodegradation efficiency. ML arrays are 100% more effective than random MLs with the same intensity at focal points and are $\sim$ 700% more effective than bare surfaces without MLs. The simulation results suggest that highly ordered ML arrays may result in a locally high concentration of active species around the focal points array, and further accelerate the photodegradation. The photodegradation efficiencies of the dye and three micropollutants in bottles functionalized with MLs were all significantly higher than those in normal bottles, demonstrating the potential application of MLs in the photodegradation of harmful compounds in water. In future work, MLs may be fabricated in commercial drinking water bottles that can be recycled for the decontamination of water. In addition, there are some degradable and environmental-friendly polymer materials that are possibly used for MLs preparation, such as PVA (poly(vinyl alcohol)) [167, 168], PNIPAM (poly(N-isopropylacrylamide)) [169, 170], and some biomacromolecules like silk protein and cellulose [171, 172].

3.5 Supplementary materials

Supplementary materials to this article can be found in the Appendix, section A.1. Additional data include ESR (electron spin resonance) spectrum of MO solution after light treatment and byproducts after the photodegradation of MO obtained by UPLC-MS, spectrum of light sources, representative absorbance spectrum of MO solution after light treatment, additional optical simulations of surface MLs, plots of photodegradation efficiency of MO over MLs median radius and surface coverage and photographs of MLs-decorated vials before and after light treatment.

Chapter 4

Enhanced photocatalytic degradation of organic contaminants in water by highly tunable surface microlenses

4.1 Introduction

Photoreactions are widely applied in different fields[34], such as data storage[39, 40], display[41], light generation[42, 43], polymerization[46, 47], and light-driven degradation[49, 50]. Many clean-energy technologies for water treatment benefits from photoreactions. [54] In many types of photoreactions[7], photocatalysis, which is the photoreactions accelerated by photocatalysts, is one of the dominant technologies to remove the organic micropollutants in natural water [79, 80]. The most common type of photocatalysis in water treatment is heterogeneous photocatalysis with semiconductor materials, such as titanium dioxide ($\mathrm{TiO_2}$)[69] and zinc oxide (ZnO)[86]. The band gap of ZnO and TiO_2 can be narrowed and be responsive to visible light.[173, 174] For example, the energy gap of ZnO reached 2.85 eV,[175] while a TiO_2-based catalyst had a band gap around 2.00 eV.[176] The action spectra of ZnO and TiO_2 also confirmed their response under visible light and solar light.[177–179] However, the application of photoreactions is often limited due to the inefficient utilization of light.[87]

One of the main reasons that restrict the development of solar-driven photocatalytic degradation of organic pollutants in the aqueous environment is the instability of solar light under different scenarios.[103, 104]. For example, sunlight is attenuated when the wastewater has high turbidity [105] or the rainy and cloudy weather appears [106]. As a result, the number of photons that can be absorbed into the system decreases, so the activity of photocatalysts is considerably inhibited. In order to maximize the potential of photocatalysts under insufficient light, strategies to increase the number of species undergoing a photo process with a given amount of photons are needed. Several strategies have been widely investigated for this purpose, including incorporating light engineering design in photoreactors to improve their performance[107, 108], establishing a flow reactor to enhance the mass transfer or to shorten the light path[12], and preparing engineering photocatalytic materials for more efficient photocatalysis[109]. Introducing lenses into photoreaction systems is a potential alternative because of the ability of lenses to redistribute light.[110] The focusing effect of a lens creates high local light intensity at the focal point, accelerating the local photoreaction rates.

There are several advantages from surface MLs in a photoreaction process. First of all, surface MLs can be integrated into various reactors due to their small dimensions.[142, 180] Besides, such lenses have short focal distances with strong near-field focusing effect.[111, 112]. Last but not the least, the MLs with well-controlled optical properties and good durability can be prepared and flexibly modified by various methods.[25, 70, 115, 119–124, 181]. The fabrication of surface MLs based on nanodroplet polymerization is one of the promising technologies that are highly tunable and affordable.[27] Through this method, surface microlenses are obtained after the polymerization of surface droplets formed in a solvent exchange. [135] Notably, the morphology and spatial arrangement of surface microlenses are tunable[140]

In the work conducted by Dongare et al[78], the feasibility of integrating lenses with light-driven membrane devices for water purification was demonstrated, where a higher energy conversion rate of the device was achieved because of the focusing effect of lenses. On a smaller scale, the acceleration of the photoreactions by surface MLs was validated through the in-situ photoreduction of silver nitrate[112] and the direct photolysis of micropollutants[32]. Therefore, such surface MLs are also expected to be effective in enhancing the solar-driven photocatalytic degradation of contaminants in water. Implementing surface MLs based on the solvent exchange process as a candidate strategy for enhancing photodegradation efficiency under insufficient irradiation is worthy of investigation. However, the mechanisms of photocatalytic degradation combined with surface MLs have not been explored, so as the influence of the properties of MLs, photocatalysts, light sources, and water matrix on the degradation process.

In this work, we evaluated the performance of surface MLs in enhancing the photocatalytic degradation of four typical organic pollutants in river water, including methyl orange (MO), norfloxacin (NFX), sulfadiazine (SFD), and sulfamethoxazole (SMX)[182–184]. Surface MLs were photopolymerized from the nanodroplets obtained in a solvent exchange process[185] and could be flexibly tailored for better performance. The optimized spatial arrangement of surface MLs was selected based on the light treatment results. The mechanisms of surface ML-assisted photocatalytic degradation were investigated with experiments and optical simulation. By tuning the light sources, irradiation intensity, water matrices, and the geometry of reactors, the practical conditions with limited irradiation were simulated where the influence of surface MLs on photocatalytic degradation efficiency is studied. Last but not least, we used two commercial photocatalysts with good stability and durability[186, 187], ZnO and TiO_2, to assess the applicability of surface MLs in varied catalytic processes. The capability of surface MLs in promoting the photocatalytic degradation of organic pollutants in water was validated.

4.2 Methodology

4.2.1 Fabrication and characterization of random surface microlenses and high-curvature microlens array on planar glass substrate

Surface microlenses (MLs) were fabricated by photopolymerization of surface droplets under UV light, as shown in Figure 4.1 (a). The size and spatial distribution of surface MLs were determined by the diameters and positions of surface droplets. The solvent exchange process enabled us to flexibly control the formation of surface droplets and further adjust the properties of surface MLs.[27, 31] In the solvent exchange process, a self-assembled chamber was filled with a solution (solution A) which was a mixture of monomer, photoinitiator, ethanol, and Milli Q water. Then, Milli Q water saturated with monomer and initiator (solution B) was inserted into the chamber at a fixed flow rate. Consequently, surface droplets composed of monomers and the photoinitiator formed on the substrates due to the oversaturation during the solvent exchange process. When the substrate was homogeneously hydrophobic, surface droplets grew and coalesced on the substrate, leading to the formation of surface MLs with non-uniform size and spatial distribution (random MLs, MLR) after UV curing. On the other hand, surface droplet arrays (MLAs) could be prepared on a pre-patterned substrate with ordered hydrophobic microdomains[140].

Random surface MLs (MLR) for photocatalytic degradation system were prepared using methyl methacrylate (MMA) ($\geq$ 98.5%, Alfa Aesar) as the monomer and 2-hydroxy-2-methylpropiophenone (96%, Fisher) as the photoinitiator. Solution A was prepared by adding 8.0 vol% MMA and 0.8 vol% photoinitiator in 40 vol% ethanol aqueous solution. Then, Milli Q water saturated with MMA and photoinitiator, namely solution B, was injected into the chamber at a flow rate of 50 mL/h. A glass slide homogeneously hydrophobized with octadecyltrichlorosilane (OTS) (98.9%, Acros Organics, Fisher Scientific) was placed on top of the chamber as the substrate for surface droplets and MLs. The OTS coating of the substrate was prepared according to the procedure described by Zhang and Ducker[185]. The condition used to fabricate the random surface MLs was the optimized one in our previous work.[32] After the standard solvent exchange process, the chamber filled with liquid was sealed and horizontally set under UV light (365 nm, Analytik Jena UV lamp) for 15 min.

Surface ML arrays (MLAs) in the photodegradation processes were fabricated with lauryl methacrylate (LMA, Acros Organics) as the monomer in solution A. The solubility of LMA in water was lower than MMA, leading to more stable surface droplets during the solvent exchange and uniformity of surface MLAs. The pre-patterned substrate used for droplet formation was decorated with circular hydrophobic microdomains arranged in an array, fabricated by a photolithography process on an OTS-coated glass slide.[140] The diameter of each circular domain was 5.0 μm, and the spacing between two adjacent domains was 2.5 μm. By repeating the process of solvent exchange and UV curing, MLAs with higher curvature could be achieved.[160] In this work, three rounds of solvent exchange-UV curing process were performed. Solution A for the solvent exchange process was prepared by adding LMA and the photoinitiator (1/10 volume of LMA) into ethanol, while solution B was the LMA and photoinitiator saturated water. The LMA concentration in solution A in the three rounds of solvent exchange was 2 vol%, 4 vol%, and 2 vol%, respectively, while the flow rate of adding solution B into solution A was 8 mL/h, 4 mL/h, and 4 mL/h, correspondingly. The UV curing step lasted for 15 min after each round of the solvent exchange process, after which the high-curvature poly(lauryl methacrylate) (PLMA) MLs were obtained. The curvature of the PLMA ML array could not further increase because the adjacent MLs would be connected if more LMA were added on top of the MLs base.

Surface random MLs and ML arrays were observed under an optical microscope equipped with a camera (Nikon H600l and Nikon DSFi3). The lateral size and surface coverage rate of MLs were calculated by analyzing optical photos with Image J. The height of random MLs and high-curvature MLs array was separately characterized

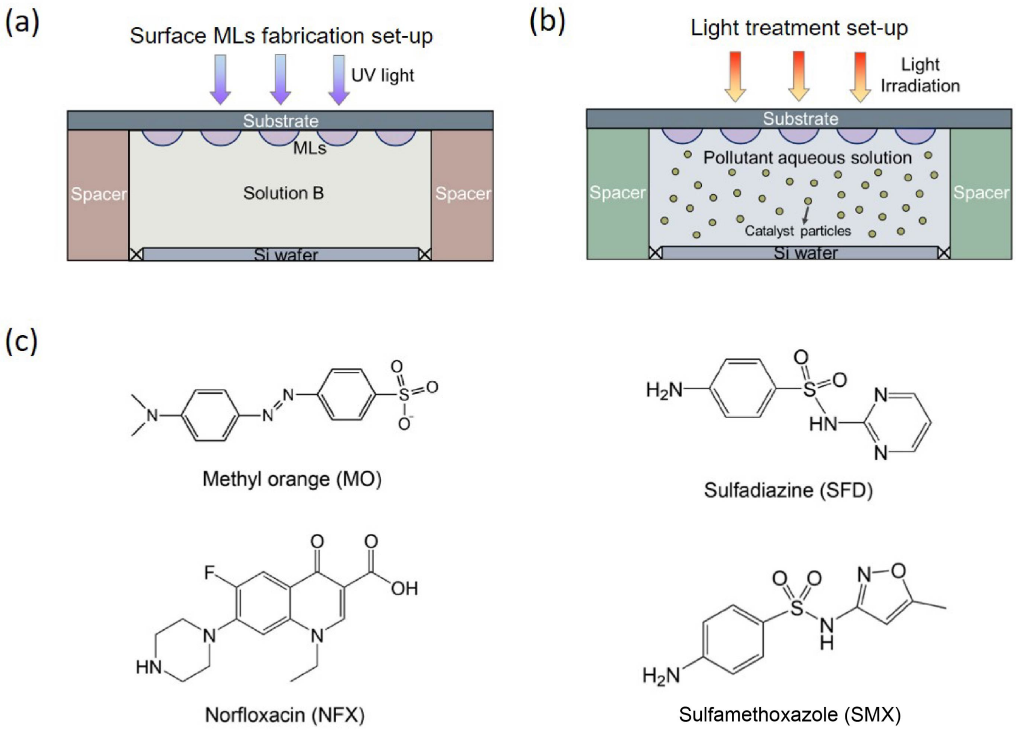

Figure 4.1: (a) Sketch of the fabrication process of surface MLs. The chamber height is 0.57 mm, the width is 12.2 mm, and the length is 56.0 mm (b) The experimental setup of light treatment with surface MLs and distributed catalysts particles. (c) Chemical structures of photodegraded pollutants, including methyl orange (MO), norfloxacin (NFX), sulfadiazine (SFD), and sulfamethoxazole (SMX)

with atomic force microscope (AFM, Bruker, tap mode) and confocal microscope (Zeiss Axio CSM 700). A transmission mode confocal microscopy (Leica SP8) was applied to measure the focal distance of MLs in the array. An intensity profile was obtained after a vertical scanning of the ML array-decorated substrate. The focal distance was defined as the distance between the brightest point in the intensity profile and the substrate surface.

4.2.2 Fabrication and characterization of MLs-decorated glass vials

The surface MLs can also be immobilized on a curved surface. The inner surface of a glass vial (Fisherbrand Class A clear glass vial) with a volume of 30 mL was hydrophobized by coating OTS onto the surface. The vial with a hydrophobic inner surface was firstly filled with 12 mL of a solution (solution A) composed of 7.6 vol% MMA, 0.8 vol % photoinitiator, 45.8 vol% water, and 45.8 vol% ethanol. Then, Milli Q water saturated with MMA and photoinitiator (solution B) was dripped into the standing vial through two tubes and two syringe pumps. The ends of the tubes were set at the opening of the vial, on the left side and right side of the vial, respectively. The flow rate in each tube was fixed at 3 mL/min. To fully replace solution A, 80 mL of solution B was added to the vial. During the solvent exchange process, the excess liquid was discharged from the vial from the opening. After the solvent exchange process, the vial was sealed and set under the UV lamp for 20 min. After removing all remaining mixtures and the washing step, the PMMA MLs-decorated vial was prepared. The morphology of the MLs-decorated vial can be observed with an optical microscope. All the parameters mentioned above were optimized in our previous work. [32]

4.2.3 Optical simulations of surface MLs on planar substrates

The optical simulations of surface MLs on planar substrates were conducted with Zemax OpticStudio. The glass substrate decorated with MLs was set in a horizontal plane (X-Y plane). A plane wave light source was set perpendicular to the horizontal plane (along the Z axis) with an intensity of 21.64 W/cm^2. Five horizontal light-flux detectors were set at different depths in the solution below the MLs-decorated substrate to demonstrate the top-view light irradiation profiles of both MLR and MLA. A rectangular X-Z plane monitor which crossed through the center of a single ML in the array was also designed to describe the cross-sectional irradiation profile of the ML.

4.2.4 Photocatalytic degradation of pollutants with surface MLs

4.2.5 Photocatalytic degradation of pollutants with surface MLs

The surface MLs were utilized in the photocatalytic degradation of common pollutants in natural water and wastewater to enhance the photodegradation efficiency (η). To evaluate the performance of random MLs and high-curvature ML array, the planar substrate with immobilized surface MLs was assembled in a homemade chamber for the light treatment of water that contained pollutants.(Figure 4.1 (b)) The light treatment was also conducted in the PMMA MLs-decorated glass vials to evaluate the efficiency of MLs on a curved surface on a larger scale. The pollutants involved in the degradation experiments include methyl orange (MO, 85%, Sigma-Aldrich), norfloxacin (NFX, Alta aesar), sulfadiazine (SFD, 99.0-101.0%, Sigma Aldrich), and sulfamethoxazole (SMX, analytical standard, Sigma Aldrich). The aqueous solutions of these pollutants with the analyte concentration of 5 mg/L were prepared with ultra-pure water (produced by Milli-Q Direct 16), synthetic river water, or real river water as the solvent. For the solution with ultra-pure water as the solvent, the pH value was measured at around 7 with a pH meter (Accumet AE150, Fisher Scientific).

To prepare the synthetic river water, 52.19 mg $Na_2SO_4 \cdot 10H_2O$ (Sigma Aldrich), 4.08 mg $NaNO_3$ ($\geq$ 99.0%, Sigma Aldrich), 106.96 mg $CaCl_2 \cdot 10H_2O$ (Sigma Aldrich), 100.81 mg $NaHCO_3$ (certified ACS, Fisher Chemical), 101.30 mg $MgSO_4 \cdot 7H_2O$ (Fisher BioReagents), 2.56 mg humic acid (technical grade, Aldrich), and 5.32 mg alginic acid (Acros organics) were dissolved in 1 L ultra-pure water. The real river water was collected from Whitemud Creek to the North Saskatchewan River in Edmonton, Alberta, Canada at 9:30 am on April 26, 2022. Both the synthetic water and real river water were characterized by a total organic carbon (TOC) analyzer (TOC-L Series, SHIMADZU), a pH meter (Accumet AE150, Fisher Scientific), and ion chromatography (Dionex ICS-5000, Thermo Scientific). The synthetic river water was at a pH value of 7.3, with a TOC value of 3.8 mg/L, and a COD value of 9.2 mg/L, while the river water was at a pH of 7.5, a TOC value of 25.6 mg/L, and a

COD value of 163.3 mg/L. The concentrations of ions in the synthetic are displayed in Table 4.1. SMX and MO were spiked in the synthetic river water and the real river water for the light treatment with the same concentration of 5 mg/L.

Ion type	${SO_4}^{2-}$	Cl^{-}	${NO_3}^{-}$	Na^{+}	Ca^{2+}	Mg^{2+}
Conc./mM	8.3	5.3	0.046	2.1	0.85	0.47

Table 4.1: Concentration of ions in the synthetic water (Unit: mM)

One of the commercialized photocatalysts, zinc oxide (ZnO, certified ACS powder, Fisher Chemical), was dispersed in the aqueous solutions containing different types of pollutants by a sonication step for 20 min. All the solutions were stored in a dark environment at a temperature of 4 °C except the light treatment process. The catalyst was dispersed in the aqueous solutions with sonication in the dark environment for 30 min to ensure sufficient adsorption of the pollutant on the surface of the catalysts. To assess the performance of surface MLs with varied amounts of ZnO, multiple concentrations of ZnO dispersed in the pollutant solutions (ultra-pure water as the solvent) were used, including 5 mg/L, 10 mg/L, 50 mg/L, and 100 mg/L. In addition to ZnO, titanium dioxide (TiO_2, 21 nm primary particle size, $\geq$ 99.5%, Aldrich chemistry) was used to verify the efficiency of surface MLs under different types of catalysts. To compare the performance of MLs when using two types of catalysts, the initial concentrations of TiO_2 and ZnO were set at 5 mg/L. The band gap of ZnO and TiO_2 was 3.26 eV and 3.25 eV, respectively, which were measured with diffusion reflectance spectrum (Hitachi U-3900H) and Tauc plot (shown in Appendix B, Figure S1 (c-d))[188].

Both the visible LED lamp (SOLIS-3C, Thorlabs) and the simulated solar light (SS200AAA Solar Simulation Systems, Photo Emission Tech) were used as light sources for the photocatalytic degradation of pollutants in water. The distance between the upper surface of the reactor and the light source was fixed at 23.5 cm for the visible light LED and 35.7 cm for the simulated solar light. A series of irradiation

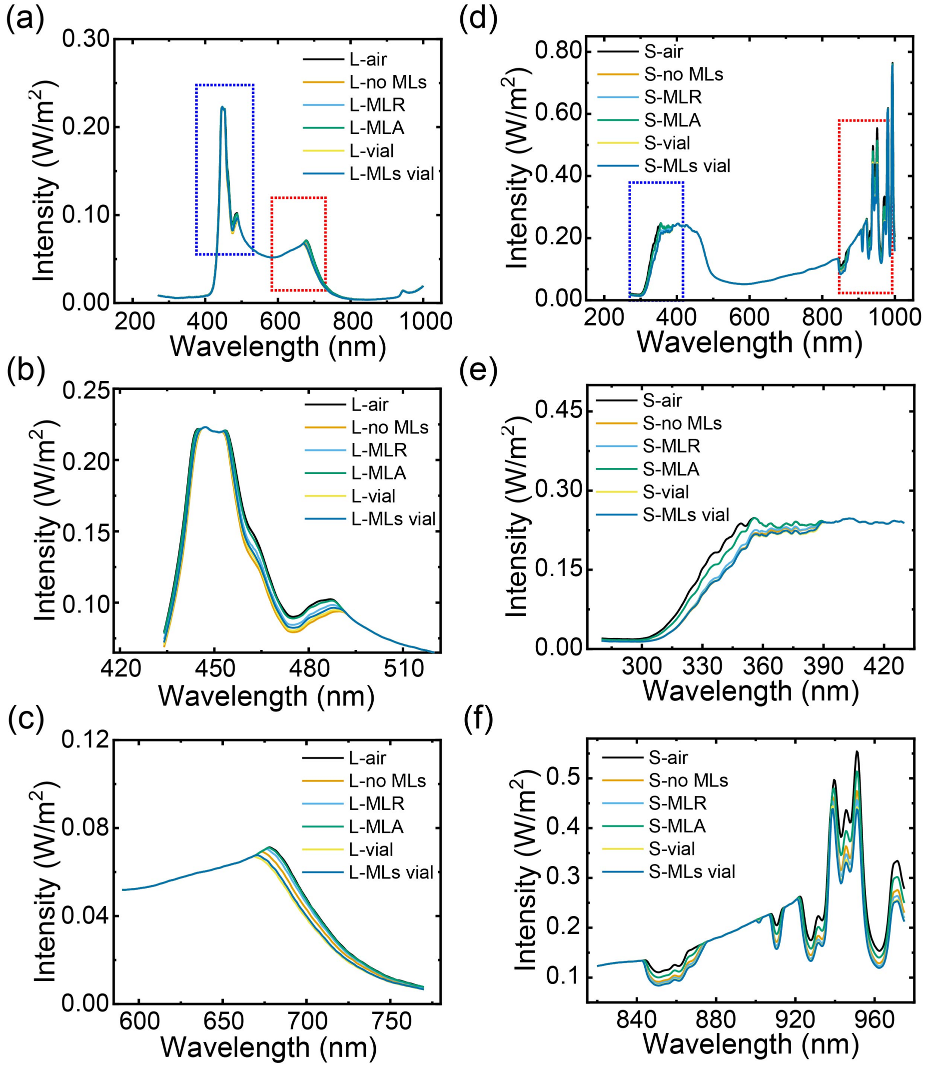

Figure 4.2: Spectra of light from visible LED lamp (intensity: 21.64 W/m^2) and from simulated solar light (intensity: 1 Sun) at the position of light treatment reactor. (a) Spectra of light from the visible LED lamp after transmitting through the air or top surface of the reactor. The zoomed-in spectra are shown in (b) (from 415 to 515 nm) and (c) (from 585 to 775 nm). (d) Spectra of the light from simulated solar light after transmitting through the air or the top surface of the reactor. The zoomed-in spectra are shown in (e) (from 285 to 435 nm) and (f) (from 820 to 775 nm).

conditions (shown in Table 4.2) were tested in this work by changing the light sources, the glass substrate, and the type of surface MLs. The spectra of the irradiation above the reactors were collected with a portable spectrometer (StellarNet Inc) at the top position of reactors, as shown in Figure 4.2 (a). In order to assess the influence of the irradiation conditions listed in Table 4.2 on the irradiation exposed to the treated solution, the spectra of light that transmitted through the top surface of the reactor (Figure 4.2 (b-g)) were obtained by setting the detection sensor of a spectrometer under the top surface of different reactors. The light intensities of the light sources were adjusted to investigate the influence of the light intensity on the MLs-enhanced photocatalytic degradation process.

Name	Light source	Substrate type	MLs type
L-air	Visible LED	/	/
L-no MLs		Planar glass substrate	/
L-MLR		Planar glass substrate	MLR
L-MLA		Planar glass substrate	MLA
L-vial		Glass vial	/
L-MLs vial		Glass vial	MLR
S-air	Simulated solar	/	/
S-no MLs		Planar glass substrate	/
S-MLR		Planar glass substrate	MLR
S-MLA		Planar glass substrate	MLA
S-vial		Glass vial	/
S-MLs vial		Glass vial	MLR

Table 4.2: Types of light sources and surface MLs in the light treatment

All the light treatments involved in this study are summarized in Table 4.3, and each condition is represented with its irradiation condition (listed in Table 2), the type of catalysts, and the concentration of catalyst (unit: mg/L). The MLs-involved photocatalytic degradation process was studied by various analytical instruments. The degradation efficiency (η) is calculated based on the equation (4.1), where C_i

Light source	MLs type	Catalyst	Catalyst Conc. (mg/L)
Visible LED	MLR	/	/
	MLA	/	/
	/	ZnO	100/50/10/5
	MLR	ZnO	100/50/10/5
	MLA	ZnO	100/50/10/5
	/	TiO_2	5
	MLR	TiO_2	5
	MLA	TiO_2	5
Simulated solar	/	ZnO	100/10
	MLR	ZnO	100/10
	MLA	ZnO	100/10
	vial	ZnO	10
	MLs vial	ZnO	10

Table 4.3: Types of surface MLs and photocatalysts used in the light treatment

is the initial concentration of a pollutant after the adsorption of pollutants reached equilibrium and C_f is the final concentration of the pollutant after the light treatment. For the solution containing pollutants prepared with ultra-pure water, the concentration change of a pollutant could be identified with UV-visible spectroscopy (UV-vis, Thermo fisher, Genesys 150) based on the Beer-Lambert Law. According to the Beer-Lambert Law, the absorbance (A) of an analyte in the solution is proportional to its concentration (C) if the analyte concentration is within a linear range. The relationship between absorbance and concentration is shown in (4.2) (ε: molar attenuation coefficient, L: light path). The concentrations of organic analytes involved in this work are within the linear range, and the evidence was included in Appendix B (Figure S1). Therefore, the η of a pollutant can be calculated by equation (4.3) by combining equation (4.1) and (4.2). A_i and A_f are the absorbance at the representative peak [151] of a pollutant before and after the treatment, respectively.

$$\eta = \frac{C_i - C_f}{C_i} \times 100\% \tag{4.1}$$

$$A = \varepsilon CL \tag{4.2}$$

$$\eta = \frac{C_i - C_f}{C_i} \times 100\% = \frac{A_i - A_f}{A_i} \times 100\% \tag{4.3}$$

For the solution containing pollutants prepared with the synthetic water, the concentration changes of analytes were characterized by an ultra-performance liquid chromatography-mass spectrum (UPLC-MS, ACQUITY UPLC H-Class, Waters). The method to detect SMX with UPLC-MS was included in supporting information. All solutions containing photocatalyst suspends were centrifuged for 10 min at 14,000 rpm, and then only the supernatant was used for analysis.

The performance of the photocatalysts is influenced by many factors associated with the irradiation conditions (such as intensity, photon absorption, light scattering, etc.), catalyst properties, adsorption of pollutants, properties of water matrices, and chemical properties of organic contaminants. In order to show the enhancement of photocatalytic degradation efficiency obtained by implementing surface MLs, all the parameters except the usage of MLs were kept constant. The ability of surface MLs to enhance η of pollutants was quantified with an enhancement factor (f) which was defined by the equation (4.4)

$$f = \frac{\eta_{(MLs+catalyst)}}{\eta_{catalyst}} \tag{4.4}$$

The reaction mechanisms may be further understood from the balance between the mass of CO_2 generated from the complete degradation of organic contaminants and the mass decrease in solutions containing contaminants.[189, 190] However, as shown in Figure 4.1 (b), our reaction systems were fully sealed with negligible mass transfer from the system during the irradiation. In addition, it was almost impossible to quantify the CO_2 production from our systems due to the small volume of our samples and the dissolution of CO_2 in water. The total amount of the model contaminant in the treated solution was 10 μg. Even from complete degradation, only 17 to 22 μg CO_2 would be produced at maximum. CO_2 production from the photodegradation of organic contaminants in MLs-enhanced photocatalytic systems may be conducted in the future after modification of the experimental set-up. Instead of mass balance to monitor the reaction mechanism, the characterization of free radicals generated in the photocatalytic system was feasible to reveal the degradation mechanism in the presence of surface MLs.[191, 192]

The presence of free radicals in the photocatalytic degradation process was verified with an electron spin resonance (ESR) spectrum (Elexsys E-500, Bruker). The ultrapure water dispersed with ZnO (10 mg/L) was irradiated by the visible LED lamp or the simulated solar light for 30 min before the ESR detection. 5,5-Dimethyl-1-pyrroline N-oxide (DMPO, Sigma Aldrich), as a spin-trapping agent, was used to capture the hydroxyl free radicals in the treated solution. DMPO was added to the treated solution with a concentration of 5.7 g/L just before the light treatment started. The solution was added into quartz (CFQ) ESR tubes (outside diameter: 5mm) to detect free radical signals immediately after the irradiation. The ESR spectrum of methanol dispersed with ZnO (10 mg/L) under MLA was also obtained after the irradiation by simulated solar light for 30 min (shown in Appendix B, Figure S2).

4.3 Results and discussion

4.3.1 Morphology and optical properties of MLs

The redistribution of light irradiation is determined by the morphology and spatial arrangement of surface MLs. The MLs on the pre-patterned substrate (MLA) are arranged in a highly-ordered array with a uniform radius of 6.5 μm due to the confinement of hydrophobic domains, as shown in Figure 4.3 (b). The surface coverage rate and the contact angle of MLA are 49 ° and 63.7%, respectively. The light intensity profiles of MLA obtained from the confocal microscope and optical simulation results of a single ML from the ML array are displayed in Figure 4.3 (c) and (d), respectively. Due to the uniform size, the focal distances of MLs in the array have the same value. From the light intensity profiles, it is found that the focal points of MLA are located in a horizontal plane which is around 16 μm away from the substrate. As a comparison, the focal distance of a single ML in the array is 16.5 μm according to the optical simulations. Therefore, the simulated focal distance is consistent with that obtained from the confocal microscope.

Another type of surface MLs, represented with MLR, is fabricated on homogeneous substrates. MLR are randomly distributed on the planar substrate, and their diameters vary from 2 μm to 200 μm with a fixed contact angle of 7.5 °. The surface coverage rate of MLR is 47.2%. The focal distances of MLR differ due to the existence of the size distribution among them. Therefore, it is difficult to measure the focal distances of MLR with a confocal microscope.

The top view intensity profiles of surface MLs in Figure 4.4 (a-b) exhibit the distribution of irradiance at the horizontal plane with certain depths. At the depth of 16.5 μm which is close to the focal distances of MLA, the maximum incident flux value under MLA is the highest, reaching 2.95×10^{-8} W. The number of the spots with the highest value is 400 on the horizontal plane with an area of 2.25×10^{-2} mm^2. In comparison, the highest maximum incident flux value under MLR is 2.26×10^{-7} W located at the depth of 225.5 μm. However, only two spots reach 2.26×10^{-7} on the horizontal plane under random MLs within the same area. Therefore, the maximum total incident flux over the horizontal plane of MLA is around 26 times larger than that of MLR.

When the depth increases, the maximum incident flux value under MLA significantly drops, while the value under MLR first increases and then gradually diminishes. As the depth changes from 16.5 μm to 797.5 μm, the maximum flux value under MLA

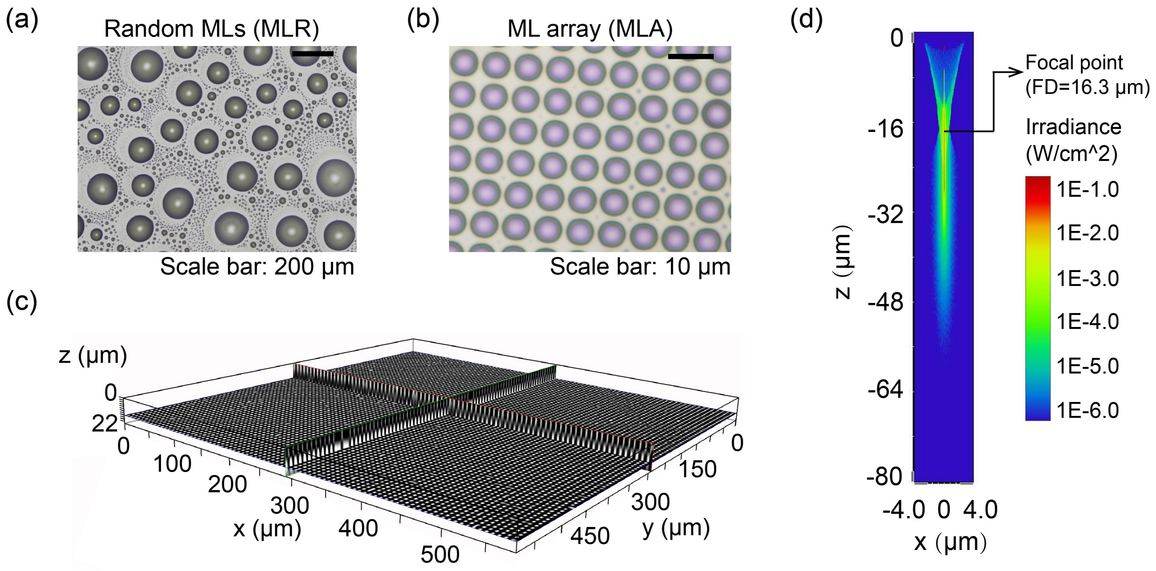

Figure 4.3: Images of (a) random MLs (scale bar: 200 μm) and (b) ML array (MLA) (scale bar: 10 μm) obtained with optical microscope (c) The light intensity profile of MLA with confocal microscope (scale bar: 100 μm) (d) The cross-sectional light intensity of a single ML in the array. The point with the highest irradiance value is the focal point. The position with z=0 is the substrate surface. The focal distance is the distance between the focal point and the substrate surface.

decreases by 56%, while the value under MLR increases by 3.6 times. The variation of focal distances of MLR avoids the sharp decay of irradiation intensity along the Z direction but also causes a lower maximum total incident flux. In summary, the uniformity of focal distances of MLA can reach a maximum flux, higher than MLR, but the decay irradiation intensity along the Z axis is much more rapid.

4.3.2 Free radicals in the presence of MLs

The reflectance spectrum of ZnO and TiO_2 powders (Figure 4.5 (a)) and the absorbance spectra of ZnO suspension with different concentrations (Figure 4.5 (b)) indicate that the catalysts applied in the light treatment partially absorb visible light under the irradiation of visible LED and simulated solar light. The existence of free radicals is verified by the electron spinning resonance (ESR) spectra. Based on the spectra obtained by ESR (Figure 4.5 (c)), no obvious signals can be observed when neither ZnO nor surface MLs are used in the light treatment. Under both visible LED

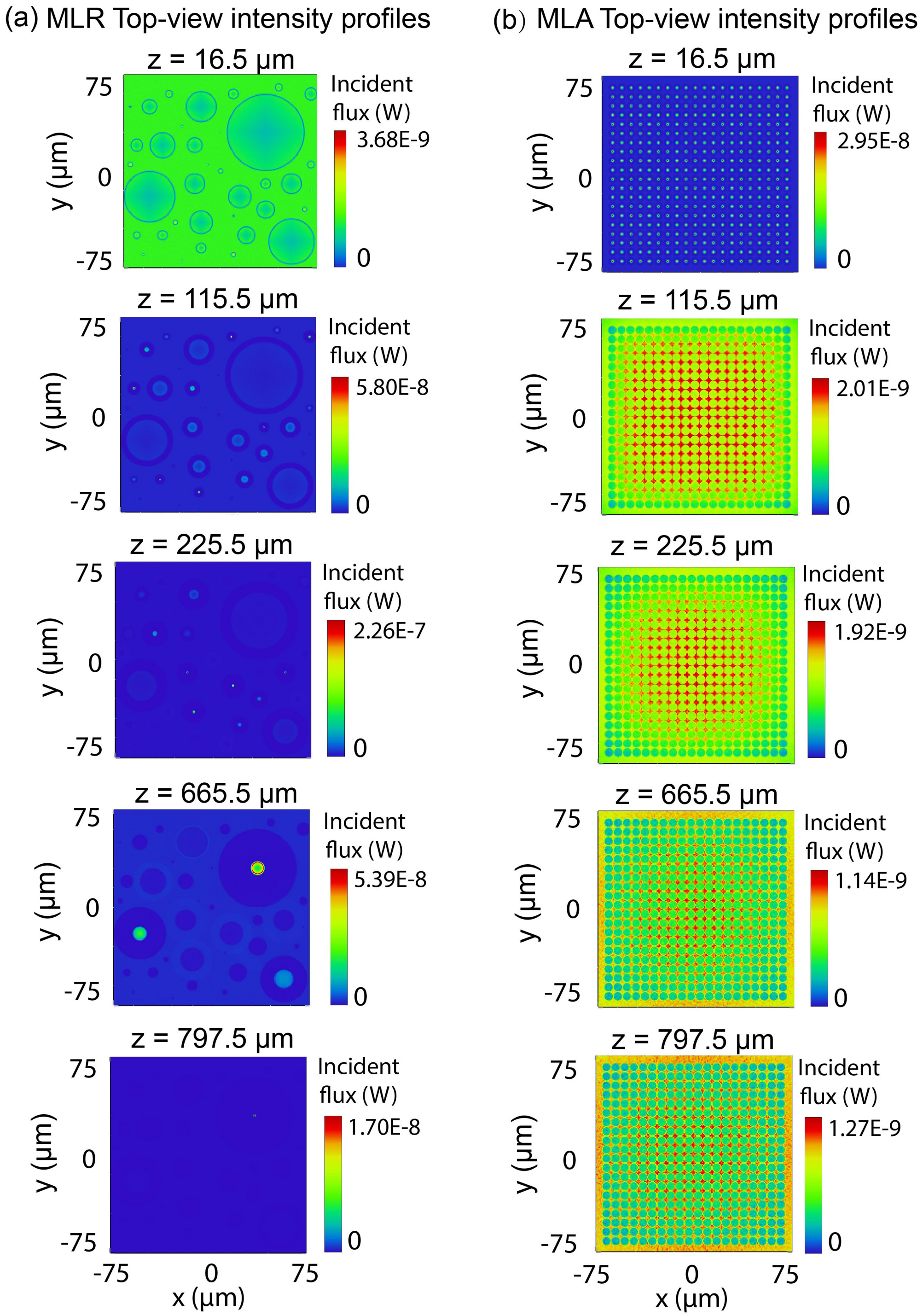
(a) MLR Top-view intensity profiles

(b) MLA Top-view intensity profiles

Figure 4.4: Top view intensity profile under (a) MLR and (b) MLA at the horizontal plane with the distance of 16.5 μm, 115.5 μm, 225.5 μm, 665.5 μm, and 797.5 μm away from the substrate surface.

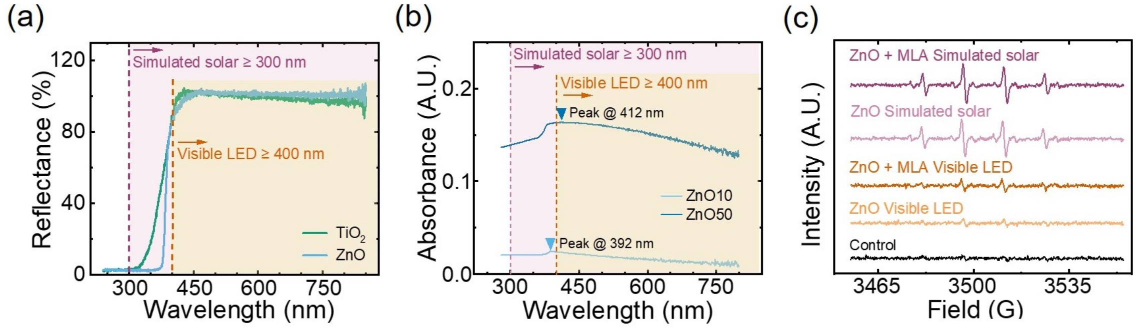

Figure 4.5: (a) Reflectance spectra for ZnO and TiO_2 particles with diffusion reflectance spectroscopy. (b) UV-vis absorbance spectra of ZnO suspension in Milli Q water with the concentration of 10 mg/L and 50 mg/L. The minimum wavelength of the visible LED and simulated solar light is 400 nm and 300 nm, respectively. (c) Electron spinning resonance (EPR) spectra under different conditions after light treatment of 30 min. (The black curve is for the condition without ZnO particles and surface MLs. The light blue curve represents the treatment with only ZnO particles, while the dark blue curve is for both ZnO and MLA under a visible LED lamp. The light orange curve is for the conditions with only ZnO particles, while the dark orange curve is for both ZnO and MLA under simulated solar light.)

light and simulated solar light, a similar curve shape is observed when ZnO is added to the system. As described in the literature [191], the spectra indicate that ·OH free radicals form after ZnO particles absorb the energy from either visible LED or simulated solar light. The formation of ·OH accelerates the degradation of pollutants. When MLA is applied together with ZnO, the signals of free radicals become stronger under both visible LED light and simulated solar light. Therefore, it is possible that more free radicals are generated by utilizing MLA. Consequently, more free radicals could cause higher degradation efficiency (η).[193]

Stronger signals of free radicals observed in the system with MLA could be attributed to the higher light intensity at the focal points of MLs. Based on the second law of photochemistry,[165, 166] higher light intensity leads to a higher concentration of reactive species, such as hydroxyl free radicals in the MLs-enhanced photocatalytic system.[194, 195] The light intensity at focal points of surface MLs increases by several times as shown by the optical simulation results (Figure 4.4). A higher concentration of active species in the MLs-induced system is confirmed by ESR characterization in our previous work. [32]. Similar to the photolysis system without catalysis, the ESR spectra in Figure 4.5 suggested that the photodegradation with ZnO as the catalyst could also be accelerated, due to the larger amount of free radicals from the focusing effect of surface MLs.

The increase in the concentration of free radicals is the consequence of the stronger local irradiance intensity in the presence of surface MLs. But the types of free radicals are not expected different from the situation without MLs, as the types are only determined by the light source and the type of photocatalyst. TiO_2 used in our experiments is a commercialized photocatalyst that has been widely studied [196, 197]. According to ESR results reported in the literature, we could conclude that hydroxyl free radicals form when TiO_2 acts as the photocatalyst, which promotes the degradation of organic pollutants.

4.3.3 Influence of catalyst concentration on the efficiency of photocatalytic degradation under visible light

The absorbance curves of the solutions containing different pollutants before and after light treatment are plotted in Figure 4.6. For the four pollutants treated under a visible LED lamp, slight enhancement can be observed by only applying surface MLs. By comparing the two types of surface MLs, MLA performs better than MLR since the decrease of absorbance peak is more obvious.

As shown in the second column of the plots in Figure 4.6, the reduction in absorbance values of all pollutants in the presence of ZnO particles improved. Such improvement becomes larger when we increase the initial concentration of ZnO. By combining surface MLs with ZnO particles, the absorbance peaks of pollutants further decrease. In the presence of ZnO, more reduction of absorbance is also observed with MLA compared with MLR, indicating the higher removal rates of pollutants with MLA.

The photodegradation efficiency of all pollutants under the visible LED light is

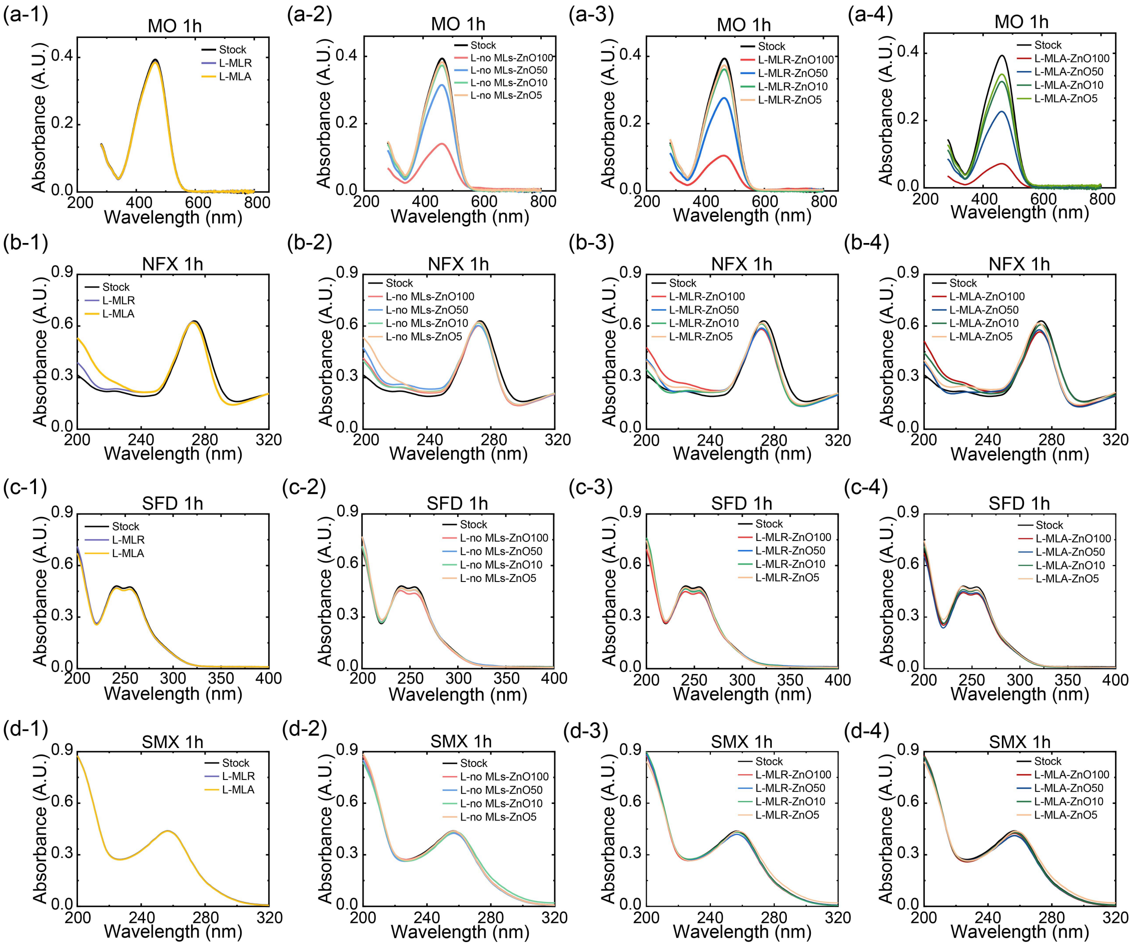

Figure 4.6: Representative absorbance spectra of pollutants (MO in (a-1) to (a-4), NFX in (b-1) to (b-4), SFD in (c-1) to (c-4), and SMX in (d-1) to (d-4)) with surface MLs and ZnO (under visible LED) after light treatment with 1 h.

plotted over the concentration of ZnO in Figure 4.7 (a). As the concentration of ZnO particles increases, η of all four pollutants is enhanced. However, the enhancement of η by adding dispersed ZnO particles into the solutions differs with the type of pollutants. For the photodegradation of MO with ZnO, η after the irradiation of 1 h is improved by 59.2% when the ZnO concentration increases from 5 mg/L to 100 mg/L. For the other three pollutants, the change of η after enhancing ZnO concentration from 5 mg/L to 100 mg/L is much smaller than that of MO, which is 5.7% for NFX, 2.9% for SFD, and 2.3% for SMX. The pollutant that is more difficult to degrade, which is SMX, has the least improvement when increasing the concentration of ZnO. The different degradation mechanisms among the pollutants may lead to the varied effectiveness of ZnO. Much higher η efficiency of MO degradation is possibly related to the sensitization mechanism for azo dyes. Charges are produced as the MO molecules are excited under irradiance and then injected in photocatalysts and oxidized dye for subsequent degradation.[198, 199] In contrast, the sensitization mechanism does not apply to other tree organic compounds, including NFX, SFD, and SMX, since they are transparent to the irradiation wavelengths. Regardless of the details in photodegradation mechanisms for those organic contaminants, the enhancement in η is achieved for all of them by adding ZnO.

Comparing with the situation only implementing ZnO or only surface MLs, the condition with both MLs and ZnO shows higher η, indicating the synergistic effect in the surface MLs-enhanced photocatalytic system. By applying surface MLs in the photocatalytic degradation process with ZnO as the catalyst, the distinguished enhancement of η can be confirmed in all four pollutants. The variance in the enhancement of η resulted not only from using surface MLs but also from the increase in ZnO concentration, which is similar to the situation only with adding ZnO in the reaction systems. The photocatalytic degradation exhibited higher η with MLA compared with that using MLR. The possible reason for the more outstanding effect of MLA is the more efficient irradiation redistribution based on the highly-ordered

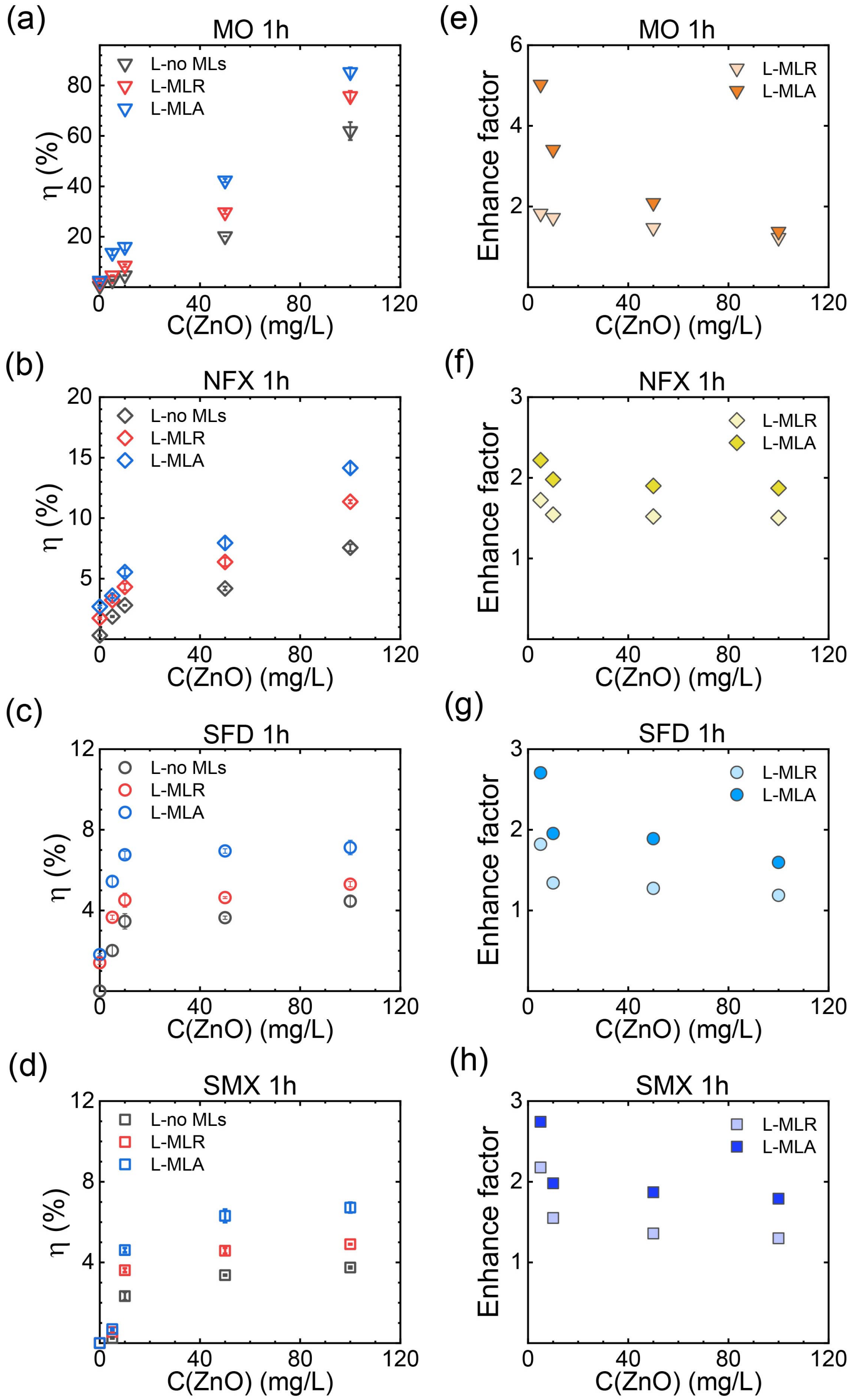

Figure 4.7: Photodegradation efficiency of (a) MO, (b) NFX, (c) SFD, (d) SMX using surface MLs and ZnO with different concentration (under visible LED). Enhancement of photodegradation efficiency of (e) MO, (f) NFX, (g) SFD, (h) SMX by using surface MLs

structure in MLA, which is also demonstrated in the optical simulations.[200]

The enhancement factor for the MLs-enhanced photodegradation using ZnO as the catalyst is calculated with equation (4.4). As shown in Figure 4.7 (e-h), the enhancement factor becomes lower at higher ZnO concentrations. The amount of active species is the key factor determining the rate of photodegradation. In the photodegradation enhanced by ZnO and surface MLs, the number of active species is up to the dosage of ZnO and the number of hot spots created by MLs.[112, 201] The total number of active species (n_{total}) can be estimated using Equation (4.5). In the equation, $n_{catalyst}$ is the number of active species generated due to the excitation of ZnO, and n_{MLs} is the number of active species attributed to the focusing effect of MLs. The photocatalytic degradation efficiency is dependent on the number of active species in the system. Therefore, the enhancement factor with MLs is positively related to the ratio of n_{MLs} and $n_{catalyst}$ in Equation (4.6). With an increase in the concentration of ZnO, $n_{catalyst}$ also increases while n_{MLs} is fixed, therefore, the enhancement factor drops down.

$$n_{total} = n_{catalyst} + n_{MLs} \tag{4.5}$$

$$f \sim \frac{n_{total}}{n_{catalyst}} = 1 + \frac{n_{MLs}}{n_{catalyst}} \tag{4.6}$$

The enhancement factor in η of ZnO-photocatalyzed degradation by surface MLs is also monitored with the elongated irradiation time of light treatment. The enhancement factor for the four organic pollutants is plotted with the irradiation time in Figure 4.8. For MO and SMX, the factor becomes smaller when the irradiation time increases from 1 h to 2 h. Reversely, the factor grows in the photocatalytic degradation of NFX and SFD during a longer treatment time. The difference in the enhancement factor not only is due to the type of pollutants but is also related to the properties of MLs. The enhancement factor obtained by MLR shows less change

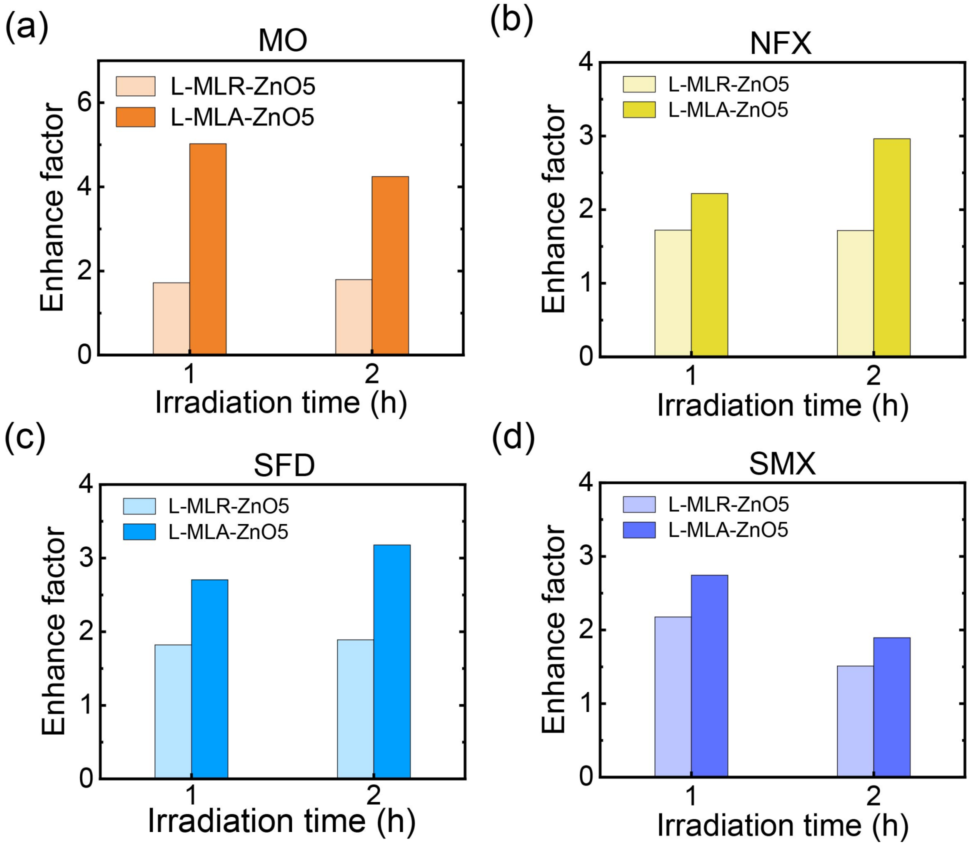

Figure 4.8: Enhancement factor of ZnO-photocatalyzed degradation efficiency of (a) MO, (b) NFX, (c) SFD, (d) SMX with surface MLs after irradiation time of 1 h and 2 h.

than that by MLA after the longer irradiation time.

4.3.4 General enhancement of photocatalytic degradation with surface MLs under visible light

The effectiveness of surface MLs is verified by using a different catalyst in the photocatalytic degradation process. As shown in Figure 4.9 (a-d), more decrease in absorbance peaks is presented when TiO_2 is used as the catalyst compared to that without a catalyst. When combining TiO_2 with surface MLs, more organic pollutants are degraded than those in the treatment with only TiO_2. After the same light treatment process, the MLA-enhanced photocatalytic degradation with TiO_2 has the most decrease in absorbance peak values.

The η values of all pollutants after the irradiation of 1 h with only TiO_2 or with both TiO_2 and MLs are displayed in Figure 4.9 (e). The η values of all four pollutants have been further improved after applying MLs in the photocatalytic degradation with TiO_2. Moreover, MLA shows more enhancement compared to MLR. The enhancement factor by using MLR and MLA are shown in Figure 4.9 (f). The effect of surface MLs on the degradation catalyzed by TiO_2 is similar to that catalyzed by ZnO. Therefore, surface MLs accelerate photocatalytic degradation, regardless of the types of catalysts.

4.3.5 MLs-enhanced photocatalytic degradation under simulated solar light

The representative absorbance spectra of SMX solution after the irradiation under different conditions are shown in Figure 4.10 (a-d). By comparing Figure 4.10 (a) and (c), it is found that the absorbance peak drops faster when the concentration of ZnO increases. As shown in Figure 4.10 (a) and (b), the decrease of absorbance peak value is higher when MLA is used in the light treatment. Such difference is also displayed in Figure 4.10 (c) and (d), where the concentration of ZnO changes to 10 mg/L.

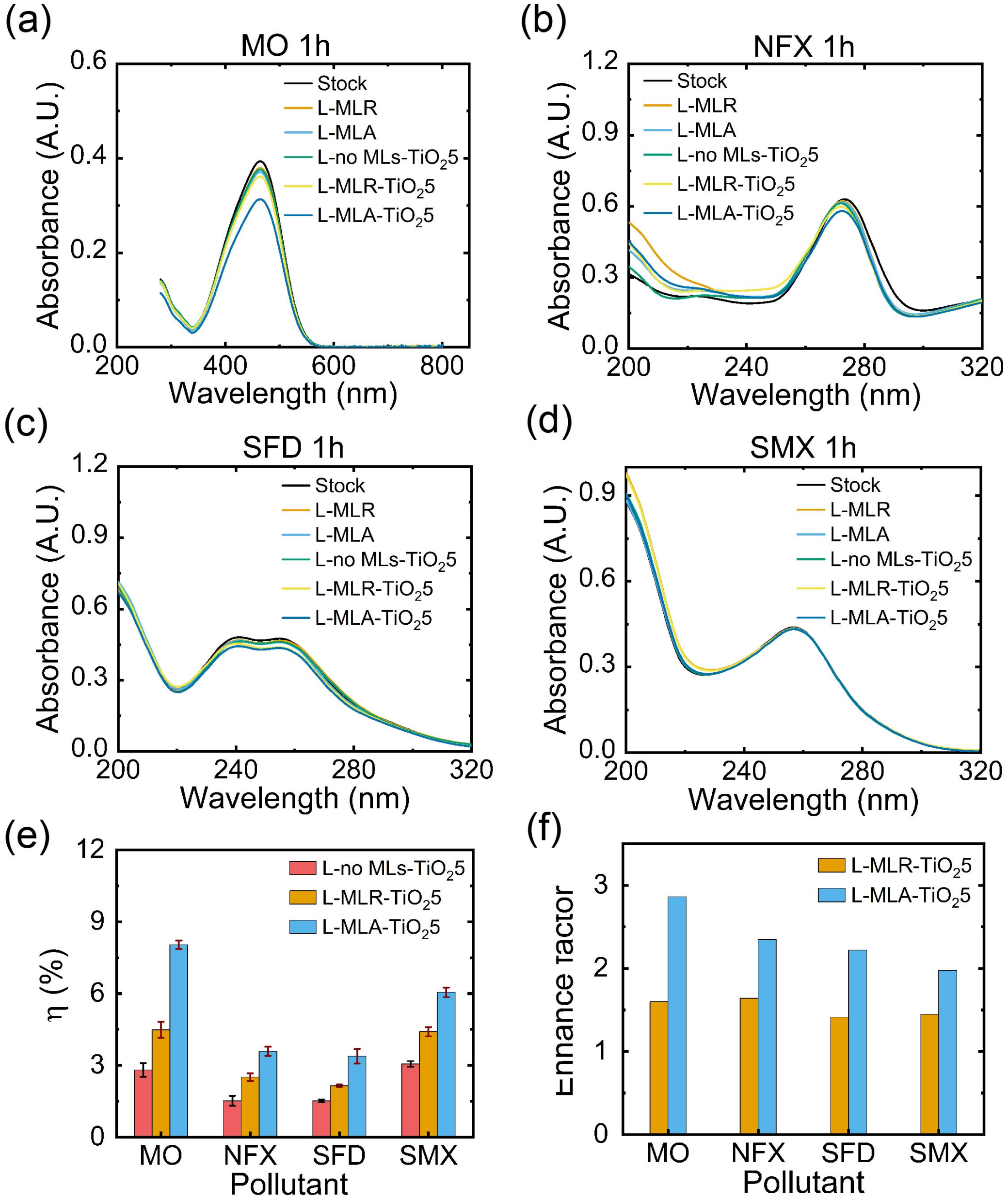

Figure 4.9: Representative absorbance curves of (a) MO, (b) NFX, (c) SFD, (d) SMX after the light treatment under the visible LED lamp for 1 h. (e) Photodegradation efficiency and (f) enhancement factor of TiO_2-photocatalytic degradation efficiency of pollutants with surface MLs after irradiation time of 1 h.

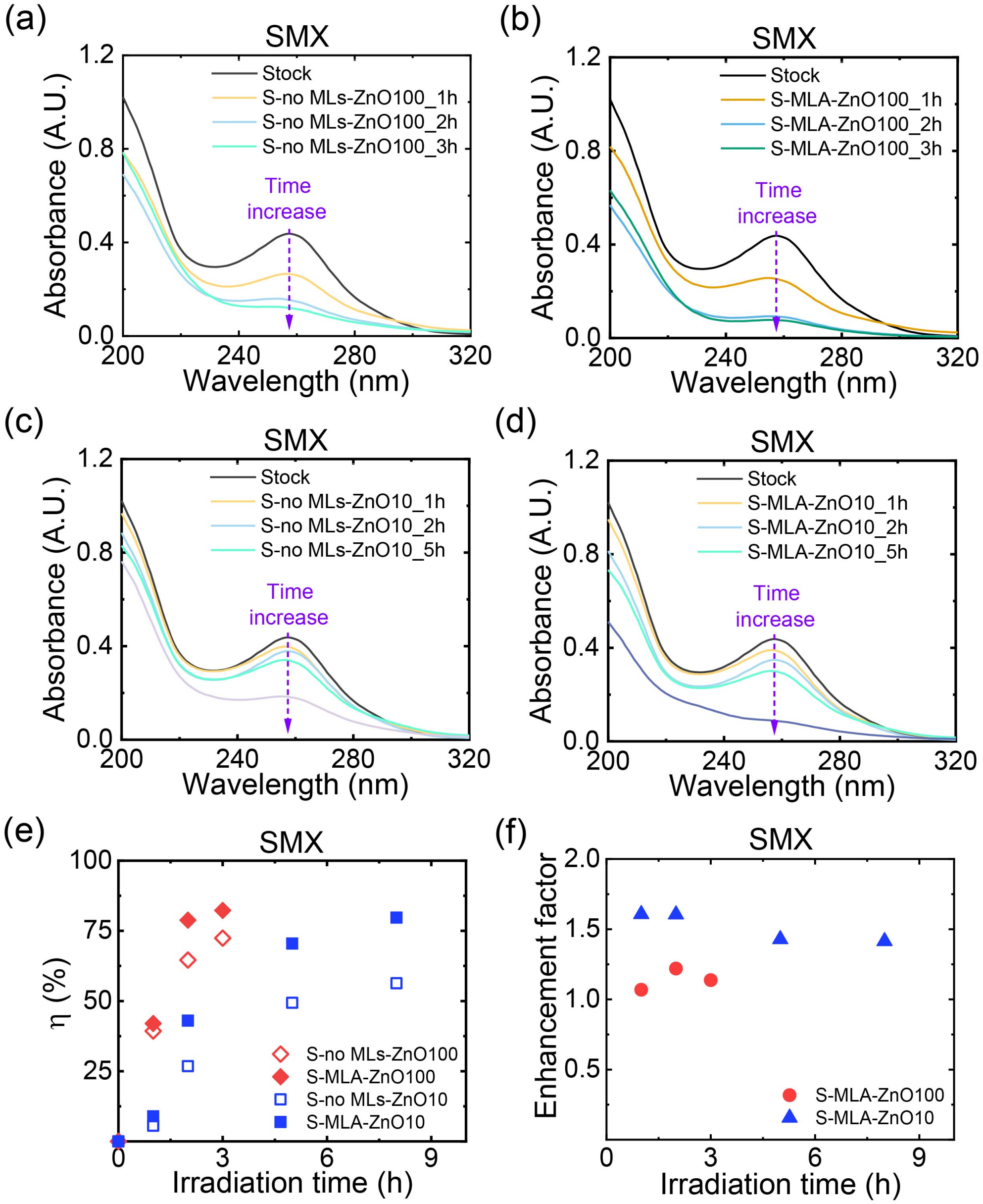

Figure 4.10: Representative absorbance curve of SMX solution after the light treatment with (a) only ZnO particles with a concentration of 100 mg/L (b) both ZnO with a concentration of 100 mg/L and MLA (c) only ZnO particles with a concentration of 10 mg/L (d) both ZnO with a concentration of 10 mg/L and MLA under the simulated solar light. (e) Photodegradation efficiency and (f) enhancement factor of SMX under different conditions.

The η values of all conditions presented in Figure 4.10 (a-d) are plotted in Figure 4.10 (e). For the concentration of ZnO equal to 100 mg/L, η reaches 72.4% within 3 h when both MLA and ZnO were used. To achieve a similar η with the ZnO concentration of 10 mg/L, around 5 h is required in the presence of MLA. The η under the simulated solar light is higher than that under the visible LED light due to the difference in light intensities and wavelength range.

The degradation efficiency of SMX with MLA is higher than that without MLA under the simulated light, which is the same phenomenon under visible light. The enhancement factors by MLA with two concentrations of ZnO under the simulated solar light are plotted with the irradiation time in Figure 4.10 (f). When the concentration of ZnO is 100 mg/L, the enhancement factor fluctuates around 1.2 as the irradiation time changes from 1 h to 3 h. For the photocatalytic degradation with a ZnO concentration of 10 mg/L, the enhancement factor by MLA is higher than that with 100 mg/L of ZnO. However, the factor drops from 1.6 to 1.4 as the irradiation time increases from 1 h to 8 h. The results under the simulated solar light reveal that the ordered spatial arrangement of MLs is optimal for photocatalytic degradation when the light source is closer to real solar light. The higher enhancement factor under the lower concentration of ZnO further validates our assumption shown in Equation (4.6) under simulated solar light.

The η of MLs-enhanced photocatalytic degradation of SMX is positively correlated with the intensity of simulated solar light in the range from 0.3 Sun to 1 Sun (Figure 4.11 (a-b)). As the irradiation time increases from 1 h to 2 h, the enhancement of η by improving the intensity of light is different. As the light intensity increases from 0.3 Sun to 1 Sun, the η increases from 2.1% to 5.6% with only ZnO after the irradiation of 1 h, while the η is enhanced from 4.3% to 9.0% by using ZnO combined with MLA. (Figure 4.11 (a)) The enhancement in η becomes larger when the irradiation time increases to 2 h based on Figure 4.11 (b).

In addition, the η of SMX with both of MLA and ZnO is always higher than that

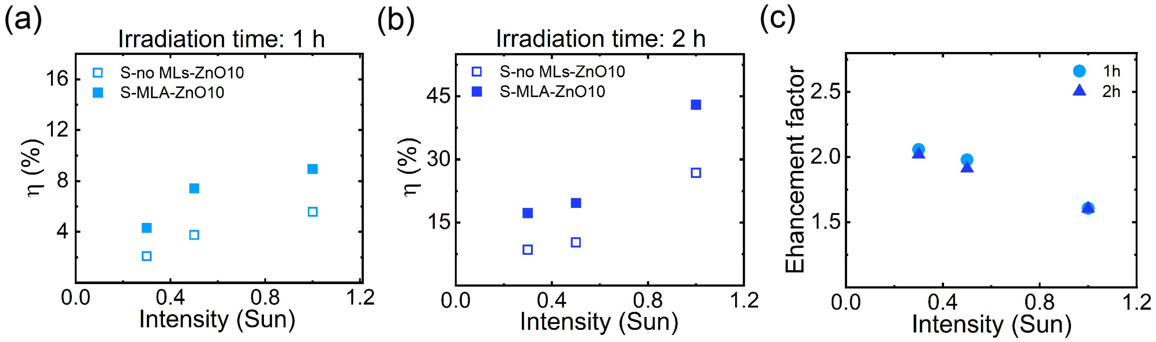

Figure 4.11: Photodegradation efficiency of SMX after the irradiation for (a) 1 h and (b) 2 h under the irradiation of the simulated solar light with different intensities (c) The enhancement factor of η by using MLA during the irradiation for 1 h and 2 h

with only ZnO under varying light intensities. The enhancement factor obtained by using MLA is shown in Figure 4.11 (c). Under irradiation with the same light intensity, the change of the enhancement factor after adding the irradiation time from 1 h to 2 h is less than 0.6. The influence of irradiation on the performance of MLA is negligible in the first two hours of photodegradation of SMX. The enhancement factor drops down when the intensity becomes higher, showing that surface MLs perform better under irradiation with low light intensity.

4.3.6 MLs-enhanced photocatalytic degradation in a glass container

The MLs-enhanced photocatalytic degradation can be conducted in the MLs-decorated glass vials. As demonstrated in Figure 4.12 (a), the glass vial keeps transparent with surface MLs immobilized on the inner wall. In the microscopic image (Figure 4.12 (b)), surface MLs on the vial gave various sizes and random spatial distributions because of the homogeneous hydrophobic coating on the inner surface of the vial. The diameter of MLs displayed in the picture is from 1.40 μm to 310 μm. The surface coverage rate of the MLs is around 50%.

The application of MLs-decorated vials can also enhance the η of degradation. As shown in Figure 4.12 (c), the η of degradation with MLA obtained from UV Vis spectra (Appendix B, Figure S3) is always higher than that using only ZnO. Under

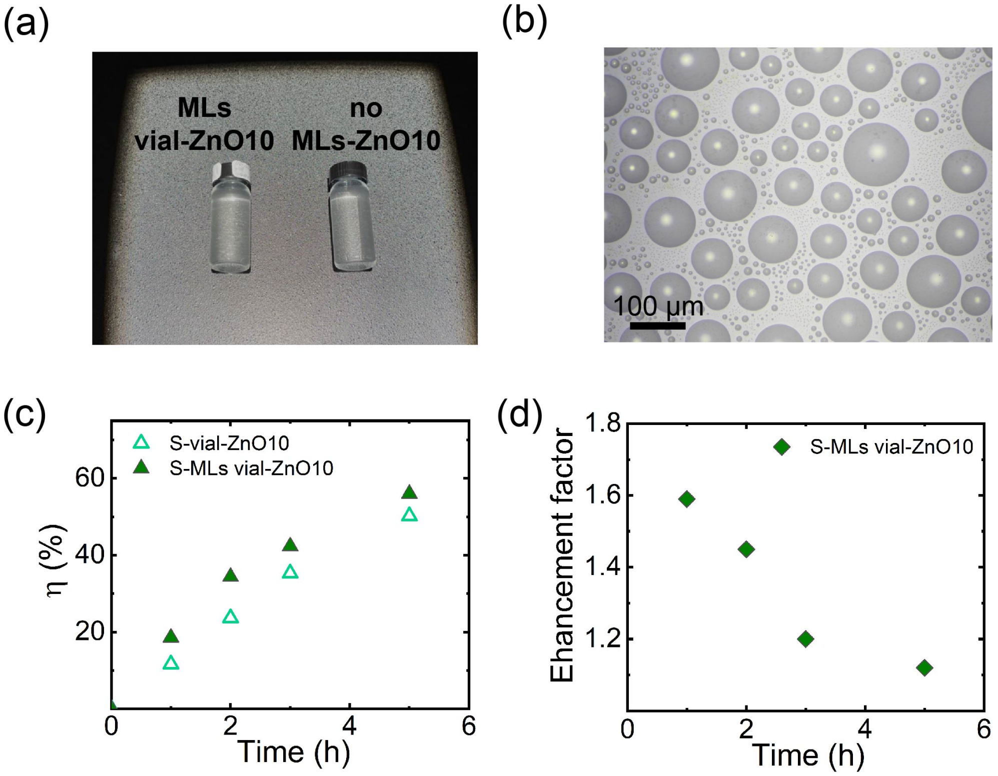

Figure 4.12: (a) Experimental set-up of ZnO-photocatalyzed degradation of SMX solution with the MLs-decorated vial (C(ZnO)=10 mg/L, C(SMX)=5mg/L, pH=7.0) (b) The optical image of the MLs on the inner wall of a glass vial (c) Photodegradation efficiency of SMX with ZnO in a bare glass vial and an MLs-decorated vial (d) Enhancement factor of ZnO-photocatalyzed degradation with the MLs-decorated vial

the irradiation of simulated solar light (1 Sun), the η of SMX with ZnO (10 mg/L) reaches 50.2% after five hours of light treatment, while the value is further improved to 56.0% after using the MLs-decorated vial. As demonstrated in Figure 4.12 (d), the enhancement factor by using MLs-decorated vials is 1.60 after the irradiation for 1 h and then continuously decreases with the irradiation time.

The degradation of SMX is significantly influenced by the concentration of SMX. When the concentration of SMX is less than 5 mg/L, a lower concentration of SMX results in a lower degradation rate.[202] The higher degradation rate with the existence of surface MLs directly leads to a lower concentration of SMX after irradiation. Therefore, the degradation rate of SMX with surface MLs drops faster than the process happening in the bare vial. As a consequence, the enhancement factor with MLs-decorated vials will decrease with time.

4.3.7 Effect of water matrix on MLs-enhanced photodegradation

The photocatalytic degradation of SMX with ZnO can be enhanced with surface MLs not only in ultra-pure water but also in synthetic river water and real river water. The photo in Figure 4.13 (a) displays the collection point of the river water. By comparing the transmittance curves of different water matrices (Figure 4.13 (b)), we find that the transparency of synthetic water and river water is less than that of river water, especially in the wavelength ranging from 200 nm to 500 nm.

As displayed in Figure 4.13 (c), the η of SMX with both MLR and MLA is improved compared with that with only ZnO. Similar to the results observed in pure water, MLA has better performance than MLR in accelerating the photodegradation of SMX. The η with the same type of MLs and irradiation time in the synthetic water is lower than that achieved in the ultra-pure water (Figure 4.10 (e)). Compared with the enhancement factor with surface MLs in ultra-pure water during the same irradiation time, the enhancement factor in synthetic river water is higher. For example,

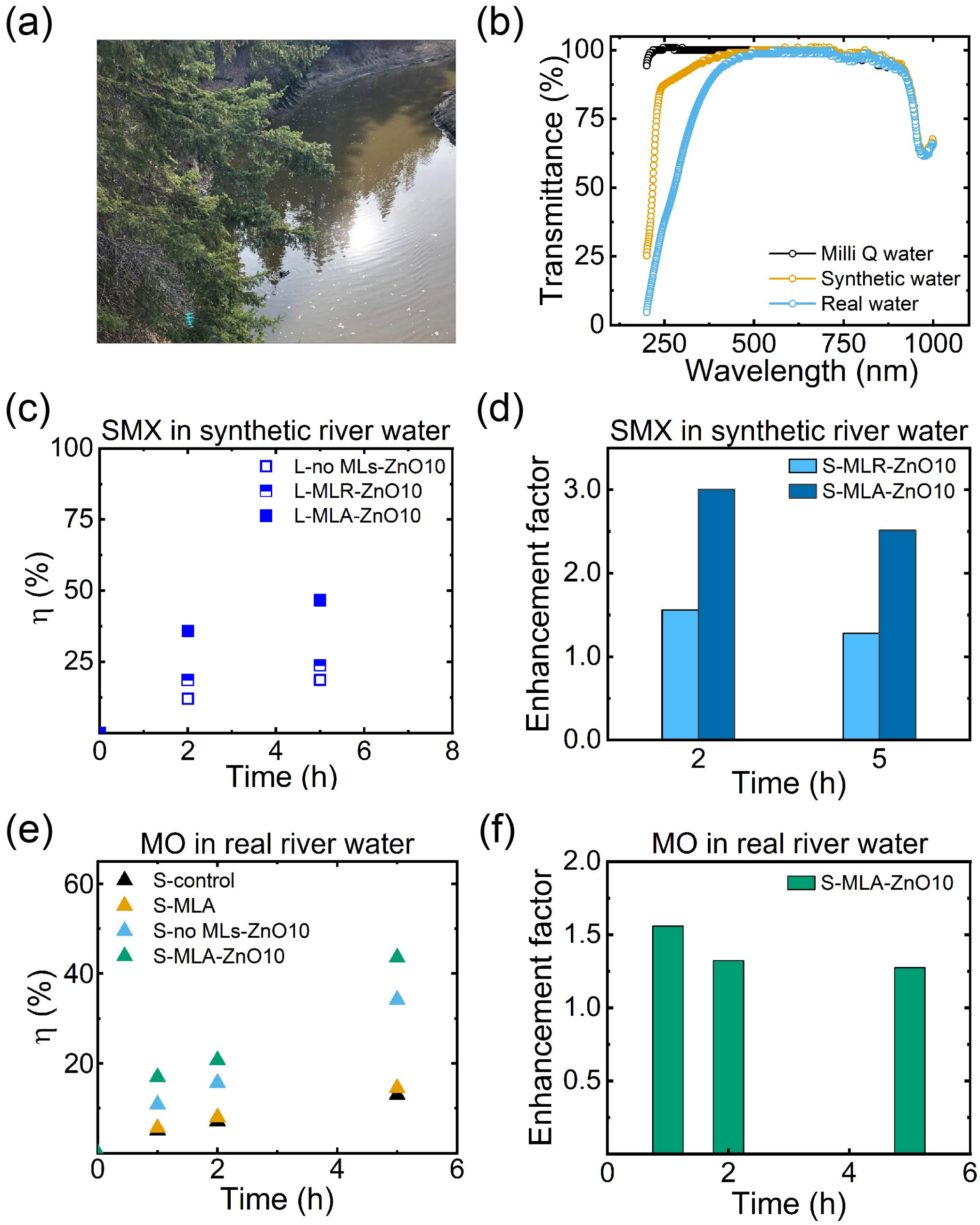

Figure 4.13: (a) A photo of the real river water collection site (b) Transmittance curves of three types of water matrices (c) Photodegradation efficiency of SMX in simulated water under simulated solar light (d) Enhancement factor of photocatalytic photodegradation efficiency of SMX achieved by MLR and MLA during 2 h and 5 h of irradiation. (e) Photodegradation efficiency of MO in the real river water under simulated solar light (f) Enhancement factor of photocatalytic photodegradation efficiency of MO obtained by MLA during 1 h, 2 h, and 5 h of irradiation.

the enhancement factor of MLR is 1.61 and 1.43 after 2 h and 5 h of irradiation, respectively. When using MLA, the factor is 3.0 for 2 h and 2.5 for 5 h (Figure 4.13 (d)).

The enhancement of photocatalytic degradation is also observed when using real river water as the matrix. The photodegradation efficiency of MO in river water and the enhancement factor of η over the irradiation time are plotted in Figure 4.13 (e) and (f), respectively. Without utilizing ZnO, around 14% enhancement is achieved by MLA after 5 h of irradiation. Compared with the condition without the catalyst and surface MLs, the degradation efficiency of MO is enhanced by a maximum of 163% with only ZnO after 5 h of irradiation. By setting MLA on the top of the light treatment chamber, the photocatalytic η of MO is further improved under the same irradiation condition, which is 235% higher than the control group and 27% higher than the group only with catalyst.

The difference in η and the enhancement factor after changing the water matrix into synthetic river water or real river water can be attributed to the variation in the transmittance of water. The transmittance of the synthetic water in the range between 200 nm and 500 nm drops as displayed in Figure 4.13 (b), while the decrease in transmittance of river water is even sharper. The decrease in the transmittance is possibly caused by more light absorption of the synthetic river water and real river water. As a consequence, the irradiation intensity in synthetic river water and river water should be lower than that in ultra-pure water, thus the enhancement of η by surface MLs is higher (as displayed in Figure 4.11 (c)).

4.4 Conclusions

In summary, our work demonstrates the microlenses (MLs)-enhanced photocatalytic degradation efficiency of micropollutants in water. More free radicals generated in the presence of surface MLs contribute to higher degradation efficiency. The enhancement is generally observed for all four targeted organic contaminants by using two kinds of photocatalysts. The microlens array is more effective than random microlenses in the photodegradation of all involved pollutants, which is attributed to the more effective redistribution of the irradiation energy. The performance of surface MLs, represented by an enhancement factor, varies with pollutants because of the difference in degradation mechanisms. Additionally, the enhancement in the η of photocatalytic degradation is higher at a lower concentration of the photocatalyst or under irradiation with lower intensity. Therefore, the results suggest that surface MLs have the potential for applications where the excitation of photocatalysts is suppressed. The feasibility of surface MLs in improving decontamination is also verified in synthetic river water and a real river water matrix. In the next stage, surface MLs may be tested in the light treatment of water samples containing multiple contaminants.

4.5 Supplementary materials

Supplementary data to this article can be found in the Appendix, section A.2.

Chapter 5

Scalable and facile formation of microlenses on curved surfaces enabling a highly customized sustainable solar-water nexus

5.1 Introduction

Sunlight is an important sustainable energy resource in the remediation of contaminated water[4, 65, 66]. For example, solar water disinfection can effectively inactivate a wide range of pathogens, due to a synergistic effect between UV irradiation and temperature.[67, 68] Solar energy can also be transformed into chemical energy for the degradation of hazardous materials in water.[203, 204] Current limitations in the application of solar-driven technologies include limited types of solar-degradable organic contaminants[205], small capacity[206], energy loss in contaminated water, in particular with high turbidity in water sources [207], and high dependence on sunlight intensity [208]. So far, to overcome the challenge of the high turbidity of contaminated water and the restricted sunlight availability, a possible solution is to redistribute and focus light with low intensity at local hot spots.[78, 209]

Among technologies to improve the efficiency of solar energy usage, microlenses (MLs) offer clear advantages in terms of flexibility[23], adaptability[78, 142], and scalability[128, 143]. MLs are able to redistribute and focus light and inhibit the loss of energy due to light reflection and scattering.[146, 147] Thanks to the strong near-field focusing effect of MLs, the focal points of MLs were hot spots with higher local irradiance intensity and temperature.[29, 78, 111, 112] Recently MLs are increasingly integrated in solar-driven optical devices [22, 144, 145]. In addition, surface MLs can enhance the photodegradation efficiency of organic pollutants in water.[32]

Several typical reactors are used for the solar-water treatment. Among them, inclined plate collectors are developed from the horizontal plates, receiving more irradiation due to the tilted angle for higher effectiveness[210]. With using tube receivers, parabolic trough collectors have the higher effective area and more concentrated solar radiation inside than planar reactors.[68, 211] Compound parabolic collectors combine the functions of multiple types of reactors and further improve the solar harvesting efficiency [212, 213]. Generally, reactors with curved surfaces are found to be more efficient for solar-driven water treatment. Integrating MLs on the surface of these reactors may have the potential for further improving the photodegradation efficiency.

Currently, most of the fabrication technologies of MLs are largely limited to flat substrates, small surface areas, and a low total number of MLs.[25, 119, 120, 122, 124, 127, 214, 215]. Multiple steps are required to fabricate MLs on curved surfaces. For instance, an ML array (MLA) can be prepared on a flexible PMMA substrate through screen printing followed by UV curing.[128] By combining a flexible mask and the reactive ion etching process, MLs were fabricated on photo-curable resin with a curved surface.[129, 130] In a multiple-templating method, arrays of MLs on a planar substrate are first copied to a flat film of siloxane elastomer that was bent into a curved template for a second round of templating.[131, 132] The technologies mentioned above are dependent on complicated devices[26, 133] and precise control of the dosage of the materials of MLs[134]. In comparison, surface MLs can be fabricated without sophisticated equipment by a solvent exchange process followed by local photopolymerization. [27, 185] The advantages of solvent exchange include various available substrate materials, solution-based fabrication processes, and flexibility for adjusting the size and curvature of MLs[28, 29, 33, 136, 138, 216–222]. However, surface MLs made by solvent exchange process are still restricted on 1D fiber or 2D planar surfaces, which limits the development of surface ML-functionalized reactors for a broader range of applications in solar water decontamination inside large reactors with curved surfaces.

In this work, we present a highly tunable and scalable approach for producing MLs on 3D topological surfaces using a solvent dilution process. We apply this method to design reactors with improved photodegradation efficiency of organic contaminants in water. The method proves to be feasible for the preparation of reactors having irregular shapes, large surface areas that are comparable to three times of a standard 4-inch wafer, or made with glass or plastics, allowing for the functionalization of a broad range of reactors with MLs. By adjusting the parameters in the solvent dilution process, we are able to alter the size distribution and surface coverage rate of MLs. The as-prepared MLs on curved surfaces may provide a simple and effective approach to enhance solar-driven photodegradation in water treatment.

5.2 Methodology

5.2.1 Fabrication and characterization of PMMA surface microlenses (MLs) on glass

Surface poly (methyl methacrylate) (PMMA) MLs were polymerized from the surface methyl methacrylate (MMA) microdroplets forming in a solvent dilution process. The solvent dilution process could be conducted in arbitrary glass reactors with functionalized inner surfaces.

A dilution process was designed to generate surface microdroplets on the complicated surface, which is based on a three-component fluidic system. The ternary system was composed of water, ethanol, and methyl methacrylate (MMA), and the phase diagram of this system was shown in Figure 5.1 (a). Before the solvent dilution process, the inner surfaces of reactors were hydrophobized with octadecyltrichlorosilane (OTS, 98.9%, Acros Organics, Fisher Scientific). The coating procedure was the same as what was described in the previous literature.[185] During the dilution process, solution A with a volume of four-tenths of the reactor capacity was first added. Solution A contained 6.2 vol% MMA ($\geq$ 98.5%, Alfa Aesar) and 0.62 vol% 2-hydroxy-2-methylpropiophenone (96%, Fisher) as a photoinitiator in 50 vol% ethanol aqueous solution. Afterwards, solution B that contained 0.05 vol % photoinitiator in MMA-saturated Milli-Q water was pumped into the vertical-set reactor through two outlets placed at the opening of the reactor with a fixed flow rate of (shown in the sketch in Figure 5.1 (c)). The total volume of solution B for the solvent dilution process was three times of the capacity of a reactor. The excess liquid in the solvent exchange process was excluded from the top of the reactors. During the solvent dilution process, the concentration of MMA changed along the dilution curve demonstrated in Figure 5.1 (a-b). MMA microdroplets containing the photoinitiator formed on the inner surface of the reactors due to the oversaturation when solution B replaced solution A.

The reactor used was optional from the self-designed arbitrary glass reactors with different shapes shown in Figure 5.1 (d). Two of the reactors had cylindrical shapes but with different dimensions. The smaller cylindrical glass reactor had a volume of 30 mL (Class A clear glass vial, Fisherbrand). The smaller cylindrical reactor was utilized as a representative reactor for the adjustment of parameters in the solvent dilution process due to its stability in dimension and simplicity of structure. The adjusted parameters include the initial volume of solution A before the solvent dilution (V_{SolA}), initial concentrations of MMA in solution A ($C_{MMA,0}$), and flow rates when adding solution B. A much larger glass cylindrical reactor was also used to verify the scalability of this method, which had an inner diameter of 8.0 cm, a height of 10.0 cm, and a volume of 503 mL. Considering the scale of the reactor, the OTS coating procedure of the inner surface was modified into a chemical vapor deposition method reported in the literature to save the use of chemicals.[223] During the solvent dilution process in the larger cylindrical reactor, a solid cylindrical object with the same height as the reactor and a diameter of 5.0 cm was set vertically in the center of the reactor to decrease the required amount of solution A and B. Three tubes instead of two were evenly set at the openings in the solvent dilution process to ensure the required flow rates. The other four irregular reactors included a snowman shape, a petal shape, a three-arms shape, and a flower shape reactor, and the volume inside was around 9 mL, 11 mL, 27 mL, and 72 mL, respectively. The shape, materials, volume, surface area, and surface area to volume ratio (S/V) of all arbitrary reactors with surface MLs functionalized and corresponding conditions in the solvent dilution process were summarized in Table 5.1.

Sample Number	$C_{MMA,0}$ /vol%	V_{SolA} /mL	Flow rate /mL·min^{-1}	Reactor shape	Reactor Volume (V) /mL	Surface area (S) /cm^2	S/V /cm^{-1}
1	6.2	12	6	Cylindrical	30	49	1.6
2	4.7	12	6				
3	7.6	12	6				
4	4.7	8	6				
5	4.7	5	6				
6	7.6	12	8				
7	7.6	12	3				
8	7.6	12	10				
9	7.6	12	15				
10	7.6	60	8	Cylindrical	503	251	0.5
11	6.2	4	6	Snowman shape	10	41	4.1
12	6.2	4	6	Petal shape	11	47	4.3
13	6.2	11	6	Three-arm	27	58	2.1
14	6.2	29	6	Flower shape	72	257	3.6

Table 5.1: Conditions of solvent dilution process for the preparation of ML-functionalized reactors

After the solvent dilution process, the glass reactors filled with the mixture of solutions were sealed and irradiated under a UV lamp (365 nm, Analytik Jena UV lamp). Surface microdroplets of MMA containing a photoinitiator were polymerized into PMMA under UV irradiation. (Figure 5.1 (e)). The reactors with microdroplets on the inner surface were irradiated for 20 min to 40 min depending on the reactor size. During the irradiation process, the glass reactors were rotated every 10 min to ensure that sufficient irradiation was all around the reactors. After photopolymerization of the droplets, the reactors functionalized with MLs were rinsed with water and ethanol subsequently and dried by air for characterization. The glass reactors functionalized with surface MLs were observed with an optical microscope (Nikon H600l and Nikon DSFi3). Each of the MLs functionalized cylindrical reactor (sample 1 to 9) was divided into three parts, bottom (15 mm), middle (28 mm), and top part (15 mm) for microscope observation. In order to analyze the surface coverage rate and the size distribution of MLs in each sample, five photos were collected for each sample and were analyzed with Image J. The inner surface of a plastic bottle without surface functionalization could be also utilized as the substrate of surface microdroplets and MLs in the presence of surfactant, which was demonstrated in the Appendix C (Figure S1 (a-b)).

5.2.2 Photodegradation inside ML-functionalized reactors

In order to evaluate the performance of ML-functionalized reactors, the photodegradation of organic contaminants in the water matrix was conducted in the reactors. Methyl orange (MO, Sigma-Aldrich, ACS reagent) was utilized as one of the organic pollutants to demonstrate the effectiveness of the ML-functionalized reactors. 5 mg/L MO aqueous solution was prepared by using ultrapure water (Milli-Q Direct 16) as the solvent, and the pH value was controlled at 3.0 by adding sulfuric acid (98%). Similarly, the aqueous solution of sulfamethoxazole (SMX, analytical standard, Sigma Aldrich), another typical organic contaminant in wastewater, with a concentration of 5 mg/L was prepared. The pH value of the SMX solution was not changed with acid or base and was measured at 7.0.

The ML-functionalized cylindrical glass reactors fabricated by altering the con-

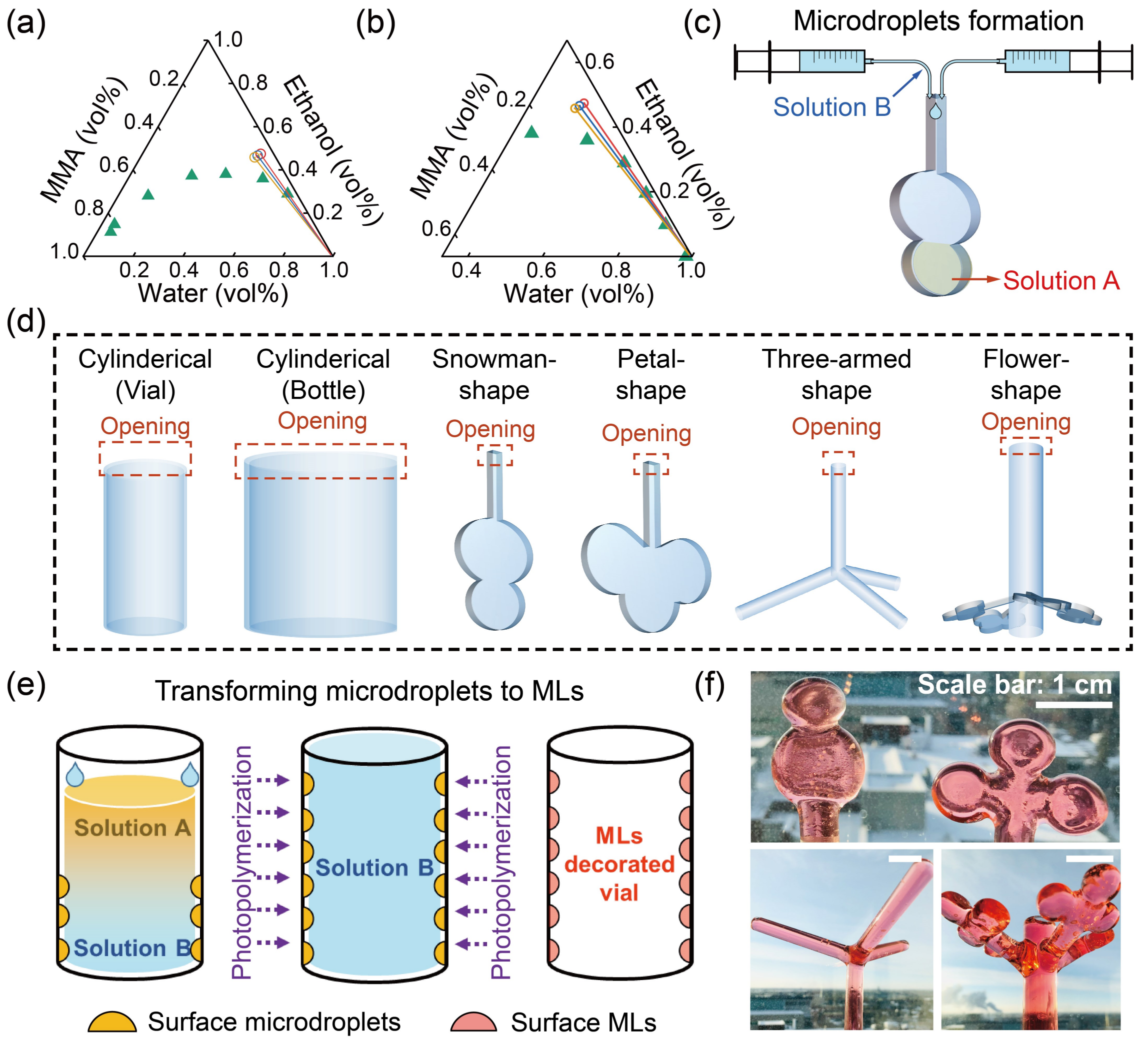

Figure 5.1: (a) The phase diagram of a ternary system composed of water, ethanol, and methyl methacrylate (MMA) and (b) the zoomed-in plot, and the dilution paths involved in the MLs fabrication are displayed. (c) The sketch of the fabrication process of a surface microlenses (MLs) functionalized-reactor based on a vertical-oriented solvent exchange process, using a snowman shape reactor as an example, and the opening of the reactor is set on top. (d) The reactors with different shapes In the solvent dilution process, the opening of each reactor was labeled with a red dashed box. (e) The sketch of the UV curing process to transform surface microdroplets to surface MLs. (f) The experimental set-up of the indoor light treatment of MO solution in an ML-functionalized petal-shape reactor, from 0 d (day) to 3 d.

ditions in the solvent dilution process (sample 1 to 9) were firstly filled with MO aqueous solution and then horizontally set under the simulated solar light (1 Sun, SS200AAA Solar Simulation Systems, Photo Emission Tech) for 1 h, 2 h, and 3 h. The ML-functionalized reactors with irregular shape (sample 11 to 14) were used for the photodegradation of MO under both simulated solar light and natural indoor sunlight (Figure 5.1 (f)). The light spectrum of the light source was shown in Appendix C, Figure S2. The photodegradation efficiency, η, was calculated via Equation (5.1) to quantify the extent of photodegradation. According to Beer-Lambert law[224] (Equation (5.2)), the absorbance value of MO at a certain wavelength is proportional to the concentration of MO in the solution. Therefore, Equation (5.1) could be transformed into Equation (5.3), where A_ini is the peak value of the absorbance curve at the wavelength of 504 nm and A_{aft} is the peak value at the same wavelength after the light treatment. The absorbance values of the MO solution were obtained from a UV-visible spectrometer (Thermoscientific, Genesys 150).

$$\eta = \frac{C_{ini} - C_{aft}}{C_{ini}} \times 100\% = \frac{A_{ini} - A_{aft}}{A_{ini}} \times 100\% \tag{5.1}$$

$$A = \log_{10}(\frac{I_0}{I}) = \varepsilon C L \tag{5.2}$$

$$\eta = \frac{A_{ini} - A_{aft}}{A_{ini}} \times 100\% \tag{5.3}$$

A bare cylindrical reactor was used to conduct the same photodegradation process as the control group. The enhancement in η achieved by the surface MLs that were functionalized on the inner surface of cylindrical glass reactors was represented by an enhancement factor defined by Equation (5.4).

$$f = \frac{\eta(MLs\ reactor)}{\eta(Control)} \tag{5.4}$$

The larger ML-functionalized glass cylindrical reactor (sample 10) was also used for the photodegradation of MO and SMX in ultra-pure water under indoor solar light. 500 mL MO or SMX aqueous solution prepared with the same method as mentioned above was added to sample 10. The solution-filled bottle was set beside the window for indoor light irradiation in Room 12-380 in Donadeo Innovation Centre for Engineering, Edmonton, Canada. For each round of light treatment, a bare glass bottle filled with the same amount of aqueous solution was set under the same light source simultaneously for comparison. The photodegradation of MO in water was conducted from December 17, 2021, to March 16, 2022, while the photodegradation of SMX in water started on March 16, 2022, and ended on May 15, 2022. η of MO and SMX was calculated by Equation (5.3) by inserting the absorbance values obtained from the UV vis spectrometer.

5.2.3 Optical simulations of surface MLs

The surface ML-functionalized reactors filled with MO solution were modeled in three-dimensional space with Zemax OpticStudio. Considering the 3D curved surface had complex geometric structures, MLs functionalized on the curved surface could be classified into two situations, as illustrated in Figure 5.2 (a). The surface ML was immobilized on a convex surface or a concave surface in situation 1 or 2, respectively (Figure 5.2 (b-c)). The whole system was illuminated by a plane wave source along the Z direction. The space within the reactor was filled with MO aqueous solution, and the yellow arrows indicated the direction of irradiation, as shown in Figure 5.2 (b-c). The source intensity was set to be the same as in the experiment (1 Sun). To identify the focal point of the ML, an X-Z plane monitor was placed along the central axis of the ML to obtain a cross-sectional intensity profile. The point in the profile with the highest irradiance intensity was identified as the focal point.

The peak irradiation intensity (I_{Peak}) in the cross-sectional light intensity profile was defined as the intensity at focal points of MLs. The peak intensity normalized

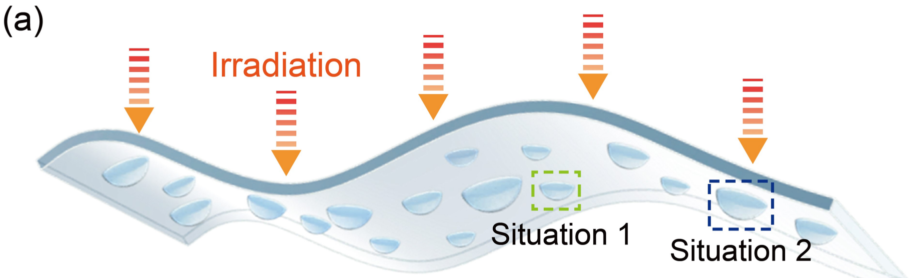

(b) Situation 1:

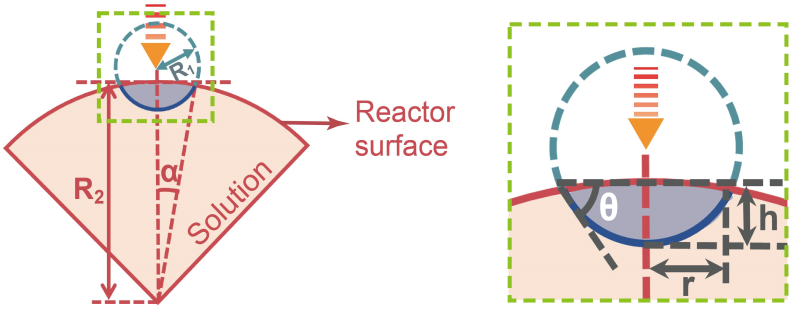

(c) Situation 2:

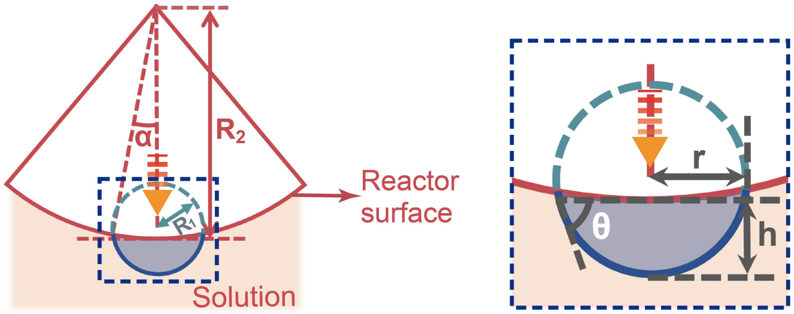

Figure 5.2: (a) Sketch of a 3D curved surface functionalized with surface MLs under light irradiation. Surface MLs can be classified into two types. The ML on a convex surface is defined as situation 1, while the ML on a concave surface is defined as situation 2. (b) Zoom-in sketch of MLs in (b) situation 1 and (c) situation 2. Here, R_1 is the curvature of the lens, and R_2 is the curvature of the surface at the position of the ML. r is the lateral radius of the ML, and h is the height of the ML. θ is the contact angle of the ML, and α is the half-central angle of the area occupied by the ML on the curved surface.

by the area covered by an ML (i_{Peak}) was calculated based on Equation (5.5), which eliminated the influence of the size of surface MLs and revealed the strength of focusing effect of MLs. I_{Total} is the total intensity at the focal points of MLs within an area of 1 cm^2 from a specific sample, which can be calculated by Equation (5.6). In Equation (5.6), N is the total number of MLs within an area of 1 cm^2 from a specific sample.

$$i_{Peak} = \frac{I_{Peak}}{\pi r^2} \tag{5.5}$$

$$I_{Total} = \sum_{n=1}^{n=N} I_{Peak} \tag{5.6}$$

The thickness of a single ML, h, is the key parameter for the optical simulation, which is obtained by Equation (5.7) based on the geometric relationship shown in Figure 5.2 (b-c). In the equation, R_1 and R_2 are the curvatures of the spherical side of the ML and the surface of the 3D curved reactor surface, respectively. r is the lateral radius of the observed ML which can be extracted by the analysis with Image J. α is half of the central angle that is occupied by the single ML, and θ is the contact angle of PMMA MLs on the OTS-coated substrate which is 7.5 $(\pm 0.2)°$.[28] In order to distinguish the difference between situation 1 and 2, R_2 had a positive value for situation 1 and a negative value for the other situation.

$$h = R_1(1 - cos\theta) + R_2(1 - cos\alpha) \tag{5.7}$$

5.3 Results and discussion

5.3.1 Light intensity of MLs functionalized on the curved surface of glass reactors

Figure 5.3 (a) and (b) show the representative cross-sectional light intensity profile of a single ML on the curved surface at the spot with a convex structure (situation

1) and concave structure (situation 2) under the light irradiation, respectively. The lateral radius (r) of the ML involved in the optical simulations is 30 μm, located on the inner surface of a glass reactor with the curvature (R_2) of 11 mm (Figure 5.3 (a)) and -11 mm (Figure 5.3 (b)). In situation 1, a focal point with the highest local intensity is found at the position of 164 μm below the top point of the inner surface of the reactor. In situation 2, no focal point exists and the light beams under the ML have higher intensity than other areas, contributed by the focusing effect of the ML. In comparison, the maximum intensity of light under the ML with the same lateral radius (r) is around 10^5 higher in situation 1 than that in situation 2. The huge difference indicates that the ML-functionalized convex surface has a much stronger focusing effect due to the shape of the reactor surface.

According to the optical simulations, the dependence of peak irradiance intensity (I_{Peak}) on the size of MLs and the curvature of the reactor surface varies in situation 1 and 2. As demonstrated in Figure 5.3 (c), I_{Peak} continuously increases with the lateral radius of the MLs in situation 1 for the reactors with different curvature. When R_2 is 30 mm, the MLs with the same radius achieve the highest intensity at focal points, while the I_{Peak} is the lowest when the R_2 is 15 mm. In situation 2, I_{Peak} maintains a similar value when the size of MLs differs (Figure 5.3 (d)). Slight enhancement I_{Peak} is observed when the curvature value of the reactor surface increases, which is possibly attributed to the weaker diffusing effect of the concave surface with a larger curvature value.

The area occupied by a single ML determines the amount of energy received from light irradiation. In order to quantify the strength of the focusing effect of MLs, i_{Peak} is defined by normalizing I_{Peak} by the area covered by the ML. The influence of MLs lateral size and reactor curvature on i_{Peak} is revealed in Figure 5.3 (e-f). In situation 1 (Figure 5.3 (e)), i_{Peak} does not continuously increase but shows a maximal value when the lateral size of the MLs reaches a certain value. The size of MLs with the highest i_{Peak} shifts with the curvature of the reactor surface. In situation 2 (Figure

5.3 (f)), i_{Peak} decreases with the lateral radius of MLs due to the negligible change of I_{Peak}.

5.3.2 Controlled fabrication of MLs on the inner surface of cylindrical reactors

The representative photos of ML-functionalized cylindrical glass reactors prepared by solvent dilution and local photopolymerization are displayed in Figure 5.4 (a). As shown in the photo, the cylindrical reactor with surface MLs functionalized remains transparent. Surface MLs are immobilized all over the inner surface of the reactors. The difference in MLs density and size is observed in the vertical direction. Based on the difference, each reactor is divided into three regions, including the top, middle, and bottom region, and the properties of MLs in each part are relatively identical. The difference in the fabrication conditions of sample 1 to 9 is quantified by the concentration change of MMA with time in the solvent dilution process, which is displayed in 5.4 (b-d). According to the varied parameters, the concentration dilution curves of MMA are classified into three groups. For sample 1, 2, and 3, only the initial concentration of MMA ($C_{MMA,0}$) in solution A is altered, for sample 2, 4, and 5, only the initial volume of solution A (V_{SolA}) is changing, and for sample 3, 6, 7, 8, and 9, only the flow rate during solvent dilution varies.

The concentration of MMA (C_{MMA}) with dilution time (t) can be calculated by equation (S1). Before the solvent dilution process, the initial concentration of MMA is $C_{MMA,0}$, and the initial volume of solution A is V_{SolA}. The dilution process can be divided into stages based on the correlation between the total volume of liquid (V_T) and t. In the first stage, V_T is smaller than the volume of the reactor (V_R), and t should be smaller than the critical time, t_R. t_R is the dilution time when V_T is the same as V_R. At this stage, V_T is equal to the addition of the volume of V_{SolA} and solution B (V_{SolB}) at the time of t. V_{SolB} can be calculated by the flow rate (Q) and t, so V_T can be calculated with equation (S2). With equation (S2), the value of t_R can

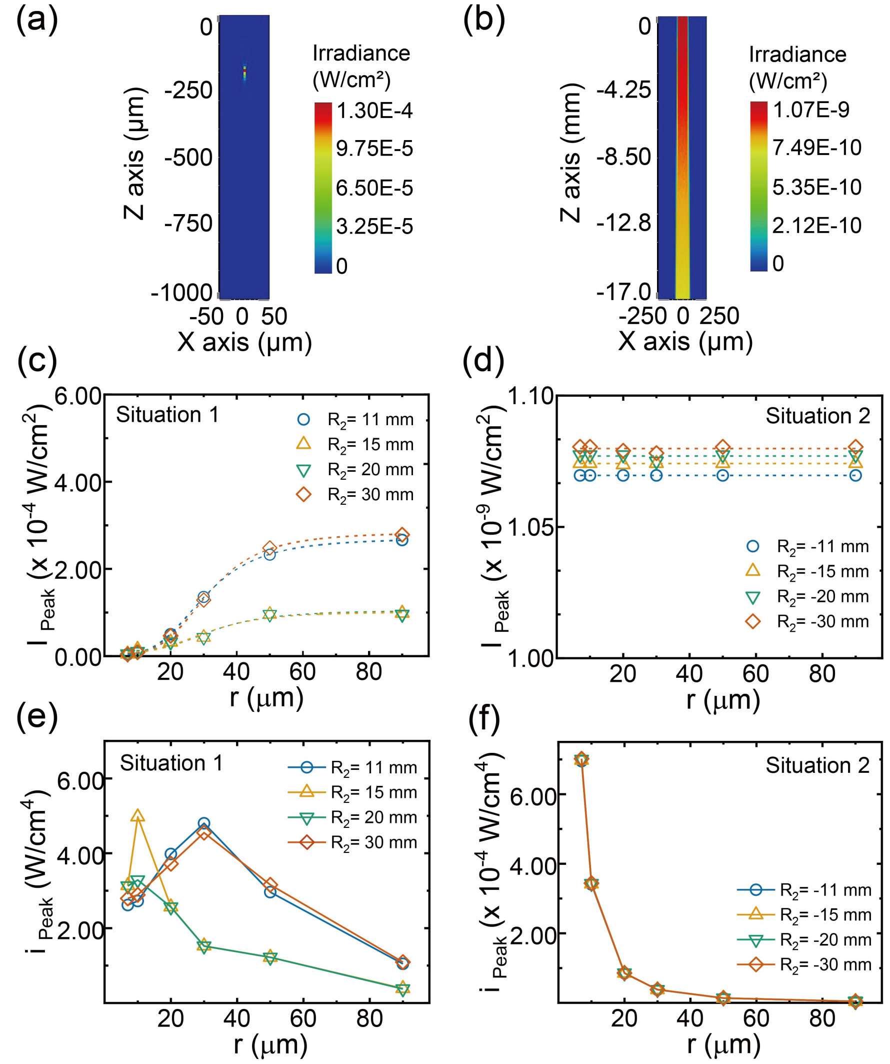

Figure 5.3: Cross-sectional view of the light intensity profile of a single ML (r=30 µm) at the curved surface reactor in (a) situation 1 (convex surface, R_2=11 mm) and (b) situation 2 (concave surface, R_2=-11 mm). Z=0 represents the top point of the inner surface of the cylindrical reactor. Peak irradiance intensity (I_{Peak}) of a single ML with different r on the surface with varied R_2 in (c) situation 1 and (d) situation 2. Peak irradiance intensity normalized by the area covered by an ML (I_{Peak}) calculated with Equation (5) of a single ML with different r functionalized on the curved surface with varied R_2 in (e) situation 1 and (f) situation 2. The dash and solid lines separately indicated the trend of I_{Peak} and i_{Peak} with the lateral radius of a single ML.

calculated according to equation (S3). By combing equation (S2) and equation (S3), C_{MMA} in the first stage can be quantified by the equation (5.8). When t is larger than t_R, which is the second stage of the dilution process, the addition of V_{SolA} and V_{SolB} is over V_R, so V_T becomes constant and equal to V_R. In the second stage, the differential change of C_{MMA} (dC_{MMA}) with differential time (dt) is demonstrated by equation (S4), and by integrating equation (S3) from time 0 to t, the C_{MMA} function with t in the second stage is obtained by equation (5.9).

Stage 1 (t$\leq t_R$):

$$C_{MMA} = \frac{C_{MMA,0} \cdot V_{SolA}}{V_{SolA} + Q \cdot t} \tag{5.8}$$

Stage 2 (t$>t_R$):

$$C_{MMA} = \frac{C_{MMA,0} \cdot V_{SolA}}{V_R} \cdot exp[-\frac{Q}{V_R} \cdot (t - t_R)] \tag{5.9}$$

The morphology and spatial distribution of surface MLs are demonstrated by the images obtained from the optical microscope in Figure 5.4 (e-g). In all three regions, surface MLs randomly distributed on the homogeneous hydrophobic surface. Size distribution variation among the top, middle, and bottom regions of each ML-functionalized cylindrical reactor is validated with size analysis in the Appendix C, Figure S3 (a-i). By comparing the size distribution curves in the bottom region and the top region, it is found that a single peak can be observed in the lateral radius range from 5 to 65 μm. However, the size distribution curve of MLs in the middle region does not present an obvious peak in the same range of size. The frequency of MLs with a lateral radius larger than 70 μm in the middle region is higher than that in the other two regions. Generally, the lateral diameters of MLs in the middle region are generally larger than the diameters of MLs in the top and bottom regions.

The spatial difference in the size distribution along the glass cylindrical glass reactor is attributed to the variation of MMA concentration gradient with the relative position in the reactor and time. The solvent dilution process in cylindrical reactors can be divided into three stages as illustrated by the sketch in Appendix C (Figure

S4). In the first stage, the ouzo effect can be observed after adding solution B to solution A. Small droplets (size: a few μm to tens μm) form and adsorb onto the hydrophobic surface. The microdroplets formed in this stage become the MLs in the bottom region after the UV curing step. In the second stage, as the ratio of water further increases, phase separation happened, resulting in the formation of larger droplets (hundreds of μm). In this stage, the droplets are transferred into the MLs in the middle region. In the third stage, the total amount of the liquid added exceeds the capacity of the reactor and starts to get out of the reactor. Due to the phase separation, the oil-rich phase sits on the upper part and is excluded from the reactor first. Therefore, the concentration of MMA drops significantly. The rapid decrease of oil concentration leads to the decrease of droplet size, so as the size of MLs size on the curved surface.

The adjustment in the parameters during the solvent dilution process brings about the variation of the overall size distribution of surface MLs on each glass cylindrical reactor as illustrated in Appendix C, Figure S5 (a-c). The overall size distribution curves consider all the MLs on the inner surface of the reactor regardless of the variance among the three regions. By comparing sample 1, 2, and 3 (Appendix C, Figure S5 (a)), the largest lateral radius among MLs in a reactor increases with $C_{MMA,0}$ in solution A. Among sample 2, 4 and 5 (Appendix C, Figure S5 (b)), higher frequency of MLs with lateral radius over 80 μm the sample is observed when V_{SolA} is larger. By controlling the flow rate of filling solution B for sample 3, 6, 7, 8, and 9 (Appendix C, Figure S5 (c)), the width of the size distribution is enlarged at the higher flow rate. In addition, the portion of MLs with lateral size smaller than 50 um becomes higher, and the maximum size of MLs becomes larger as the flow rate increases, which is more obvious in the sample prepared with a flow rate higher than 8 mL/min.

The influence of each parameter in the solvent dilution process is analyzed based on the MMA dilution curves in Figure 5.4 (b-d) and the corresponding size distribution in sample 1 to 9. Higher $C_{MMA,0}$ in solution A contributes to the higher oversaturation level during the solvent dilution process, so larger surface MLs are generated in sample 3. Except the $C_{MMA,0}$ in solution A, the total amount of MMA determines the oversaturation level during the solvent dilution. For sample 2, 4, and 5, the concentration gradient of MMA is larger under the condition with a higher V_{SolA}. Therefore, more MLs with a radius over 80 μm were observed in sample 2. By increasing the flow rate in the solvent dilution process, the oversaturation level decreases more rapidly. Simultaneously, the higher flow rate also results in a faster mass transfer rate, contributing to the growth of droplets. Therefore, we could see a broader size distribution in the sample at a higher flow rate (Appendix C, Figure S5 (c)).

The surface coverage rate of all ML-functionalized cylindrical glass reactors is plotted in Figure 5.4 (h). The minimum surface coverage rate is 30.6% obtained from sample 1, and the maximum rate is 49.9% in sample 3. By comparing the samples fabricated with varied C_{MMA}, it is found that the surface coverage rate increases with the volume ratio of MMA. Among the samples with the only difference in the V_{SolA}, the surface coverage rate first decreases and then increases with the volume of solution A. By only adjusting the flow rates during the solvent exchange process, the surface coverage rate first increases and then remains at a similar level when increasing the flow rate from 3 mL/min to 15 mL/min. The total intensity at the focal points of MLs in each sample (I_{Total}) can be calculated based on the optical simulations of MLs on the curved surface and the size information extracted from optical images of MLs. Sample 6 has the highest I_{Total}, while sample 5 has the lowest I_{Total}. The difference in the value of I_{Total} of ML-functionalized cylindrical glass reactors is determined by the variation of MLs properties, including the surface coverage rate and size distribution of MLs.

The correlation of I_{Total} and the parameters in the solvent dilution process is investigated for the optimization of the ML-functionalized reactors. The correlation between I_{Total} and $C_{MMA,0}$ in solution A is demonstrated in Figure 5.4 (i). As $C_{MMA,0}$ increases from 4.7 vol% (sample 2) to 7.0 vol% (sample 3), I_{Total} decreases first and then increases. As displayed in Figure 5.4 (i), I_{Total} of the samples increases when the V_{SolA} is improved from 5 mL to 12 mL. The improvement in I_{Total} is the possible consequence of the higher surface coverage rate of MLs in the sample prepared with larger V_{SolA} (Figure 5.4 (h)) and more MLs with the lateral radius over 80 μm (Appendix C, Figure S5 (b)). The correlation between I_{Total} and the flow rate in the solvent dilution process is illustrated in Figure 5.4 (j). When the dilution rate varies between 3 mL/min and 15 mL/min, I_{Total} first increases and then decreases as the dilution rate becomes higher. Among the five samples fabricated with different flow rates in solvent dilution, sample 6 has the highest I_{Total}. The possible reason for the high I_{Total} in sample 6 is the relatively high surface coverage (Figure 5.4 (h)) and more MLs with lateral size between 20 μm to 60 μm (Appendix C, Figure S5 (c)), which is the size range of MLs with relatively higher focusing effect as shown in Figure 5.3 (e).

Among the three involved parameters in the solvent dilution process, the flow rate causes the most significant change of I_{Total}. The effect of changing $C_{MMA}, 0$ and V_{SolA} is mainly revealed in MLs with larger radius (over 70 $/mum$), and those larger MLs play a less important role in the focusing effect as indicated in Figure 5.3 (e). In comparison, the size distribution width can be adjusted by controlling the flow rate in the solvent dilution process. According to the experimental results, the I_{Total} reaches the maximum value when the flow rate is 8 mL/min. However, if the flow rate further increases, C_{MMA} changes too fast to ensure a stable concentration gradient. In this situation, some large MLs ($r > 200$ μm) form and escape from the surface due to the increasing buoyancy, and then the portion of small MLs ($r < 20$ μm) becomes higher, leading to a lower value I_{Total} and the weakened focusing effect.

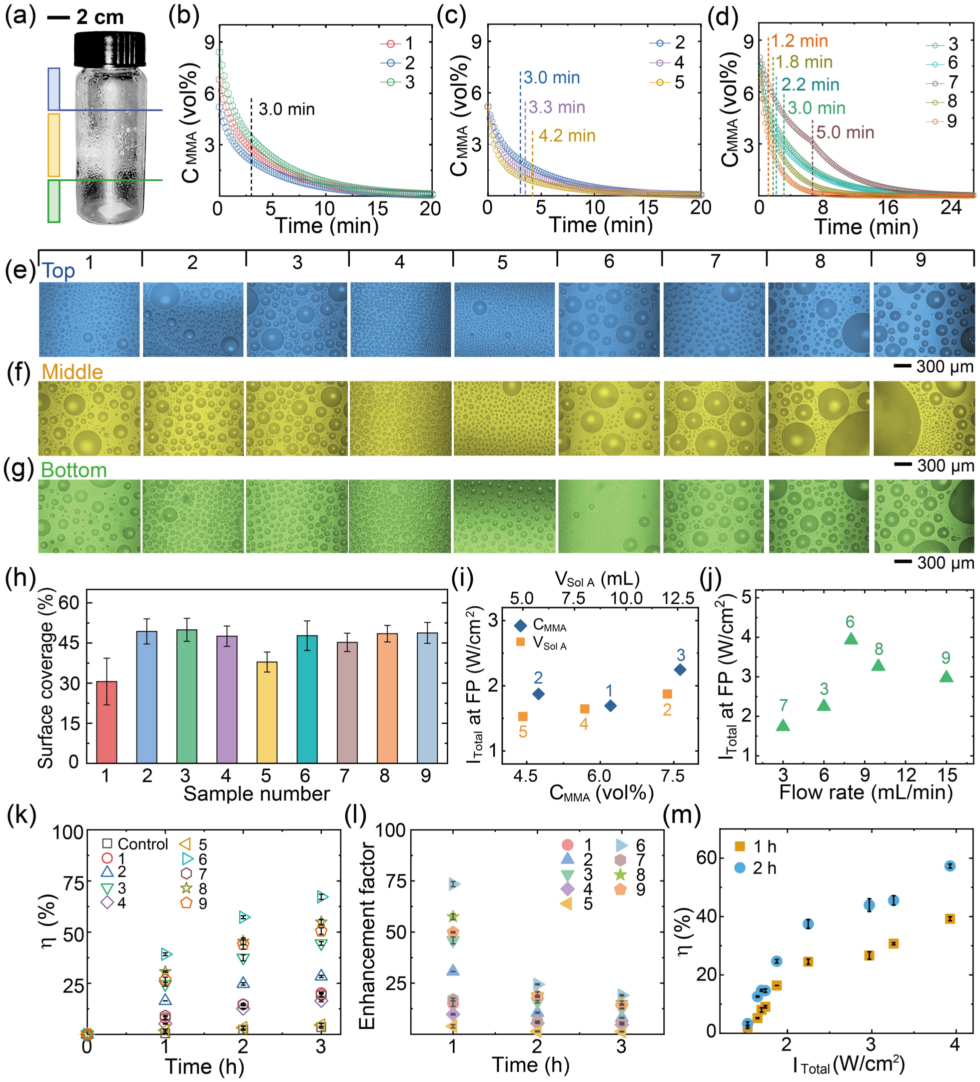

Figure 5.4: (a) The photos of ML-functionalized cylindrical glass reactors from sample 1 to 9 (scale bar: 2 cm). Each reactor is divided into three regions, including the top (15 mm), middle (28 mm), and bottom (15 mm) regions. The concentration of MMA (C_{MMA}) with the time in solvent dilution process within samples prepared with (b) different initial MMA concentrations (sample 1, 2, and 3), (c) varied initial volume of solution A (sample 2, 4 and 5), and (d) varied dilution rates (sample 3, 6, 7, 8 and 9). Optical images of MLs on the inner surface of sample 1 to 9 in the (e) top region, (f) middle region, and (g) bottom region (scale bar: 300 μm). (h) Surface coverage rates of MLs on the inner surface of sample 1 to 9. Correlation between I_{Total} in an area of 1 cm^2 and (i) initial MMA concentrations in solution A (sample 1, 2, and 3) and varied initial volume of solution A (sample 2, 4, and 5), (j) varied dilution rates (sample 3, 6, 7, 8 and 9). (k) The photodegradation efficiency (η) of MO and (l) enhancement factor of η under the simulated solar irradiation of 1 h, 2 h, and 3 h with bare cylindrical glass reactor (control group) and ML-functionalized sample 1 to 9. (m) η of MO after the light treatment of 1 h and 2 h with the I_{Total} over the area of 1 cm^2 in sample 1 to 9.

5.3.3 Enhancement of photodegradation of MO in ML-functionalized cylindrical reactors under simulated solar light

Based on the representative absorbance spectra in Appendix C (Figure S6), the enhancement of photodegradation of MO by ML-functionalized cylindrical glass reactors is confirmed. Based on the UV-visible spectra, the photodegradation efficiency of MO under the simulation light is calculated and plotted with irradiation time in Figure 5.4 (k). In the control experiment conducted in the bare cylindrical glass reactor, the degradation of MO during the irradiation of 3 h is negligible. For the photodegradation of MO in the ML-functionalized cylindrical glass reactors, the photodegradation efficiency obviously increases under the same irradiation condition. The enhancement factor calculated with Equation (5.4) helps to quantify the improvement in η of MO in ML-functionalized cylindrical glass reactors (Figure 5.4 (l)). The enhancement factor of MO photodegradation in ML-functionalized cylindrical glass reactors decreases with the irradiation time. During the same time of light treatment, the difference in the enhancement of η is observed among sample 1 to 9. Sample 6 shows the highest enhancement factor of 73.5, while the least enhancement is found in sample 5. The difference in the performance of ML-functionalized cylindrical glass reactors is attributed to the varied properties of surface MLs in each sample that are caused by altering fabrication conditions in the solvent dilution process. In brief conclusion, the size and number of MLs determine the strength of the focusing effect, quantified by I_{Total}, which is revealed in the variation of η of MO in the ML-functionalized reactors (Figure 5.4 (m)).

5.3.4 MLs on the surface of the reactors in complex geometry: properties and performance in photodegradation

Aside from cylindrical reactors, surface MLs can be immobilized on the inner wall of more complex reactors, such as snowman-shaped, petal-shaped, tree-armed, and flower-shaped glassware. As shown in Figure 5.5 (a-d), the whole inner surface of glass reactors with irregular shapes are functionalized by surface MLs, and the ML-functionalized reactors remain transparent. By zooming on the smaller area, surface MLs are observed to be randomly distributed over the inner wall of the reactors. The details of MLs morphology and surface coverage rates are obtained from the representative microscope images of sample 11 (snowman shape) and sample 12 (petal shape) in Appendix C (Figure S7 (a-d)). The surface coverage rate of MLs in sample 12 is around 6% higher than that in sample 11. By plotting the size distribution curves of MLs on the inner surface of the two reactors in Appendix C, Figure S7 (c), we can observe that the frequency of MLs decreases with the lateral radius of MLs in both reactors. The frequency of MLs with a radius smaller than 7 μm is higher in the petal shape reactor than that in the snowman shape one, while a larger portion of MLs with a radius larger than 50 μm are found in the snowman shape reactor.

The reactors from sample 11 to 14 are utilized for the photodegradation of organic pollutants under either natural light or simulated solar light. The experimental set-up shown in Figure 5.5 (e) enables the MO solution-filled reactors to receive solar light through the glass window. As the irradiation time increases, an obvious decay of color is observed in the ML-functionalized reactors (Figure 5.5 (f)), but the color change of solution in the bare glass reactors is indistinguishable. The more rapid color change in ML-functionalized irregular reactors indicates the faster degradation rate of MO, which is confirmed by the photodegradation efficiency calculated by Equation (5.1). In Figure 5.5 (g-h), η of MO in reactors without surface MLs and with surface MLs is plotted with irradiation time, respectively. In comparison, η in the ML-functionalized petal shape reactor is the highest, reaching 71.0% after 11 d of irradiation, achieving around 2 times enhancement compared with that without surface MLs.

The improvement of photodegradation of MO by surface MLs functionalized on the wall of irregular reactors under simulated solar light is significant. With the experimental setup demonstrated in Figure 5.5 (i), the light source is set on top of the reactors. During the irradiation of 2 hours, the color change of MO solution in the

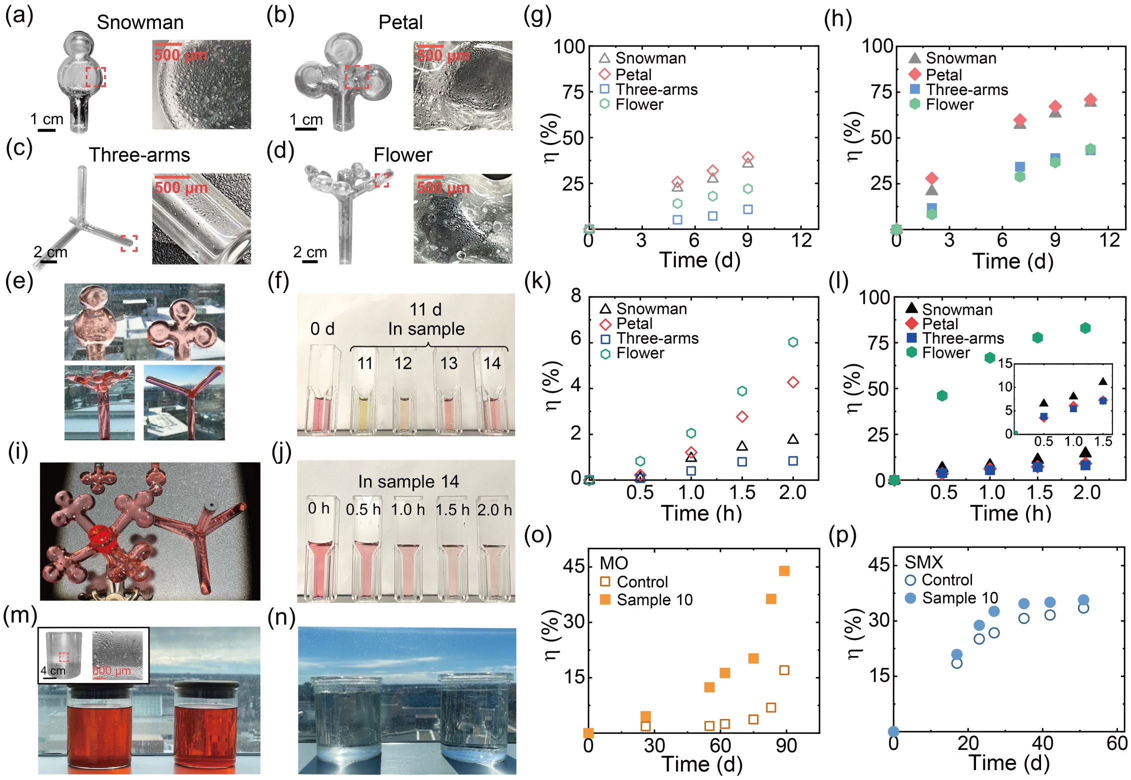

Figure 5.5: The photo and zoom-in photo of surface MLs-decorated (a) snowman shape (sample 11), (b) petal shape (sample 12), (c) three-arms (sample 13), and (d) flower shape (sample 14) glass reactor. (e) ML-functionalized reactors filled with MO solution (5 mg/L, pH=3.0) irradiated by the natural light indoor treatment for 6 days. (f) The color change of MO solution after the irradiation of 11 d in sample 11 to 14. η of MO in (g) bare and (h) ML-functionalized arbitrary glass reactors with irradiation time. (i) Experimental set-up of the simulated solar light treatment of MO in sample 11 to 14. (j) The color change of MO solution in sample 14. η of MO in the (k) bare and (l) ML-functionalized irregular glass reactors under simulated solar light. Experimental set-up of the natural light indoor treatment of (m) MO (5 mg/L, pH=3.0) and (n) SMX solution (5 mg/L, pH=7.0), and a photo of an ML-functionalized large cylindrical reactor (sample 10) and the zoom-in image of MLs on the inner surface are attached on (m). η of (o) MO and (p) SMX under the natural light indoor with a bare glass bottle (control) and sample 10.

unmodified reactors is negligible (Appendix C, Figure S8), while the decolorization of MO solution is more obvious in the ML-functionalized reactors after the irradiation, especially the ML-functionalized flower shape reactor (Figure 5.5 (j)). The photodegradation efficiency of MO in the irregular glass reactors without and with surface MLs is plotted in Figure 5.5 (k) and (l). On one hand, η of MO is less than 7% in all bare irregular glass reactors after the irradiation under simulated solar of 2 hours. On the other hand, η of MO in the ML-functionalized irregular reactors is substantially increased. Among all ML-functionalized irregular glass reactors, the flower shape reactor has the best performance, in which η of MO reaches 83.0% after the treatment of 2 h, which is more than 12 times higher than the η in the nonfunctionalized flower shape reactor.

As shown in photodegradation efficiency, we can conclude that surface MLs generally improve the photodegradation efficiency of MO under natural indoor light and simulated solar light. In addition, the effect of surface MLs varies correspondingly while the shape of the reactor changes. One of the possible reasons is the variance in the surface area to volume ratio of reactors with different shapes. In the experiments under the irradiation of office light, η of MO increases with the surface area to volume ratio of reactors. However, after changing the direction of irradiance, the actual area receiving the irradiation of light sources is also altered, further affecting the performance of ML-functionalized reactors. (shown in Appendix C, Figure S9). As shown in the photodegradation under the simulated solar light, the flower shape reactor presents much higher η than any other reactors due to the highest irradiated area with the light source set on top of the 'multi-petals' side. Additionally, the properties of surface MLs, such as surface coverage rate and size distribution, vary with the reactor shape because different geometric structures of the reactor may disturb the formation and growth of microdroplets during the solvent dilution process. Last but not least, the curvature of the reactor surface also influences the strength of the focusing effect, as shown in Figure 5.3. To optimize the design of ML functionalized reactors with complicated shapes, further studies are required in the future.

5.3.5 3.5 Enhanced photodegradation under indoor solar light

The fabrication method of surface MLs with solvent dilution can be scaled up by 16.7 times larger in volume and 5.6 times larger in the surface area inside a cylindrical glass reactor. The scaled-up ML-functionalized glass reactor (sample 10) and the zoom-in image of MLs on the inside wall are displayed in Figure 5.5 (m), showing the high transparency of the ML-functionalized glass bottle and the morphology of surface MLs.

With the experimental setup in Figure 5.5 (m-n), higher photodegradation efficiency of either MO or SMX in the ML-functionalized bottle under natural indoor light is acquired than that in a bare bottle (Figure 5.5 (o-p)). The improvement of photodegradation under natural indoor light firstly increases with the irradiation time and then decreases, which is observed in the degradation of both MO and SMX. The highest enhancement factor in η by the ML-functionalized bottle is 6.57 for the degradation of MO after 62 d of irradiation, while the highest enhancement is 1.22 for the degradation of SMX after 27 d of light treatment. Such a difference in the enhancement factor of organic pollutants is due to the variation of photodegradation mechanisms.[33] In addition, compared with the enhancement of η achieved in the wide cylindrical reactors is much lower than that in the narrower cylindrical reactors (sample 1 to 9) and the reactors with irregular shapes (sample 11 to 14). One of the important reasons may be the much lower surface area to volume ratio of the wider cylindrical reactor (Table 5.1). Last but not least, the ML-functionalized glass bottle can be reused multiple times without observing any difference in the chemical properties of MLs (as shown in Appendix C, figure S10).

5.4 Conclusions

MLs are fabricated on curved surfaces for enhanced photodegradation of organic contaminants in water through the polymerization of surface microdroplets made by a solvent dilution process. The solution components, solution amount, and flow conditions during the dilution process can be controlled to obtain customized size distribution and surface coverage rate of MLs. Enhanced photodegradation efficiency is demonstrated in six types of ML-functionalized reactors. Both optical simulations and experimental results show that the strength of the focusing effect of MLs on a reactor quantified by the total intensity at the focal points of MLs is correlated with the dimensions and spatial arrangement of MLs and the curvature of the surface. The photodegradation efficiency is improved by over 80 times at maximum with MLs on the reactor wall. Furthermore, the method is applied to fabricate MLs over the surface of a large reactor with a capacity of up to 500 mL, demonstrating the scalability of the approach. The technology demonstrated in this work may be implemented to design compact and efficient reactors for sustainable solar-driven water treatment. We envision that the fabrication technology of MLs on 3D curved surfaces developed in this work opens up a wide range of applications of MLs in novel optical devices and sensing, with potential impact far beyond photodegradation in sustainable solar-driven water treatment focused in the current study.

5.5 Supplementary materials

Supplementary data to this article can be found in the Appendix, section A.3. Additional data include the morphology of ML-functionalized PET reactor, spectra of simulated solar light and natural light indoor, equations for the calculation of MMA concentration during the solvent dilution process, the size distribution of MLs on cylindrical reactors and corresponding analysis, a sketch of the mechanism of droplets formation in the solvent dilution process, representative UV-visible spectra of MO solution during the light treatment in cylindrical reactors under simulated solar light, characterization of surface MLs on the surface of irregular reactors (for sample 11 and 12), color change of the MO solution before and after the light treatment in irregular reactors, the light treatment results in ML-functionalized irregular reactors (sample 13 and 14) by changing the irradiation direction, and the stability of surface MLs after irradiation confirmed by FT-IR spectra.

Chapter 6

Convex and concave microlens arrays with tunable curvatures for enhanced photodegradation of organic pollutants in water: a contact or non-contact approach

6.1 Introduction

Currently, the challenges of the practical application of solar-driven photodegradation include the restricted conversion rate of solar energy to chemical energy[13], the difficulty in scaling up the reactor[14], and the decentralized and intermittent features of solar irradiation[15, 16]. Some strategies have partially addressed the problems occurring in the solar-driven photodegradation process. For example, diverse photocatalysts, such as ZnO[225–227], TiO_2[227, 228], Bi_2WO_6[229, 230], carbon-based materials[231, 232], and biological materials[233, 234], have been proven effective in improving the utilization efficiency of solar energy by lowering the energy barrier of the photodegradation of organic pollutants. However, the effectiveness of photocatalysts is significantly suppressed when solar becomes weaker[103, 106]. Some reactors for solar-driven processes, such as compound parabolic collectors[104, 213], successfully increase the amount of treated wastewater with a fluidic system and concentrate the solar irradiation by the curved surfaces, but those reactors require precise manufacturing and extra maintenance.[235] Therefore, a technology is required to conveniently integrate with other technology and improve the light-harvesting efficiency under various irradiation conditions.

Microlens arrays (MLAs) are lenses with the dimension between a few μm to hundreds μm, that are arranged in specific patterns.[236] MLAs are widely applied in optical systems to optimize the redistribution of light.[237, 238] MLAs are not only able to converge or diverge the light similar to the macroscopic lenses but also act as important components in the devices for imaging[17, 18], photo-responsive sensors[239, 240], light emitting devices[25, 241], and fluorescence detection[242, 243] because of the near-field effect. In addition, MLAs are easy to be integrated with diverse devices due to their relatively small size.[24] The outstanding optical properties and small dimensions of MLAs also make them promising in the applications of MLAs in the solar harvesting process. The usage of MLAs has successfully improved the power conversion efficiency of solar cells.[23, 125] MLA-functionalized reactors have been reported to significantly enhance the water desalination efficiency driven by solar energy by creating hot spots with much higher light intensity and temperature via the strong focusing effect.[78] Importantly, enhanced photodegradation efficiency of organic contaminants in water has been observed by implementing the MLAs in direct or catalytic photodegradation, especially when solar irradiation becomes weaker.[32, 33]

The optical properties of MLAs are found to be closely related to their geometry. Curvature is one of the important parameters that influence the redistribution of light that transmits through the MLAs. Previous work has found that the MLA with a larger curvature and similar lateral size has higher light intensity at the focal points.[244, 245] Concave MLA with adjustable curvature showed different scattering ability[124] and focusing performance[246]. In our previous work, the photodegradation of methyl orange in the presence of the PMMA MLA with larger curvatures had higher enhancement.[32] Therefore, tuning the curvature is an effective method to optimize the optical properties of MLA according to the requirements of the design of solar-driven reactors. However, most of the fabrication methods of MLAs with adjustable curvatures have certain limitations.

Mechanical machining[247] or direct laser writing[26, 248] helps to precisely control the curvature and shape of MLAs, while the precision requirements and the expenses are too high to achieve for most practical applications. The aforementioned direct formation techniques are restricted to a chip scale and are hard to meet the requirements of real reactors. Changing the surface tension of precursor liquid is one of the commonly used methods to tune the curvature of MLAs.[245, 249, 250] For the inkjet printing technology, the surface tension of viscous ink before UV curing can be tuned by coating different silane layers onto the substrate.[134] Alternatively, the surface tension can also be gradually changed by controlling the temperature of precursors, and larger curvature is obtained under lower temperatures with stronger surface tension.[251, 252] However, the range of the tunable curvature is limited in the methods based on the surface tension adjustment. For most of the methods mentioned above, the size of a single microlens in the MLA is over 100 μm, which restricted the study of the potential of MLAs with even smaller dimensions. In addition, MLAs manufactured by the majority of the technologies are confined on planar surfaces since the devices for pattern formation, such as photolithography, are not adaptable to curved surfaces.[24, 253] Therefore, a scalable technology to fabricate the MLAs with tunable curvature, smaller dimensions till a few μm, and flexible substrate is worthwhile to develop for more effective solar-driven photodegradation reactors.

Surface MLAs produced by a solvent exchange process and in-situ photopolymerization have been reported to have tunable curvatures[140, 160]. Surface microdroplets arrays composed of monomers and photoinitiators form on hydrophobic domains on the pre-patterned substrate due to the oversaturation during the solvent exchange process.[27] As the concentration gradient of monomer and flow conditions during the exchange of process, the growth of the microdroplets is correspondingly influenced, leading to the variance of contact angles.[28] After transforming the microdroplets arrays into MLAs, the variance of contact angle is reflected in the difference of curvatures[135]. Furthermore, surface MLA can also be utilized as a new pre-patterned substrate with the MLAs acting as the new hydrophobic domains for the formation of the secondary MLA on top[30, 160] MLAs fabricated by such method could achieve great uniformity and precise dimension to a few microns, which are also able to enhance the photodegradation of organic contaminants in water. However, no systematic work has been conducted to optimize the method to prepare the MLAs suitable for solar-driven reactors for contaminated water. Furthermore, MLAs prepared by this fabrication technology are restricted to a limited scale on 2D surfaces and can hardly be integrated with real reactors. Last but not least, the polymeric MLAs that have been reported used for the photodegradation enhancement are set inside the reactors and immersed in the contaminated water, possibly introducing secondary pollution.[32]

In this work, we develop both convex polymeric MLAs and concave MLAs with tunable curvatures to enhance the photodegradation of organic contaminants in water. The polymeric convex MLAs are obtained through photopolymerizing surface microdroplets nucleating on a pre-patterned substrate during the solvent exchange process. Surface microdroplets can form on top of the convex MLA base and then merge with the base MLA into a new convex MLA with higher curvatures after the photopolymerization. By adjusting the flow rates, monomer concentrations, and rounds of solvent exchange, we are able to finely tune the curvature and lateral radius of the MLAs. These polymeric convex MLAs can be repeatably imprinted on elastic PDMS films by soft lithography to create concave MLAs embedded on PDMS films. The optical properties of convex and concave MLAs are characterized by optical simulations and confocal microscopy. The performance of PLMA convex MLAs and concave MLAs with various curvatures is evaluated by the photodegradation efficiency of organic contaminants under simulated solar light. Based on the strength of focusing effects which is correlated with the curvature of MLA, the influence of curvatures on the effectiveness of convex and concave MLs is investigated. To explore the potential of MLAs with tunable curvatures, we conduct light treatment under suppressed irradiation conditions in real river water and synthetic high-turbidity water. The convex and concave MLAs with tunable curvatures fabricated in this study provide a sustainable approach to enhance solar-driven photodegradation in complicated water matrices and can be easily coupled with diverse systems.

6.2 Methodology

6.2.1 Fabrication and characterization of convex polymeric microlens array with varied curvatures through solvent exchange

Surface convex polymeric microlenses array (MLA) were fabricated by in-situ photopolymerization of nanodroplets array. The formation of surface nanodroplets array is carefully controlled through a highly-tunable solvent exchange process which has been reported in the literature [27, 30, 160]. In a confined 2D fluidic chamber fully filled with solution A, solution B was added to replace solution A at certain flow rates. Solution A consisted of a UV-curable monomer, photoinitiator, and a mixture of good solvent and poor solvent of monomer, while solution B was the poor solvent saturated with the monomer and photoinitiator. The UV-curable monomers used for the work included lauryl methacrylate (LMA, Acros Organics) and 1,6-hexanediol diacrylate (HDODA, 98.5%, Alfa Aesar). Surface nanodroplets formed on the hydrophobic substrate due to the oversaturation induced by the solvent exchange process. (Figure 6.1 (a-1)) By using a pre-patterned substrate that had circular hydrophobic domains and hydrophilic surrounding areas, the formation of monomer nanodroplets was restricted in the circular domains, and a highly ordered array of surface nanodroplets was generated. The pre-patterned substrate was fabricated with the photolithography method reported in the literature [140]. After the UV curing step under irradiation at the wavelength of 365 nm (Analytik Jena UV lamp) for 15 min, surface nanodroplet arrays were transformed into polymeric convex microlens arrays (MLAs). (Figure 6.1 (a-2))

Surface polymeric MLA that was fabricated with one round of solvent exchange and local photopolymerization can be used as the new substrate for more rounds of solvent exchange process (Figure 6.1 (a-3)), and surface nanodroplets would prefer to form on top of MLA due to the lower surface energy than on the spacing area.[160] After the UV curing step, the surface nanodroplets on top of the MLA were cured into the polymer and merged with the base structure, creating a new MLA.(Figure 6.1 (a-4)) During each round of solvent exchange, the volume of nanodroplets could be carefully controlled by adjusting the composition of solution A or the flow rates when solution B was added to solution A.[27, 28] The conditions of preparing MLA samples and the corresponding sample name were listed in Table 6.1. For sample 1 to 7, surface MLAs were fabricated on a pre-patterned substrate with an area of 672 mm^2 ($56\ mm \times 12\ mm$). For sample 8 to 11, the area covered by MLA with tunable curvature was expanded to 100 cm^2 ($10\ cm \times 10\ cm$) by scaling up the chamber and substrate, plus customized flow conditions during the solvent exchange.

The morphology of polymeric convex MLAs was characterized by the optic microscope (Nikon H600l) equipped with a camera (Nikon DSFi3). Combining the photos from the microscope and the analysis by Image J, the lateral size of a single ML and the surface coverage rate of MLA in every sample were measured. The 3D structure of polymeric MLA was characterized by an atom force microscope (AFM, tapping mode, Bruker Innova) and a confocal microscope (Axio CSM 700, Zeiss). The intensity profiles of polymeric MLA was acquired by capturing the light intensity around sample 1 to 11 through a confocal laser scanning microscope (SP8, Leica).

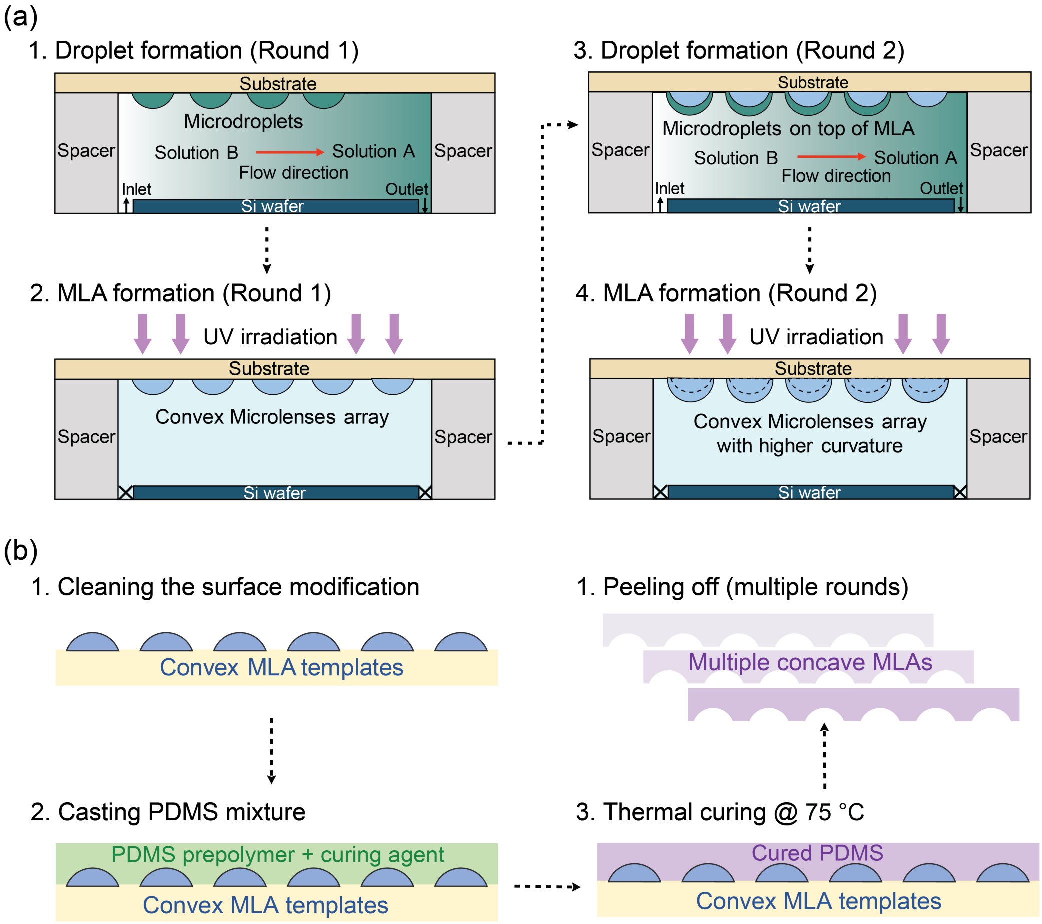

Figure 6.1: (a) Steps of fabricating convex MLAs with tunable curvatures. In step 1 (a-1), the microdroplets form on pre-patterned substrates during the first round of solvent exchange; In step 2 (a-2), the microdroplets are polymerized under UV light and transformed into an MLA; In step 3 (a-3), the microdroplets form on top of the MLA obtained in previous step; In step 4 (a-4), the microdroplets are polymerized and combined with the MLA base. (b) Steps of fabricating concave MLAs embedded in PDMS films. In step 1 (b-1), the convex MLAs are functionalized with silane; In step 2 (b-2), the degassed mixture of PDMS pre-elastomer and curing agent is cast on top of functionalized convex MLAs; In step 3 (b-3), the mixture of PDMS pre-elastomer and curing agent are cured in the oven at the temperature of 75 °C for 45 min; In step 4 (b-4), the PDMS films are peeled off from the convex MLAs. The step (b-2) to step (b-4) can be repeated for multiple times.

Sample	Substrate	Solution A	Flow rate (mL/h)
1	Pre-patterned glass (672 mm^2)	2.0 vol% LMA, 0.2 vol% initiator in ethanol	8
2	Sample 1	1.0 vol% LMA, 0.1 vol% initiator in ethanol	6
3	Sample 1	2.0 vol% LMA, 0.2 vol% initiator in ethanol	6
4	Sample 1	3.0 vol% LMA, 0.3 vol% initiator in ethanol	4
5	Sample 1	4.0 vol% LMA, 0.4 vol% initiator in ethanol	3
6	Sample 1	4.0 vol% LMA, 0.4 vol% initiator in ethanol	4
7	Sample 6	2.0 vol% LMA, 0.2 vol% initiator in ethanol	4
8	Pre-patterned glass (100 cm^2)	2.0 vol% LMA, 0.2 vol% initiator in ethanol	45
9	Sample 8	2.0 vol% LMA, 0.2 vol% initiator in ethanol	35
10	Pre-patterned glass (100 cm^2)	3.8 vol% HDODA, 0.4 vol% initiator in 50 vol% ethanol/water solution	35
11	Sample 10	2.0 vol% HDODA, 0.2 vol% initiator in 50 vol% ethanol/water solution	30

Table 6.1: Conditions of solvent exchange process for the preparation of convex polymeric MLAs

6.2.2 Fabrication and characterization of reverse microlens array with varied curvatures through soft lithography

Flexible concave MLAs could be repeatedly prepared by using the polymeric convex MLAs as the templates. Polymeric convex MLAs prepared with the same condition with sample 8 to 11 were used as templates, and those polymeric MLAs were functionalized before the soft lithography.(Figure 6.1 (b-1)) For PLMA convex MLAs, a commercialized spray (Pro-Tex protector spray, Moneysworth & Best) was used to make the PLMA MLA templates more hydrophobic at room temperature. For PHDODA MLAs, perfluorodecyltrichlorosilane (PFOTS, 97%, Sigma Aldrich) was coated through a chemical vapor deposition (CVD) process. During CVD coating process, a desiccator was pre-purged by a vacuum pump (MZ1C, BrandTech) for 30 min and then placed in an oven at 100 °C for 60 min. Then the cleaned and dried PHDODA MLAs were placed in the preheated desiccator with a well of 150 μL PFOTS. After purging out the air with the vacuum pump for 30 min, the desiccator was kept in the oven at 80 °C for 60 min.

To obtain the reverse structure of polymeric MLA, PDMS pre-elastomer and curing agent (SYLGARD 184, Dow) was thoroughly mixed with a weight ratio of 15 to 1. The mixture was degassed within a desiccator connected to the vacuum pump for 3 hours to remove the bubbles. Afterwards, 20 g of the mixture was poured into a petri dish (diameter: 150 mm, PYREX), in which the functionalized polymeric surface MLA template (10 $cm \times 10$ cm) was set at bottom center.(Figure 6.1 (b-2)) After a curing process at 80 °C for 25 min in an oven, a flexible crosslinked PDMS film with a concave MLA structure with a thickness of around 1 mm was peeled off from the polymeric MLA template and then sonicated in acetone and ethanol for 10 min, respectively.(Figure 6.1 (b-3)) As shown in Figure 6.1 (b-4), the surface functionalized polymeric convex MLA could be repeatedly used as the template for the fabrication of the PDMS film with a concave MLA structure. The PDMS films were defined as concave PDMS MLAs. Similar to convex polymeric MLAs, the morphology and intensity profiles of concave PDMS MLAs were caught by optical microscope and confocal microscope. Aside from AFM, the scanning electron microscope (SEM, Sigma FESEM, Zeiss) was utilized to observe both the top view and cross-sectional view of the PDMS concave MLA, which provided more accurate depths of the concave MLAs.

6.2.3 Photodegradation of organic pollutants in an aqueous environment with convex microlens arrays and reverse microlens arrays

Convex polymeric and concave PDMS MLAs were both applied in the photodegradation of organic pollutants in water. Two typical organic contaminants, methyl orange (MO, 85%, Sigma-Aldrich) and carbendazim (CBZ, analytical standard, Sigma Aldrich), were chosen as the model compounds to compare the performance of different MLA samples in improving the photodegradation efficiency, and the chemical structures were shown in Figure 6.2 (a-b). Since convex polymeric MLAs were immobilized on glass substrates, the MLA-decorated substrate was set on top of a self-assembled light treatment reactor with the side with MLA facing down, shown in Figure 6.2 (c). In the light treatment reactor equipped with concave PDMS MLAs, the MLAs were set on top with MLAs facing down. To avoid the adsorption of target

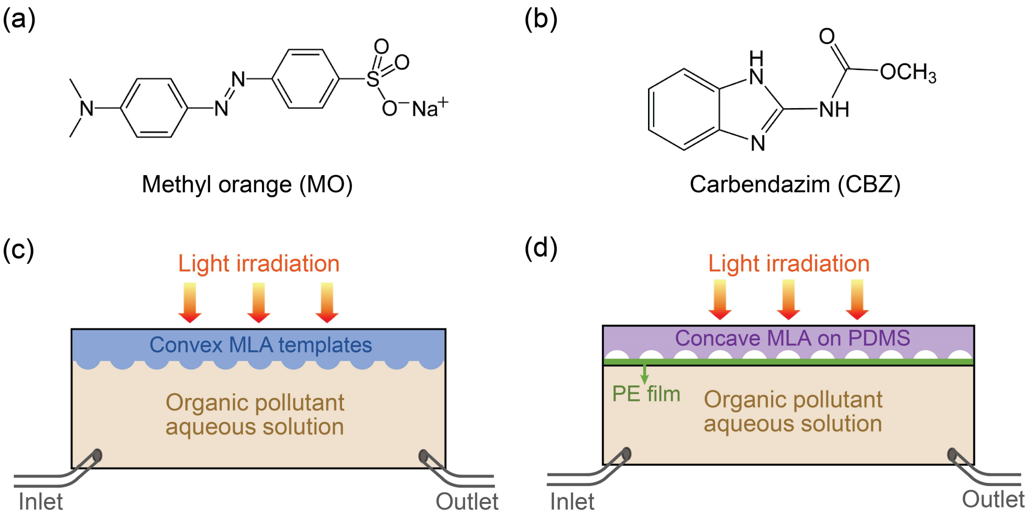

Figure 6.2: Chemical structures of the organic pollutants used in the photodegradation, including (a) methyl orange (MO) and carbendazim (CBZ). The sketch of the self-assembled reactors for the light treatment with (b) convex MLAs or (c) concave MLAs on PDMS films.

contaminants on the PDMS surface, PDMS MLAs were separated from the water solution by a transparent PE film (thickness: 12 μm) (Figure 6.2 (d)).

To investigate the performance of convex polymeric MLAs with different curvatures, the light treatment of MO solution (5 mg/L, pH=3.0) was conducted with bare glass (control) and sample 1 to 7 under the irradiation of simulated solar light (1 Sun) of 1 h. The reactor scale for the convex polymeric MLAs was 12 mm in width, 56 mm in length, and 0.57 in height. The performance of concave PDMS MLAs was verified in the photodegradation of model compound solution in a scaled-up reactor under the irradiation of simulated solar light. The influence of irradiation intensity on the effectiveness of PDMS MLAs in photodegradation enhancement was discussed by shifting the irradiation intensity from 1 Sun to 0.4 Sun.

In addition, the effectiveness of concave PDMS MLA was applied in the photodegradation of 5 mg/L MO solution prepared in different water matrices. The water matrices used for the preparation of MO solution included ultrapure water (produced by Milli-Q Direct 16), real river water (collected from Whitemud Creek to the North

Saskatchewan River in Edmonton, Alberta, Canada on July 25, 2022), and ultrapure water dispersed with 0.2 g/L SiO_2 particles. The original real river water had a pH value of 7.5 (Accumet AE150, Fisher Scientific), a TOC value of 25.6 mg/L (TOC-L Series, SHIMADZU), and a COD value of 163.3 mg/L (pre-dosage HANNA vials), and the SiO_2 dispersed water had a turbidity of 154.0 (±3.9) NTU (T-100 Handheld Turbidity Meter, Oakton), helping to simulate the practical wastewater[254]. The pH value of the MO solution prepared in all water matrices was adjusted to 3.0 by adding 1 M sulfuric acid solution, and MO solution with SiO_2 particles was stocked in the dark at 4 °C overnight until the adsorption of MO reached the equilibrium. The photodegradation of another typical organic pollutant in ultrapure water, CBZ, was conducted in the presence of concave PDMS MLA to prove that concave PDMS MLAs were not only effective for MO. The concentration of CBZ solution was 5 mg/L at a pH value of 7.0. In contrast to the direct photolysis process used for MO solution, the photodegradation of CBZ in the presence of concave PDMS MLA was studied through both direct photolysis and photocatalytic degradation. The photocatalytic degradation of CBZ was conducted by dispersing 10 mg/L commercial ZnO nanoparticles (certified ACS powder, Fisher Chemical, with a band gap of 3.26 eV) as photocatalysts in the solution.

The photodegradation efficiency (η) of specific contaminant was defined in Equation (6.1). C_{bef} and C_{aft} were the concentration of the contaminant before and after the light treatment, respectively. According to Beer-Lambert Law, the concentration of the analyte is proportional to the absorbance value when the concentration is within a linear range. Therefore, the η of the contaminant could be A_{bef} and A_{aft} obtained with UV-visible spectroscopy (UV-vis, Thermo fisher, Genesys 150), which was the peak absorbance value of the solution before and after the light treatment, respectively. To quantify the enhancement from the surface MLAs, an enhancement factor was defined by Equation (6.2). In the equation, η_{MLA} was the degradation efficiency with MLA-involved treatment, and η_{ctrl} was the degradation efficiency of the contaminant in the control group, i.e. the same treatment without MLA.

$$\eta = \frac{C_{bef} - C_{aft}}{C_{bef}} \times 100\% = \frac{A_{bef} - A_{aft}}{A_{bef}} \times 100\% \tag{6.1}$$

$$f = \frac{\eta_{MLA}}{\eta_{ctrl}} \tag{6.2}$$

6.2.4 Optical simulations of convex and concave MLAs

Convex polymeric MLAs and concave MLAs involved in light treatment systems were modeled in three-dimensional space with Zemax OpticStudio. The light treatment system was composed of a plane wave light source (along the Z axis), a convex or concave MLA, substrates, and water phase containing organic contaminants, and those components were organized according to the same set-up shown in Figure 6.2 (c-d). The intensity of light sources was equal to the intensity of the simulated solar light (1 Sun). For each convex polymeric MLA sample, an X-Z plane detector (6.6 μm × 80 μm) was placed along the central axis of a single ML to obtain a cross-sectional intensity profile. Horizontal light-flux (X-Y plane) detectors (37 μm × 37 μm) were inserted below convex or concave MLAs at different Z positions to capture the top-view light irradiation profiles of each sample.

Light through the convex polymeric MLA would be focused at the focal point of each ML in the array, and the focal distance was demonstrated by the cross-sectional intensity profiles of a single ML in specific convex MLA sample. The focus points were considered as the hot spots of convex polymeric MLAs. In comparison, the light passing through concave PDMS MLA would diverge, but the diverged light would interfere with each other and form points with higher light intensity below the concave MLA. The points with the maximum irradiation flux in all the horizontal detectors below the concave MLA were defined as the hot spots of PDMS concave MLAs. To quantify the strength of enhancing the local intensity of irradiance of all MLAs, the intensity at hot spots of MLs (I_{hs}) in each MLA sample within the area of 1 cm^2 was added up and defined as I_{Total}, and the total number of MLs within the area was N, as shown in Equation (6.3).

$$I_{Total} = \sum_{n=1}^{n=N} I_{hs} \tag{6.3}$$

6.3 Results and discussion

6.3.1 Geometric morphology and optical properties of convex MLAs

The change of the lateral size and height of PLMA convex MLAs (sample 1 to 7) on the pre-patterned substrate prepared by solvent exchange has been demonstrated in Figure 6.3. The top view of each PLMA convex is presented in the photos captured through an optical microscope (6.3 (a-g)), showing the highly-ordered structures in each convex MLA sample. A representative 3D profile of MLA obtained by AFM is shown in Figure 6.3 (h). The cross-sectional profiles of single MLs from 7 samples are extracted from the 3D graph and are displayed by the Z-X plot in 6.3 (i). With the analysis with ImageJ, the lateral radius and surface coverage rate of sample 1 to 7 are measured (Figure 6.3 (j)). The lateral radius (r) of a convex ML in the array increases between 2.3 μm and 3.2 μm from sample 1 to sample 7, resulting in a larger surface coverage rate. The maximum surface coverage rate reaches around 65% in sample 7. According to the Z-X plot from AFM, the MLA with a larger sample number is higher, and the pitch height (h) reaches around 3 μm in sample 7. The contact angles of convex MLAs in different samples are calculated by assuming the MLs in spherical shape in Figure 6.3 (k), which can be tuned from 32° to 49°.

Based on the lateral size and height of PLMA convex MLAs, the volume of a single ML in each convex MLA is obtained and summarized in Figure 6.3 (l). With our method, the volume of each ML can be controlled on a femtoliter scale, which involves only 10^{-14} M monomers in the photopolymerization process. The precise control of

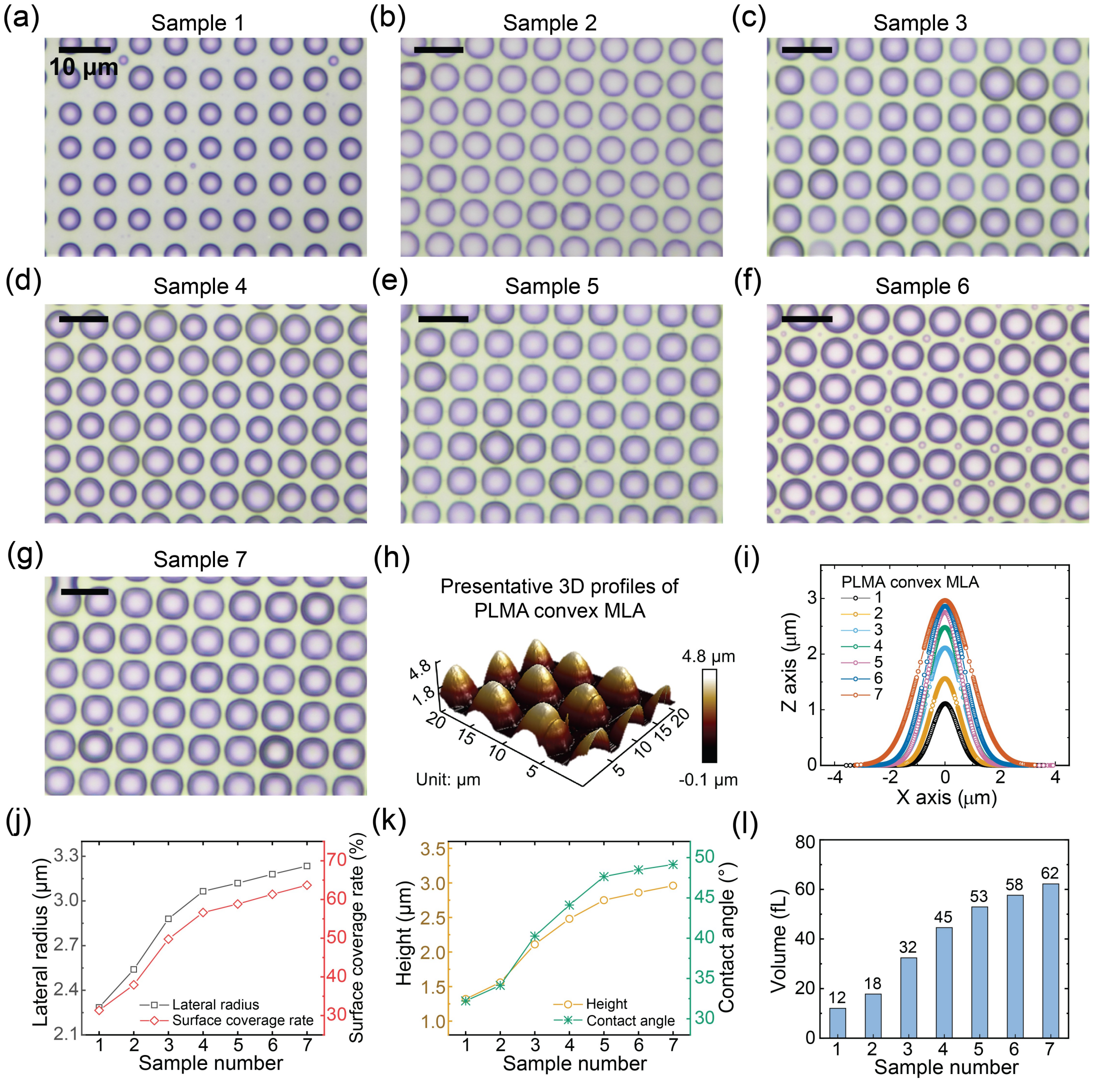

Figure 6.3: Optical images of (a) sample 1, (b) sample 2, (c) sample 3, (d) sample 4, (e) sample 5, (f) sample 6, and (g) sample 7 obtained by optical microscope equipped with a camera. (h) The 3D profile of a representative PLMA MLA from an AFM. (i) Cross-sectional profiles of single MLs from each PLMA convex MLA sample, obtained by a confocal microscope. (j) Lateral size of a single ML and surface coverage rate in each PLMA convex MLA sample. (k) Height and contact angle of a single ML in each PLMA convex MLA sample (l) The volume of a single ML in each PLMA convex MLA sample (Unit: femtoliter, i.e. fL).

the volume of each ML is attributed to the well-controlled diffusive growth of the microdroplets during the solvent exchange. The diffusive growth process is driven by the concentration gradient of the monomer at the wavefront and affected by the flow rate during the solvent exchange. Either a higher concentration of monomer in solution A or the larger flow rate of solvent exchange speeds up the diffusive growth of the microdroplets. Surface microdroplets selectively form within hydrophobic domains on the pre-patterned substrate or on top of previous convex MLA due to the lower surface tension at those spots. As a result, the microdroplets with higher diffusive growth rates present slight lateral expansions but obvious enhancement of height.

The focusing effect of MLAs is is revealed via optical simulations and confocal microscopy. The possible light paths of light through a convex MLA are illustrated in Figure 6.4 (a) in comparison to the situation with a bare glass substrate. With the optical simulations, the top view of the light intensity profiles of convex MLAs and the cross-sectional view of the intensity profiles of a single ML in an MLA is captured (Appendix D, Figure S1 and S2). Here, the light intensity profiles of two samples with the largest difference in curvature, sample 1 (Figure 6.4 (b,d)) and sample 7 (Figure 6.4 (c,e)), are displayed as examples. As shown in the intensity profiles of all PLMA convex MLAs from optical simulations, an array of focal points with the strongest light intensity exists at the horizontal plane, the distance of which from the MLA substrate is equal to the focal distance of a single ML. The highest intensity of light at the focal points of each convex MLAs varies from 3.89×10^{-10} W to 5.17×10^{-10} W, while the focal distance changes between 14 μm and 8 μm. The PLMA convex MLA with higher curvature has the stronger intensity at the focal points and a shorter focal distance. The highest peak intensity value is observed in sample 7, which is around 33% higher than that under the lowest one in sample 1.

The confocal microscope experimentally captures the actual 3D light intensity profiles of MLAs (Appendix D, Figure S3). The representative top view and cross-sectional view intensity profiles extracted from 3D intensity profiles in sample 1 and

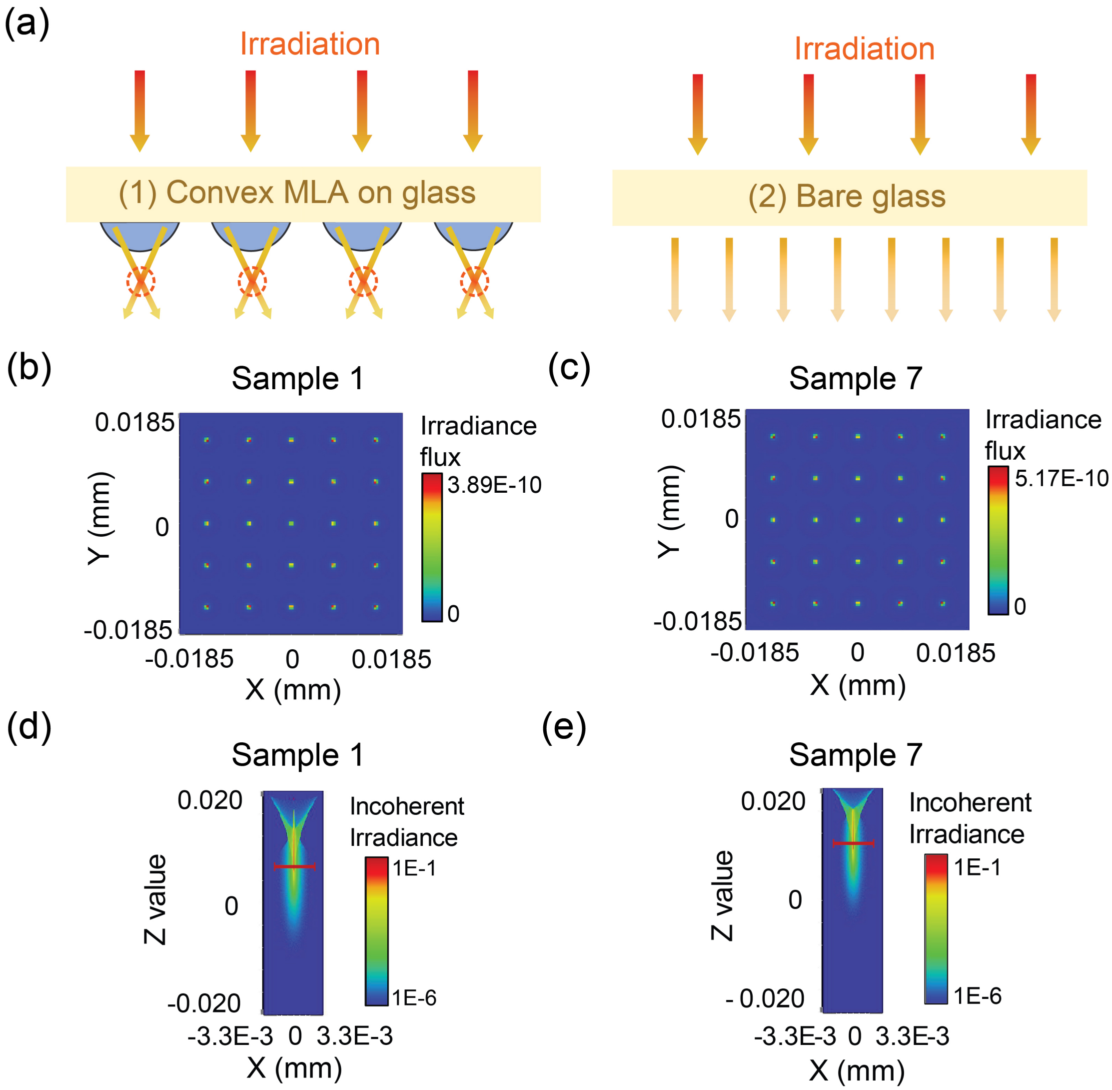

Figure 6.4: (a) A sketch of the possible light path through (1) a convex MLAs on a glass substrate or (2) a bare glass substrate. Top view of light intensity profiles around the focal distance away from the substrate of (b) sample 1 and (c) sample 7 by optical simulations. Cross-sectional view of a single ML in (d) sample 1 and (e) Sample 7 by optical simulations.

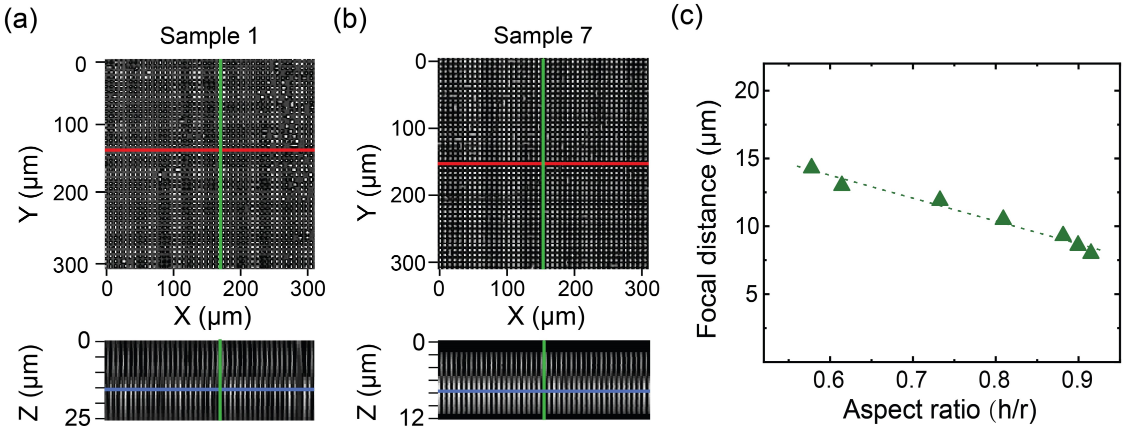

Figure 6.5: Top view (at focal points) and cross-sectional view of light intensity profiles of sample 1 captured by the confocal microscope for (a) sample 1 and (b) sample 7. (c) The correlation between the focal distance and the aspect ratio (h/r) of each PLMA convex MLA.

7 are displayed in (Figure 6.5 (a-b)). The brightest light spots arranged in arrays validate the focusing effect that is also observed in optical simulations. The brightest light spots in the 3D intensity profiles are identified as the focal points of the MLAs, and the vertical distance between the focal points and the convex MLA is the focal distance. The focal distance decreases from 16 μm in sample 1 to 7 μm in sample 7, close to the results from optical simulations. It is observed in Figure 6.5 (c) that the focal distance of a convex MLA gradually decreases with the ratio of height (h) to the lateral radius (r) of an ML in the array (h/r), showing a linear relationship when the aspect ratio is between 0.57 to 0.92.

6.3.2 Geometric morphology and optical properties of concave MLAs

The polymeric convex MLAs with varied curvatures can function as the template for preparing PDMS concave MLAs. By adjusting the flow rate and solution A composition, PLMA and PHDODA MLAs are immobilized on a square glass substrate with an area of 100 cm^2. As shown in Figure 6.6 (a), the array of colorful light spots is captured under the flashlight of a smartphone, indicating the highly ordered structures within a large area. After the soft lithography process, the concave MLAs were obtained on the surface of a PDMS film with a thickness of around 1 mm, and the appearance of the PDMS film with a concave is displayed in Figure 6.6 (b). The array of colorful light spots is also observed but weaker due to the distortion of the flexible PDMS film. The cross-sectional view of a single ML in the concave MLA is demonstrated in the sketch in 6.6 (c), where r is the lateral radius, d is the depth, and θ is the reverse contact angle of the ML. The concave MLA structure is validated by the SEM images of the top and cross-sectional surface of the PDMS film in 6.6 (d).

The images by optical microscope of the polymeric MLAs and corresponding concave MLAs on PDMS films demonstrated the highly ordered structures and the difference between the convex and concave structures. As shown in the photos of convex MLAs made with PLMA or PHDODA (sample 8 to 11, Figure 6.6 (e-h)), the lateral radius of two rounds of solvent exchange is larger. The darker color in sample 9 and 11 can be considered as evidence of the formation of higher MLAs after a second round of solvent exchange and photopolymerization. As shown in Figure 6.6 (i-j) and the r and h of concave MLAs extracted from SEM images (Table 6.2), smaller lateral radius and poorer circularity are observed in the concave MLAs obtained from the PLMA convex MLAs than the original convex MLAs. Meanwhile, the concave MLAs prepared by using PHDODA convex MLAs as templates remain the almost same shape and lateral size (Figure 6.6 (k-l)). To verify the stability of PHDODA convex MLAs after peeling off the PDMS film with concave MLA structures, the microscope images of PHDODA convex MLAs after 1 to 4 rounds of structure replication are presented in Appendix D, Figure S4. The PHDODA convex MLAs remain on the substrate without any deformation, suggesting the preparation of the concave MLAs on PDMS films is repeatable.

The changes in dimension and shape in concave MLAs made from PLMA convex MLAs are possibly caused by the deformation of PLMA MLAs during the thermal

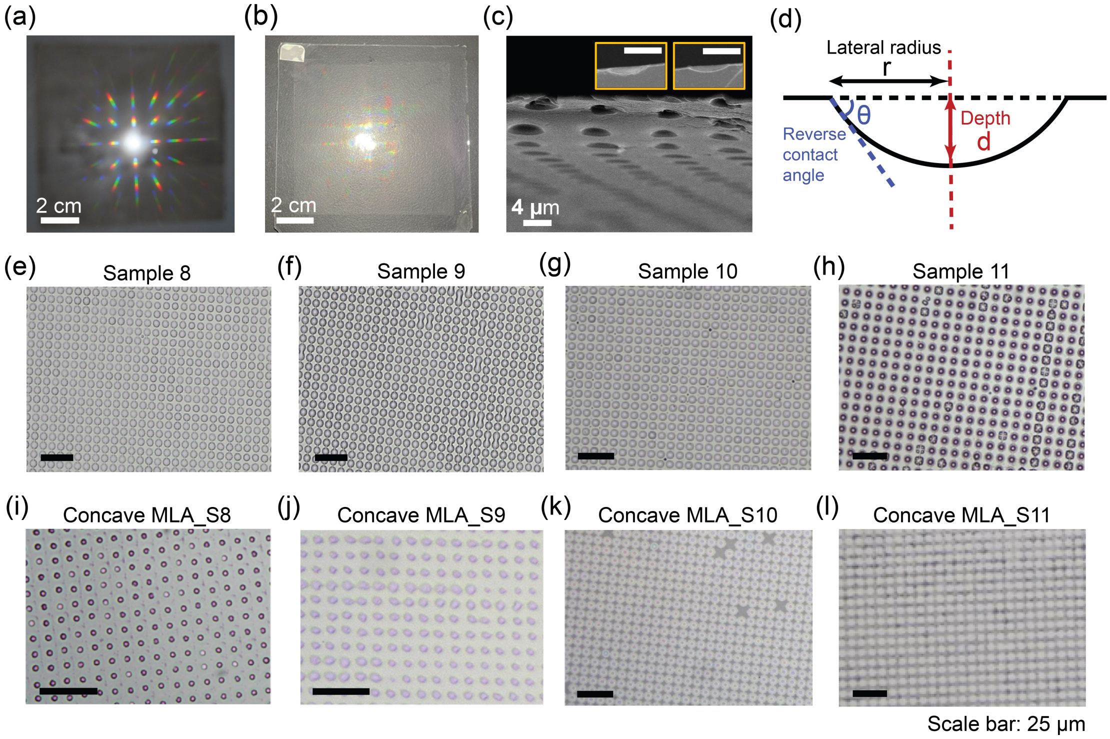

Figure 6.6: The photo of (a) a representative convex MLA (sample 10) on a 4-inch square glass substrate and (b) a PDMS film with a concave MLA which is copied from sample 10 (concave MLA_S10), and the photos are taken by a phone camera with flashlight. (c) Images of concave MLA_S10 in top view and cross-sectional view by SEM (scale bar: 4 μm). (d) A sketch of a single concave ML on PDMS film, r is the lateral radius, d is the depth, and θ is the reverse contact angle of the ML. The images by the microscope of convex MLAs, including (e) PLMA convex MLA with OTS-coated 4-inch square glass as substrate (sample 8), (f) PLMA convex MLA with sample 8 as substrate (sample 9), (g) PHDODA convex MLA with OTS-coated 4-inch square glass as substrate (sample 10), and (h) PHDODA convex MLA with sample 8 as substrate (sample 11). The images by the microscope of concave MLAs on PDMS film (thickness: 1 mm), including (i) the concave MLA using sample 8 as a template (concave MLA_S8), (j) the concave MLA using sample 9 as a template (concave MLA_S9) (k) the concave MLA using sample 10 as a template (concave MLA_S10) (l) the concave MLA using sample 11 as a template (concave MLA_S11). From (e) to (l), the scale bar is 25 μm.

Sample	r (μm)	h (μm)	θ (°)
8	2.29	1.32	58
9	2.54	1.59	64
10	2.63	1.31	53
11	2.78	1.45	55

Table 6.2: Geometric parameters of concave MLAs on PDMS films

curing steps of PDMS elastomer. Such deformation of convex MLAs is attributed to the relatively low glass transition temperature of PLMA.[255] PHDODA has a higher glass transition temperature, so PHDODA MLAs do not reflow during the thermal curing step, making the corresponding PDMS concave MLAs remain in the same size and shape. Therefore, concave MLAs using PHDODA convex MLAs as templates are mainly discussed below due to the repeatable geometric features.

The cross-sectional light intensity profiles at different depths below the concave MLAs on PDMS films are acquired with optical simulations. Optical simulations reveal that light is diverged by the concave MLAs when passing through the PDMS film. Then, the diverged light interferes with each other, creating hot spots in the space close to the concave MLA, which is interpreted in the sketch in Figure 6.7 (a). The possible light paths are validated in the cross-sectional light intensity profiles obtained from optical simulations (Figure 6.7 (b)). The depth with the highest incident flux under the PDMS concave MLAs is defined as the focal distance of concave MLAs. By using the concave MLA made from sample 10 as an example, the intensity change with the depth below the concave MLA is demonstrated in Figure 6.7 (c). As a comparison, the top-view intensity profiles under a bare PDMS film at the same depths are displayed in Figure 6.7 (d). At the depth around 15 μm below the MLA spots with intensity is nearly 10 times higher than the situation without concave MLAs. In the intensity profiles under the concave MLA, the light intensity rapidly decreases, and the peak intensity becomes 5 times smaller at the depth of 45 μm compared with the peak intensity at the depth of 15 μm. Meanwhile, the intensity across the detection plane under the planar PDMS film is uniform and keeps stable

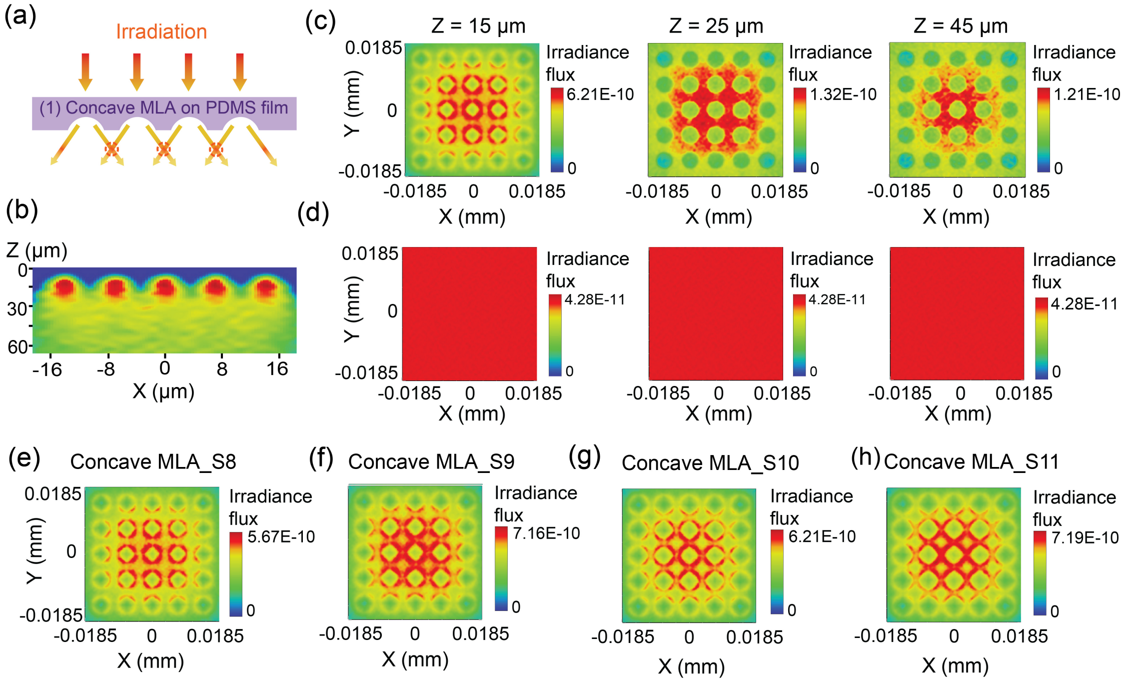

Figure 6.7: (a) A sketch of the possible light path through a PDMS film with concave MLAs. (b) Simulated cross-sectional view of light intensity profiles between two rows of MLs in a representative concave MLA on the PDMS film (concave MLA_S10). Top view light intensity profiles at the horizontal plane 15 μm, 25 μm, and 45 μm below (c) concave MLA_S10 and (d) a bare PDMS film. Top view light intensity profiles by optical simulations of (e) concave MLA_S8, (f) concave MLA_S9, (g) concave MLA_S10, and (h) concave MLA_S11.

across the region from the depth of 15 μm to 45 μm, which is continuously lower than that under concave MLA.

To compare the strength of focusing effect of all the concave MLAs, the top view of the light intensity profiles with the maximum index flux of each sample is captured for analysis. As displayed in Figure 6.7 (e-h), the concave MLAs made from the convex MLA with 2 rounds of the solvent exchange process and local photopolymerization exhibit a higher peak irradiation flux. For the concave MLAs made from PLMA convex MLAs, the peak flux increases by around 22%, while around 16% enhancement is also presented in the concave MLA made from PHDODA MLA with higher curvature. According to the parameter in 6.2, the concave MLA with a larger θ tends to have a stronger focusing effect. Comparing with the highest peak intensity achieved by PLMA convex MLA (sample 7), the peak intensity in concave MLAs is comparable, making the concave MLAs promising in enhancing the degradation of organic contaminants as well. However, this conclusion is somewhat limited in the concave MLAs made from PHDODA convex MLAs because the deviation between actual properties and simulation results may vary due to the deformation of PLMA convex MLAs during the thermal curing steps.

The light spots with stronger intensity can be also identified in the intensity profiles obtained by a confocal microscope. As shown in Figure 6.8 (a-d), the spots with the strongest points are not located at the same planar surface, which is attributed to the deformation of the flexible PDMS film during the characterization. The deformation of concave MLAs fabricated by using PLMA convex MLAs as templated is also displayed in the intensity profiles by confocal microscope (Figure 6.8 (a-b)). In comparison, the concave MLAs on PDMS made from sample 10 and 11 displayed in Figure 6.8 (c-d) are much more uniform. The focal distances of concave MLA_S10 and concave MLA_S11 are estimated by analyzing the focal point of each ML included in the 3D intensity profiles, which are around 17 μm and 9 μm, respectively. The focal distance displayed in the intensity profiles by confocal microscope verifies the results in optical simulations. The decay of the intensity is indicated in the cross-sectional intensity profiles obtained by a confocal microscope, which is also consistent with what is observed in the optical simulations.

6.3.3 Photodegradation efficiency of an organic contaminant with convex MLAs having tunable curvatures

Photodegradation efficiency (η) of MO in an aqueous solution with convex MLAs is obviously enhanced, especially with the MLs with higher curvature. The absorbance spectra of MO solution that is irradiated with different convex PLMA MLAs under 1-h irradiation of visible LED light are shown in Figure 6.9 (a). With the peak absorbance values, η of MO after the irradiation of 1 h is calculated with Equation

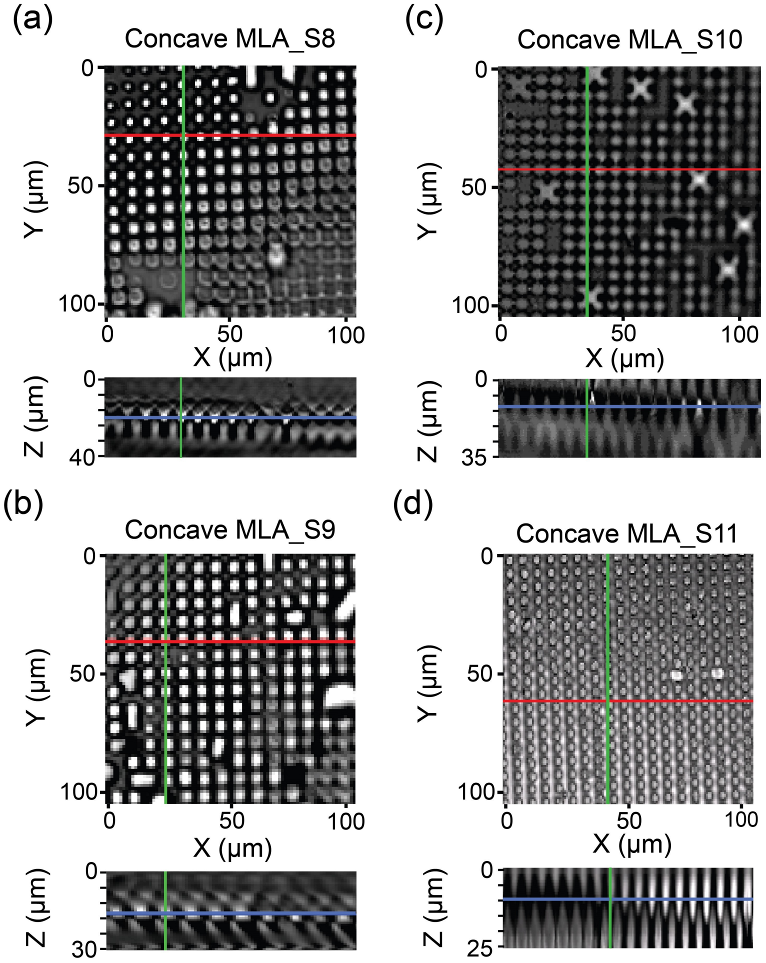

Figure 6.8: Top view and cross-sectional view of light intensity profiles obtained by confocal microscope of (a) concave MLA_S8, (b) concave MLA_S9, (c) concave MLA_S10, and (d) concave MLA_S11 at the horizontal plane where the maximum irradiance flux values are observed.

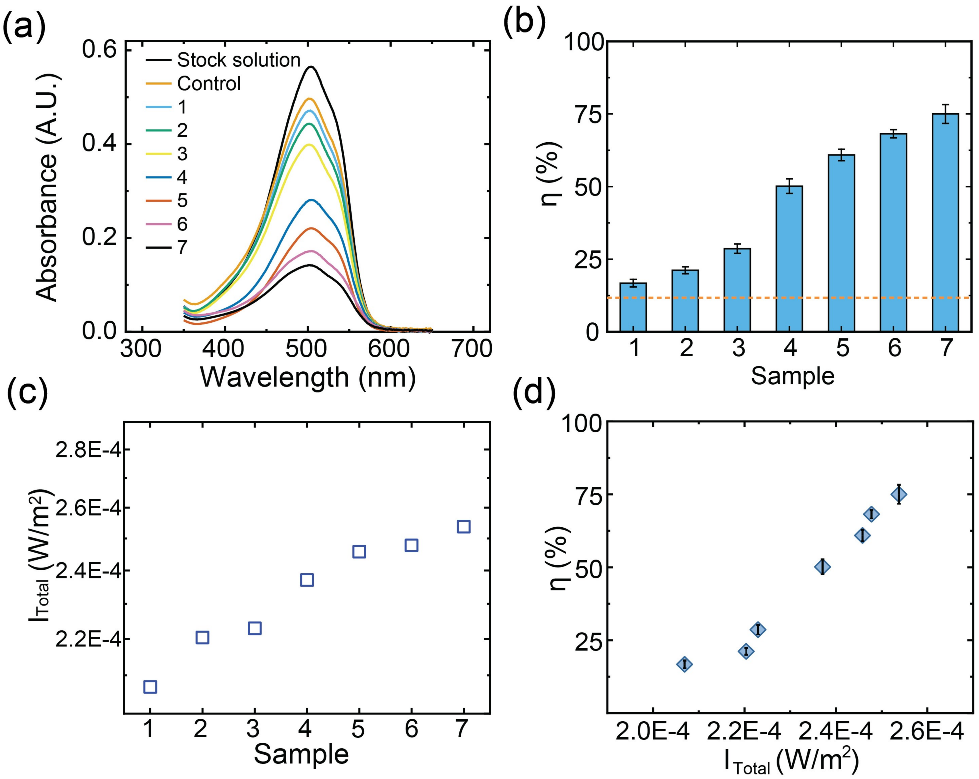

Figure 6.9: (a) Representative absorbance spectra of MO solution (5 mg/L, pH=3.0) before and after 1-h irradiation of visible LED light (intensity: 21.64 W/cm^2) with PLMA convex MLAs with different curvatures (from sample 1 to 7). (b) Photodegradation efficiency (η) of MO in the reactor equipped with different PLMA convex MLA, and the dashed line indicates the efficiency in the control group. (c) The total intensity at the focal points of MLs (I_{Total}) within an area of 1 cm^2 in each PLMA convex MLA (sample 1 to 7). (d) The correlation between η of MO and I_{Total} of each MLA within an area of 1 cm^2.

(6.1) and plotted in Figure 6.9 (b). All groups with PLMA convex MLAs achieve higher (η) than the control group. From sample 1 to 7, the (η) continuously increases, reaching the maximum value of 75% when sample 7 is applied.

Such enhancement in η is possibly correlated with the stronger focusing effect of MLs with larger curvature. To verify the correlation, I_{Total} is in each convex MLA among sample 1 to 7, which is the total intensity at the focal points of MLs in the array with an area of 1 cm^2, is defined to quantify the focusing effect of each convex MLAs. Based on the optical simulations, I_{Total} of sample 1 to 7 is figured out (Figure 6.9 (c)). As mentioned above, the PLMA convex MLA with a larger sample number has the larger curvature (Figure 6.3), which also has a larger I_{Total}, indicating a stronger focusing effect. In Figure 6.9 (d), η of MO is correlated with I_{Total} of convex MLA, and an approximately positive linear relationship is presented between the two parameters. Such correlation may assist the design of MLAs for photodegradation reactors with enhanced η. However, the enhancement in η can hardly increase due to the upper limit of the curvature of PLMA convex MLAs in the current method (Appendix D, Figure S5).

6.3.4 Photodegradation efficiency of organic contaminants with concave MLAs in different water matrices

The performance of the concave MLAs on PDMS films is investigated in the degradation of MO in different water matrices (Figure 6.10 (a)) under the simulated solar light. Due to the flexibility and robustness of concave MLAs, they can be equipped in a non-contact set-up illustrated in Figure 6.2 (d). To avoid the possible side effect on light focusing by the non-uniformity of concave MLAs made from sample 8 and 9, only the concave MLAs copied from PHDODA MLAs are studied in light treatment. The transmittance of all concave MLA samples utilized in photodegradation experiments is over 90% under the light with wavelength from 300 nm to 1000 nm (Appendix D, Figure S6) For the photodegradation of MO in ultrapure water under the simulated solar light with the intensity of 1 Sun or 0.4 Sun, η of the groups with concave MLAs made from sample 10 to 11 is higher than the control group without concave MLAs (Figure 6.10 (b-c)). When decreasing the light intensity of irradiation during the light treatment, η of MO after the light treatment is lower no matter whether concave MLAs are applied or not, but the variation between groups caused by different concave MLA samples becomes larger under the irradiation with lower intensity. Among all the concave MLAs, the one made from sample 11 achieved the most enhancement of the η of MO. Concave MLAs on PDMS films fabricated with PHDODA convex MLAs perform better than those made from PLMA convex MLAs in accelerating the degradation of MO.

The variance of η obtained from different concave MLAs comes from several factors. Firstly, the highly ordered structure of concave MLAs contributes to the focusing effect of concave MLAs, which is influenced by the template materials. Deformation of PLMA convex materials during thermal curing of PDMS leads to poorer regularity in corresponding concave MLAs, suppressing the focusing effect of the concave MLAs. Secondly, higher transmittance of concave MLAs on PDMS films also does a favor to the photodegradation rate. As shown in the transmittance spectra in Appendix D, Figure S6, concave MLAs made from PLMA convex MLAs have lower transmittance than those from PHDODA MLAs in the wavelength range of the simulated solar light. Last but not least, the strength of focusing effect of concave MLAs plays an important role to enhance the η of organic pollutants. For two concave MLAs obtained from the PHDODA convex MLAs, both the regularity of MLs and transmittance are similar to each other, but the peak irradiance flux of the concave MLA made from sample 11 is larger according to the simulation results. As a result, more enhancement of η is observed in the concave MLA using sample 11 as the template.

The photodegradation of MO assisted by the concave MLAs on PDMS films is also conducted in river water. The concave MLAs made from sample 10 and 11 are selected as examples due to the better performance in enhancing η in light treatment using ultrapure water as the water matrix. Similar to the degradation in ultrapure water, the concave MLA using sample 11 as the template still has the best effectiveness in improving the η of MO in river water under the irradiation of 1 Sun or 0.4 Sun. Meanwhile, the photodegradation under the weaker irradiation is slower in river water, the same as in ultrapure water. However, the η of MO in river water is generally lower than that in ultrapure water under the same irradiation conditions (Figure 6.10 (d-e)), especially for the control group. With the application of concave MLAs, the gaps of η resulting from different water matrices are narrowed. For the concave MLA presenting the highest enhancement, the η after the irradiation of 45 min under 1-

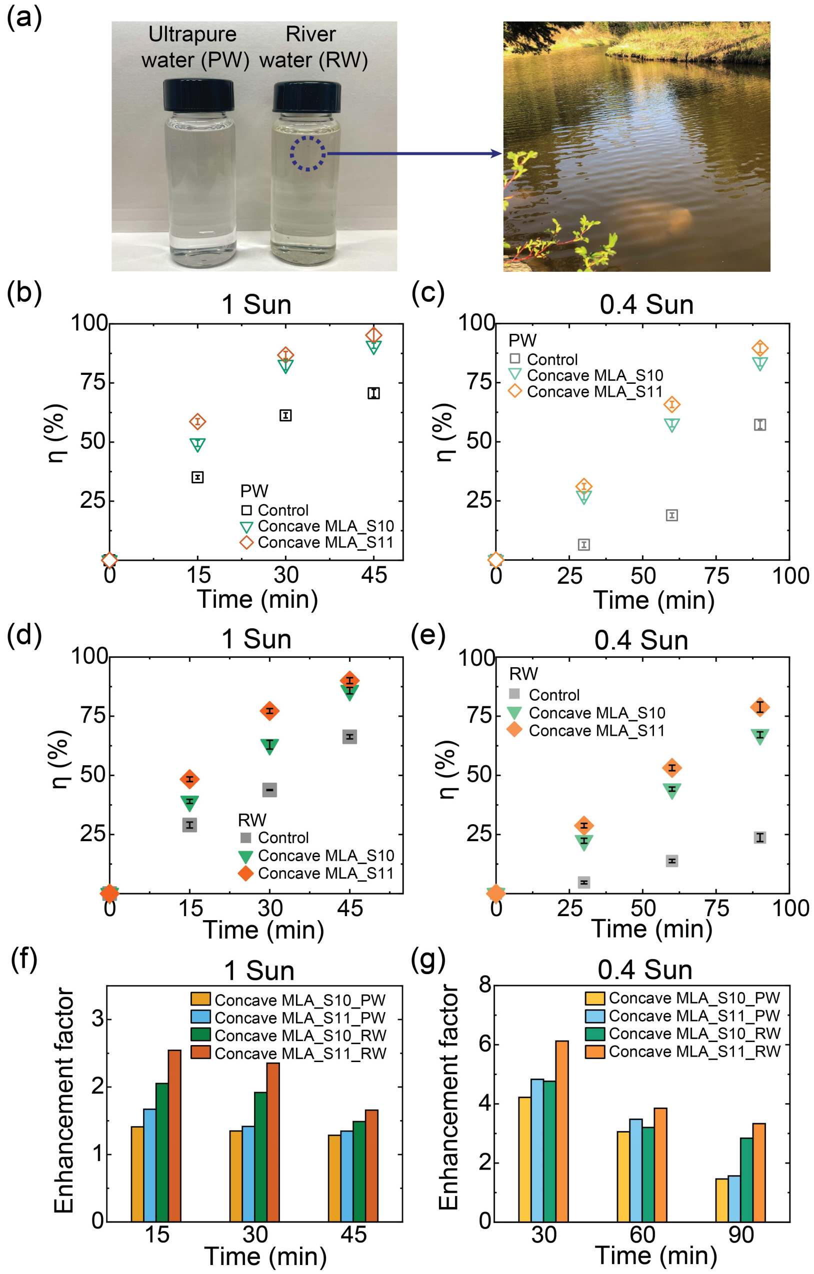

Figure 6.10: (a) Photos of ultrapure water (PW) and river water used in the preparation of MO solution for light treatment. Photodegradation efficiency (η) of MO in the solution prepared with ultrapure water with four concave MLAs made from sample 10 and 11 after the irradiation of simulated solar light with the intensity of (b) 1 Sun or (c) 0.4 Sun. η of MO in the solution prepared with river water with concave MLAs made from sample 10 and 11 after the irradiation of simulated solar light with the intensity of (d) 1 Sun or (e) 0.4 Sun. Enhancement factors of MO photodegradation in different water matrices and with varied concave MLAs under the irradiation of (f) 1 Sun or (g) 0.4 Sun.

Sun simulated solar can be even neglected. Besides the two water matrices above, the function of the concave MLA made from sample 11 is also studied in a water matrix with high turbidity. SiO_2 particles are dispersed into the MO solution prepared with ultrapure water. As shown in the plot in Appendix D, Figure S7, the degradation rate decreases while the enhancement of η achieved by the concave MLA is more obvious in the solution with higher turbidity.

The effectiveness of concave MLAs is quantified by the enhancement factor defined in Equation (6.2) and plotted with the time of irradiation in Figure 6.10 (f-g). Based on the change of enhancement, the influence of different factors on the performance of concave MLAs is investigated. As the irradiation time becomes longer, the enhancement factor decreases due to the lower degradation rate of MO with concave MLAs in the later stage of the reaction. The concentration MO in the reactor with concave MLAs is lower than that in the control group, resulting in lower degradation rates. When the intensity of irradiation decreases from 1 Sun to 0.4 Sun, the enhancement factor by concave MLAs significantly increases. In the situation of weak irradiation, such as 0.4 Sun, the energy barrier of the degradation of MO is hard to go over. Nevertheless, the hots spots with higher intensity are created in the top layer of the solution by using concave MLAs, making the photodegradation easier to happen under weak irradiation. The higher enhancement factor in river water and highly turbid water than that in ultrapure water also benefits from the redistribution of light by concave MLAs when light energy is not sufficient. Less energy from light can be used for photodegradation because of the stronger absorbance in river water caused by impurities or the lower transmittance in highly turbid water. Concave MLAs improve the intensity in the space with focusing effects, reducing the loss of light energy. In brief conclusion, the concave MLAs are able to effectively enhance the photodegradation of MO, especially when the irradiation is weakened due to the condition of light sources or the properties of water matrices.

The effect of concave MLAs on PDMS films in enhancing η is also validated with

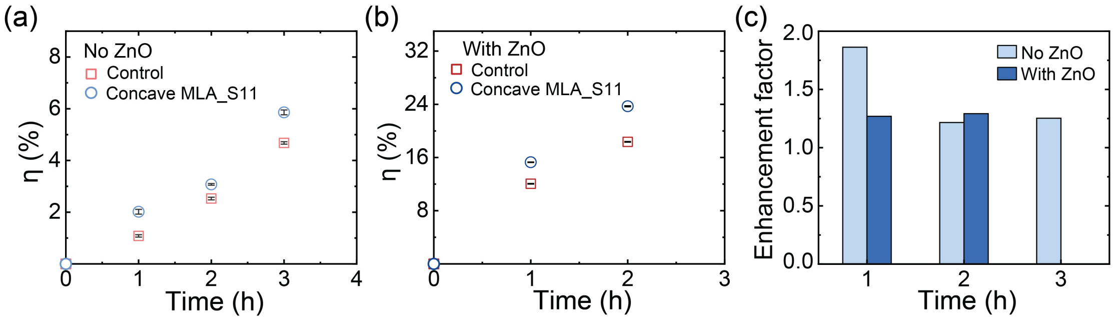

Figure 6.11: Photodegradation efficiency (η) of CBZ in ultrapure water (a) without or (b) without ZnO as photocatalyst after the irradiation of simulated solar light (intensity: 1 Sun). (c) Enhancement factors of MO photodegradation achieved by the concave MLA made from sample 11 (concave MLA_11) without and with ZnO in the light treatment.

the photodegradation of another typical organic contaminant, carbendazim (CBZ), in ultrapure water. Direct photodegradation without photocatalysts and the ZnO-photocatalytic degradation process are both conducted in the presence of the concave MLA made from sample 11. According to the η obtained after the light treatment in Figure 6.11 (a-b), the concave MLA contributes to faster degradation of CBZ regardless of the existence of the photocatalyst. In the photocatalyst-assisted degradation, η significantly increases for both the control group and the concave MLA-involved group. However, the enhancement factor by the concave MLA in photocatalytic degradation is relatively smaller than that in direct photodegradation (Figure 6.11 (c)), since the η in the control group containing catalysts is already improved.

Even though the enhancement factor by the concave MLA is not outstanding, the usage of concave MLA to enhance the photodegradation of organic contaminants is still promising. On one hand, concave MLAs are able to enhance the η of different organic pollutants. On the other hand, the effectiveness of concave MLAs is proven in diverse scenarios, including different irradiation intensity, varied water matrices, and alternative degradation mechanisms (with and without photocatalysts). Furthermore, the concave MLAs can be set outside of the reactor, avoiding the adsorption of contaminants and possible photocatalysts particles, which is difficult to realize for convex MLA. Multiple concave MLAs on PDMS films can be obtained from a single convex MLA with highly tunable curvature. The thermal stability and hydrophobicity of PDMS film also make the concave MLA easy to maintain in some outdoor applications.

6.4 Conclusions

Polymeric convex microlens arrays (MLA) with controllable curvatures are fabricated with a scalable and reproducible method based on multiple solvent exchange processes and local photopolymerization processes. Combing with soft lithography technology, multiple concave MLAs with tunable curvatures can be reproduced by imprinting the convex MLAs on PDMS films. The validation through confocal microscopy and optical simulations shows that focal points with stronger light intensity exist under both convex and concave MLAs, which can serve as hot spots of photoreactions and contribute to the higher degradation efficiency of organic contaminants. Furthermore, the focusing effect of MLAs also becomes stronger by increasing the curvature of convex and concave MLAs, which is revealed by the improved total light intensity at focal points, contributing to higher enhancement in photodegradation efficiency. The flexible structure and stable physiochemical properties enable the concave MLAs to be easily implemented to photoreactors in a non-contact setup, avoiding possible secondary contamination. Notably, the effectiveness of concave MLAs is also approved under irradiation with lower intensity, real river water samples, the water with high turbidity. In summary, the fabrication technology of convex and concave MLAs with tunable curvatures developed in this work would inspire the design of solar-driven devices providing enhanced decontamination performance and strong adaptability to complicated wastewater treatment.

6.5 Supplementary materials

Supplementary data to this article can be found in the Appendix, section A.4. Additional data include the optical simulations results and 3D light intensity profiles by the confocal microscope of PLMA convex MLAs from sample 2 to sample 6, the photos of PHDODA convex MLA after 4 rounds of soft lithography under the optical microscope, the images of PLMA convex MLAs with equal to or more than 3 rounds of solvent exchange and photopolymerization, transmittance test of the concave MLAs embedded PDMS films, and the photodegradation efficiency of MO enhanced by concave MLA_S11 in water with higher turbidity.

Chapter 7

Conclusions and outlook

7.1 Conclusions

In summary, this work focuses on microlenses (MLs), an effective solution to enhance the utilization efficiency of solar energy in the treatment of polluted water containing organic contaminants. The implementation of MLs brought about significant enhancement in the photodegradation efficiency under various conditions. The fabrication procedures of MLs were developed based on solvent exchange processes, expanding the formation of MLs from 2D surfaces to 3D topological spaces. The systematic analysis provided a deeper understanding of how parameters during the solvent exchange or dilution process influenced the properties of MLs, including size distribution, spatial arrangement, and curvatures. Furthermore, the scale-up fabrication of MLs facilitated their application in more types of solar-driven reactors. This work also demonstrated, for the first time, the mechanisms of MLs-involved photolysis and photocatalytic degradation through experimental and simulation results. A quantitative analysis methodology was proposed to assess the focusing effects of MLs, enabling the correlation between MLs' properties and the enhancement of photodegradation efficiency and providing guidance on the optimization of MLs fabrication and reactor design.

In **Chapter 3**, the enhancement of photodegradation efficiency by surface MLs was observed under various solution conditions while the degradation pathway remained the same. The morphology, number density, and spatial arrangement of MLs were found significantly affect the MLs-involved photodegradation efficiency. Compared with the control group without surface MLs, random MLs forming on homogeneous hydrophobic substrates could be $\sim 600\%$ more effective in the photodegradation of methyl orange, while the improvement of the efficiency by microlens arrays (MLAs) was extra 100% higher than random MLs. The simulation results indicated that highly ordered MLA might result in a locally high concentration of active species around the focal points array, and further accelerate the photodegradation. The photodegradation efficiency of four organic contaminants in glass vials functionalized with MLs was all significantly higher than those in unmodified bottles, which was considered as a potential application of MLs in practical solar-water treatment reactors.

The MLs-enhanced photocatalytic degradation of typical micropollutants was investigated in **Chapter 4**. The presence of surface MLs led to higher photodegradation efficiency, which was attributed to increased concentrations of free radicals, as determined by electron spin resonance spectra. The enhancement in degradation efficiency was generally observed for all four targeted organic contaminants when either ZnO or TiO_2 was used as the photocatalyst. The ability of surface MLs in improving decontamination was validated in not only ultrapure water but also synthetic river water and a real river water matrix. Comparing highly ordered microlens arrays (MLAs) with randomly distributed MLs, MLAs showed superior performance in the photocatalytic degradation of all organic pollutants due to more effective redistribution of the irradiation energy. The enhancement factor, representing the improvement in photodegradation efficiency, varied among pollutants because of different degradation mechanisms. Furthermore, the enhancement factor was higher at lower photocatalyst concentrations or under irradiation with lower intensity, indicating the potential of surface MLs to boost photodegradation efficiency in scenarios where photocatalyst excitation is suppressed.

A novel method of fabricating MLs on curved surfaces was introduced in **Chapter 5**, in which surface microdroplets were generated in a solvent dilution process and then photopolymerized into MLs. The size distribution and surface coverage rate of MLs were controlled by adjusting the solution components, solution amount, and flow conditions during the dilution process. The scalability of the approach was demonstrated by successfully fabricating MLs over the wall of a large reactor with a capacity of up to 500 mL. Reactors with arbitrary shapes were functionalized by surface MLs via the method and evaluated for their ability in enhancing the photodegradation of organic contaminants in the aqueous phase. Enhanced photodegradation efficiency is observed in all six types of ML-functionalized reactors, and the efficiency was improved by over 80 times at maximum. Both optical simulations and experimental results revealed that the strength of the focusing effects of MLs on a reactor, quantified by the total intensity at the focal points of MLs, was dependent on the dimensions, spatial arrangement of MLs, and curvature of the reactor wall. The technology demonstrated in the chapter might be implemented to design compact and efficient reactors for sustainable solar-driven water treatment. Moreover, the fabrication method of MLs on 3D curved surfaces might have the potential to be applied in a wide range of applications, particularly in novel optoelectronic and sensing devices, extending its impact beyond the realm of photodegradation in solar-driven water treatment.

The potential of MLAs in enhancing the photodegradation of organic contaminants was further explored in **Chapter 6**. Polymeric convex MLAs with tunable curvatures were fabricated by several rounds of solvent exchange and local photopolymerization, which was a scalable and reproducible method. Multiple concave MLAs with tunable curvatures were reproduced by imprinting a convex MLA on PDMS films as well. Both experimental observations through confocal microscopy and theoretical analysis by optical simulations provided evidence of the presence of focusing effects in both convex and concave MLAs. Furthermore, the higher total light intensity at focal points was obtained as the curvature of convex and concave MLAs increased, suggesting stronger focusing effects and more enhanced photodegradation efficiency of organic contaminants. Unlike the rigid nature of convex MLAs immobilized on glass substrates, the flexible structure and stable physiochemical properties of concave MLAs allowed for easy implementation to photoreactors in a non-contact setup, thereby minimizing the risk of secondary contamination. Importantly, the effectiveness of concave MLAs was demonstrated under various conditions, such as lower irradiation intensity, real river water samples, and highly turbid solution. In summary, the developed fabrication technology for convex and concave MLAs in this chapter presented new possibilities for designing solar-driven devices with enhanced decontamination capabilities and exceptional adaptability for complex wastewater treatment.

7.2 Outlook

Despite considerable efforts invested in studying the principles of MLs-enhanced photodegradation and optimizing the properties of MLs for more efficient solar-driven water decontamination reactors, certain limitations in terms of time and techniques hinder further investigation into some specific topics. Here are several promising directions that deserve continued exploration in future research:

(1) In this thesis, the materials of surface MLs are limited to a few types of acrylic polymers, such as poly (methyl methacrylate) (PMMA), poly (lauryl methacrylate) (PLMA), and poly (1,6-Hexanediol diacrylate) (PHDODA). Even though the stability of those materials under the irradiation of real or simulated solar of over 30 h has been proven, the durability of those materials after a longer period of usage is uncertain. As the currently used materials start to degrade with time, harmful byproducts may be generated and cause secondary contamination. One of the candidate solutions to this problem is to utilize degradable and environmental-friendly polymer materials for MLs preparation, such as PVA (poly(vinyl alcohol)) [167, 168], PNIPAM (poly(N-isopropyl acrylamide)) [169, 170], and some biomacromolecules like silk protein and

cellulose [171, 172].

(2) Till now, the fabrication of MLs on 3D topological surfaces has been realized. However, the MLs immobilized on curved surfaces via the solvent dilution process still are randomly distributed over the whole substrate. As we know from this work, MLAs functionalized on planar substrates provide stronger focusing effects and more enhancement in photodegradation efficiency. According to the premises, functionalizing 3D topological spaces by MLAs with tailored properties us is promising to further improve the effectiveness of MLs-functionalized reactors in water decontamination.

(3) The physiochemical properties of MLs need to be further verified during the solar-driven photodegradation processes. The possibility of physical abrasion and the risk of detachment of MLs is relatively low due to their tiny size. Most MLs have a lateral radius between a few μm and 100 μm, with a height less than 3 μm according to the results obtained from the optical microscope or AFM microscopy. Meanwhile, when the contaminated aqueous solution is added to the reactor for light treatment, the flow is laminar flow, and the thickness of the boundary layer[27] is much larger than the height of MLs. Therefore, the flow velocity near the MLs is too slow to cause the abrasion or detachment of MLs during the light treatment process. Except for physical stability, the chemical stability of polymeric convex MLs still requires systematic study, including leaching tests and aging tests for the materials of convex MLs. However, for concave MLs which are separated from the aqueous phase, only the influence of the aging of PDMS under a long period of irradiation on the properties of concave MLAs needs to be studied.

(4) As inspired by the surface functionalization of convex MLAs before the PDMS casting step in Chapter 6, the modification of the functional group of the surface of MLAs may open up the applications of surface MLs. For example, the practical application of photocatalysts is restricted due to the excessive steps to separate and recycle the photocatalysts during the water treatment. Immobilizing the photocatalysts on certain matrices is one of the popular strategies to address the problem. With

the surface-modified surface MLs, it is possible to immobilize photocatalysts onto the surface of surface MLs, enabling a synergistic effect between MLs and photocatalysts.

(5) In order to understand the principle of MLs-enhanced photodegradation, only the degradation pathway of a single organic contaminant is monitored during the light treatment with MLs. However, in most cases of practical wastewater treatment, multiple types of organic contaminants are mixed with each other, resulting in complicated degradation pathways. In the next stage of research, surface MLs may be evaluated in the light treatment of water samples containing multiple contaminants. Chromatography, mass spectrum, and other advanced analytical technique will be more frequently used for the accurate analysis of the composition of each target contaminant. Whether the selective enhancement by MLs of certain organic pollutants exists is pending to verify.

(6) In our work, the concentration of organic contaminants is from 2.5 mg/L to 50 mg/L for the convenience of the analysis of photodegradation kinetics and mechanisms in the presence of MLs. However, MLs, as an effective component for photodegradation, are more suitable to be used in the post-treatment of contaminated water where the actual concentration of organic contaminants is at ppb level (i.e. at μg/L). UV vis spectrum is the main technique we used to measure the concentration difference of contaminants during the photodegradation, with a limit of detection (LOD) at around 0.3 ppm[256], which is not qualified for calculating the photodegradation efficiency of contaminants at the ppb level. Some techniques with higher precision and a lower LOD, such as liquid chromatography–mass spectrometry, are required to verify the effectiveness of MLs in situations with a trace amount of pollutants.

(7) As demonstrated in this work, surface MLs developed based on solvent exchange or solvent dilution process can be functionalized on reactors with a volume as large as 500 mL, indicating the scalability of this method. In addition, the enhancement of photodegradation efficiency with MLs-functionalized reactors has been observed under solar light with different intensity. Therefore, it is promising to apply MLs-

functionalized reactors for the solar-driven water decontamination process, especially in remote areas where advanced oxidation facilities are not available. Another advantage of the MLs-functionalized reactors is their portability, which would be convenient for household water treatment or basic water treatment during traveling[257].

Bibliography

[1] M. Salehi, "Global water shortage and potable water safety; today's concern and tomorrow's crisis," *Environment International*, vol. 158, p. 106 936, 2022.

[2] C. Loubser, B. M. Chimbanga, and H. Jacobs, "Intermittent water supply: A south african perspective," *Water SA*, vol. 47, no. 1, pp. 1–9, 2021.

[3] M. T. Van Vliet *et al.*, "Global water scarcity including surface water quality and expansions of clean water technologies," *Environmental Research Letters*, vol. 16, no. 2, p. 024 020, 2021.

[4] Y. Lu, H. Zhang, D. Fan, Z. Chen, and X. Yang, "Coupling solar-driven photothermal effect into photocatalysis for sustainable water treatment," *Journal of Hazardous Materials*, vol. 423, p. 127 128, 2022.

[5] R. Djellabi *et al.*, "Recent advances and challenges of emerging solar-driven steam and the contribution of photocatalytic effect," *Chemical Engineering Journal*, vol. 431, p. 134 024, 2022.

[6] J. Lin *et al.*, "Carbon nitride-based z-scheme heterojunctions for solar-driven advanced oxidation processes," *Journal of Hazardous Materials*, p. 128 866, 2022.

[7] M. P. Callao and M. S. Larrechi, "Simultaneous determination of organic dyes using second-order data," in *Data Handling in Science and Technology*, vol. 29, Elsevier, 2015, pp. 399–426.

[8] T. Nakajima, T. Kitamura, and T. Tsuchiya, "Visible light photocatalytic activity enhancement for water purification in cu (ii)-grafted wo3 thin films grown by photoreaction of nanoparticles," *Applied Catalysis B: Environmental*, vol. 108, pp. 47–53, 2011.

[9] S. Dong *et al.*, "Recent developments in heterogeneous photocatalytic water treatment using visible light-responsive photocatalysts: A review," *Rsc Advances*, vol. 5, no. 19, pp. 14 610–14 630, 2015.

[10] R. J. Braham and A. T. Harris, "Review of major design and scale-up considerations for solar photocatalytic reactors," *Industrial & Engineering Chemistry Research*, vol. 48, no. 19, pp. 8890–8905, 2009.

[11] A. P. Carvalho, S. O. Silva, J. M. Baptista, and F. X. Malcata, "Light requirements in microalgal photobioreactors: An overview of biophotonic aspects," *Applied microbiology and biotechnology*, vol. 89, pp. 1275–1288, 2011.

[12] M. Nakano, Y. Nishiyama, H. Tanimoto, T. Morimoto, and K. Kakiuchi, "Remarkable improvement of organic photoreaction efficiency in the flow microreactor by the slug flow condition using water," *Organic Process Research & Development*, vol. 20, no. 9, pp. 1626–1632, 2016.

[13] T. Banerjee, F. Podjaski, J. Kröger, B. P. Biswal, and B. V. Lotsch, "Polymer photocatalysts for solar-to-chemical energy conversion," *Nature Reviews Materials*, vol. 6, no. 2, pp. 168–190, 2021.

[14] S. Nahim-Granados, G. Rivas-Ibanez, J. A. S. Pérez, I. Oller, S. Malato, and M. I. Polo-López, "Fresh-cut wastewater reclamation: Techno-economical assessment of solar driven processes at pilot plant scale," *Applied Catalysis B: Environmental*, vol. 278, p. 119 334, 2020.

[15] J. Gong, C. Li, and M. R. Wasielewski, "Advances in solar energy conversion," *Chemical Society Reviews*, vol. 48, no. 7, pp. 1862–1864, 2019.

[16] P. Zhang and X. W. Lou, "Design of heterostructured hollow photocatalysts for solar-to-chemical energy conversion," *Advanced Materials*, vol. 31, no. 29, p. 1 900 281, 2019.

[17] S.-I. Bae, K. Kim, K.-W. Jang, H.-K. Kim, and K.-H. Jeong, "High contrast ultrathin light-field camera using inverted microlens arrays with metal–insulator–metal optical absorber," *Advanced Optical Materials*, vol. 9, no. 6, p. 2 001 657, 2021.

[18] Y. Zhong *et al.*, "Novel optofluidic imaging system integrated with tunable microlens arrays," *ACS Applied Materials & Interfaces*, 2023.

[19] J. Lim, P. Gruner, M. Konrad, and J.-C. Baret, "Micro-optical lens array for fluorescence detection in droplet-based microfluidics," *Lab on a Chip*, vol. 13, no. 8, pp. 1472–1475, 2013.

[20] Y. M. Song *et al.*, "Digital cameras with designs inspired by the arthropod eye," *Nature*, vol. 497, no. 7447, pp. 95–99, 2013.

[21] X. Jin, D. Guerrero, R. Klukas, and J. F. Holzman, "Microlenses with tuned focal characteristics for optical wireless imaging," *Applied Physics Letters*, vol. 105, no. 3, p. 031 102, 2014.

[22] D. A. Keane *et al.*, "Solar photocatalysis for water disinfection: Materials and reactor design," *Catalysis Science & Technology*, vol. 4, no. 5, pp. 1211–1226, 2014.

[23] Q. Liu, H. Liu, D. Li, W. Qiao, G. Chen, and H. Ågren, "Microlens array enhanced upconversion luminescence at low excitation irradiance," *Nanoscale*, vol. 11, no. 29, pp. 14 070–14 078, 2019.

[24] S. Cai, Y. Sun, H. Chu, W. Yang, H. Yu, and L. Liu, "Microlenses arrays: Fabrication, materials, and applications," *Microscopy Research and Technique*, 2021.

[25] N. Jürgensen *et al.*, "A single-step hot embossing process for integration of microlens arrays in biodegradable substrates for improved light extraction of light-emitting devices," *Advanced Materials Technologies*, vol. 6, no. 2, p. 1 900 933, 2021.

[26] S. Luan, P. Xu, Y. Zhang, L. Xue, Y. Song, and C. Gui, "Flexible superhydrophobic microlens arrays for humid outdoor environment applications," *ACS Applied Materials & Interfaces*, vol. 14, no. 47, pp. 53 433–53 441, 2022.

[27] X. Zhang *et al.*, "Formation of surface nanodroplets under controlled flow conditions," *Proceedings of the National Academy of Sciences*, vol. 112, no. 30, pp. 9253–9257, 2015.

[28] Z. Lu, S. Peng, and X. Zhang, "Influence of solution composition on the formation of surface nanodroplets by solvent exchange," *Langmuir*, vol. 32, no. 7, pp. 1700–1706, 2016.

[29] L. Bao, Z. Werbiuk, D. Lohse, and X. Zhang, "Controlling the growth modes of femtoliter sessile droplets nucleating on chemically patterned surfaces," *The journal of physical chemistry letters*, vol. 7, no. 6, pp. 1055–1059, 2016.

[30] L. Bao *et al.*, "Control of femtoliter liquid on a microlens: A way to flexible dual-microlens arrays," *ACS applied materials & interfaces*, vol. 11, no. 30, pp. 27 386–27 393, 2019.

[31] J. Qian, G. F. Arends, and X. Zhang, "Surface nanodroplets: Formation, dissolution, and applications," *Langmuir*, vol. 35, no. 39, pp. 12 583–12 596, 2019.

[32] Q. Lu *et al.*, "Surface microlenses for much more efficient photodegradation in water treatment," *ACS ES&T Water*, vol. 2, no. 4, pp. 644–657, 2022.

[33] Q. Lu, L. Yang, P. Chelme-Ayala, Y. Li, X. Zhang, and M. G. El-Din, "Enhanced photocatalytic degradation of organic contaminants in water by highly tunable surface microlenses," *Chemical Engineering Journal*, vol. 463, p. 142 345, 2023.

[34] D. R. Arnold, N. Baird, and J. R. Bolton, *Photochemistry: an introduction.* Academic Press, 2014.

[35] R. C. Evans, P. Douglas, and H. D. Burrow, *Applied photochemistry.* Springer, 2013, vol. 36.

[36] Y. Furukawa, M. Hayashi, S. Hayase, T. Nokami, and T. Itoh, "Visible light-driven direct 2.2-difluoroacetylation using organic pigment catalyst," *ACS Sustainable Chemistry & Engineering*, 2020.

[37] J. V. Goldstone, "Direct and indirect photoreactions of chromophoric dissolved organic matter: Roles of reactive oxygen species and iron," Ph.D. dissertation, Massachusetts Institute of Technology, 2002.

[38] H. D. Burrows, J. Santaballa, S Steenken, *et al.*, "Reaction pathways and mechanisms of photodegradation of pesticides," *Journal of photochemistry and photobiology B: Biology*, vol. 67, no. 2, pp. 71–108, 2002.

[39] F. Li *et al.*, "A rewritable optical data storage material system by [2+ 2] photocycloreversion- photocycloaddition," *Chemistry of Materials*, vol. 20, no. 4, pp. 1194–1196, 2008.

[40] N.-Y. Li, J.-M. Chen, X.-Y. Tang, G.-P. Zhang, and D. Liu, "Reversible single-crystal-to-single-crystal conversion of a photoreactive coordination network for rewritable optical memory storage," *Chemical Communications*, vol. 56, no. 13, pp. 1984–1987, 2020.

[41] N. R. Pradhan *et al.*, "High photoresponsivity and short photoresponse times in few-layered wse2 transistors," *ACS applied materials & interfaces*, vol. 7, no. 22, pp. 12 080–12 088, 2015.

[42] A. Kimoto, J.-S. Cho, K. Ito, D. Aoki, T. Miyake, and K. Yamamoto, "Novel hole-transport material for efficient polymer light-emitting diodes by photoreaction," *Macromolecular rapid communications*, vol. 26, no. 8, pp. 597–601, 2005.

[43] Y. Zhou, H.-Y. Zhang, Z.-Y. Zhang, and Y. Liu, "Tunable luminescent lanthanide supramolecular assembly based on photoreaction of anthracene," *Journal of the American Chemical Society*, vol. 139, no. 21, pp. 7168–7171, 2017.

[44] M. N. Chong, B. Jin, C. W. Chow, and C. Saint, "Recent developments in photocatalytic water treatment technology: A review," *Water research*, vol. 44, no. 10, pp. 2997–3027, 2010.

[45] K. Yoshikawa *et al.*, "Silicon heterojunction solar cell with interdigitated back contacts for a photoconversion efficiency over 26%," *Nature energy*, vol. 2, no. 5, pp. 1–8, 2017.

[46] N. Corrigan, J. Yeow, P. Judzewitsch, J. Xu, and C. Boyer, "Seeing the light: Advancing materials chemistry through photopolymerization," *Angewandte Chemie International Edition*, vol. 58, no. 16, pp. 5170–5189, 2019.

[47] A. Bagheri and J. Jin, "Photopolymerization in 3d printing," *ACS Applied Polymer Materials*, vol. 1, no. 4, pp. 593–611, 2019.

[48] J. F. Ribeiro *et al.*, "Pdms microlenses for optical biopsy microsystems," *IEEE Transactions on Industrial Electronics*, vol. 64, no. 12, pp. 9683–9690, 2017.

[49] A. Kumar, M. Khan, J. He, and I. M. Lo, "Recent developments and challenges in practical application of visible–light–driven tio2–based heterojunctions for ppcp degradation: A critical review," *Water research*, vol. 170, p. 115 356, 2020.

[50] Z. Luo *et al.*, "Treatment of oil sands process water by the ferric citrate under visible light irradiation," *Chemical Engineering Journal*, vol. 429, p. 132 419, 2022.

[51] R. Lindsey, "Climate and earth's energy budget," *NASA Earth Observatory*, vol. 680, 2009.

[52] J. Song, S. A. Messele, L. Meng, Z. Huang, and M. G. El-Din, "Adsorption of metals from oil sands process water (ospw) under natural ph by sludge-based biochar/chitosan composite," *Water Research*, vol. 194, p. 116 930, 2021.

[53] S. A. Messele, P. Chelme-Ayala, and M. G. El-Din, "Catalytic ozonation of naphthenic acids in the presence of carbon-based metal-free catalysts: Performance and kinetic study," *Catalysis Today*, 2020.

[54] J. Edzwald, *Water quality & treatment: a handbook on drinking water*. McGraw-Hill Education, 2011.

[55] B. Sommer *et al.*, "Sodis- an emerging water treatment process," *AQUA(OXFORD)*, vol. 46, no. 3, pp. 127–137, 1997.

[56] S. Dejung *et al.*, "Effect of solar water disinfection (sodis) on model microorganisms under improved and field sodis conditions," *Journal of Water Supply: Research and Technology—AQUA*, vol. 56, no. 4, pp. 245–256, 2007.

[57] R. Toor and M. Mohseni, "Uv-h2o2 based aop and its integration with biological activated carbon treatment for dbp reduction in drinking water," *Chemosphere*, vol. 66, no. 11, pp. 2087–2095, 2007.

[58] C. Chen, W. Ma, and J. Zhao, "Semiconductor-mediated photodegradation of pollutants under visible-light irradiation," *Chemical Society Reviews*, vol. 39, no. 11, pp. 4206–4219, 2010.

[59] F. Li *et al.*, "Internal electric field construction on dual oxygen group-doped carbon nitride for enhanced photodegradation of pollutants under visible light irradiation," *Applied Catalysis B: Environmental*, vol. 256, p. 117 705, 2019.

[60] J. Carbajo, M. Jiménez, S. Miralles, S. Malato, M. Faraldos, and A. Bahamonde, "Study of application of titania catalysts on solar photocatalysis: Influence of type of pollutants and water matrices," *Chemical Engineering Journal*, vol. 291, pp. 64–73, 2016.

[61] M. Kovacic, D. J. Perisic, M. Biosic, H. Kusic, S. Babic, and A. L. Bozic, "Uv photolysis of diclofenac in water; kinetics, degradation pathway and environmental aspects," *Environmental Science and Pollution Research*, vol. 23, no. 15, pp. 14 908–14 917, 2016.

[62] Y.-H. Chuang, S. Chen, C. J. Chinn, and W. A. Mitch, "Comparing the uv/-monochloramine and uv/free chlorine advanced oxidation processes (aops) to the uv/hydrogen peroxide aop under scenarios relevant to potable reuse," *Environmental science & technology*, vol. 51, no. 23, pp. 13 859–13 868, 2017.

[63] N. Jallouli *et al.*, "Heterogeneous photocatalytic degradation of ibuprofen in ultrapure water, municipal and pharmaceutical industry wastewaters using a tio2/uv-led system," *Chemical Engineering Journal*, vol. 334, pp. 976–984, 2018.

[64] Q. Zheng *et al.*, "Visible-light-responsive graphitic carbon nitride: Rational design and photocatalytic applications for water treatment," *Environmental science & technology*, vol. 50, no. 23, pp. 12 938–12 948, 2016.

[65] E. Kabir, P. Kumar, S. Kumar, A. A. Adelodun, and K.-H. Kim, “Solar energy: Potential and future prospects,” *Renewable and Sustainable Energy Reviews*, vol. 82, pp. 894–900, 2018.

[66] S. Malato, P. Fernández-Ibáñez, M. I. Maldonado, J. Blanco, and W. Gernjak, “Decontamination and disinfection of water by solar photocatalysis: Recent overview and trends,” *Catalysis today*, vol. 147, no. 1, pp. 1–59, 2009.

[67] K. McGuigan, T. M. Joyce, R. M. Conroy, J. Gillespie, and M Elmore-Meegan, “Solar disinfection of drinking water contained in transparent plastic bottles: Characterizing the bacterial inactivation process,” *Journal of applied microbiology*, vol. 84, no. 6, pp. 1138–1148, 1998.

[68] A. Martínez-García *et al.*, “Assessment of a pilot solar v-trough reactor for solar water disinfection,” *Chemical Engineering Journal*, vol. 399, p. 125 719, 2020.

[69] H. Dong *et al.*, “An overview on limitations of tio2-based particles for photocatalytic degradation of organic pollutants and the corresponding countermeasures,” *Water research*, vol. 79, pp. 128–146, 2015.

[70] Y. Bao *et al.*, “One-step block copolymer templated synthesis of bismuth oxybromide for bisphenol a degradation: An extended study from photocatalysis to chemical oxidation,” *ACS ES&T Water*, vol. 1, no. 4, pp. 837–846, 2021.

[71] N. Liu *et al.*, “Trash into treasure: Converting waste polyester into c3n4-based intramolecular donor-acceptor conjugated copolymer for efficient visible-light photocatalysis,” *Journal of Environmental Chemical Engineering*, vol. 10, no. 1, p. 106 959, 2022.

[72] D Faust *et al.*, “Immobilized photosensitizers for solar photochemical applications,” *Solar Energy*, vol. 65, no. 1, pp. 71–74, 1999.

[73] Y. Xiao, C. Li, X. Zhou, N. Tao, and M. Ye, “Removal of typical volatile organic compounds in condensed freshwater by activated persulfate during interfacial solar distillation,” *ACS ES&T Water*, vol. 1, no. 11, pp. 2423–2430, 2021.

[74] X. Yang *et al.*, “Recent advances in photodegradation of antibiotic residues in water,” *Chemical Engineering Journal*, p. 126 806, 2020.

[75] J. C. Colmenares, R. S. Varma, and V. Nair, “Selective photocatalysis of lignin-inspired chemicals by integrating hybrid nanocatalysis in microfluidic reactors,” *Chemical Society Reviews*, vol. 46, no. 22, pp. 6675–6686, 2017.

[76] K. G. McGuigan, R. M. Conroy, H.-J. Mosler, M. du Preez, E. Ubomba-Jaswa, and P. Fernandez-Ibanez, “Solar water disinfection (sodis): A review from bench-top to roof-top,” *Journal of hazardous materials*, vol. 235, pp. 29–46, 2012.

[77] J. Moreno-SanSegundo *et al.*, “Sodis potential: A novel parameter to assess the suitability of solar water disinfection worldwide,” *Chemical Engineering Journal*, vol. 419, p. 129 889, 2021.

[78] P. D. Dongare, A. Alabastri, O. Neumann, P. Nordlander, and N. J. Halas, "Solar thermal desalination as a nonlinear optical process," *Proceedings of the National Academy of Sciences*, vol. 116, no. 27, pp. 13 182–13 187, 2019.

[79] D. Chen *et al.*, "Photocatalytic degradation of organic pollutants using tio2-based photocatalysts: A review," *Journal of Cleaner Production*, vol. 268, p. 121 725, 2020.

[80] D. S. Bhatkhande, V. G. Pangarkar, and A. A. C. M. Beenackers, "Photocatalytic degradation for environmental applications–a review," *Journal of Chemical Technology & Biotechnology: International Research in Process, Environmental & Clean Technology*, vol. 77, no. 1, pp. 102–116, 2002.

[81] R. Pawar and C. S. Lee, *Heterogeneous Nanocomposite-Photocatalysis for Water Purification*. William Andrew, 2015.

[82] M. A. Fox and M. T. Dulay, "Heterogeneous photocatalysis," *Chemical reviews*, vol. 93, no. 1, pp. 341–357, 1993.

[83] M. Rauf and S. S. Ashraf, "Fundamental principles and application of heterogeneous photocatalytic degradation of dyes in solution," *Chemical engineering journal*, vol. 151, no. 1-3, pp. 10–18, 2009.

[84] L. Li, P. A. Salvador, and G. S. Rohrer, "Photocatalysts with internal electric fields," *Nanoscale*, vol. 6, no. 1, pp. 24–42, 2014.

[85] S. G. Kumar and K. K. Rao, "Comparison of modification strategies towards enhanced charge carrier separation and photocatalytic degradation activity of metal oxide semiconductors (tio2, wo3 and zno)," *Applied Surface Science*, vol. 391, pp. 124–148, 2017.

[86] K. M. Lee, C. W. Lai, K. S. Ngai, and J. C. Juan, "Recent developments of zinc oxide based photocatalyst in water treatment technology: A review," *Water research*, vol. 88, pp. 428–448, 2016.

[87] J. Liu *et al.*, "Slow photons for photocatalysis and photovoltaics," *Advanced Materials*, vol. 29, no. 17, p. 1 605 349, 2017.

[88] A Rey, P. García-Muñoz, M. D. Hernández-Alonso, E Mena, S. García-Rodríguez, and F. Beltrán, "Wo3–tio2 based catalysts for the simulated solar radiation assisted photocatalytic ozonation of emerging contaminants in a municipal wastewater treatment plant effluent," *Applied Catalysis B: Environmental*, vol. 154, pp. 274–284, 2014.

[89] J. Sun, L. Qiao, S. Sun, and G. Wang, "Photocatalytic degradation of orange g on nitrogen-doped tio2 catalysts under visible light and sunlight irradiation," *Journal of hazardous materials*, vol. 155, no. 1-2, pp. 312–319, 2008.

[90] Z. Li, Y. Fang, and S. Xu, "Squaraine dye sensitized tio2 nanocomposites with enhanced visible-light photocatalytic activity," *Materials Letters*, vol. 93, pp. 345–348, 2013.

[91] Q. Li, L. Zong, Y. Xing, X. Wang, L. Yu, and J. Yang, “Preparation of g-c3n4/tio2 nanocomposites and investigation of their photocatalytic activity,” *Science of Advanced Materials*, vol. 5, no. 9, pp. 1316–1322, 2013.

[92] Y. Ni, W. Wang, W. Huang, C. Lu, and Z. Xu, “Graphene strongly wrapped tio2 for high-reactive photocatalyst: A new sight for significant application of graphene,” *Journal of colloid and interface science*, vol. 428, pp. 162–169, 2014.

[93] D. Chen, K. Wang, D. Xiang, R. Zong, W. Yao, and Y. Zhu, “Significantly enhancement of photocatalytic performances via core–shell structure of zno@ mpg-c3n4,” *Applied Catalysis B: Environmental*, vol. 147, pp. 554–561, 2014.

[94] F. Wang, S. Min, Y. Han, and L. Feng, “Visible-light-induced photocatalytic degradation of methylene blue with polyaniline-sensitized tio2 composite photocatalysts,” *Superlattices and Microstructures*, vol. 48, no. 2, pp. 170–180, 2010.

[95] F. Deng, L. Min, X. Luo, S. Wu, and S. Luo, “Visible-light photocatalytic degradation performances and thermal stability due to the synergetic effect of tio 2 with conductive copolymers of polyaniline and polypyrrole,” *Nanoscale*, vol. 5, no. 18, pp. 8703–8710, 2013.

[96] S. Dong, J. Sun, Y. Li, C. Yu, Y. Li, and J. Sun, “Znsno3 hollow nanospheres/reduced graphene oxide nanocomposites as high-performance photocatalysts for degradation of metronidazole,” *Applied Catalysis B: Environmental*, vol. 144, pp. 386–393, 2014.

[97] D. Fang, Z. Qin, W. Qufu, S. Dongjian, and C. Mingqing, “Control of photocatalytic property of bismuth-based semiconductor photocatalysts,” *Progress in Chemistry*, vol. 26, no. 1, pp. 30–40, 2014.

[98] L. Zhang, Y. Li, Q. Li, J. Fan, S. A. Carabineiro, and K. Lv, “Recent advances on bismuth-based photocatalysts: Strategies and mechanisms,” *Chemical Engineering Journal*, vol. 419, p. 129 484, 2021.

[99] M.-h. Wu, L. Li, N. Liu, D.-j. Wang, Y.-c. Xue, and L. Tang, “Molybdenum disulfide (mos2) as a co-catalyst for photocatalytic degradation of organic contaminants: A review,” *Process Safety and Environmental Protection*, vol. 118, pp. 40–58, 2018.

[100] A. Rahman, J. R. Jennings, A. L. Tan, and M. M. Khan, “Molybdenum disulfide-based nanomaterials for visible-light-induced photocatalysis,” *ACS omega*, vol. 7, no. 26, pp. 22 089–22 110, 2022.

[101] L. Hu, G. Deng, W. Lu, S. Pang, and X. Hu, “Deposition of cds nanoparticles on mil-53 (fe) metal-organic framework with enhanced photocatalytic degradation of rhb under visible light irradiation,” *Applied Surface Science*, vol. 410, pp. 401–413, 2017.

[102] W.-Q. Li *et al.*, "Metal organic framework decorated with molybdenum disulfide for visible-light-driven reduction of hexavalent chromium: Performance and mechanism," *Journal of Cleaner Production*, vol. 318, p. 128 513, 2021.

[103] M. Diepens and P. Gijsman, "Influence of light intensity on the photodegradation of bisphenol a polycarbonate," *Polymer Degradation and Stability*, vol. 94, no. 1, pp. 34–38, 2009.

[104] M. Tanveer and G. T. Guyer, "Solar assisted photo degradation of wastewater by compound parabolic collectors: Review of design and operational parameters," *Renewable and Sustainable Energy Reviews*, vol. 24, pp. 534–543, 2013.

[105] A. M. Khaksar, S. Nazif, A. Taebi, and E. Shahghasemi, "Treatment of phenol in petrochemical wastewater considering turbidity factor by backlight cascade photocatalytic reactor," *Journal of photochemistry and photobiology A: chemistry*, vol. 348, pp. 161–167, 2017.

[106] J. V. Vaghasiya, K. K. Sonigara, L. Suresh, M. Panahandeh-Fard, S. S. Soni, and S. C. Tan, "Efficient power generating devices utilizing low intensity indoor lights via non-radiative energy transfer mechanism from organic ionic redox couples," *Nano Energy*, vol. 60, pp. 457–466, 2019.

[107] M. M. Kandy and V. G. Gaikar, "Enhanced photocatalytic reduction of co2 using cds/mn2o3 nanocomposite photocatalysts on porous anodic alumina support with solar concentrators," *Renewable Energy*, vol. 139, pp. 915–923, 2019.

[108] C. Zhang *et al.*, "Development of a novel solar energy controllable linear fresnel photoreactor (lfp) for high-efficiency photocatalytic wastewater treatment under actual weather," *Water Research*, vol. 208, p. 117 880, 2022.

[109] W. Li *et al.*, "Enhanced biological photosynthetic efficiency using light-harvesting engineering with dual-emissive carbon dots," *Advanced Functional Materials*, vol. 28, no. 44, p. 1 804 004, 2018.

[110] J.-W. F. Zijffers, S. Salim, M. Janssen, J. Tramper, and R. H. Wijffels, "Capturing sunlight into a photobioreactor: Ray tracing simulations of the propagation of light from capture to distribution into the reactor," *Chemical Engineering Journal*, vol. 145, no. 2, pp. 316–327, 2008.

[111] J. Y. Lee *et al.*, "Near-field focusing and magnification through self-assembled nanoscale spherical lenses," *Nature*, vol. 460, no. 7254, pp. 498–501, 2009.

[112] B. Dyett, Q. Zhang, Q. Xu, X. Wang, and X. Zhang, "Extraordinary focusing effect of surface nanolenses in total internal reflection mode," *ACS central science*, vol. 4, no. 11, pp. 1511–1519, 2018.

[113] D. Daly, *Microlens arrays*. CRC Press, 2000.

[114] N. Ong, Y. Koh, and Y. Q. Fu, "Microlens array produced using hot embossing process," *Microelectronic Engineering*, vol. 60, no. 3-4, pp. 365–379, 2002.

[115] S. Moore, J. Gomez, D. Lek, B. H. You, N. Kim, and I.-H. Song, "Experimental study of polymer microlens fabrication using partial-filling hot embossing technique," *Microelectronic Engineering*, vol. 162, pp. 57–62, 2016.

[116] X. Lin, A. Hosseini, X. Dou, H. Subbaraman, and R. T. Chen, "Low-cost board-to-board optical interconnects using molded polymer waveguide with 45 degree mirrors and inkjet-printed micro-lenses as proximity vertical coupler," *Optics express*, vol. 21, no. 1, pp. 60–69, 2013.

[117] M. T. Gale, M. Rossi, J. Pedersen, and H. Schuetz, "Fabrication of continuous-relief micro-optical elements by direct laser writing in photoresists," *Optical Engineering*, vol. 33, no. 11, pp. 3556–3566, 1994.

[118] J. Shao, Y. Ding, H. Zhai, B. Hu, X. Li, and H. Tian, "Fabrication of large curvature microlens array using confined laser swelling method," *Optics letters*, vol. 38, no. 16, pp. 3044–3046, 2013.

[119] Y. Huang, Y. Qin, P. Tu, Q. Zhang, M. Zhao, and Z. Yang, "High fill factor microlens array fabrication using direct laser writing and its application in wavefront detection," *Optics Letters*, vol. 45, no. 16, pp. 4460–4463, 2020.

[120] J.-G. Hua *et al.*, "Convex silica microlens arrays via femtosecond laser writing," *Optics letters*, vol. 45, no. 3, pp. 636–639, 2020.

[121] M. V. Kunnavakkam *et al.*, "Low-cost, low-loss microlens arrays fabricated by soft-lithography replication process," *Applied physics letters*, vol. 82, no. 8, pp. 1152–1154, 2003.

[122] M. Li, Q. Yang, H. Bian, T. Yang, X. Hou, and F. Chen, "Microlens arrays enable variable-focus imaging," *Optics & Laser Technology*, vol. 153, p. 108 260, 2022.

[123] J. Liu, M.-J. Chang, Y. Ai, H.-L. Zhang, and Y. Chen, "Fabrication of microlens arrays by localized hydrolysis in water droplet microreactors," *ACS Applied Materials & Interfaces*, vol. 5, no. 6, pp. 2214–2219, 2013.

[124] L. Mei *et al.*, "Facile fabrication of microlens array on encapsulation layer for enhancing angular color uniformity of color-mixed light-emitting diodes," *Optics & Laser Technology*, vol. 142, p. 107 227, 2021.

[125] C. Fang *et al.*, "Antireflective paraboloidal microlens film for boosting power conversion efficiency of solar cells," *ACS applied materials & interfaces*, vol. 10, no. 26, pp. 21 950–21 956, 2018.

[126] H. Bai, C. Du, A. Zhang, and L. Li, "Breath figure arrays: Unconventional fabrications, functionalizations, and applications," *Angewandte Chemie International Edition*, vol. 52, no. 47, pp. 12 240–12 255, 2013.

[127] W. Yuan, L.-H. Li, W.-B. Lee, and C.-Y. Chan, "Fabrication of microlens array and its application: A review," *Chinese Journal of Mechanical Engineering*, vol. 31, no. 1, p. 16, 2018.

[128] W. Wang *et al.*, "Large-scale microlens arrays on flexible substrate with improved numerical aperture for curved integral imaging 3d display," *Scientific Reports*, vol. 10, no. 1, pp. 1–9, 2020.

[129] H. Zhang, L. Li, D. L. McCray, D. Yao, and Y. Y. Allen, “A microlens array on curved substrates by 3d micro projection and reflow process,” *Sensors and Actuators A: Physical*, vol. 179, pp. 242–250, 2012.

[130] M. Xu, S. Li, J. Li, L. Zhang, and H. Lu, “Fabrication of a bionic compound eye on a curved surface by using a self-assembly technique,” *Optics Express*, vol. 30, no. 17, pp. 30 750–30 759, 2022.

[131] Y.-S. Cherng and G.-D. J. Su, “Fabrication of polydimethylsiloxane microlens array on spherical surface using multi-replication process,” *Journal of Micromechanics and Microengineering*, vol. 24, no. 1, p. 015 016, 2013.

[132] J. Li, W. Wang, Z. Fu, R. Zhu, and Y. Huang, “Fabrication of a dual-focus artificial compound eye with improved imaging based on modified microprinting and air-assisted deformation,” *Applied Optics*, vol. 62, no. 10, pp. D125–D130, 2023.

[133] C. Shu, X. Guo, S. Yin, S. Huang, and Z. Mao, “Fabrication of curved aspheric compound eye microlens array with high surface quality by precision glass molding,” *Precision Engineering*, 2023.

[134] Q. Zhang *et al.*, “Fabrication of microlens arrays with high quality and high fill factor by inkjet printing,” *Advanced Optical Materials*, vol. 10, no. 14, p. 2 200 677, 2022.

[135] X. Zhang, J. Ren, H. Yang, Y. He, J. Tan, and G. G. Qiao, “From transient nanodroplets to permanent nanolenses,” *Soft Matter*, vol. 8, no. 16, pp. 4314–4317, 2012.

[136] H. Yu, S. Peng, L. Lei, J. Zhang, T. L. Greaves, and X. Zhang, “Large scale flow-mediated formation and potential applications of surface nanodroplets,” *ACS applied materials & interfaces*, vol. 8, no. 34, pp. 22 679–22 687, 2016.

[137] V. Charlot, A. Ibrahim, X. Allonas, C Croutxé-Barghorn, and C. Delaite, “Photopolymerization of methyl methacrylate: Effects of photochemical and photonic parameters on the chain length,” *Polymer Chemistry*, vol. 5, no. 21, pp. 6236–6243, 2014.

[138] S. Peng, C. Xu, T. C. Hughes, and X. Zhang, “From nanodroplets by the ouzo effect to interfacial nanolenses,” *Langmuir*, vol. 30, no. 41, pp. 12 270–12 277, 2014.

[139] G. Gebel and R. B. Moore, “Small-angle scattering study of short pendant chain perfuorosulfonated ionomer membranes,” *Macromolecules*, vol. 33, no. 13, pp. 4850–4855, 2000.

[140] L. Bao, A. R. Rezk, L. Y. Yeo, and X. Zhang, “Highly ordered arrays of femtoliter surface droplets,” *Small*, vol. 11, no. 37, pp. 4850–4855, 2015.

[141] Y. Xia and G. M. Whitesides, “Soft lithography,” *Annual review of materials science*, vol. 28, no. 1, pp. 153–184, 1998.

[142] L. Dong, A. K. Agarwal, D. J. Beebe, and H. Jiang, "Adaptive liquid microlenses activated by stimuli-responsive hydrogels," *Nature*, vol. 442, no. 7102, pp. 551–554, 2006.

[143] I.-B. Sohn, H.-K. Choi, Y.-C. Noh, J. Kim, and M. S. Ahsan, "Laser assisted fabrication of micro-lens array and characterization of their beam shaping property," *Applied Surface Science*, vol. 479, pp. 375–385, 2019.

[144] Y. Chen *et al.*, "Microlens array induced light absorption enhancement in polymer solar cells," *Physical chemistry chemical physics*, vol. 15, no. 12, pp. 4297–4302, 2013.

[145] W. Wang and L. Qi, "Light management with patterned micro-and nanostructure arrays for photocatalysis, photovoltaics, and optoelectronic and optical devices," *Advanced Functional Materials*, vol. 29, no. 25, p. 1 807 275, 2019.

[146] P. Kumar, A. Khanna, S.-Y. Son, J. S. Lee, and R. K. Singh, "Analysis of light out-coupling from microlens array," *Optics Communications*, vol. 284, no. 19, pp. 4279–4282, 2011.

[147] A. Salehi, X. Fu, D.-H. Shin, and F. So, "Recent advances in oled optical design," *Advanced Functional Materials*, vol. 29, no. 15, p. 1 808 803, 2019.

[148] K. K. Chenab, B. Sohrabi, A. Jafari, and S. Ramakrishna, "Water treatment: Functional nanomaterials and applications from adsorption to photodegradation," *Materials Today Chemistry*, vol. 16, p. 100 262, 2020.

[149] Z. Dong, L. Zhang, J. Gong, and Q. Zhao, "Covalent organic framework nanorods bearing single cu sites for efficient photocatalysis," *Chemical Engineering Journal*, vol. 403, p. 126 383, 2021.

[150] H. Choi, Z. Wei, J. B. You, H. Yang, and X. Zhang, "Effects of chemical and geometric microstructures on the crystallization of surface droplets during solvent exchange," *Langmuir*, 2021.

[151] A. Zhang and Y. Fang, "Influence of adsorption orientation of methyl orange on silver colloids by raman and fluorescence spectroscopy: Ph effect," *Chemical physics*, vol. 331, no. 1, pp. 55–60, 2006.

[152] K. Dai, H. Chen, T. Peng, D. Ke, and H. Yi, "Photocatalytic degradation of methyl orange in aqueous suspension of mesoporous titania nanoparticles," *Chemosphere*, vol. 69, no. 9, pp. 1361–1367, 2007.

[153] Y. He, F. Grieser, and M. Ashokkumar, "The mechanism of sonophotocatalytic degradation of methyl orange and its products in aqueous solutions," *Ultrasonics sonochemistry*, vol. 18, no. 5, pp. 974–980, 2011.

[154] X.-Z. Niu, E. G. Moore, and J.-P. Croué, "Excited triplet state interactions of fluoroquinolone norfloxacin with natural organic matter: A laser spectroscopy study," *Environmental science & technology*, vol. 52, no. 18, pp. 10 426–10 432, 2018.

[155] H. Xue, M. Li, B. Liu, and Q. Meng, "Photochemical degradation kinetics and mechanisms of norfloxacin and oxytetracycline," *Environmental Science and Pollution Research*, vol. 28, no. 7, pp. 8258–8265, 2021.

[156] V. L. Dos Louros, C. P. Silva, H. Nadais, M. Otero, V. I. Esteves, and D. L. Lima, "Photodegradation of sulfadiazine in different aquatic environments–evaluation of influencing factors," *Environmental Research*, vol. 188, p. 109 730, 2020.

[157] M. W. Lam and S. A. Mabury, "Photodegradation of the pharmaceuticals atorvastatin, carbamazepine, levofloxacin, and sulfamethoxazole in natural waters," *Aquatic Sciences*, vol. 67, no. 2, pp. 177–188, 2005.

[158] F. Bonvin *et al.*, "Direct photolysis of human metabolites of the antibiotic sulfamethoxazole: Evidence for abiotic back-transformation," *Environmental science & technology*, vol. 47, no. 13, pp. 6746–6755, 2013.

[159] S. Peng, D. Lohse, and X. Zhang, "Microwetting of supported graphene on hydrophobic surfaces revealed by polymerized interfacial femtodroplets," *Langmuir*, vol. 30, no. 33, pp. 10 043–10 049, 2014.

[160] L. Lei, J. Li, H. Yu, L. Bao, S. Peng, and X. Zhang, "Formation, growth and applications of femtoliter droplets on a microlens," *Physical Chemistry Chemical Physics*, vol. 20, no. 6, pp. 4226–4237, 2018.

[161] J. Oakes and P. Gratton, "Kinetic investigations of the oxidation of methyl orange and substituted arylazonaphthol dyes by peracids in aqueous solution," *Journal of the Chemical Society, Perkin Transactions 2*, no. 12, pp. 2563–2568, 1998.

[162] K. M. Reza, A. Kurny, and F. Gulshan, "Parameters affecting the photocatalytic degradation of dyes using tio 2: A review," *Applied Water Science*, vol. 7, no. 4, pp. 1569–1578, 2017.

[163] T. Tasaki *et al.*, "Degradation of methyl orange using short-wavelength uv irradiation with oxygen microbubbles," *Journal of hazardous materials*, vol. 162, no. 2-3, pp. 1103–1110, 2009.

[164] D. Ren, B. Huang, T. Bi, D. Xiong, and X. Pan, "Effects of ph and dissolved oxygen on the photodegradation of 17α-ethynylestradiol in dissolved humic acid solution," *Environmental Science: Processes & Impacts*, vol. 18, no. 1, pp. 78–86, 2016.

[165] R. G. Zepp and D. M. Cline, "Rates of direct photolysis in aquatic environment," *Environmental Science & Technology*, vol. 11, no. 4, pp. 359–366, 1977.

[166] M. Persico and G. Granucci, *Photochemistry: A modern theoretical perspective.* Springer, 2018.

[167] Y. Hou, C. Chen, K. Liu, Y. Tu, L. Zhang, and Y. Li, "Preparation of pva hydrogel with high-transparence and investigations of its transparent mechanism," *RSC Advances*, vol. 5, no. 31, pp. 24 023–24 030, 2015.

[168] X.-J. Zha *et al.*, "Nanofibrillar poly (vinyl alcohol) ionic organohydrogels for smart contact lens and human-interactive sensing," *ACS applied materials & interfaces*, vol. 12, no. 20, pp. 23 514–23 522, 2020.

[169] A. Halperin, M. Kröger, and F. M. Winnik, "Poly (n-isopropylacrylamide) phase diagrams: Fifty years of research," *Angewandte Chemie International Edition*, vol. 54, no. 51, pp. 15 342–15 367, 2015.

[170] K. Kratz, T. Hellweg, and W. Eimer, "Structural changes in pnipam microgel particles as seen by sans, dls, and em techniques," *Polymer*, vol. 42, no. 15, pp. 6631–6639, 2001.

[171] R. Li *et al.*, "Facile control over the supramolecular ordering of self-assembled peptide scaffolds by simultaneous assembly with a polysacharride," *Scientific reports*, vol. 7, no. 1, pp. 1–8, 2017.

[172] R. Melikov *et al.*, "Silk-hydrogel lenses for light-emitting diodes," *Scientific Reports*, vol. 7, no. 1, pp. 1–8, 2017.

[173] S. Rehman, R. Ullah, A. Butt, and N. Gohar, "Strategies of making tio2 and zno visible light active," *Journal of hazardous materials*, vol. 170, no. 2-3, pp. 560–569, 2009.

[174] K. Davis, R. Yarbrough, M. Froeschle, J. White, and H. Rathnayake, "Band gap engineered zinc oxide nanostructures via a sol–gel synthesis of solvent driven shape-controlled crystal growth," *RSC advances*, vol. 9, no. 26, pp. 14 638–14 648, 2019.

[175] Y. Tang, H. Zhou, K. Zhang, J. Ding, T. Fan, and D. Zhang, "Visible-light-active zno via oxygen vacancy manipulation for efficient formaldehyde photodegradation," *Chemical Engineering Journal*, vol. 262, pp. 260–267, 2015.

[176] C. Dette *et al.*, "Tio2 anatase with a bandgap in the visible region," *Nano letters*, vol. 14, no. 11, pp. 6533–6538, 2014.

[177] S. Hotchandani and P. V. Kamat, "Photoelectrochemistry of semiconductor zno particulate films," *Journal of the Electrochemical Society*, vol. 139, no. 6, p. 1630, 1992.

[178] X. Li *et al.*, "Ga doped zno photonic crystals with enhanced photocatalytic activity and its reaction mechanism," *Applied Catalysis B: Environmental*, vol. 195, pp. 29–38, 2016.

[179] S. P. Pitre, T. P. Yoon, and J. C. Scaiano, "Titanium dioxide visible light photocatalysis: Surface association enables photocatalysis with visible light irradiation," *Chemical Communications*, vol. 53, no. 31, pp. 4335–4338, 2017.

[180] J. Seo and L. P. Lee, "Disposable integrated microfluidics with self-aligned planar microlenses," *Sensors and actuators B: Chemical*, vol. 99, no. 2-3, pp. 615–622, 2004.

[181] X. Wu, C. Fang, W. Xu, and D. Zhang, "Bioinspired compound eyes for diffused light-harvesting application," *ACS Applied Materials & Interfaces*, 2022.

[182] X. Luo, Y. Zhan, Y. Huang, L. Yang, X. Tu, and S. Luo, "Removal of water-soluble acid dyes from water environment using a novel magnetic molecularly imprinted polymer," *Journal of hazardous materials*, vol. 187, no. 1-3, pp. 274–282, 2011.

[183] S. Ren *et al.*, "Development of a fast and ultrasensitive black phosphorus-based colorimetric/photothermal dual-readout immunochromatography for determination of norfloxacin in tap water and river water," *Journal of Hazardous Materials*, vol. 402, p. 123 781, 2021.

[184] S. Bahnmüller, U. von Gunten, and S. Canonica, "Sunlight-induced transformation of sulfadiazine and sulfamethoxazole in surface waters and wastewater effluents," *Water research*, vol. 57, pp. 183–192, 2014.

[185] X. H. Zhang and W. Ducker, "Formation of interfacial nanodroplets through changes in solvent quality," *Langmuir*, vol. 23, no. 25, pp. 12 478–12 480, 2007.

[186] G. Tian, H. Fu, L. Jing, and C. Tian, "Synthesis and photocatalytic activity of stable nanocrystalline tio2 with high crystallinity and large surface area," *Journal of Hazardous Materials*, vol. 161, no. 2-3, pp. 1122–1130, 2009.

[187] W. Chen, Q. Liu, S. Tian, and X. Zhao, "Exposed facet dependent stability of zno micro/nano crystals as a photocatalyst," *Applied Surface Science*, vol. 470, pp. 807–816, 2019.

[188] P. Makuła, M. Pacia, and W. Macyk, *How to correctly determine the band gap energy of modified semiconductor photocatalysts based on uv–vis spectra*, 2018.

[189] L. Saikia, D. Bhuyan, M. Saikia, B. Malakar, D. K. Dutta, and P. Sengupta, "Photocatalytic performance of zno nanomaterials for self sensitized degradation of malachite green dye under solar light," *Applied Catalysis A: General*, vol. 490, pp. 42–49, 2015.

[190] S. Ahluwalia, N. T. Prakash, R. Prakash, and B. Pal, "Improved degradation of methyl orange dye using bio-co-catalyst se nanoparticles impregnated zns photocatalyst under uv irradiation," *Chemical Engineering Journal*, vol. 306, pp. 1041–1048, 2016.

[191] A. Lipovsky, Z. Tzitrinovich, H. Friedmann, G. Applerot, A. Gedanken, and R. Lubart, "Epr study of visible light-induced ros generation by nanoparticles of zno," *The Journal of Physical Chemistry C*, vol. 113, no. 36, pp. 15 997–16 001, 2009.

[192] X. Li, P. Zhang, L. Jin, T. Shao, Z. Li, and J. Cao, "Efficient photocatalytic decomposition of perfluorooctanoic acid by indium oxide and its mechanism," *Environmental science & technology*, vol. 46, no. 10, pp. 5528–5534, 2012.

[193] C. S. Turchi and D. F. Ollis, "Photocatalytic degradation of organic water contaminants: Mechanisms involving hydroxyl radical attack," *Journal of catalysis*, vol. 122, no. 1, pp. 178–192, 1990.

[194] S. Ahmed, M. Rasul, R. Brown, and M. Hashib, “Influence of parameters on the heterogeneous photocatalytic degradation of pesticides and phenolic contaminants in wastewater: A short review,” *Journal of environmental management*, vol. 92, no. 3, pp. 311–330, 2011.

[195] A. Rafiq *et al.*, “Photocatalytic degradation of dyes using semiconductor photocatalysts to clean industrial water pollution,” *Journal of Industrial and Engineering Chemistry*, vol. 97, pp. 111–128, 2021.

[196] Z. Wang, W. Ma, C. Chen, H. Ji, and J. Zhao, “Probing paramagnetic species in titania-based heterogeneous photocatalysis by electron spin resonance (esr) spectroscopy—a mini review,” *Chemical Engineering Journal*, vol. 170, no. 2-3, pp. 353–362, 2011.

[197] Y. Kim, H. M. Hwang, L. Wang, I. Kim, Y. Yoon, and H. Lee, “Solar-light photocatalytic disinfection using crystalline/amorphous low energy bandgap reduced tio2,” *Scientific reports*, vol. 6, no. 1, pp. 1–10, 2016.

[198] K Vinodgopal, D. E. Wynkoop, and P. V. Kamat, “Environmental photochemistry on semiconductor surfaces: Photosensitized degradation of a textile azo dye, acid orange 7, on tio2 particles using visible light,” *Environmental Science & Technology*, vol. 30, no. 5, pp. 1660–1666, 1996.

[199] X. Yan, T. Ohno, K. Nishijima, R. Abe, and B. Ohtani, “Is methylene blue an appropriate substrate for a photocatalytic activity test? a study with visible-light responsive titania,” *Chemical Physics Letters*, vol. 429, no. 4-6, pp. 606–610, 2006.

[200] M. Martín-Sómer, C. Pablos, R. van Grieken, and J. Marugán, “Influence of light distribution on the performance of photocatalytic reactors: Led vs mercury lamps,” *Applied Catalysis B: Environmental*, vol. 215, pp. 1–7, 2017.

[201] S. Selvaraj *et al.*, “Effect of sr doping in zno microspheres for solar light-driven photodegradation of organic pollutants,” *Journal of Materials Science: Materials in Electronics*, vol. 33, no. 11, pp. 8777–8788, 2022.

[202] N. P. Xekoukoulotakis *et al.*, “Kinetics of uv-a/tio2 photocatalytic degradation and mineralization of the antibiotic sulfamethoxazole in aqueous matrices,” *Catalysis Today*, vol. 161, no. 1, pp. 163–168, 2011.

[203] S. Malato, J. Blanco, D. C. Alarcón, M. I. Maldonado, P. Fernandez-Ibanez, and W. Gernjak, “Photocatalytic decontamination and disinfection of water with solar collectors,” *Catalysis Today*, vol. 122, no. 1-2, pp. 137–149, 2007.

[204] H. Wu *et al.*, “Photocatalytic and photoelectrochemical systems: Similarities and differences,” *Advanced Materials*, vol. 32, no. 18, p. 1 904 717, 2020.

[205] B. E. Cowie, V. Porley, and N. Robertson, “Solar disinfection (sodis) provides a much underexploited opportunity for researchers in photocatalytic water treatment (pwt),” *ACS Catalysis*, vol. 10, no. 20, pp. 11 779–11 782, 2020.

[206] Y. Zhang, M. Sivakumar, S. Yang, K. Enever, and M. Ramezanianpour, "Application of solar energy in water treatment processes: A review," *Desalination*, vol. 428, pp. 116–145, 2018.

[207] C. K. Pooi and H. Y. Ng, "Review of low-cost point-of-use water treatment systems for developing communities," *NPJ Clean Water*, vol. 1, no. 1, pp. 1–8, 2018.

[208] B. J. M. Chaúque and M. B. Rott, "Solar disinfection (sodis) technologies as alternative for large-scale public drinking water supply: Advances and challenges," *Chemosphere*, vol. 281, p. 130 754, 2021.

[209] A. Alkhalidi, S. Arabasi, A. A. Othman, T. Sabanikh, L. Mahmood, and Q. Abdelal, "Using wood's glass to enhance the efficiency of a water solar disinfection (sodis) apparatus with a fresnel lens," *International Journal of Low-Carbon Technologies*, vol. 16, no. 2, pp. 628–634, 2021.

[210] H. A. Kumar *et al.*, "Recent advancements, technologies, and developments in inclined solar still—a comprehensive review," *Environmental Science and Pollution Research*, vol. 28, no. 27, pp. 35 346–35 375, 2021.

[211] W. Fuqiang, C. Ziming, T. Jianyu, Y. Yuan, S. Yong, and L. Linhua, "Progress in concentrated solar power technology with parabolic trough collector system: A comprehensive review," *Renewable and Sustainable Energy Reviews*, vol. 79, pp. 1314–1328, 2017.

[212] E. Isarain-Chávez *et al.*, "Degradation of pharmaceutical beta-blockers by electrochemical advanced oxidation processes using a flow plant with a solar compound parabolic collector," *Water research*, vol. 45, no. 14, pp. 4119–4130, 2011.

[213] Q. Zheng *et al.*, "3d printed photoreactor with immobilized graphitic carbon nitride: A sustainable platform for solar water purification," *Journal of Hazardous Materials*, vol. 399, p. 123 097, 2020.

[214] S. Thiele, K. Arzenbacher, T. Gissibl, H. Giessen, and A. M. Herkommer, "3d-printed eagle eye: Compound microlens system for foveated imaging," *Science advances*, vol. 3, no. 2, e1602655, 2017.

[215] H. Zhang *et al.*, "3d printing of a pdms cylindrical microlens array with 100% fill-factor," *ACS Applied Materials & Interfaces*, vol. 13, no. 30, pp. 36 295–36 306, 2021.

[216] H. Yang, S. Peng, X. Hao, T. A. Smith, G. G. Qiao, and X. Zhang, "Surfactant-mediated formation of polymeric microlenses from interfacial microdroplets," *Soft Matter*, vol. 10, no. 7, pp. 957–964, 2014.

[217] H. Yu, Z. Lu, D. Lohse, and X. Zhang, "Gravitational effect on the formation of surface nanodroplets," *Langmuir*, vol. 31, no. 46, pp. 12 628–12 634, 2015.

[218] Z. Lu, H. Xu, H. Zeng, and X. Zhang, "Solvent effects on the formation of surface nanodroplets by solvent exchange," *Langmuir*, vol. 31, no. 44, pp. 12 120–12 125, 2015.

[219] S. Peng, D. Lohse, and X. Zhang, "Spontaneous pattern formation of surface nanodroplets from competitive growth," *ACS nano*, vol. 9, no. 12, pp. 11 916–11 923, 2015.

[220] Z. Lu, M. H. K. Schaarsberg, X. Zhu, L. Y. Yeo, D. Lohse, and X. Zhang, "Universal nanodroplet branches from confining the ouzo effect," *Proceedings of the National Academy of Sciences*, vol. 114, no. 39, pp. 10 332–10 337, 2017.

[221] M. Li, L. Bao, H. Yu, and X. Zhang, "Formation of multicomponent surface nanodroplets by solvent exchange," *The Journal of Physical Chemistry C*, vol. 122, no. 15, pp. 8647–8654, 2018.

[222] L. Bao *et al.*, "Flow-induced dissolution of femtoliter surface droplet arrays," *Lab on a Chip*, vol. 18, no. 7, pp. 1066–1074, 2018.

[223] E. Dietrich, E. S. Kooij, X. Zhang, H. J. Zandvliet, and D. Lohse, "Stick-jump mode in surface droplet dissolution," *Langmuir*, vol. 31, no. 16, pp. 4696–4703, 2015.

[224] D. F. Swinehart, "The beer-lambert law," *Journal of chemical education*, vol. 39, no. 7, p. 333, 1962.

[225] R. Sabouni and H. Gomaa, "Photocatalytic degradation of pharmaceutical micro-pollutants using zno," *Environmental Science and Pollution Research*, vol. 26, pp. 5372–5380, 2019.

[226] T. T. Guaraldo, R. Vakili, J. Wenk, and D. Mattia, "Highly efficient zno photocatalytic foam reactors for micropollutant degradation," *Chemical Engineering Journal*, vol. 455, p. 140 784, 2023.

[227] I. Ani, U. Akpan, M. Olutoye, and B. Hameed, "Photocatalytic degradation of pollutants in petroleum refinery wastewater by tio2-and zno-based photocatalysts: Recent development," *Journal of cleaner production*, vol. 205, pp. 930–954, 2018.

[228] S. Lotfi, K. Fischer, A. Schulze, and A. I. Schäfer, "Photocatalytic degradation of steroid hormone micropollutants by tio2-coated polyethersulfone membranes in a continuous flow-through process," *Nature Nanotechnology*, vol. 17, no. 4, pp. 417–423, 2022.

[229] H. B. Truong, B. T. Huy, S. K. Ray, Y.-I. Lee, J. Cho, and J. Hur, "Visible light-activated ngqd/nsc3n4/bi2wo6 microsphere composite for effluent organic matter treatment," *Chemical Engineering Journal*, vol. 415, p. 129 024, 2021.

[230] L. Meng, Z. T. How, P. Chelme-Ayala, C. Benally, and M. G. El-Din, "Z-scheme plasmonic ag decorated bi2wo6/nio hybrids for enhanced photocatalytic treatment of naphthenic acids in real oil sands process water under simulated solar irradiation," *Journal of Hazardous Materials*, vol. 454, p. 131 441, 2023.

[231] N Madima, S. Mishra, I Inamuddin, and A. Mishra, "Carbon-based nanomaterials for remediation of organic and inorganic pollutants from wastewater. a review," *Environmental Chemistry Letters*, vol. 18, pp. 1169–1191, 2020.

[232] D. Liu *et al.*, "Recent advances in mof-derived carbon-based nanomaterials for environmental applications in adsorption and catalytic degradation," *Chemical Engineering Journal*, vol. 427, p. 131 503, 2022.

[233] J. Fito, K. K. Kefeni, and T. T. Nkambule, "The potential of biochar-photocatalytic nanocomposites for removal of organic micropollutants from wastewater," *Science of the Total Environment*, vol. 829, p. 154 648, 2022.

[234] X. Duan, C. Zhang, S. Wang, N.-q. Ren, S.-H. Ho, *et al.*, "Graphitic biochar catalysts from anaerobic digestion sludge for nonradical degradation of micropollutants and disinfection," *Chemical Engineering Journal*, vol. 384, p. 123 244, 2020.

[235] K Kowalska, M Roccamante, A. C. Reina, P Plaza-Bolanos, I Oller, and S Malato, "Pilot-scale removal of microcontaminants by solar-driven photofenton in treated municipal effluents: Selection of operating variables based on lab-scale experiments," *Journal of Environmental Chemical Engineering*, vol. 9, no. 1, p. 104 788, 2021.

[236] R Stevens and T Miyashita, "Review of standards for microlenses and microlens arrays," *The Imaging Science Journal*, vol. 58, no. 4, pp. 202–212, 2010.

[237] Y. Wei *et al.*, "Fabrication of high integrated microlens arrays on a glass substrate for 3d micro-optical systems," *Applied Surface Science*, vol. 457, pp. 1202–1207, 2018.

[238] M. Lee *et al.*, "An amphibious artificial vision system with a panoramic visual field," *Nature Electronics*, vol. 5, no. 7, pp. 452–459, 2022.

[239] W. Jiang *et al.*, "Tunable liquid microlens arrays actuated by infrared light-responsive graphene microsheets," *Journal of Micromechanics and Microengineering*, vol. 27, no. 8, p. 085 006, 2017.

[240] Y. Ma *et al.*, "Skin-like electronics for perception and interaction: Materials, structural designs, and applications," *Advanced Intelligent Systems*, vol. 3, no. 4, p. 2 000 108, 2021.

[241] Y. Qu, J. Kim, C. Coburn, and S. R. Forrest, "Efficient, nonintrusive outcoupling in organic light emitting devices using embedded microlens arrays," *ACS photonics*, vol. 5, no. 6, pp. 2453–2458, 2018.

[242] A. C. Vinayaka, T. A. Ngo, T. Nguyen, D. D. Bang, and A. Wolff, "Pathogen concentration combined solid-phase pcr on supercritical angle fluorescence microlens array for multiplexed detection of invasive nontyphoidal salmonella serovars," *Analytical chemistry*, vol. 92, no. 3, pp. 2706–2713, 2020.

[243] B.-H. Kang *et al.*, "Ultrafast plasmonic nucleic acid amplification and real-time quantification for decentralized molecular diagnostics," *ACS nano*, 2023.

[244] Y. Ding *et al.*, "High-throughput and controllable fabrication of soft screen protectors with microlens arrays for light enhancement of oled displays," *Advanced Materials Technologies*, vol. 5, no. 10, p. 2 000 382, 2020.

[245] Y. Long *et al.*, "Fabrication of uniform-aperture multi-focus microlens array by curving microfluid in the microholes with inclined walls," *Optics Express*, vol. 29, no. 8, pp. 12 763–12 771, 2021.

[246] G. Lv *et al.*, "Facile fabrication of flexible concave microlens arrays with a well-controlled curvature," *Materials Chemistry Frontiers*, vol. 5, no. 21, pp. 7759–7766, 2021.

[247] J. Mo, X. Chang, D. Renqing, J. Zhang, L. Liao, and S. Luo, "Design, fabrication, and performance evaluation of a concave lens array on an aspheric curved surface," *Optics Express*, vol. 30, no. 18, pp. 33 241–33 258, 2022.

[248] X.-Q. Liu *et al.*, "Optical nanofabrication of concave microlens arrays," *Laser & Photonics Reviews*, vol. 13, no. 5, p. 1 800 272, 2019.

[249] Y. Peng *et al.*, "Fabrication of microlens arrays with controlled curvature by micromolding water condensing based porous films for deep ultraviolet leds," *ACS Photonics*, vol. 4, no. 10, pp. 2479–2485, 2017.

[250] D. Zhang *et al.*, "Fabrication of a microlens array with controlled curvature by thermally curving photosensitive gel film beneath microholes," *ACS Applied Materials & Interfaces*, vol. 9, no. 19, pp. 16 604–16 609, 2017.

[251] X. Zhang *et al.*, "Fabrication of heteromorphic microlens arrays built in the tio 2/ormosils composite films for organic light-emitting diode applications," *Applied Physics A*, vol. 127, pp. 1–12, 2021.

[252] Q. Zhang, Z. Guo, Z. Ma, S. Wang, and B. Peng, "Fabricating su-8 photoresist microstructures with controlled convexity–concavity and curvature through thermally manipulating capillary action in poly (dimethylsiloxane) microholes," *Langmuir*, 2023.

[253] D. Gonzalez-Hernandez, S. Varapnickas, A. Bertoncini, C. Liberale, and M. Malinauskas, "Micro-optics 3d printed via multi-photon laser lithography," *Advanced Optical Materials*, vol. 11, no. 1, p. 2 201 701, 2023.

[254] M. Lapointe and B. Barbeau, "Characterization of ballasted flocs in water treatment using microscopy," *Water research*, vol. 90, pp. 119–127, 2016.

[255] Y. Murai and M. Yoshikawa, "Polymeric pseudo-liquid membranes from poly (dodecyl methacrylate): Kcl transport and optical resolution," *Polymer journal*, vol. 45, no. 10, pp. 1058–1063, 2013.

[256] A. Kumbhar, S. Narasimhan, and P. Mathur, "Spectrophotometric method for determination parts per million levels of cyclohexylamine in water," *Talanta*, vol. 47, no. 2, pp. 421–437, 1998.

[257] J. A. Cotruvo and M. D. Sobsey, "Point-of-use water treatment for home and travel," *Water Health*, vol. 2, p. 103, 2009.

Appendix A: Supplementary information for Chapter 3

Supplementary Information_Ch3

Surface microlenses for much more efficient photodegradation in water treatment

Electron spin resonance (ESR) detection

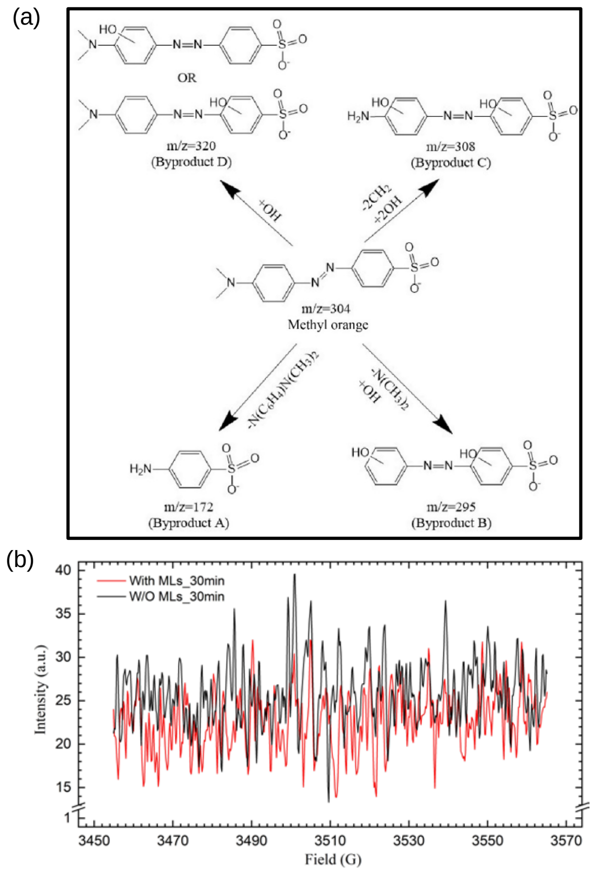

Figure S1. (a) The possible cleavage position (m/z is the mass-to-charge ratio of certain species. Byproduct A: m/z=172.0059, byproduct B: m/z=294.9452, byproduct C: m/z=308.0758, byproduct D: m/z=320.0653) in a MO molecule in the photodegradation. (b) The electron spin resonance spectrum of methyl orange (MO) solution after the light treatment without MLs and with MLs for 30 min, using 50 mM DMPO as the spin trap.

The electron spin resonance (ESR) technology is utilized to verify if free radicals play an important role in the photodegradation process. The ESR spectrum of samples that are irradiated for 30 min in presence of a spin trap is displayed in Figure S1 (b). There are no characteristic signals of free radicals, such as hydroxyl radicals and superoxide radicals, detected in samples after light treatment no matter surface MLs are used or not. The ESR spectrum indicates that the above-mentioned free radicals do not participate in the photodegradation in the first 30 min of photodegradation. The results also prove that the use of surface MLs does not cause the formation of free radicals.

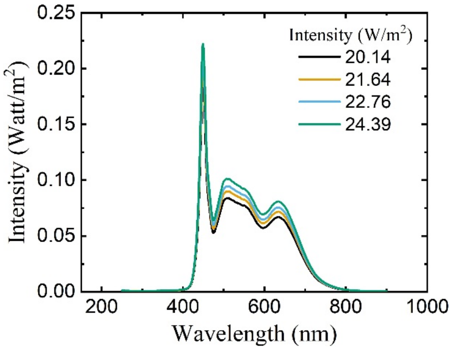

Figure S2. Light spectrum of the light resource (wavelength: 300-900 nm) with different intensities (20.12, 21.64, 22.76, and 24.39 W/m^2).

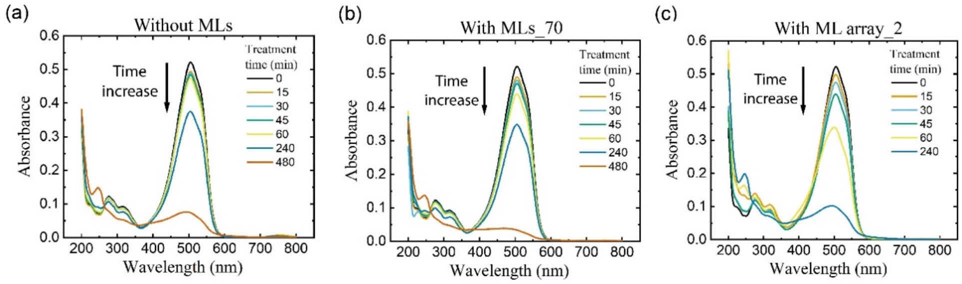

Figure S3. The UV-vis absorbance curves of MO solution after irradiation (a) without MLs, (b) with MLs_70, and (c) with ML array_2 as the light treatment time increased. The concentration of MO solution was 5 mg/L, with pH=3.0. The MO solution was degassed for 15 min before light treatment, and the light intensity was 21.64 W/m^2.

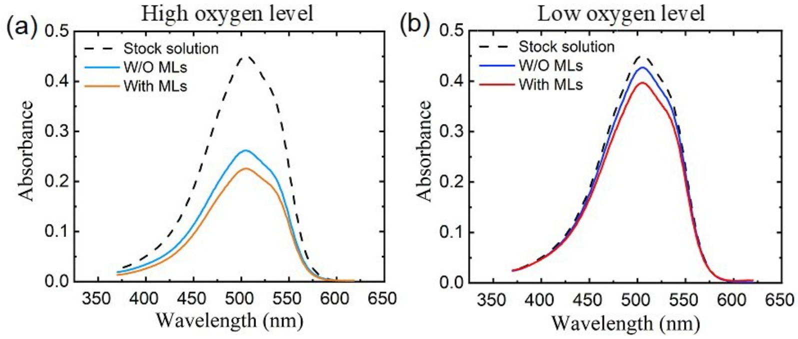

Figure S4. Absorbance curves of MO solution at (a) high oxygen level (no degassing step before treatment) and (b) low oxygen level (degassing for 15 min before light treatment). The MO solution (initial MO concentration: 5 mg/L, pH value: 3.0) was irradiated for 1 hour. The black dashed lines represent the solution before treatment, while the colorful solid lines show the solution after treatment without (W/O) and with MLs.

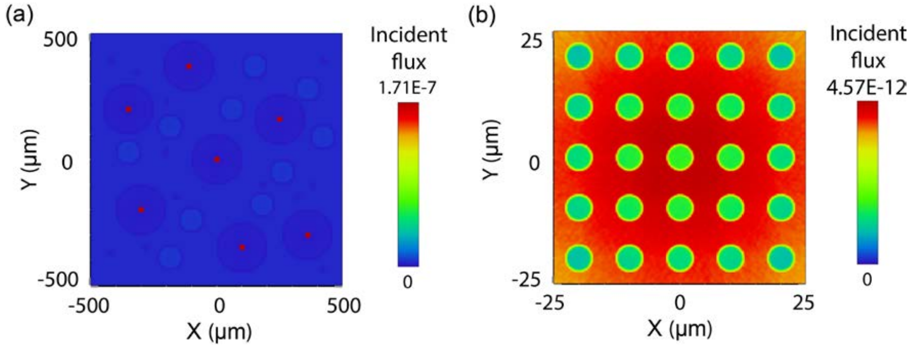

Figure S5. Top-view intensity profiles of (a) random MLs on homogeneous hydrophobic substrate and (b) ML array at the depth of 224 μm.

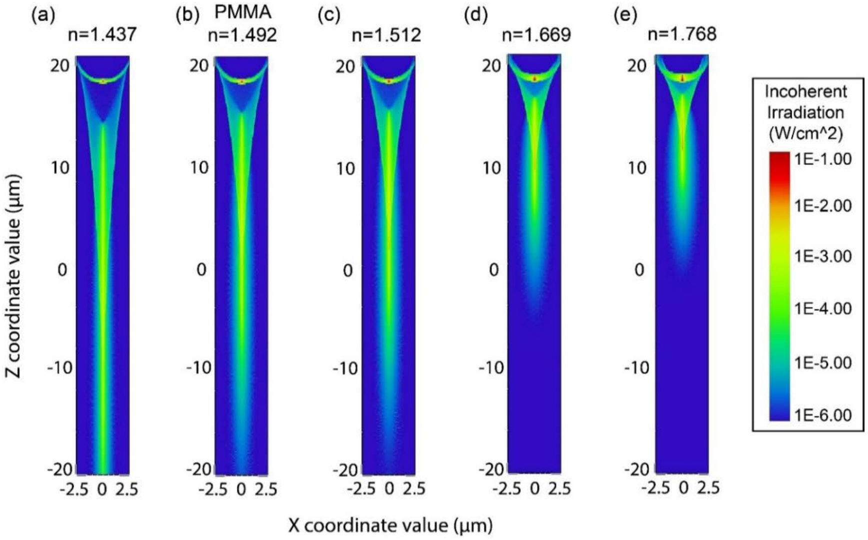

Figure S6. Cross-sectional intensity profile of a single ML with refractive index (n) equal to (a) 1.437, (b) 1.492 (PMMA MLs used in this work), (c) 1.512, (d) 1.669, and (e) 1,768 on a prepatterned substrate with diameter of 5 μm and contact angle of 73°.

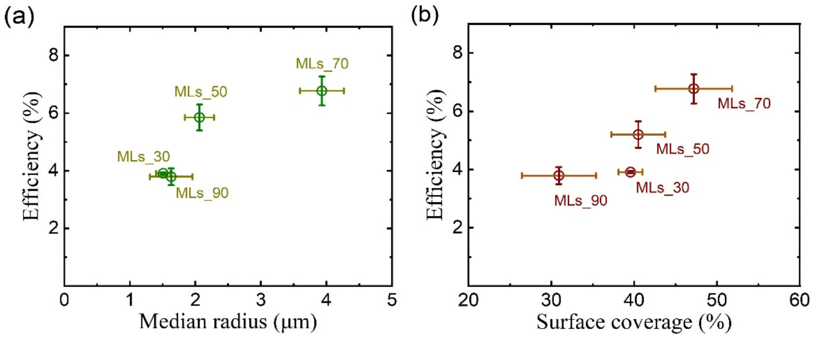

Figure S7. The photodegradation efficiency of MO solution after irradiation of 30 min with (a) surface coverage and (b) median lateral radius of random MLs.

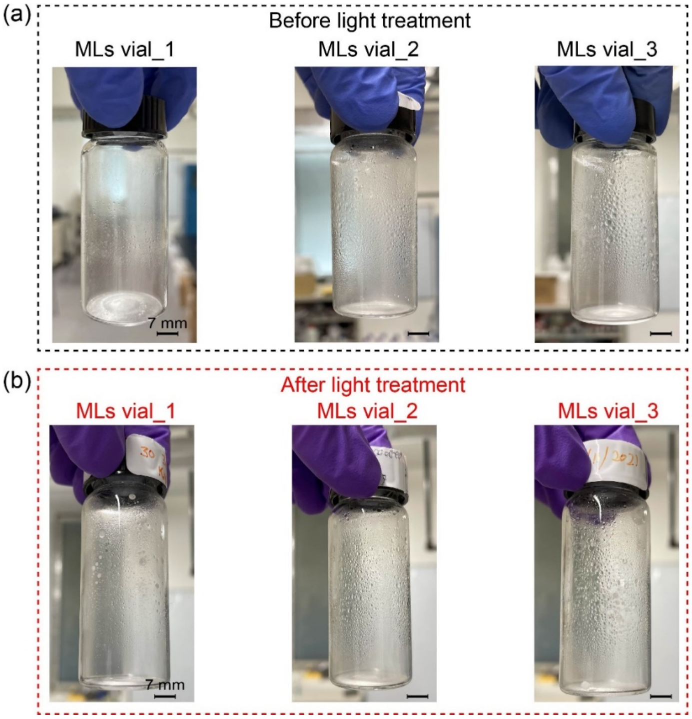

Figure S8. Photos of the glass bottles functionalized by MLs (a) before and (b) after light treatment (indoor solar light of more than 30 days and simulated solar light of more than 30 hours). The bottles are labelled as MLs vial_1, _2, and _3, corresponding to the volume of methyl methacrylate in solution A for solvent exchange equal to 3 mL, 4 mL, and 5 mL.

Appendix B: Supplementary information for Chapter 4

Supplementary Information_Ch4

Enhanced photocatalytic degradation of organic contaminants in water by highly tunable surface microlenses

1. Physicochemical properties of commercial photocatalysts

Characteristics of the commercial ZnO and TiO_2 nanoparticles. A_{BET}: BET surface area; V_{po}: pore volume; D_{po}: mean pore size.

Table S1. Physicochemical properties of photocatalysts[1]

Catalyst	A_{BET} (m^2/g)	Porosity*	V_{po} (cc/g)	D_{po} (nm)
ZnO	3.34	0.112	0.0226	27.1
TiO_2	46.8	0.644	0.465	39.8

*: *Porosity test is based on the particle densities of 5.60 g/cc and 3.90 g/cc for ZnO and TiO_2,*

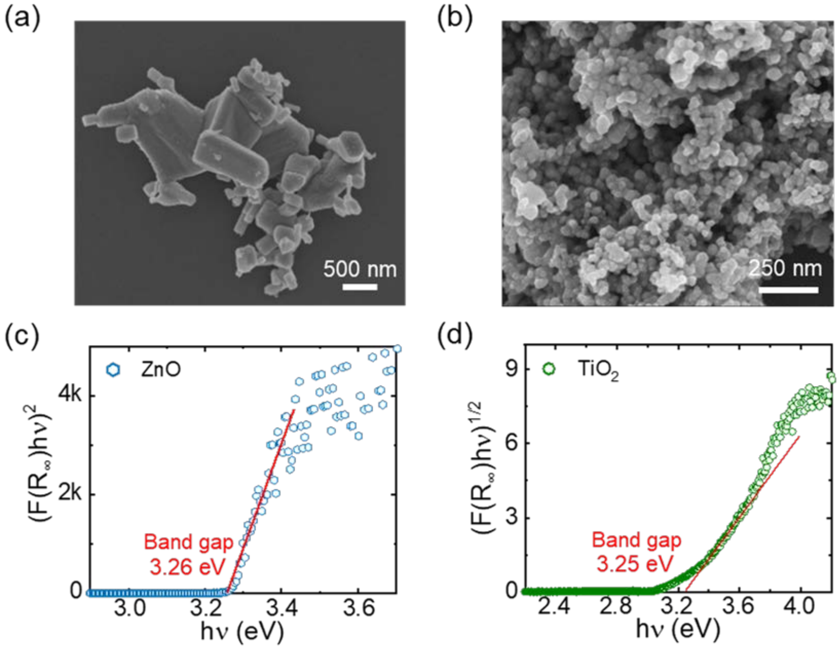

---

[1] Suara, M. A.; Ganiyu, S. O.; Paul, S.; Stafford, J. L.; El-Din, M. G. Solar-activated zinc oxide photocatalytic treatment of real oil sands process water: Effect of treatment parameters on naphthenic acids, polyaromatic hydrocarbons and acute toxicity removal. *Science of The Total Environment* **2022**, *819*, 153029

respectively. [1]

Figure S1. The morphology of (a) ZnO particles and (b) TiO_2 particles was characterized by a scanning electron microscope (SEM, Zeiss Sigma FESEM). The samples for SEM characterization were immobilized on a Si substrate and coated with Au/Pd layer by metal sputtering (Leica ACE600 Carbon/Metal coater) before SEM observation. Tauc plot of (c) ZnO and (d) TiO_2 were obtained with diffusion reflectance spectroscopy (Hitachi U-3900H).

2. Correlation between absorbance value obtained by UV-Vis spectrometer and the concentration of organic pollutants

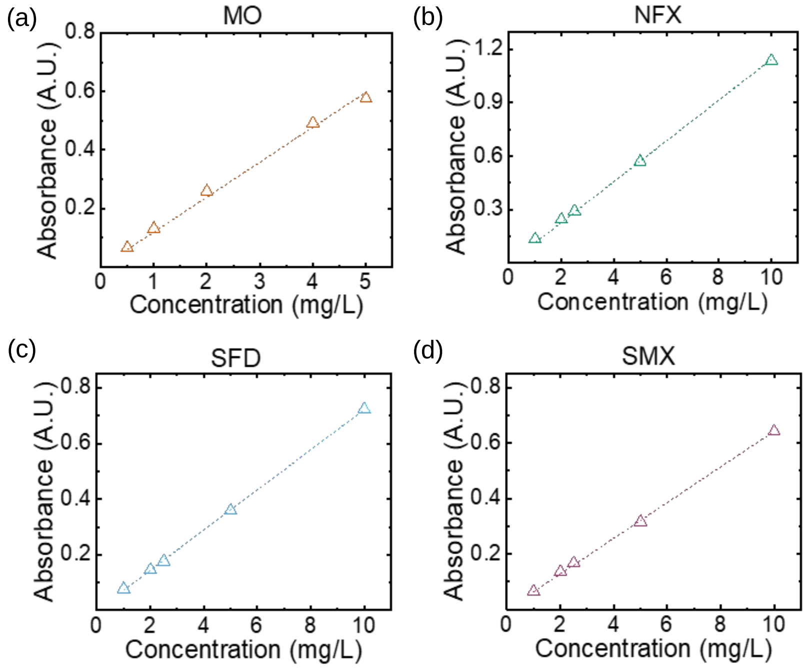

Figure S2. Absorbance values of standard aqueous solutions with varied concentration for four organic pollutants, including (a) methyl orange (MO), (b) norfloxacin (NFX), (c) sulfadiazine (SFD), and (d) sulfamethoxazole (SMX). The linear relationship between absorbance value and concentration proved that the concentration range of organic pollutants involved in this work obeyed the Beer-Lambert Law.

3. Measurement of the concentration of sulfamethoxazole (SMX) in synthetic river water with an ultra-performance liquid chromatography

The sulfamethoxazole (SMX) in synthetic river water were measured on an ultra-performance liquid chromatography (Acquity H-class UPLC, Waters, USA) coupled to a single quadrupole mass spectrometer (SQ Detector 2, Waters, USA). The electrospray ionization (ESI) source was operated in positive ion mode and monitored the SMX at 254.06 (m/z) with a cone voltage of 22 V. Chromatographic separations were performed on an ACQUITY UPLC® BEH C18 column (1.7 µm, 2.1 × 50 mm, Waters, USA) with mobile phases of 4 mM ammonium acetate and 0.1% acetic acid in water (A), and acetonitrile (B). The elution gradient was 0-0.5 min, 5% B; 0.5-3 min, increased from 5% to 95% B; then returned to the initial condition 95% B at 3.1 min and held for 1.5min to equilibrate column with a flow rate of 0.4 mL/min. The column was controlled at 40 ˚C, and the injection volume was 5 µL. Data was acquired using MassLynx (Waters, UAS) and data were processed using TargetLynx (Waters, UAS).

4. Electron spinning resonance (EPR) spectra of ZnO in methanol after the irradiation of simulated solar light

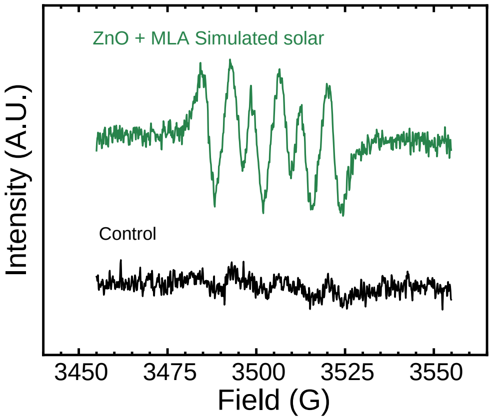

Figure S3. Electron spinning resonance (ESR) spectra in methanol after the irradiation of simulated solar light for 30 min. (The black curve is for the condition without ZnO particles and surface MLs. The green curve represents the treatment with both ZnO (10 mg/L) and MLA under a visible. DMPO with the concentration of 50 mM was added in to the system as the spinning trap.

5. UV-Vis spectra of SMX solution with ZnO in MLs-decorated vials under simulated solar light

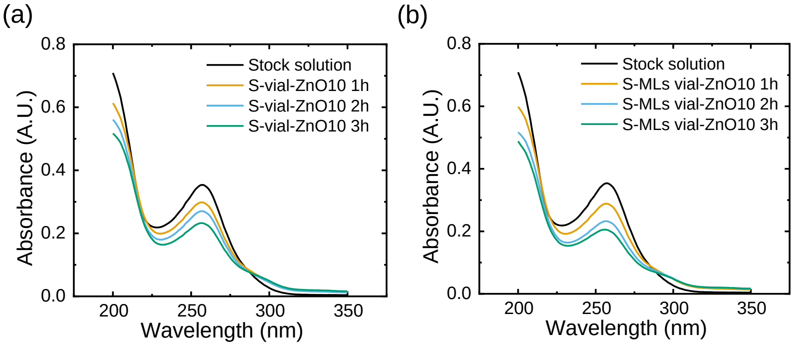

Figure S4. UV-vis spectra of SMX solution (5 mg//L, pH = 7.0) before and after the light treatment with a concentration of ZnO at 10 mg/L under simulated solar light with (a) bare glass vial and (b) a MLs vial.

6. Elongated light treatment of MO, NFX, SFD, and SMX aqueous solution under simulated solar light

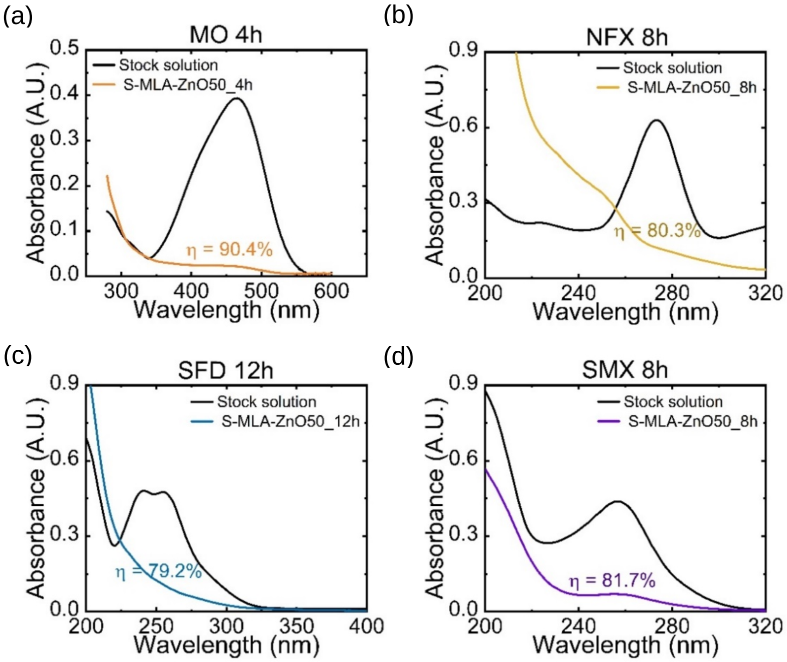

Figure S5. UV-vis spectra of MO, NFX, SFD, and SMX solution (5 mg//L, pH = 7.0) before and after the light treatment with surface MLA and a concentration of ZnO at 50 mg/L under simulated solar light (intensity: 1 Sun) after (a) 4 h for MO solution, (b) 8 h for NFX solution, (c) 12 h for SFD solution, and (d) 8 hours for SMX solution. The concentration of all contaminants in aqueous solution is 5 mg/L at pH value of 7.0. The photodegradation efficiency for each organic contaminant is labelled in the corresponding spectrum.

7. Stability of surface MLs after light treatment with photocatalysts

The surface MLs, including both random MLs and ML array, before and after all rounds of experiments were characterized by optical microscope to check their stability in the photocatalytic system.

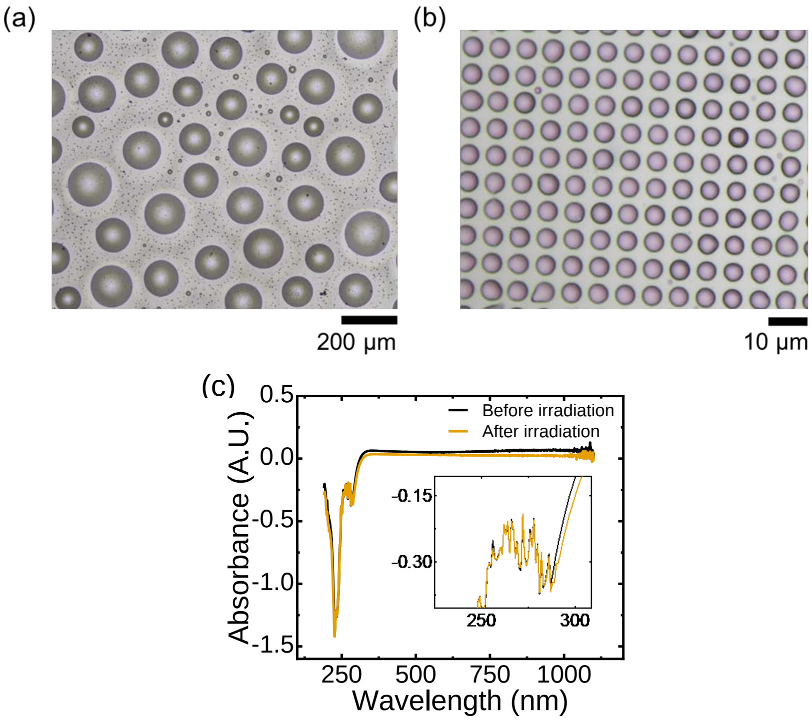

Figure S6. Images of (a) random MLs (scale bar: 200 μm) and (b) ML array (MLA) (scale bar: 10 μm) after visible light treatment of 60 h and simulated solar light of 30 h. The total irradiation time under different light sources is not continuous. (c) UV vis absorbance spectrum for the PLMA MLA immobilized on glass substrate before and after the irradiation of simulated solar light of 30 h.

Appendix C: Supplementary information for Chapter 5

Supplementary Information_Ch5

Scalable and Facile Formation of Microlenses on Curved Surface enabling a Highly Customized Sustainable Solar-Water Nexus

1. Morphology of polymethylmethacrylate (PMMA) surface MLs on PET bottle assisted with surfactant

The inner surface of a plastic bottle without surface functionalization could be utilized as the substrate of surface microdroplets and MLs in the presence of surfactant. A PET (polyethylene terephthalate) plastic bottle purchased from a grocery shop with an inner diameter of 3.2 cm, a height of 7.4 cm, and a volume of 60 mL was used in the solvent B. Instead of MMA saturated Milli Q water, solution B was the cetrimonium bromide (CTAB) aqueous solution with a concentration of 1.2 critical micelle concentration (CMC), while other procedures kept the same as for other samples. 18 mL solution A composed of 45.8 vol% Milli Q water, 45.8 vol% ethanol, 7.6 vol% MMA, and 0.8 vol\% photoinitiator was first added into the plastic bottle. Then, solution B was added to the plastic bottle with a flow rate of 7 mL/min. After the solvent dilution process, UV curing, washing, and drying steps, the plastic bottles with PMMA surface MLs functionalized were obtained for the characterization of the optical microscope.

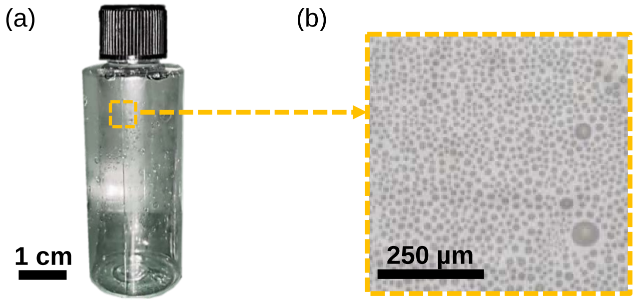

Figure S1. (a) An optical image (scale bar: 1 cm) and (b) and a zoom-in image (scale bar: 250 μm) of the MLs on the inner surface of the plastic bottle.

Surface microdroplets and microlenses can form not only on a functionalized hydrophobic substrate but also on an untreated, non-uniform plastic surface with the assistance of a surfactant. As shown in Figure S1 (a), surface MLs are successfully immobilized on the inner surface of a plastic bottle, and the bottle remains transparent after surface MLs are functionalized on the inner surface. The morphology of surface MLs on the curved plastic surface is displayed in Figure S1 (b). Surface MLs on the plastic surface present a more uniform size distribution and smaller lateral size than that on the hydrophobic curved glass surface, which is corresponding with the phenomenon observed in surface MLs on a planar substrate. [1] By using the cationic surfactant aqueous solution with a concentration of 1.2 critical micelle concentration as solution B, the untreated plastic surface will be coated with surfactant molecules by an adsorption process. Surface microdroplets are pinned onto the plastic surface before the adsorption of surfactant molecules reaches the equilibrium state, and then transformed into surface MLs locally through photopolymerization.

2. Light spectrum of the simulated solar light and indoor sunlight

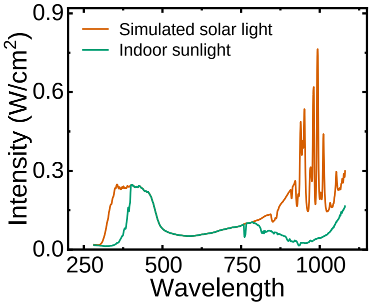

Figure S2. Light spectra of the light resource utilized in light treatment with MLs functionalized reactors, including simulated solar light and indoor sunlight (2022 May 15, Room 12-380 in DICE, Edmonton, Canada).

3. Equations for deriving the concentration of MMA (C_{MMA}) in solvent dilution process

C_{MMA} is the concentration of MMA in the reactor at the dilution time of t. The initial concentration of MMA is defined as $C_{MMA,0}$, and the initial volume of solution A is $V_{Sol\ A}$. At the time of t, the total volume of liquid is V_T. t_R is the dilution time when V_T is the same as the volume capacity of the reactors, V_R. Q is the flow rate of adding solution B into the reactor during the dilution process.

$\mathrm{C_{MMA}} = \frac{\mathrm{C_{MMA,0}} \cdot \mathrm{V_{Sol\,A}}}{\mathrm{V_T}}$ (Equation S1)

when $\mathrm{t} < \mathrm{t_R}, \mathrm{V_T} = \mathrm{V_{Sol\,A}} + Q \cdot t$ (Equation S2)

when $\mathrm{t} \geq \mathrm{t_R}, \mathrm{V_T} = \mathrm{V_R}$ (Equation S2′)

$\mathrm{t_R} = \frac{\mathrm{V}_R - \mathrm{V}_{Sol\,A}}{Q}$ (Equation S3)

$dC_{MMA} = -\frac{\mathrm{C_{MMA}} \cdot Q \cdot dt}{\mathrm{V}_R}$ (Equation S4)

4. Size distribution of surface MLs in top, middle, and bottom regions of cylindrical reactors (sample 1 to 9)

Compared with the size distribution of surface MLs fabricated in a 2D confined channel through the solvent exchange process, [2] the size distribution of surface MLs on the 3D curved surface by the solvent dilution process presents different features. First of all, the size

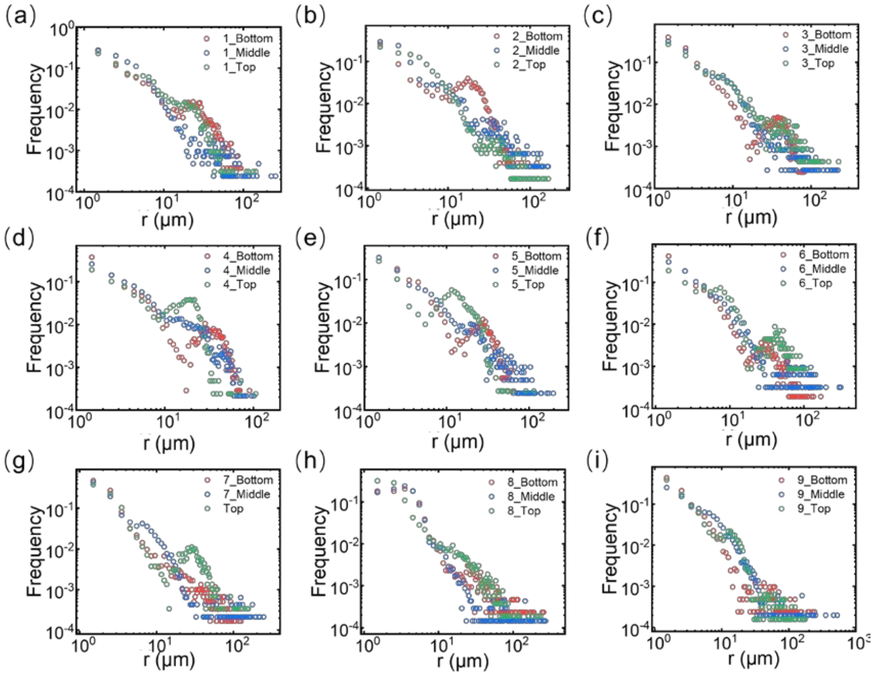

Figure S3. Size distribution curves of surface MLs located in bottom, middle, and top region in (a) sample 1, (b) sample 2, (c) sample 3, (d) sample 4, (e) sample 5, (f) sample 6, (g) sample 7, (h) sample 8 , and (i) sample 9.

distribution of MLs made with solvent dilution is broader than that in the confined channel. In the confined channel, it is supposed that the mixing of solution A and B is sufficient at the wave front. However, in the situation of solvent dilution, solution A and B are not well mixed in the region where the nucleation of surface microdroplets happens. In addition, the dilution process includes three stages where the concentration change of MMA differs. Therefore, the concentration gradient is more difficult to control in the solvent dilution process than that in a confined space, resulting in a broader size distribution. Secondly, the frequency of MLs with smaller lateral radius on the curved surface is significantly higher than those obtained in the confined 2D channel. The possible explanation is that smaller droplets are easier to pin on the curved surface. As the droplets become larger, the buoyant force becomes larger than the pinning force of oil droplets, and the droplets will easily detach from the surface.

5. The sketch of the process of solvent dilution process

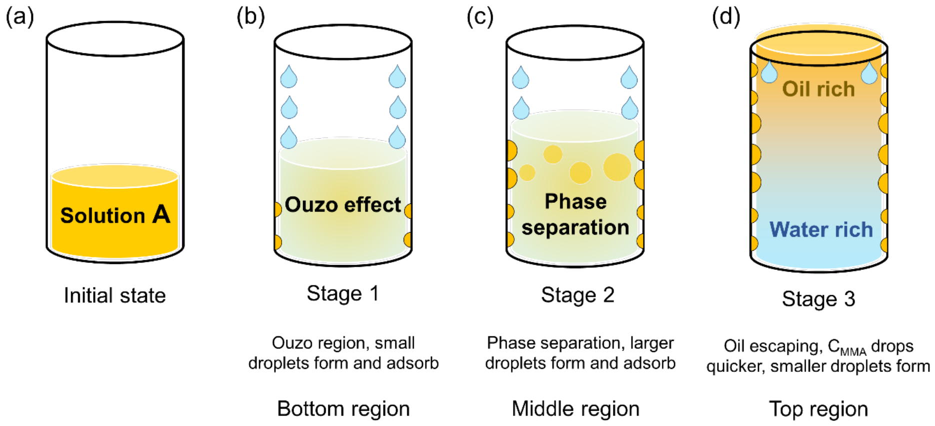

Figure S4. Sketch of surface nanodroplets formation during the solvent dilution process, including (a) the initial sate with only solution A. (b) step 1: the composition of ternary system locating in the ouzo region, (c) step 2: phase separation happening in the reactors, and (d) step 3: the oil-rich phase escaping from the reactor.

6. Overall size distribution of surface MLs in each cylindrical reactor (sample 1 to 9)

The overall size distribution of surface MLs on each glass cylindrical reactor is demonstrated in Figure S5 (a-c). The influence of the C_{MMA} on the size distribution of MLs is reflected in

Figure S5 (a), where the size distribution curves of samples prepared with varied $\mathrm{C_{MMA}}$ (sample 1, 2, and 3) are displayed. It can be observed that the peak positions in the size distribution curves vary with samples. The peak position in sample 1 is the smallest, at the radius of 8 µm. As a comparison, the positions of peaks of sample 2 and 3 are located around 29 µm and 59 µm, respectively.

The initial volume of solution A ($\mathrm{V}_{Sol\ A}$) also influences the size distribution of surface MLs on the curved surface. By comparing the size distribution curves of sample 2, 4, and 5 (Figure S5 (b)), it is observed that there is a peak in the interval where the lateral radius ranges from 10 to 80 µm in all three samples. The variation of peak positions in the size distribution of MLs caused by different $\mathrm{V}_{Sol\ A}$ is less than 10 µm, which is much smaller than that resulted from the change of $\mathrm{C_{MMA}}$. Comparing with the difference in the peak position, the deviation in the frequency of MLs with the lateral radius larger than 80 µm is more obvious among samples prepared with varied $\mathrm{V}_{Sol\ A}$. When the $\mathrm{V}_{Sol\ A}$ added to the reactor is larger before the solvent dilution process, the higher frequency of MLs with the lateral radius over 80 µm is observed on the reactor surface.

The size distribution of samples fabricated with various flow rates in the solvent dilution process is displayed in Figure S5 (c). For samples made with flow rates smaller than 8 mL/min in the solvent dilution process, the size frequency drops with the lateral radius and shows a peak between 20 µm and 200 µm. The peak in the size distribution curve of sample 6 starts from 24 µm and ends at 117 µm, with a width of 93 µm. The peak width in the sample made with the lowest flow rate (sample 7) is only 66 µm, which is the narrowest peak. Therefore, the

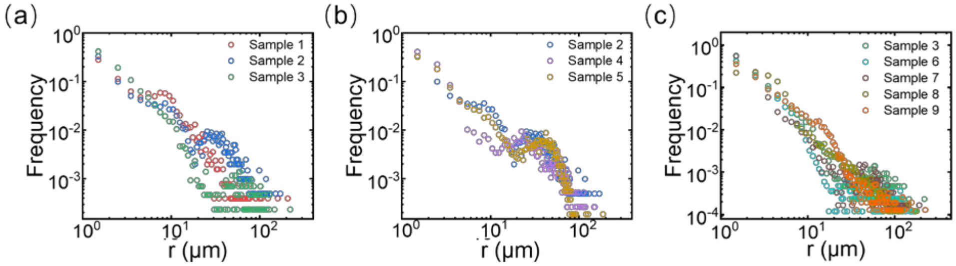

Figure S5. Overall size distribution of MLs-decorated cylindrical reactors (sample 1-9) with with (a) varied $\mathrm{C_{MMA,0}}$, (b) $\mathrm{V_{Sol\ A}}$, and (c) varied flow rates in the solvent exchange process.

width of the size distribution peak decreases when the flow rate increases from 3 to 8 mL/min. If further speeding up the dilution process (sample 8 and 9), the full width of the size distribution is further widened, but the peak between 20 to 200 µm is not obviou and the portion of MLs with lateral radius less than 50 µm also increases.

7. Representative UV-visible spectra of MO solution before and after the irradiation of simulated solar light in sampple 1 to 9

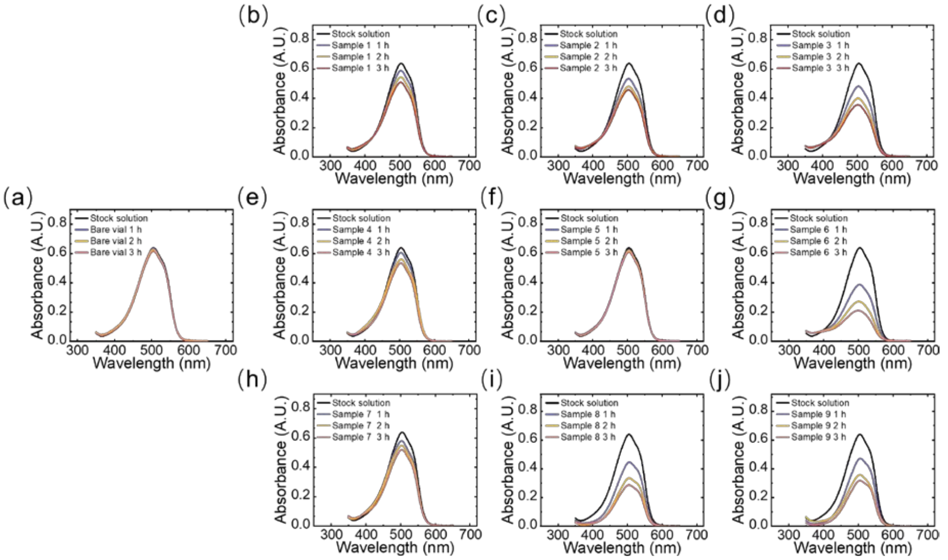

Figure S6. Absorbance spectra of methyl orange (MO) before and after the light treatment under the simulated solar light for 1 h, 2 h, and 3 h with (a) bare glass vial (b) sample 1, (c) sample 2, (d) sample 3, (e) sample 4, (f) sample 5, (g) sample 6, (h) sample 7, (i) sample 8, and (j) Sample 9.

8. Presentative optical images of MLs on irregular reactors (sample 12 and 13)

The variance in the size distribution and surface coverage of MLs on irregular reactors is caused by the differentiated geometry. For example, due to the similar capacity of sample 12 and 13, the amount of solution A and B consumed and the flow rate in the solvent dilution process in the two reactors is almost the same, so as the concentration gradient in the reactors after the same period of time. However, during the unit time, the increased surface area covered by the rising liquid level is larger in the reactor with a larger width, which is sample 13. Therefore, more surface nanodroplets are generated with a similar concentration gradient, resulting in smaller sizes and a higher surface coverage rate of MLs.

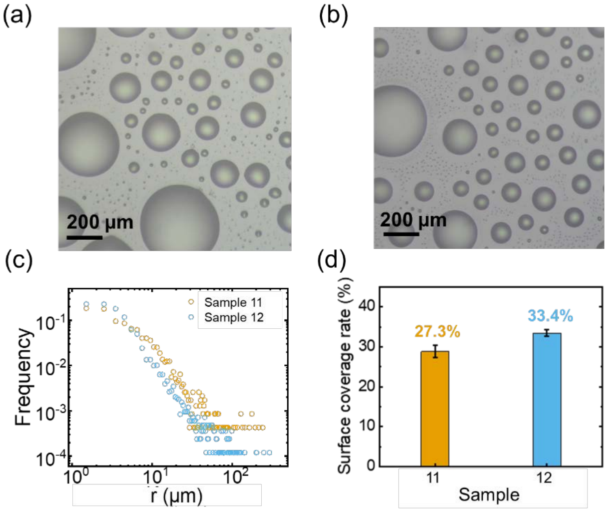

Figure S7. Optical microscope image of MLs-functionalized (a) snowman shape (Sample 12) and (b) petal shape glass reactors (Sample 13). (c) Size distribution and (d) surface coverage rate of surface MLs on the inner wall of double piece and triple piece glass container.

9. Color change of MO solution before and after the light treatment in irregular reactors

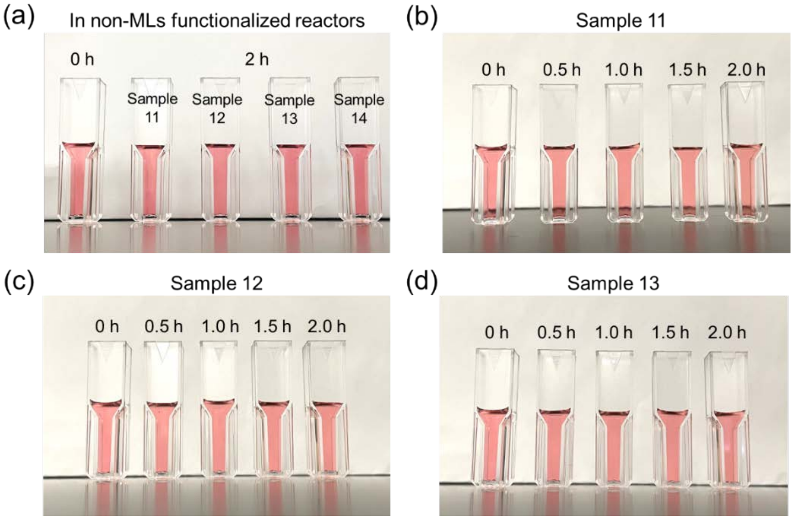

Figure S8. Color change of MO solution (5 mg/L, pH= 3.0) in (a) unfunctionalized irregular glass reactors (sample 11 to 14) under simulated solar light for 2 h. Color change of MO solution (5 mg/L, pH= 3.0) under the irradiation of simulated solar light for different time in MLs-funtionalized (b) snowman shape reactor (sample 11), (c) petal shape reactor (sample 12), (d) three-arms shape reactor (sample 13).

10. The influence of the irradiation direction on the performance of MLs-funtionalized irreagular reactors in the photodgeradation of MO

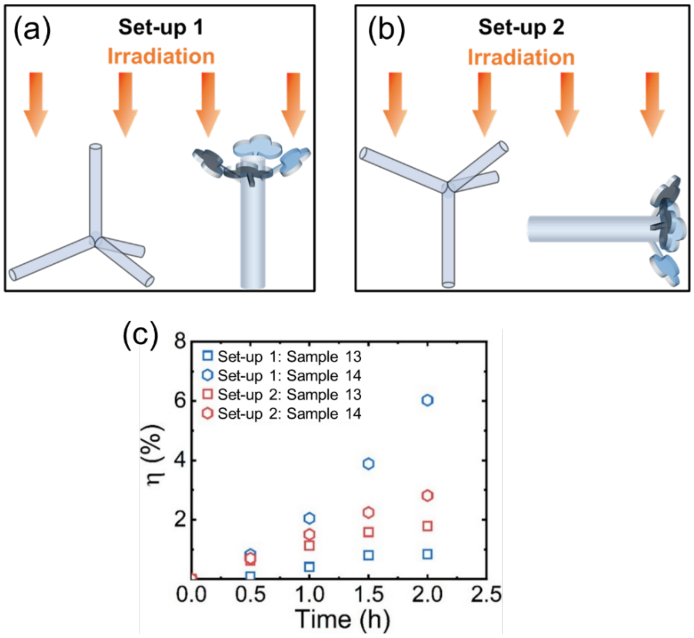

Figure S9. (a-b) Different set-ups for the MLs-functionalized three-arms shape reactor (sample 13) and flower shape reactor (sample 14). (c) The photodegradation efficiency of MO solution (5 mg/L, pH =3.0) under the simulated solar light (1 Sun) with different set-up.

11. Stability of surface MLs after the irradiation of simulated solar light

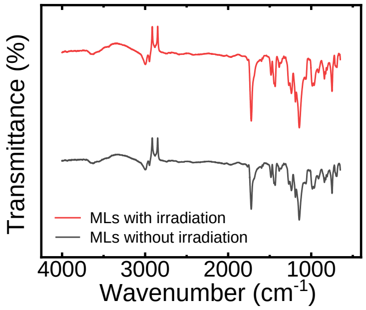

Figure S10. FTIR spectrum of PMMA MLs funtionalized on cylindrical glass reactors (a) before and (b) after the light treatment of more than 10 hours.

References:

[1] Yang, H., Peng, S., Hao, X., Smith, T. A., Qiao, G. G., & Zhang, X. (2014). Surfactant-mediated formation of polymeric microlenses from interfacial microdroplets. Soft Matter, 10(7), 957-964.

[2] Lu, Z., Xu, H., Zeng, H., & Zhang, X. (2015). Solvent effects on the formation of surface nanodroplets by solvent exchange. Langmuir, 31(44), 12120-12125.

Appendix D: Supplementary information for Chapter 6

Supplementary Information_Ch6

Convex and Concave Microlens Arrays with Tunable Curvatures for Enhanced Photodegradation of Organic Pollutants in Water: A Contact or Non-contact Approach

1. Optical simulations of PLMA convex MLAs with varied curvature

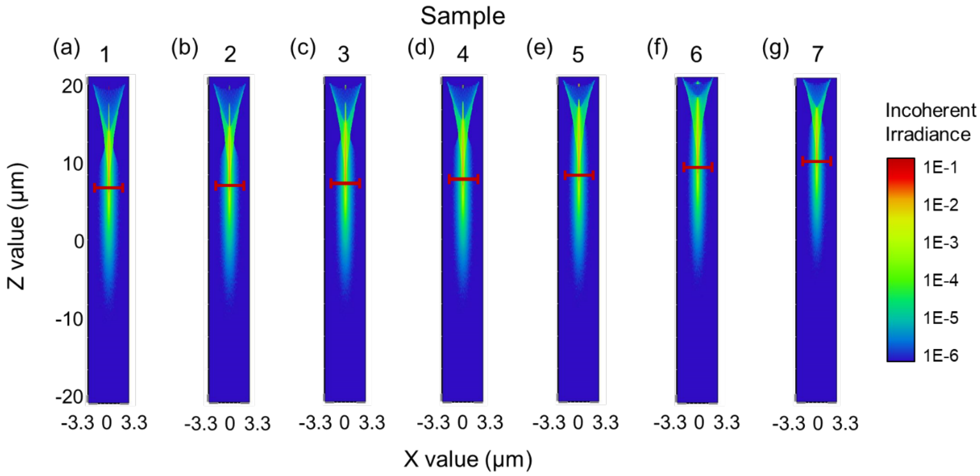

Figure S1. Cross-sectional view of the light intensity profile of a single ML in (a) sample 1, (b) sample 2, (c) sample 3, (d) sample 4, (e) sample 5, (f) sample 6, and (g) Sample 7 by optical simulations. The focal points are labeled by the red bars.

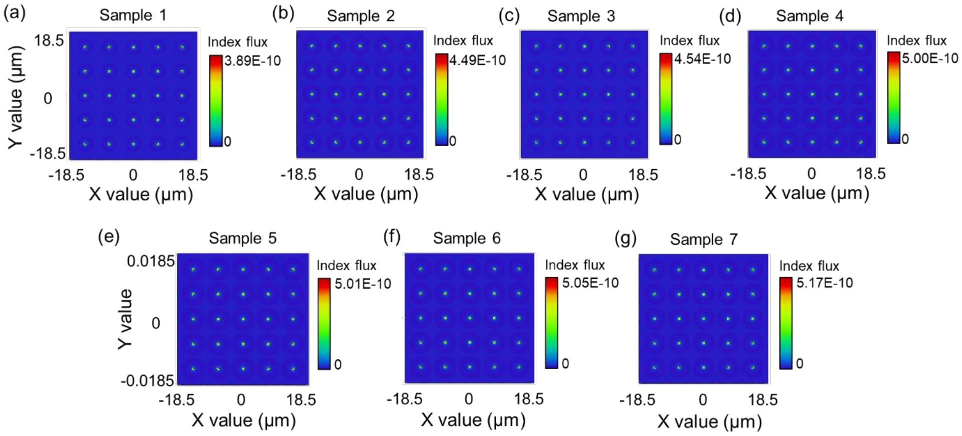

Figure S2. Top view of the light intensity profile of a 5×5 MLA in (a) sample 1, (b) sample 2, (c) sample 3, (d) sample 4, (e) sample 5, (f) sample 6, and (g) Sample 7 by optical simulations.

2. 3D light intensity profiles of PLMA convex MLAs by confocal microscopy

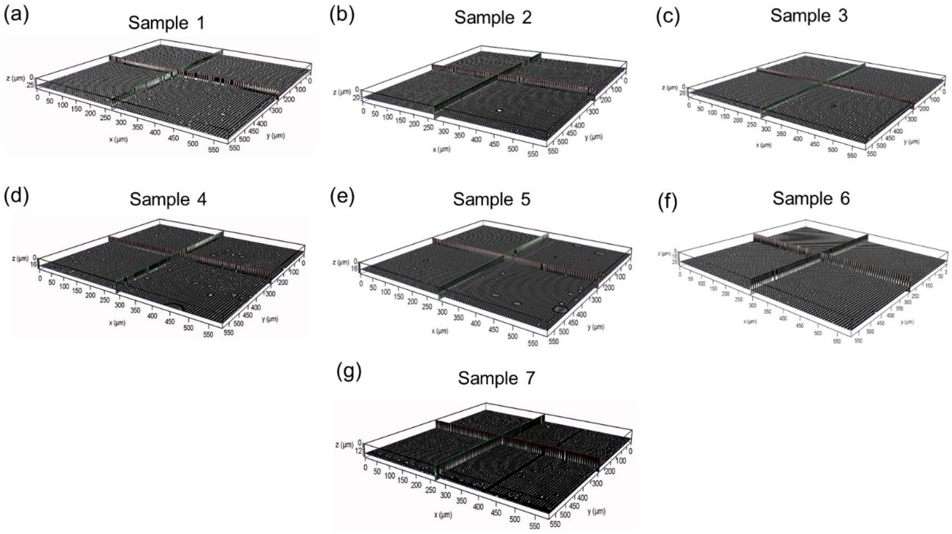

Figure S3. 3D light intensity profiles of PLMA convex MLAs, including (a) sample 1, (b) sample 2, (c) sample 3, (d) sample 4, (e) sample 5, (f) sample 6, and (g) Sample 7 by confocal microscopy.

3. Durability of PHDODA MLA on silicon substrates after peeling concave MLAs-embedded PDMS films off

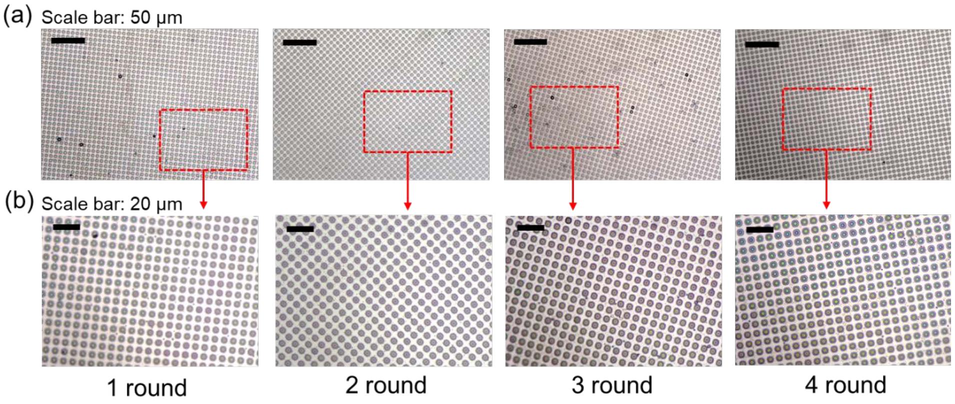

Figure S4. Photos of a hydrophobized PHDODA convex MLA on a silicon substrate after 1 to 4 rounds of replication by PDMS elastomer by optical microscope, under (a) ×20 objective lens and (b) ×40 objective lens.

4. The upper limit of the curvature of PLMA convex MLAs by multi rounds of solvent exchange

For the second round of solvent exchange, the maximum LMA concentration is 4 vol% and the maximum flow rate is 4 mL/h when using sample 1 as the base MLA, or 2 vol% LMA and flow rate at 4 mL/h when using sample 6 as the base MLA. The MLA used as the base for another

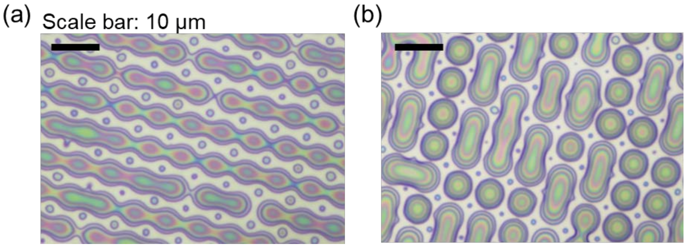

Figure S5. Optical images of the photopolymerized LMA microdroplets after coalescence due to (a) higher concentrations of LMA than the upper limit (b) an MLA with higher curvature than sample 6 being used as the base.

round of solvent exchange process should not have larger curvature than sample 6. If the LMA concentration, flow rate or solvent exchange round go over the limitation mentioned above, the microdroplets coalescence will frequently happen and destroy the highly ordered structure of MLA (as shown in the image below). Therefore, the lateral radius and curvature of the ML can not be infinitely decrease.

5. Transmittance of concave MLA-embedded PDMS films

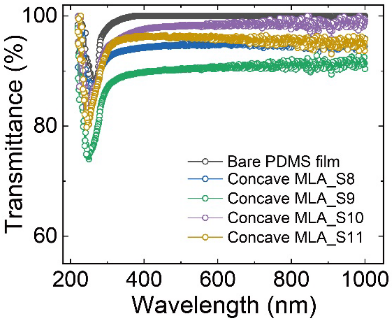

Figure S6. Transmittance curves of the bare PDMS film and concave MLAs embedded PDMS films. The thickness of all films is around 1 mm.

5. Photodegradation of MO in high-turbidity water enhanced by a concave MLA

The turbidity of the Milli Q water dispersed with 0.2 g/L SiO_2, and MO solution with 0.2 g/L SiO_2 dispersed was tested with the turbidity meter. Each sample was tested for 4 times to collect an average value and the error.

Sample	**Turbidity (Unit: NTU)**
Milli Q water with SiO_2 dispersed	154.0 (±3.9)
MO solution (5 mg/L) with SiO_2 dispersed	154.5 (±6.4)

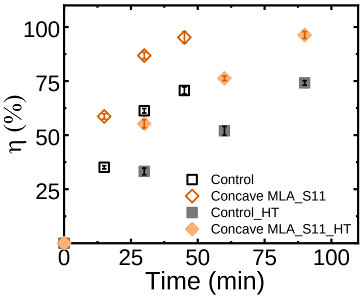

Figure S7. Photodegradation efficiency of MO in Milli-Q water and high turbidity (HT) Milli-Q water prepared by dispersing SiO_2 particles without (Control) and with the concave MLA prepared from sample 11 (Concave MLA_S11).